INAUGURAL-DISSERTATION

zur Erlangung der Doktorwürde der
Naturwissenschaftlich-Mathematischen Gesamtfakultät
der Ruprecht-Karls-Universität Heidelberg

vorgelegt von
Dipl.-Chem. Patricia Maria Wolny
Geboren in Beuthen/Polen

Tag der mündlichen Prüfung: 02.03.2010

NOVEL MODEL SYSTEMS FOR THE INVESTIGATION OF POLYVALENT PROTEIN-HYALURONAN INTERACTIONS ON THE CELL SURFACE

Gutachter/ Referees

Prof. Dr. J. P. Spatz

Physikalisch-Chemisches-Institut
Universität Heidelberg
Max-Planck-Institut für
Metallforschung, Stuttgart

Prof. Dr. Alain R. Brisson

Laboratoire d`Imagerie Moleculaire et
Nano-Bio-Technologie
Université Bordeaux 1

In den Wissenschaften ist viel Gewisses, sobald man sich von den Ausnahmen nicht irre machen läßt und die Probleme zu ehren weiß.

Johann Wolfgang von Goethe, (1749 - 1832),
deutscher Dichter der Klassik, Naturwissenschaftler und Staatsmann

Für meine Eltern.

Für Johannes.

Abstract

The gel-like hyaluronan (HA) rich coat that surrounds many cells has been linked to a variety of vital cellular functions, but the regulatory mechanisms at the cell-HA matrix interface remain poorly understood. For the thorough investigation of specific interactions between the cell surface and HA as well as the structural properties of this supra-molecular matrix, it is desirable to switch from the complex cellular environment to simplified systems. This work aims to find routes towards the development of new *in-vitro* model systems of HA-rich coats.

One approach relies on the immobilization of ectodomains of HA's main cell surface receptor, CD44, on supported lipid membranes (SLBs). Model surfaces with tunable receptor density are exploited to investigate the polyvalent interaction between HA and CD44 in a biologically relevant arrangement. On surfaces that provide a high density of receptors, HA binding increases in a sigmoidal fashion with molecular weight, and becomes reversible below 30 kDa. The physico-chemical properties of these HA films reveal many similarities between the binding behavior of HA chains and flexible polymer chains adsorbing to a homogeneously attractive surface. On surfaces with low receptor surface density binding of HA of sufficiently high molecular weight is irreversible for all, and proportional to the amount of receptors. Quantifying the number of receptors that are available per HA chain provides insight how polyvalent interactions stabilize HA binding on receptor covered surfaces. HA binding is though regulated by both polyvalency and the intrinsic affinity of individual receptors, and we outline a method to disentangle the contributions of both effects.

Another approach envisages the immobilization of HA *via* a terminal biotin moiety at controlled anchor separation. The binding and activity of biotin-receptors on gold and silica is systematically examined with the objective to selectively functionalize gold nanostructured surfaces. We find that streptavidin adsorbs in a functional conformation on gold while resisting binding to silica. First attempts to exploit this selectivity on gold nanostructures are presented.

The confinement of the model systems to solid supports enables qualitative and quantitative characterization by complementary surface sensitive techniques. Here, quartz crystal microbalance with dissipation monitoring and ellipsometry - alone or in combination - as well as microinterferometry provide detailed insight into the formation, stability and morphology of the model surfaces and the HA films, and involved molecular interactions.

The developed model systems with tunable properties can serve as a well-controlled experimental platform for the investigation of the interactions between proteins and HA in a supra-molecular context, and between cells and HA-matrices.

Kurzzusammenfassung

Viele Zellen umgeben sich mit einer gelartigen Hülle aus Hyaluron (HA). Solche Hyaluron-Hüllen spielen eine wichtige Rolle bei einer Reihe essentieller Zellfunktionen. Die Mechanismen, welche die Interaktion im speziellen and der Grenzfläche zwischen HA und Zelle regulieren, sind jedoch nur mangelhaft erforscht. Für ein eingehendes Studium der spezifischen Wechselwirkung zwischen der Zelloberfläche und HA sowie der strukturellen Eigenschaften dieser supramolekularen Matrix, erscheint es sinnvoll, weg von der Komplexität der Zelle zu einem vereinfachten System zu gehen. Es war daher das Ziel dieser Doktorarbeit, Wege zur Entwicklung neuer *in-vitro*-Modelsysteme der HA-Matrix zu finden.

Einer der Ansätze bedient sich der Immobilisierung von Ectodomänen des primären Zelloberflächenrezeptors für HA, CD44, auf substratgebundenen Modelmembranen (SLBs). Solche Modeloberflächen, deren Dichte an Oberflächenrezeptoren kontrolliert eingestellt werden kann, werden benutzt, um polyvalente Wechselwirkungen zwischen HA und CD44 in einer biologisch relevanten Umgebung und Anordnung zu untersuchen. Auf Oberflächen mit hoher Rezeptorbedeckung ist die Bindung von HA mit geringem Molekurlargewicht (unter 30 kDa) reversibel und nimmt sigmoidal mit dem Molekulargewicht der HA-Kette zu. Die physikalisch-chemischen Eigenschaften dieser HA-Filme zeigen viele Parallelen zum Adsorptionsverhalten von flexiblen Polymerketten an eine homogen attraktive Oberfläche. Auf der anderen Seite, ist die Bindung von HA - gegeben das Molekulargewicht ist ausreichen - auch bei geringen Rezeptordichten irreversibel und proportional zur Menge der Rezeptoren. Bestimmt man quantitativ die Anzahl der Rezeptoren, die jeder HA-Kette zur Verfügung stehen, wird deutlich, dass polyvalente Wechselwirkungen die Bindung von HA an die oberflächengebundenen Rezeptoren stabilisieren. Die Regulierung der Bindung von HA unterliegt jedoch sowohl Polyvalenzeffekten als auch der intrinsischen Affinität der individuellen Rezeptoren, und wir leiten hier eine Methode ab, mit der sich die Beiträge beider Effekte voneinander abgrenzen lassen.

In einem weiteren Ansatz soll HA über eine terminale Biotin-Einheit in kontrollierten Abständen auf einer Oberfläche immobilisiert werden. Mit dem Ziel, gold-nanostrukturierte Oberflächen selektiv zu diesem Zweck zu funktionalisieren, werden die Bindung und Aktivität verschiedener biotin-bindender Proteine an Gold und Siliziumoxid-Oberflächen systematisch untersucht. Es stellt sich heraus, dass Streptavidin die besondere Eingenschaft hat, in aktiver Form auf Goldoberflächen zu adsorbieren, während es keinerlei Interaktion mit

der Siliziumoxid-Oberfläche eingeht. Wir zeigen, wie diese Selektivität in ersten Versuchen zur Funktionalisierung der nanostrukturierten Oberflächen ausgenutzt werden kann.

Alle vorgestellten Modelsysteme basieren auf festen Substraten, eine Eigenschaft, die die qualitative und quantitative Charakterisierung mit Hilfe komplementärer, oberflächensensitiver Untersuchungsmethoden ermöglicht. Die Verwendung der Quartz-Kristall-Mikrowage mit Dissipationskontrolle (QCM-D) und Ellipsometrie - einzeln oder in einem kombinierten Aufbau - sowie Mikrointerferometrie erlauben detailierte Einsichten in die Bildung, Stabilität und Morphologie der Modeloberflächen, der HA-Filme und der damit einhergehenden molekularen Wechselwirkungen.

Die hier entwickelten Modelsysteme, die sich dadurch auszeichnen, dass sie gezielt eingestellt und kontrolliert manipuliert werden können, eignen sich als gut charakterisierte experimentelle Plattformen zur Untersuchung der spezifischen supramolekularen Wechselwirkungen zwischen Proteinen und HA. Sie können des Weiteren interessante Anwendungen bei Studien der Interaktion zwischen Zellen und den HA-Filmen finden.

Contents

CHAPTER 2

ON THE FUNCTIONALIZATION OF HOMOGENEOUS AND NANOSTRUCTURED SURFACES WITH BIOTIN-RECEPTORS 35

Chapter 1

Introduction

1.1 Objectives

A major aim of this thesis work was to develop new designs for *in-vitro* model systems which enable the in-depth investigation of carbohydrate-rich cell coats in a biological and physico-chemical aspect for the quantitative study of regulatory mechanisms of in protein-carbohydrate interactions. Another objective was the detailed characterization of the adsorption behavior of biotin-receptors to find a suitable and simple method for the funcionalization of biotechnologically relevant materials: homogenous and nanostructured surfaces of gold and silica.

1.2 Structure of the thesis

In the present chapter 1 the biological background and relevance of the pericellular coat (PCC), and the experimental, conceptual and theoretical approaches that were employed for this work will be introduced.

In chapter 2 a study on the interaction of proteins of the avidin familiy with various surfaces will be described, which led to a method for simple protein immobilization on gold surfaces.[1] The results will be employed in first steps towards the grafting of hyaluronan (HA) to nanoarrays of gold particles.

Chapter 3 will present the design of model systems of HA-rich coats with the premise to closely resemble the natural coat in its typical dimensions, its ability to self-organize into supra-molecular assemblies and, wherever possible, to use the relevant natural biomolecules. It will also focus on the quantitative characterization of these model systems by means of quartz crystal microbalance with dissipation monitoring (QCM-D), ellipsometry and

reflection interference contrast microscopy (RICM) with special interest dedicated to the interaction between HA and its main cell surface receptor CD44.

Chapter 4 will follow up with unraveling quantitatively the mechanisms and the polyvalent character underlying CD44-HA interactions under varying conditions such as amount, type and presentation of CD44 to HA. The analysis will take advantage from the use of a new combined set-up of QCM-D and ellipsometry.

Concluding remarks and perspectives will be depicted in chapter 5. A detailed description of the employed techniques and experimental procedures will be provided in chapter 6. For additional information on used abbreviations, materials and protocols the reader is referred to the appendix.

1.3 The cell membrane

The outer cell surface represents a fascinating interface with utmost importance for the life of organisms. In animal cells this boundary is defined by the plasma membrane, which encloses the cell and establishes the differences between the cytosolic and the extracellular enviroment.[2] The plasma membrane is made up of a bilayer of laterally arranged phospholipid (and few other lipid-) molecules, which self-assemble such that their hydrophobic tails face each other, while the hydrophilic head groups are exposed to the aqueous environment (figure 1.1). This lipid bilayer of about 5 nm thickness contains numerous transmembrane (integral) proteins. Some function as e.g. transporters of hydrophilic species through the otherwise impermeable membrane. Others act as specific receptors to trigger signaling cascades into and out of the cell. While proteins on the inner cell surface link the membrane to filaments of the cytoskeleton (actin filaments, microtubules and intermediate filaments), protein domains on the outer cell surface mediate interactions of the cell with the extracellular environment and with other cells. The latter often carry carbohydrates, which contribute to regulate various receptor-ligand interactions or act as ligands themselves. Additionally, other carbohydrate residues can be covalently linked to certain lipids.

Biological membranes have been studied extensively.[3] Model membranes have emerged as objects for the investigation of chemico-physical properties[4, 5] and have since been exploited for the study of membrane dynamics and components,[6] protein interactions,[7-9] toxins[10] or as experimental platforms for the immobilization of different types of molecules.[11-13] The model

membranes that were used for a part of this thesis were supported lipid bilayers (SLBs). These will be introduced in chapter 3.

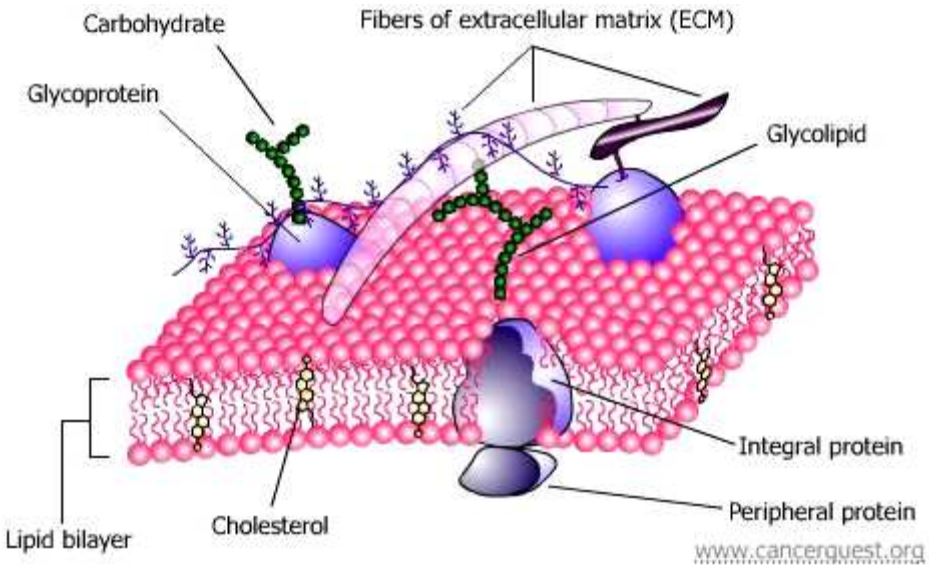

Figure 1.1: Scheme of the cell membrane and extracellular matrix components. Reproduced from ref.[14].

1.3.1 Outside the cell

Above the cell surface different coat-like regions can be distinguished. Lipid or protein linked, membrane proximal carbohydrates are often referred to as glycocalix. Further, cells built, and manipulate their environment by secreting a number of components that sum up to what is called extracellular matrix (ECM). This matrix provides mechanical support and contributes to the communication of the cell with its environment. The macromolecular components of the ECM are fibrous proteins (such as fibronectin, keratin or elastin) and polysaccharides. Many of these polysaccharides belong to the family of glycosaminoglycans (GAGs). Some mammalian cells create another special environment in their immediate surrounding that is different from the rest of the extracellular space. This additional layer has been termed pericellular coat (PCC)[15, 16]. Such coats are typically highly hydrated, and therefore invisible by conventional light microscopy. They can be visualized, however, by particle exclusion assays (PEA)[17, 18] (figure 1.2). In-vivo and in-vitro PCCs have been shown to be sensitive to treatment with hyaluronidase, an enzyme that digests hyaluronan (HA), illustrating that HA forms the backbone of the PCC.[15, 19] HA is tethered to the surface via

non-covalent, protein-carbohydrate interactions. Gaining insight into the composition, structure, properties and function of the PCC is a main motivation of this thesis work.

It should be mentioned that it is difficult to define clear boundaries between the parts of the extracellular space, which are termed glycocalix, ECM or PCC. These terms have been used in the literature in various ways and leave room for ambiguous interpretations.[19-25] In the context of this thesis work, I define the PCC as the HA dependent matrix that is linked to the cell membrane.

1.4 How can model systems improve the understanding of biological phenomena?

Working at the crossover of biology, chemistry and physics often opens up new points of view regarding the way to approach an unsolved question. Not least the interdisciplinary work of scientists with backgrounds, e.g., in biology, biotechnology, (surface) chemistry, physics and engineering, led to the development of highly sensitive analysis methods, gave rise to a new generation of tools, which reduced the accessible length scales to micro-and nanometers and opened doors to the fusion of scientific communities. Biological surface science [26] is today a wide field that includes, for example, microarray technology, lab-on-a-chip, medical implants, MEMS (Micro-Electro-Mechanical Systems) or NEMS (Nano...) - only a few of many popular catchwords, which became familiar during the last two decades.[27, 28] The gathered knowledge on the fabrication of surfaces on the micro-and nanoscale, chemical and biotechnological methods of surface functionalization and a pool of available biological probes can be exploited to create well-defined mimics of natural systems. Such mimics or model-systems are, of course, not capable of capturing the entire complexity of a biological system. Their advantage is their simplified architecture. By reducing the complexity of the system to a few parameters that can be controlled, the quantitative investigation of specifically chosen individual interactions becomes accessible. In contrast, cells often employ a complex machinery of regulatory mechanisms, which can compensate for each other and the effect of an experimental intervention may be vague.

It may be difficult to directly correlate a single detail of an entire system with its function. To add an additional level of complexity, the function of proteins, compartments of a cell or a tissue, for example, underlie a highly dynamic regulation and are tightly connected to external conditions within an organism,[2, 29, 30] which can hardly be realized in an artificial system. Nevertheless, the thorough knowledge about the very details is an inevitable piece of a puzzle

to be added in order to finally obtain a true understanding of complex biological systems. It is the virtue of model-systems that they address a very specific question starting from a rather simplified point of view, but still remain expandable for an up-grade in complexity.

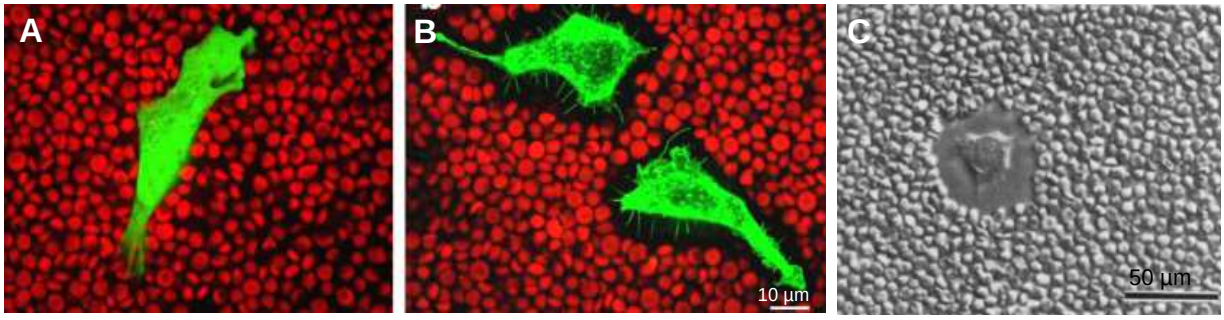

Figure 1.2: Pericellular coat (PCC) visualized by a particle exclusion assay (PEA). The erythrocytes added to the cultured cells cannot penetrate to the plasma membrane when a PCC is present around the cells (B, C). A and B: human breast adenocarcinoma cells (MCF-7) lacking (A) and expressing (B) hyaluronan synthase3. Erythrocytes are shown in red, the cultured cells in green. Micrographs adapted from[17]. Scale bar applies for A and B. C: A human bladder carcinoma cell presenting a PCC visualized by a PEA. Adapted from[18].

1.5 The pericellular coat (PCC)

1.5.1 Structure and function

The pericellular coat (PCC) is a carbohydrate-rich, multifunctional soft layer around many cells acting as sensitive regulator for cell behavior, such as adhesion or cell shape.[15] The cell is capable to dynamically regulate its coat, and its extension strongly depends on cell type or state and its thickness covers an amazing range between a few nanometers and several micrometers (figure 1.2).[15, 19, 22, 23] Such coats are typical for chondrocytes in articular cartilage,[31] vascular endothelial cells,[32] smooth muscle cells[33] or oocytes,[34] to mention a few examples. A long, linear polysaccharide - hyaluronan - constitutes the backbone of the often hydro-gel-like film.[15, 16] As hyaluronan is the cardinal molecule of this thesis, it merits an own paragraph on its nature (see next section). Because of its gel-like, highly viscous behavior and its extension, HA and the PCC were initially thought of as a cushion-like, protective structure with the function to damp external mechanical forces.[35-37] The functions of the PCC are, however, more multifaceted. It is a barrier for the diffusion of certain molecules within the extracellular space.[2, 38, 39] Furthermore it was found to act as a mechanotransducer[38, 40] of fluid

shear stress in blood vessels to the cytoskeleton, thereby also playing a role in different signaling pathways.[41-44]

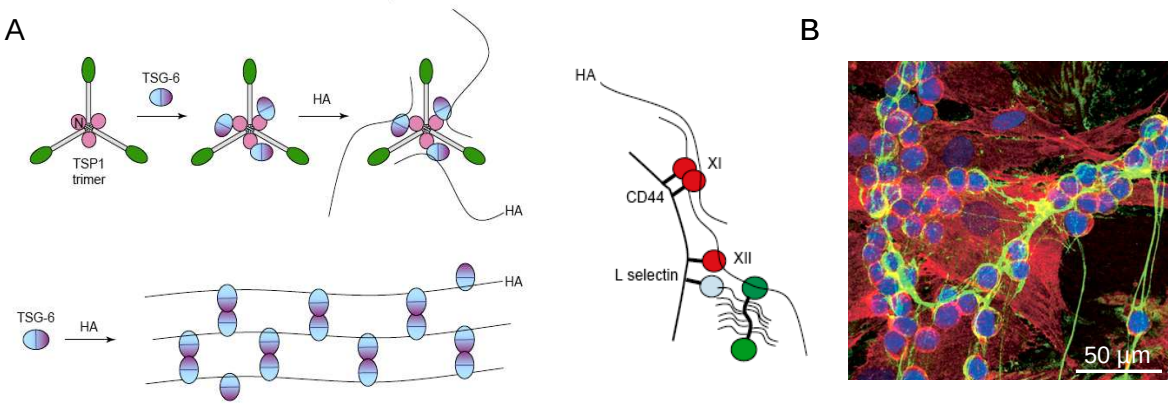

Figure 1.3: A) Putative structures of complexes of HA with different hyaladherins as proposed to be involved in inflammation. Scheme adapted from ref.[45] B) Cable-like structure of crosslinked HA *(bright green)*, which exhibits strong pro-adhesive properties for monocytes *(nuclei in blue)*. Micrograph adapted from ref.[33].

How can a matrix that consists of rather simple components (HA and water) display such a diversity of functions? How can the cell regulate the presence and performance of this coat? In fact, HA is always in company of various soluble and cell membrane bound proteins, so-called hyaladherins.[42] These interact with the long HA chain - often in a multiple fashion - thereby modulating the chain's conformation or its linkage to the plasma membrane (figure 1.3).[41, 46, 47] Due to this interaction, HA can self-organize into different types of supramolecular architectures, thus influencing the assembly, the morphology and the material properties of the PCC.[15] CD44, for example, is a main cell surface receptor for HA. In contrast to CD44, aggrecan, product of the tumor necrosis factor-secreted gene-6 (TSG-6), inter-α-inhibitor (IαI), pre-α-inhibitor (PαI) or pentraxin 3 (PTX-3), are soluble proteins that are present in the matrix. Some of them have been proposed to be involved in crosslinking of HA,[45] which can result in the formation of cable-like structures of HA (figure 1.3) or expanded matrices.[48] Such ultra-structures often define the performance of the PCC with different functions. For example, cable-like HA appears to be pro-adhesive for leukocytes[33] and, therefore could be pro-inflammatory.

Taken together, the PCC is a complex supra-molecular edifice. Investigating the role of the individual players in their interaction with HA is a field that is today studied intensively.

1.6 Hyaluronan is a simple polysaccharide with intriguing properties

1.6.1 Structure and characteristics

Hyaluronan (HA), also called hyaluronic acid, is a naturally occurring biopolymer that was discovered by Meyer in 1934 as a main component of the vitreous hmor of cattle eye.[49] It is composed of repeating disaccharide units of glucuronic acid and N-acetylglucosamine (figure1.4). HA is a linear, unbranched and highly negatively charged polysaccharide and the only known glycosaminoglycan that is not sulfated.

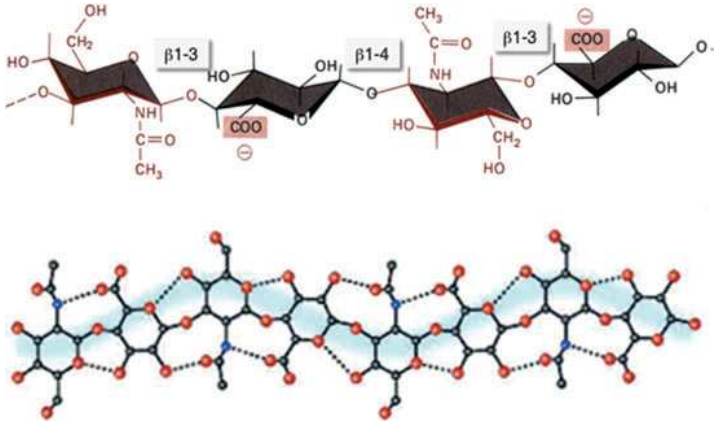

Figure 1.4: Structure of hyaluronan (HA). Top: repeating disaccharide units. Bottom: hydrogen bonds within the chain (shown for an 8-mer), which stiffen the polymer. Scheme from ref. [50].

HA is abundant in the pericellular space of many mammalian cells.[41] It is synthesized by cell membrane associated enzymes inside the cell - hyaluronan synthases (HAS1, HAS2 and HAS3) - which extrude the polymer through the plasma membrane into the extracellular space[51, 52] (figure 1.5). Typically, molecular masses from 10^6 to 10^7 Da are reached, corresponding to up to 25,000 disaccharide units or contour lengths between 2 and 25 µm.[16] However, somewhat shorter HA chains ($\approx 10^5$ Da) were detected, too, as a product of HAS1.[53] HA can be degraded into fragments of different size by hyaluronidases.[16, 54] There is strong indication that the biological activity of HA depends on HA's molecular weight.[55-57] Whereas high molecular weight HA was proposed to have a quieting and anti-inflammatory effect,[37, 58] low molecular weight HA was linked to the expression of several pro-inflammatory agents.[59, 60]

In solution HA readily retains large amounts of water and ions and forms a viscoelastic liquid.[61, 62] This property makes it an essential component for the maintenance of tissue integrity, e.g. in cartilage[63] or during morphogenesis.[64]

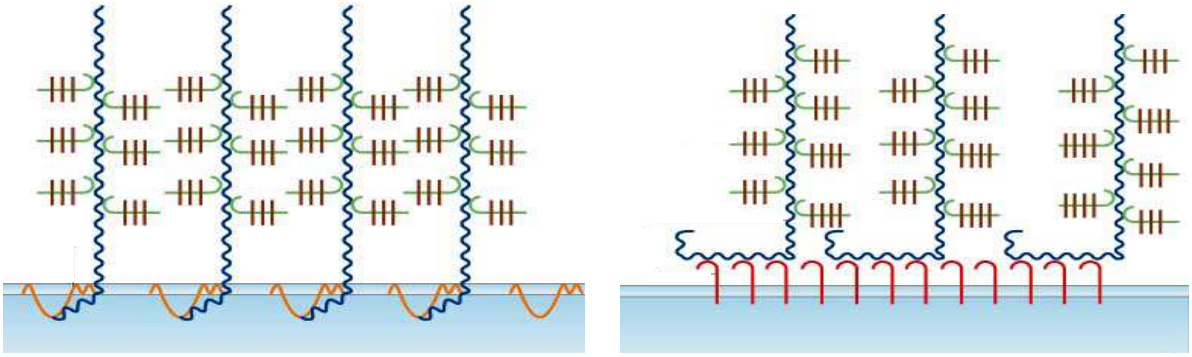

Figure 1.5: Proposed mode of HA anchorage to the cell surface. Left: HA is tethered to the cell surface through retention by hyaluronan synthases. Right: HA is anchored to the cell surface by binding to specific receptors as CD44. Within the PCC HA can be associated to other HA binding molecules like the proteoglycan aggrecan as depicted here. Cartoon adapted from ref.[16] (not drawn to scale).

1.7 CD44 - a main cell surface receptor for HA

1.7.1 Protein structure

CD44 is a type I* membrane glycoprotein that was identified by several groups and initially named differently (as Pgp-1 (phagocytic glycoprotein-1),[65] ECMRIII,[66] HUTCH-1 or gp85.[67, 68]) due to the different context in which it has been studied.[67] The established name today catalogues the protein into a family of cell surface receptors mainly involved in immune responses.[68] The **c**luster of **d**ifferentiation (CD...). CD44 consists of a C-terminal cytosolic tail, which anchors it to the cytoskeleton, a transmembrane part and an extracellular part

* Transmembrane proteins are classified into different types depending on the transmembrane domain and the orientation of the C- and N-terminus, respectively. Type I means that the protein contains a single transmembrane stretch with the C-terminal part on the cytosolic site of the membrane.

consisting of a membrane proximal region and the N-terminal HA binding domain (figure 1.6A).

The HA binding domain - a sequence of about 100 amino acids - forms a disulfide-linked loop and is centered around the link module, the most conserved region in the structure of the hyaladherin[42] family (LYVE-1, TSG-6, link protein, aggrecan, versican, among others).[69] In contrast to link modules of other hyaladherins the HA binding domain of CD44 is extended towards the membrane proximal region with direct effect on CD44`s HA binding affinity.[69] The most common form, the so-called hematopoietic CD44 (CD44H - the term arises from its abundance on hematopoietic cells) has an apparent molecular weight of 80-100kDa,[70] which exceeds the mass as estimated from the amino acid composition. This deviation has its origin in posttranslational N- and O-linked glycosylation. DNA cloning experiments revealed that CD44 exists in various isoforms depending on the cellular function.[68] The membrane proximal region is, additionally, subject to alternative splicing, which results in the expression of variant exons in various isoforms of CD44 (but not in CD44H) (figure 1.6A). The role of the ECD has not been solved yet. It may be speculated whether the ECD comprises binding sites for carbohydrates, which could contribute to more sterical hindrance among the receptors, or, on the contrary, stabilize a favorable conformation of the receptor. A study suggests an ECD specific homodimerization and oligomerization among splice variants of CD44 (but not for hematopoetic CD44), which results in increased HA binding ability.[71]

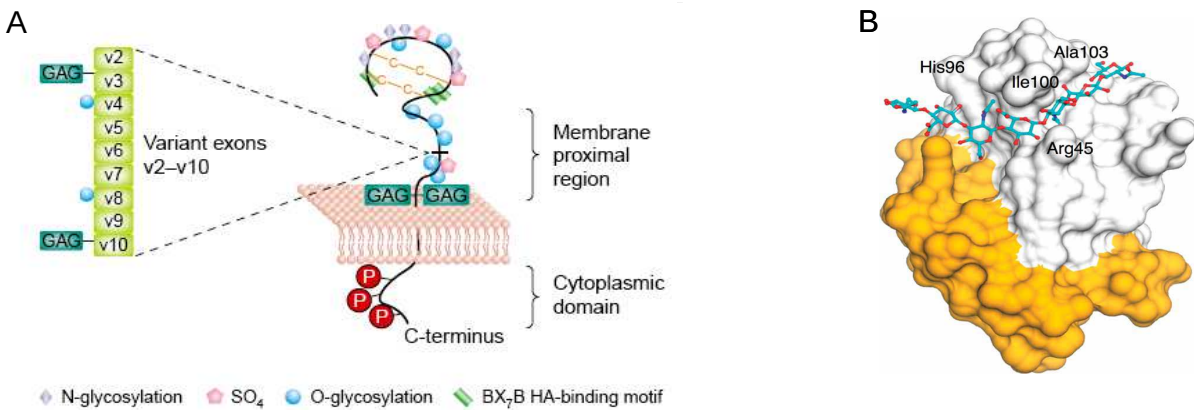

Figure 1.6: A) Scheme of CD44 showing the intracellular C-terminal end, the variable membrane proximal region and the N-terminal HA-binding domain[70]. B) Model of the CD44 HA binding domain in complex with a part of the HA chain as derived from crystal structures[72]. The HA binding site is shown in white, whereas the extension lobes are depicted in yellow. A representative HA chain *(blue)* fragment of 8 sugars monomers is embedded into the binding grove.

1.7.2 Interaction with HA

Although CD44 carries binding sites for a number of extracellular molecules, like fibronectin or chondroitinsulfate, it shows most specificity for hyaluronan (HA), for which it constitutes the primary cell surface receptor (figure 1.5).[73]

The repetitive structure of the long HA chain is an important premise for polyvalent protein-HA interactions[41, 46, 47] as has been proposed for CD44.[41, 47, 74] A rather small footprint of 4 sugars along the HA chain is embedded into the groove of the HA binding domain and contributes to the core interaction.[72] However, 6-10 sugars, depending on the cell type, have been found to effectively compete for binding with polymeric HA, indicating that it is 6-10 sugars, which constitute one binding site for CD44.[47, 72, 75] A single HA chain can, thus, display more than a hundred bindings sites.

Recently, Banerji and coworkers successfully crystallized CD44 in two conformational states: alone and in complex with HA. They could thus demonstrate the structural origin of the HA binding, which is dominated by hydrogen bonds (figure 1.6B).[72] Noteworthy, this is the first crystal structure that was obtained for a hyaladherin in complex with HA.[72]

CD44, similar to other hyaladherins, was proposed to establish polyvalent bindings events with HA[41, 47, 74] thereby turning a low affinity system to a high avidity system[*]. Such a strategy is common to many cell surface recpetors.[77] It was shown that HA binding avidity increases with increasing expression of CD44[47, 78] or local enrichment of the receptors induced from within the cell.[47, 79]

1.7.3 CD44 binds HA with low affinity

The K_D (dissociation constant) was estimated to be around 5-150 µM[72, 80] (at physiological pH) - which is rather low if compared with, for example, aggrecan (≈ 20 nM[81]) or TSG-6 (< 1µM[82] at pH, where the affinity of TSG-6 is highest[83]).

[*] The terms *affinity* and *avidity* will be employed frequently throughout this thesis. It is therefore reasonable to distinguish them clearly. A more detailed description of the definitions will be given in chapter 3. The affinity of binding between two molecular counterparts is an intrinsic measure for the stability of the binding and is described by the equilibrium constant for the dissociation of the complex K_D[76]. Avidity, in contrast, describes the collective effect of multiple receptors, which together can bind to multiple binding sites on a ligand. By acting collectively, many low affinity interactions can be stabilized to form a persistent complex

The rather wide range of K_D (5-150 µM) raises the question, what determines the different affinity states of CD44. Several mechanisms have been discussed.

The crystallization of the hyaluronan binding domain of HA revealed two different conformational states of the binding site.[72] It was found that upon binding of HA a certain amino acid residue in the binding groove shifted into a position, in which it could additionally interact with the bound HA, suggesting the possible existence of a high and a low affinity state of CD44.[69] To date, it is, however, not known, whether such conformations occur *in-vivo*, too, and if so, whether the high affinity state exists per se on certain CD44 isoforms or it is induced by binding of HA.[72]

CD44`s intrinsic affinity for HA was demonstrated to partly arise from the type and the degree of posttranslational glycosylation.[47, 80, 84, 85] N- and O-linked glycans on the protein were shown to drastically alter the intrinsic affinity of CD44.[80, 84] Such glycosylations can have both, positive and negative effect on HA binding.[80, 86] In general, N-glycosylation reduces HA binding, when terminal sialic acid is present.[86] It was demonstrated that removal of sialic acid enhanced HA binding.[80, 85, 87] N-glycans with residues of N-acetylglucosamine (GlcNAc), however, were found to have a positive effect on HA binding.[80] O-glycosylation can have an enhancing effect in the absence of N-glycans.[80, 88] The inhibitory effect on HA binding was proposed to be caused by the steric hindrance or charge repulsion between either the receptor and HA or between the receptors themselves (figure 1.7).[78, 86, 87] Another possiblity is that the presence or absence of glycans affects the conformation of the protein, which may be critical for HA binding.[47, 86]

Notably, the presence of glycan residues on CD44 does not necessarily have to change the intrinsic affinity for HA.[80] For example, if less steric hindrance (due to bulky residues) or charge repulsion allows the receptors to organize close-by, HA binding would be enhanced simply due to increased avidity (not afffinity).[47, 78] Heterogenity in HA binding within one cell population indicates that (de-)glycosylation is probably not the only mechanism to regulate CD44-HA interaction, as CD44 expressed in the same cell population was shown to display the same glycosylation pattern.[80]

Unlike other hyaladherins, CD44 does not necessarily bind HA constitutively. Lesley et al.[89] identified three different activation states on lymphoid cell lines: 1. inactive (no HA binding), 2. inducible (binding, if activated by e.g. certain monoclonal antibodies (mAbs) or

phorbolester*) and 3. constitutively active (always binding HA).[47, 84, 89] What is the origin of different activation states? It has been speculated that a conformational change in the HA binding domain, as crystallized by Banerji and coworkers, may be one possible mechanism for the switching between different activation states.[72] Alternatively, several studies demonstrated that N-linked glycosylation on CD44 was responsible for a decreased affinity of CD44 to HA[78, 80, 87]. Cells exposing inducible forms of CD44 could be rendered active after site-specific N-deglycosylation.[78, 80, 87] These findings suggest that at least part of the activation state is linked to the intrinsic affinity of the receptors. However, the effect of inducing monoclonal antibodies (mAbs) implies an alternative activation pathway that is related to polyvalent interactions and changes in avidity, rather that affinity. There is some evidence that certain mAbs increase the efficiency in HA-binding in inducible and active cell lines by oligomerization of the receptor.[47, 91]

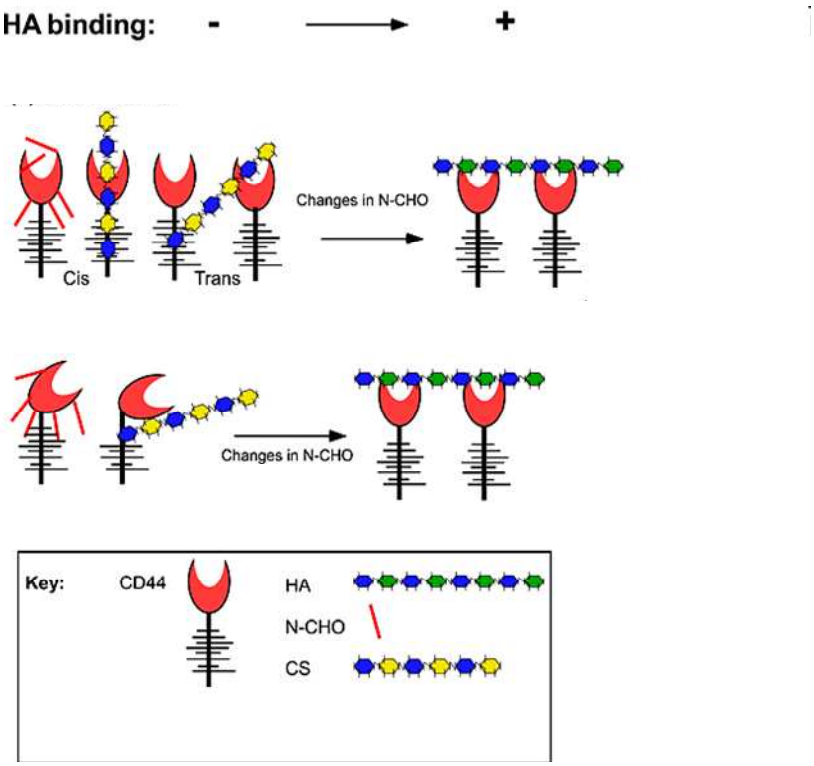

Figure 1.7: Putative effects of CD44 glycosylation. Reduced HA binding by CD44 can either arise from steric hindrance *(top)* or conformational changes *(bottom)* due to different types of glycosylation. Cartoon adapted from ref. [86].

* Phorbol ester are biologically occuring organic compounds that have been linked to tumor promotion via a protein kinase C activating pathway.[90]

1.7.4 Modifications on HA can alter binding by CD44

There is evidence that the way in which HA is presented to CD44 can alter the interaction of both molecules. For example, up-regulated levels of HA have been shown to stimulate CD44 dependent leukocyte interaction[92]. Also, soluble hyaladherins like TSG-6 and SHAP* (Serum-derived Hyaluronan-Associated Proteins) can bind to HA and enhance HA binding by CD44.[33, 74, 95] It was proposed that the binding of certain soluble hyaladherins can crosslink HA, thus enhancing the interaction with CD44,[33, 45, 74] probably due to increased avidity.

1.7.5 Résumé

HA binding by CD44 is determined by a number of factors like expression level of CD44,[47, 78] post-translational glycosylation,[80, 84, 87] activation state[47, 89] or mode of presentation of HA to the receptor.[33, 45, 56, 74] Considering the available information on HA binding by CD44, it remains difficult to correlate each factor explicitly to an affinity or an avidity effect. Different mechanisms for the regulation of CD44-HA interaction could be identified. Given the multiple and sometimes apparently antagonistic cellular functions the CD44-HA interaction was proposed to be involved in, it is not clear yet, which mechanisms - alone or in combination - come into action under specific physiological conditions.[86] In particular, the contribution of the specific interaction between CD44 and HA to the relationship of structure and function of the PCC remains to be elucidated.

1.8 Mimicking the PCC

Although progress has been made in understanding the impact of protein-HA interactions on the cellular level and to some extent also on the molecular level, there is still a gap of knowledge for the intermediate scale - the supra-molecular level. One big question is the mechanism and magnitude of the polyvalent interaction of many hyaladherins with HA.[41] How different hyaladherins interact with HA and how they contribute to the supra-molecular structure still remains largely elusive. Well-defined model systems - mimics of the PCC - are

* SHAPs have been identified as the heavy chains of inter-α-inhibitor (IαI).[93] So far, the SHAP-hyaluronan complex represents the only case with covalent hyaluronan-protein linkage.[94]

one approach for a qualitative and quantitative investigation of HA and its interaction with selected proteins.

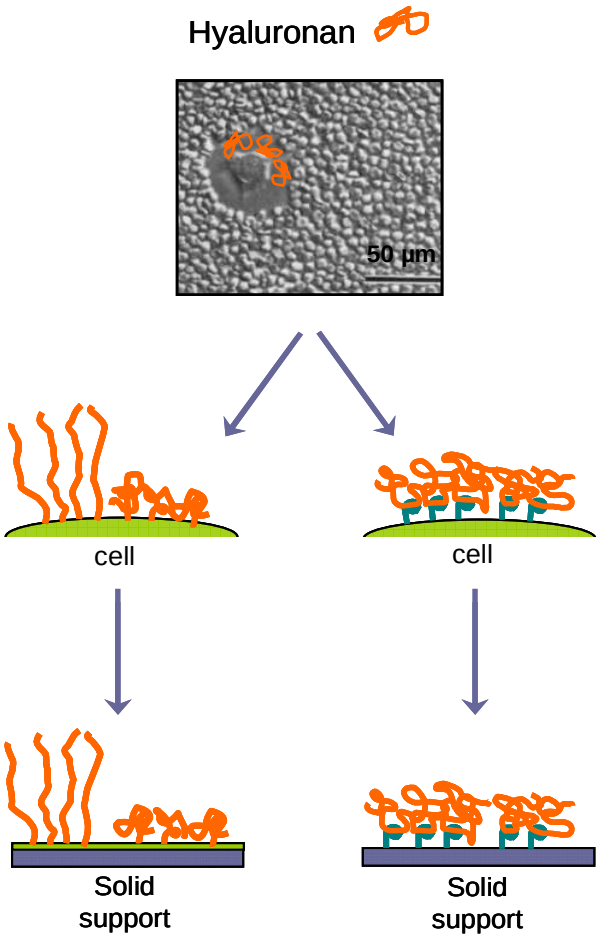

Figure 1.8: From living cells toward surface based model systems of the PCC. Left panel: end-grafted HA in either brush or mushroom conformation. Right panel: HA chains bound to a specific cell surface receptor. Micrograph adapted from[18].

Pericellular matrices depend on the anchorage of HA to the cell surface, which occurs either by HA synthases in an end-on manner or by multiple binding of specific receptors along the chain (figure 1.5). Within this thesis work model systems of the PCC that represent both situations have been employed (figure 1.8).

1.8.1 Existing approaches towards HA immobilization

As the present work introduces new approaches towards the immobilization of HA to surfaces, it is mandatory to mention here what has been reported for HA linkage to surfaces

until today. Prominent approaches were recently reviewed and discussed in detail by Morra.[96] Next to the simplest approach of passive adsorption of HA to plastic lab ware,[97] the formation of polyelectrolyte multilayers by alternating polycationic and polyanionic layers was investigated, e.g., for combinations of chitosan or poly(L-lysine) with HA.[98, 99] Covalent coupling of HA chains via carbodiimide chemistry or photoactivation of azide precursors was realized on a variety of materials including glass, polystyrene and mixed supported lipid bilayers.[5, 100, 101] Whereas the polyelectrolyte multilayers are mostly employed for the assembly of rather thick layers and the study of interactions with the HA film, the covalently linked films were used to investigate the morphology and the behavior of the HA films themselves.[96]

Sengupta et al.[102] reported HA immobilization by employing the trivalent HA binding protein p32[103]. The protein was equipped with a histidine-tag and coupled to a mixed supported lipid bilayer via Ni^{2+}-NTA complex formation[102]. The viscoelastic properties of the HA film were probed as a function of film thickness. The thickness of these films was inhomogenous (probably due to a big molecular weight distribution of the HA sample) and did not exceed 250 nm for HA of about 1 MDa in molecular weight.

The grafting of end-biotinylated HA of well-controlled size to streptavidin (SAv) coated supported lipid bilayers was presented recently by Richter et al..[12] Therein, the grafted HA chains formed films with thicknesses up to 600 nm depending on the molecular weight of HA and the density of the anchor points.[12] This model system represents the mode of attachment pertinent to HA synthases. Another group used the SAv-biotin interaction for immobilization of HA, too,[101] however lacking the high degree of control over HA size and HA functionalization. In this case the HA chains were biotinylated randomly along the chain resulting in films of different morphology in terms of thickness and HA organization as those reported by Richter et al..[12]

Together, these strategies provide a range of possibilities to asses the formation of HA films of different kind. In the context of this thesis work I investigated two new approaches for the immobilization of HA with the objective to build mimics of the PCC. One of these, aimed to investigate how the PCC structure depends on the surface distribution of HA grafting points, which mimic the HA synthases. First steps towards how such model systems can look like, are presented in chapter 2. In the second approach, described in chapter 3 and 4, HA is immobilized through binding to its natural cell surface receptor CD44. With this approach, I aimed to investigate the polyvalent interaction of HA with its main cell surface receptor CD44.

1.9 Proteins and surfaces

The immobilization of fully functional protein layers was a central point and the basis for the establishment of reliable model systems in the present thesis work.

Protein immobilization onto different kind of surfaces has become a wide and intensively studied field.[104, 105] On the one hand side this is because the potential of proteins to act as highly sensitive probes on biochips, and the possibility to investigate protein interactions on the other side were recognized.[27, 104] Furthermore, protein-surface interactions are of great interest in, for example, the prevention of bio-fouling processes or development of biocompatible implants.[26] Although progress has been made in the development of methods for the immobilization and characterization of proteins, there is need for further investigations. It is generally accepted that turning the sensitive biochemistry of proteins from solution to the surface requires careful handling. The challenges can be summarized into four main issues:

1. Denaturation upon surface contact may occur and lead to a full or partial loss of the protein's biological activity.[106-108]
2. Finding the optimum protein surface coverage and orientation is essential.Too little amounts of protein do not provide the desired sensitivity, whereas too high densities may perturb the protein's activity by steric effects.[109-111]
3. The adsorbed protein layer must be stable against various washing steps.
4. Unspecific adsorption of the protein has to be prevented to optimize the performance of the functional surface.

A lot of effort was made to find the optimum strategy for immobilization. The abundance of literature, however, clearly demonstrates that each investigated system has to be reconsidered individually. A recent review by Rusmini et al.[105] has focused on a number of established protein immobilization strategies.

Another crucial aspect for the study of surface confined protein layers is the detection and characterization of such assemblies.[26] Surface sensitive techniques, like AFM, quartz crystal microbalance and ellipsometry, originally well established for the use in air, have been further developed for operation in liquid - the proteins` natural environment. The development of these techniques led to a sensitivity level that is suitable for detecting surface coverages, which correspond to a few percent of a protein monolayer.[1, 112, 113] It is noteworthy that the above mentioned techniques are label-free. This can be of critical importance, as engineered

labels or tags go along with a manipulation of the original protein structure and can potentially influence its biological activity[114, 115] in terms of kinetics or binding strength.
I used specially designed fusion proteins, which allowed for highly oriented immobilization, as well as native proteins for the functionalization of surfaces. The use of various complementary techniques (QCM-D, ellipsometry and RICM, see next section) in the present work was vital to improve the qualitative understanding of adsorption behavior and enable quantitative insight.

1.10 Surface sensitive characterization techniques

1.10.1 Quartz crystal microbalance with dissipation monitoring (QCM-D)

Already in the 1950s QCM was discovered as a highly sensitive tool to measure adsorbed species, at that time operated in air or vacuum.[116] The possibility to detect smallest surface coverages is based on the resonance behavior of a quartz crystal. As shown by Sauerbrey,[116] the resonance frequency is directly proportional to the crystal's thickness; hence, a change in frequency (Δf) upon deposition of material on the crystal is correlated to adsorbed mass[116-119] (figure 1.9). This tool became attractive for biologically inspired science, once operation in liquid was possible and adsorption processes at the solid liquid interface could be studied.[120] Despite the high sensitivity, quantitative determination of adsorbed mass was not accessible for all kinds of films, as Sauerbrey`s mass-frequency relation is only valid for thin, homogenous, and rigid adlayers (for details see chapter 6). Many proteins or polymer films, however, are not homogenous or not rigid. In such cases the accurate estimation of the deposited film mass fails. Historically, a huge step forward in the development of this technique was made in the 1990s, when a second parameter was acquired simultaneously during the measurement - the dissipation D.[121, 122] The dissipation change, ΔD, provides valuable information about the morphology of the adsorbed film. Qualitatively, a low dissipation indicates a rather rigid layer, while a high dissipation is attributed to soft films.

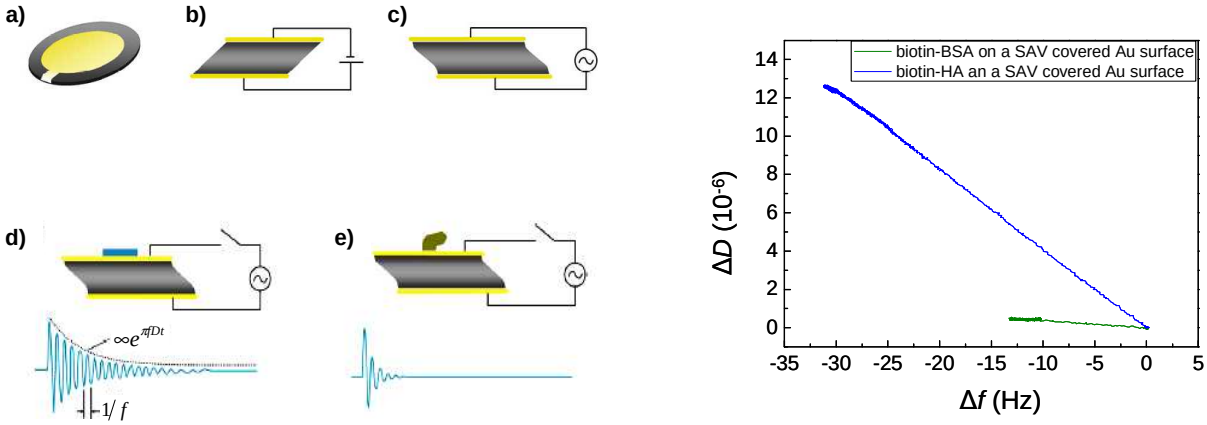

Figure 1.9: Left: basic principle of Quartz Crystal Microbalance with Dissipation. a) sensor crystal b) sandwiched between two gold electrodes and c) excited to resonance. d) and e) show the behavior of the oscillating crystal loaded with material, which is either rigid (d) or soft (e). The soft material film contributes more to the damping of the crystal's oscillation than a rigid film. Right: difference in the evolution of dissipation upon adsorption of a film that is either rigid *(green)* or soft *(blue)*.

The access to both parameters provided improved interpretation on, e. g., the conformation of adsorbed proteins, effect of ambient conditions on conformation and adsorption, or differences between various proteins,[123, 124] but also the characterization of surface modifications by a variety of materials.[125-127] QCM-D made an important contribution towards the understanding of lipid bilayer formation when the phase transition between intact adsorbed lipid vesicles and the formation of supported lipid bilayers could be demonstrated[12, 128-131] (figure 1.10). The investigation of lipid bilayers and the use of model membranes as an experimental basis by means of QCM-D have since found broad application.[132-135] The established technique of bilayer deposition is of special interest in the context of this thesis work, as supported lipid bilayers play a substantial role in the development of the model systems that are presented. Here, the monitoring of the SLB-formation process by QCM-D is an important quality control.

The dissipation signal gains even more significance when hyaluronan is introduced. In solution, this macromolecule entraps large amounts of water due to its hydrophilic character and its voluminous conformation.[61] It, therefore, forms a very soft film and generates relatively high dissipation[12] which contrasts the protein layers (figure 1.9). The coupled also water gives rise to a signal enhancement in frequency for an otherwise hardly detectable mass.

In the frame of this work, QCM-D was the main technique for the characterization of the adsorption behavior of proteins and the formation of various biomolecular layers. All adsorption steps were monitored in real-time, providing information on layer formation kinetics, the morphology and the stability of the deposited biomolecular layers. For rather rigid layers, including SLBs and protein films, the film thickness could also be estimated.
A typical QCM-D experiment is shown in figure 1.10.

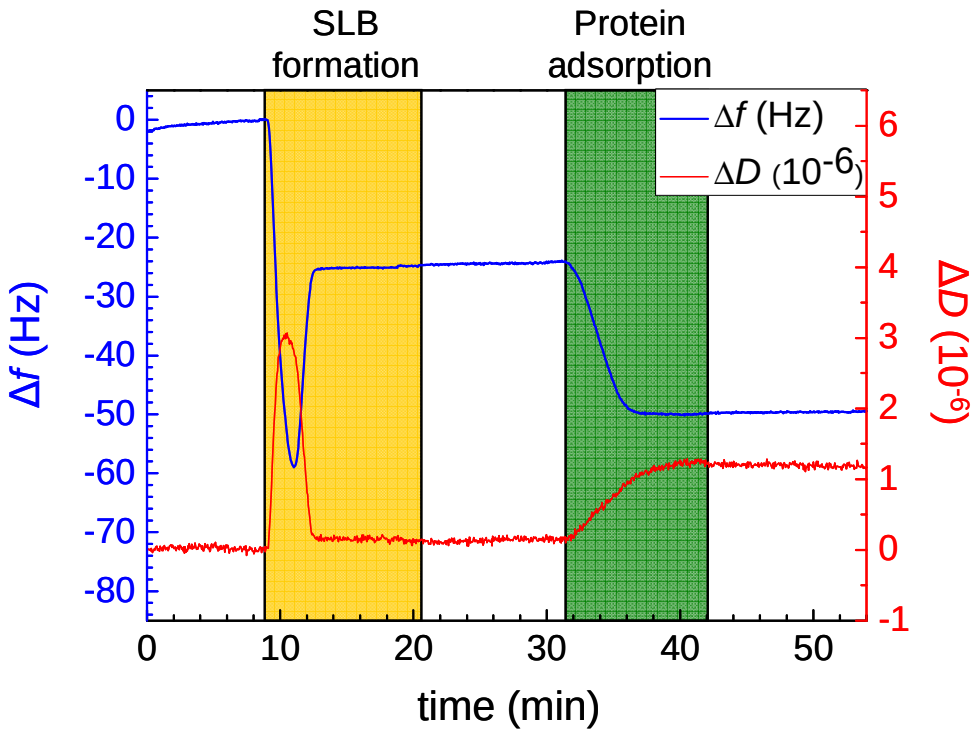

Figure 1.10: A typical QCM-D measurement of the formation of a SLB and the subsequent adsorption of a protein is shown. The frequency *(blue)* decreases upon mass deposition on the sensor surface. Simultaneously acquired dissipation *(red)* provides information of the mechanical properties of the adsorbed film. During SLB formation the minimum in Δ*f* (and the corresponding maximum in Δ*D*) indicate the typical transition from intact adsorbed lipid vesicles (SUVs) to a supported lipid bilayer. In a successive step a protein (annexinA5-Z) is added that associates with the (here) negatively charged SLB. The equilibration of both curves (Δ*f* and Δ*D*) indicates saturation of the adsorption. The absence of any changes in both signals upon rinsing gives evidence for the stability of the deposited layers. Several overtones, n, are recorded (n = 1, 3 .... 13), the 7th of which is depicted here.

Limitations. Adsorbed material at the solid-liquid interface will always contain a fraction of water.[117, 119] The QCM-D senses deposited material as a film that is mechanically coupled to the sensor surface, i.e. the adsorbed molecules including water.[123, 136] In most cases, the

absolute adsorbed biomolecular mass cannot be determined from QCM-D data alone. How exactly the liquid contributes to the QCM-D signal was and still is subject of intensive studies.[137-142] It turns out that the contribution can vary considerably for different molecules[138, 139] and also depends on surface coverage.[139, 140] In order to quantify absolute adsorbed masses, a complementary technique is needed. Optical techniques, which only rely on the changes in the refractive index, like for example, ellipsometry, reflectometry, surface plasmon resonance (SPR) or optical waveguide lightmode spectroscopy (OWLS) can be used for the quantification of adsorbed biomolecular masses.[138-140, 143]

Moreover, it is not always straightforward to derive the thickness of adsorbed layers from QCM-D data. The Sauerbrey equation can provide reasonable estimates for homogenous and rigid films. For soft films, viscoelastic modeling of the QCM-D data can provide reliable information on thickness[141] in some, but not all cases. An alternative technique that provides information on film thickness is colloidal probe reflection interference contrast microscopy (RICM).

1.10.2 Ellipsometry

Ellipsometry is an optical technique, in which the change in polarization of a light beam upon reflection at a surface (figure 1.11) is measured to derive information about the thickness and the refractive index of a surface adlayer.[144, 145] Thin films (down to less than 1 nm) deposited on the surface can be detected. The way and degree, how the ellipsometric angles Δ and Ψ change upon reflection depends on the material properties of the interface, more precisely, on its optical properties.

During the measurement two parameters are obtained: Δ and Ψ. These parameters describe the light wave in terms of phase shift and amplitude ratio between the s (perpendicular) and p (parallel) polarized contributions to the light wave. Fresnel's equations relate Δ and Ψ to the refractive index n and the thickness d of the film. By fitting an appropriate layer model to the experimental data, n and d can hence be determined. From n and d, the adsorbed mass m can be obtained with a resolution around 1 ng/cm^2[112] (see chapter 6.3.3 for details).

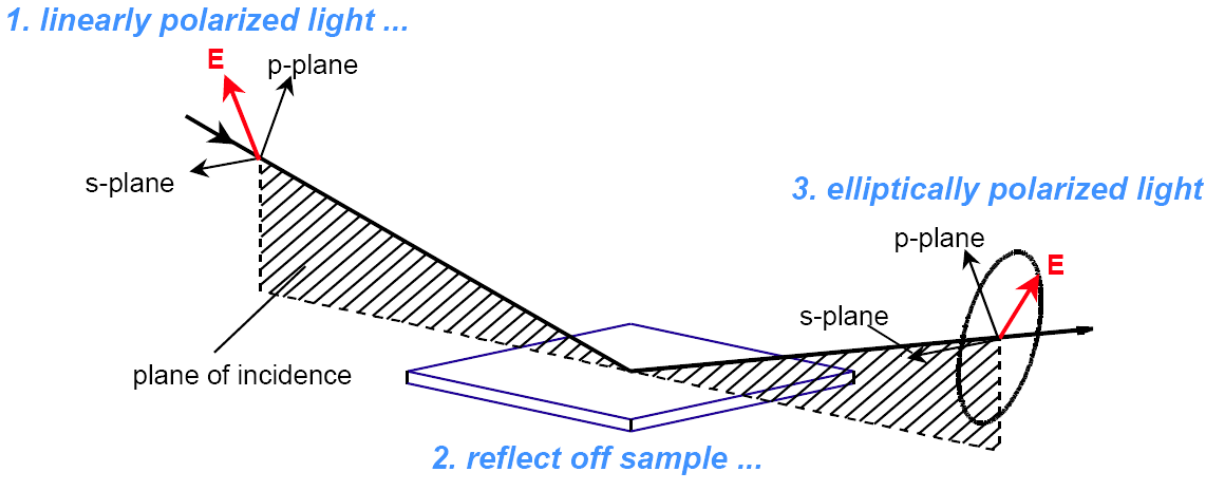

Figure 1.11: Basic principle of ellipsometry. Linearly polarized light changes its polarization upon reflection on a surface. The phase and the amplitude shifts between s- and p-polarized contributions to the light wave are determined. These depend on the properties of the surface. Cartoon from ref.[146].

Limitations. The dependence of an accurate fitting model is the major limitation for ellipsometry. The optical properties of the underlying substrate, as well as the solution and the angle of incidence of the light enter into this model, and have to be calibrated carefully. Exact notion of substrate properties are thus required to correctly fit values of *n*, *d* and *m*.[144, 145]

Also, the ellipsometric set-up used here allows only one experiment to be performed at the same time and is more cumbersome in operation that the QCM-D. The throughput is thus considerably slower than for the QCM-D set-up in which up to four measurements can be run in parallel.

In the frame of this work, ellipsometry was employed for quantitative analysis of the adsorbed masses of each layer of the model system as described in chapters 3 and 4. Data obtained from a typical experiment is shown below (figure 1.12). Therein, in an analogue experiment as shown in figure 1.10, a SLB was spread on a silica wafer followed by the adsorption of a protein onto the bilayer.

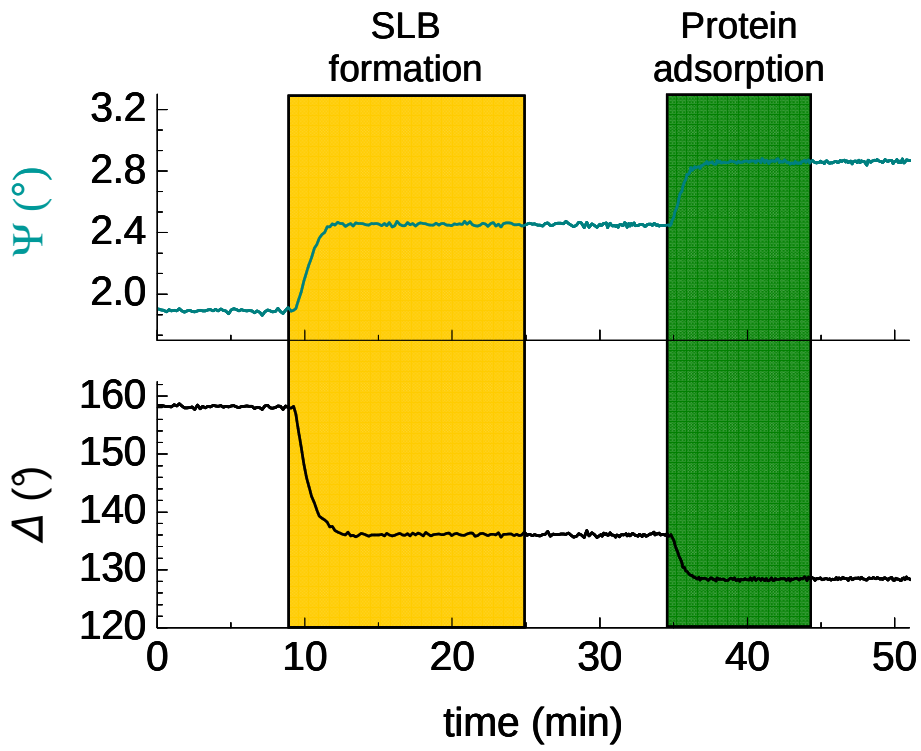

Figure 1.12: The ellipsometric parameters *Δ (black)* and *Ψ (cyan)* as obtained during the formation of a SLB on silica and the subsequent adsorption of a protein (annexinA5-Z). The incubation steps shown here are identical to those in figure 1.10.

1.10.3 QCM-D and ellipsometry - combining complementary techniques

The combination of QCM-D with optical (and other complementary) techniques and its role for the characterization of biomolecular films was motivated and encouraged as soon as QCM-D was developed.[122] Complementary techniques can compensate for limitations of a given technique. The combination of such techniques in one instrument, has further advantages: (i) the data from both techniques is obtained on the same substrate with the same experimental components. (ii) two datasets are acquired with the same time axis and the same kinetics. (iii) data collection is faster than for two independent experiments.[139, 140, 142, 147]

Combined ellipsometry/QCM-D set-up. The combination was implemented by using the standard ellipsometer set-up combined with a purpose designed QCM-D/ellipsometry fluid cell. similar approach using a combination of QCM-D and reflectometry has been reported recently.[139, 140, 147]

Of particular importance for the present work, was the correlation between the QCM-D frequency shift, Δf, upon adsorption and the biomolecular mass, Δm, as determined by ellipsometry. For a given (bio-) molecule that adsorbs to a surface the Δf signal can be "calibrated" in terms of adsorbed mass per area for any value of Δf between zero and saturation. Such a calibration of Δf makes it then possible to translate frequency shifts obtained from multiple QCM-D measurements into absolute adsorbed masses.

1.10.4 Reflection Interference Contrast Microscopy (RICM)

The technique was first introduced in 1964 by Curtis and coworkers who observed cells and visualized focal contacts by identifying areas of close and loose attachment.[148] Almost 30 years later colloidal beads hovering above different types of surfaces, combined with RICM, were used to determine film heights and interfacial interactions.[149-151] RICM is based on the interference of two light beams after reflection on different interfaces. For colloidal probes, close to a transparent interface a characteristic pattern, known as Newtonian rings, results (figure 1.13). Here, the first beam is reflected at the planar substrate surface and the second beam is reflected at the curved surface of the (colloidal) probe. The resulting radially symmetric diffraction pattern represents intensity maxima and minima, the position of which depends on the distance of the colloidal probe from the surface and on the wavelength. From the intensity profile and the geometry of the probe the distance between the probe and the substrate can be calculated.

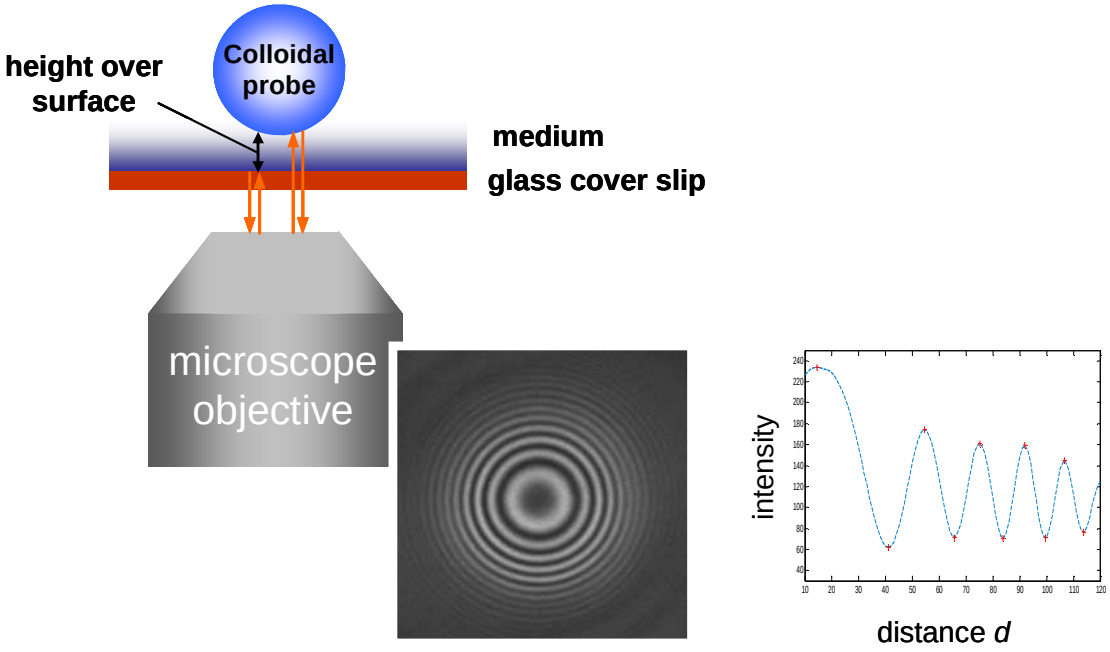

Figure 1.13: Basic principle of RICM. An interference pattern is generated by the interference of two beams reflected from the glass-solution interface and the probe-solution interface, respectively. From the obtained intensity profile the distance of the probe from the glass slide can be determined. The Intensity profile *(rightmost graph)* represents the Newtonian rings as intensity maxima and minima as a function of the distance, *d*, from the center of the probe.

For RICM experiments the model systems were built on glass cover slips. A 3W-RICM set-up as reported in ref.[12] and data treatment according to a parallel plate approximation model[12, 150] were used in this thesis work to asses the thickness of hyaluronan films of different HA chain lengths with a resolution of a few nm.

1.11 Concepts from polymer theory

An important physical aspect of the interdisciplinary work in the area of life sciences is the use of theories and theoretical concepts in order to describe or even predict experimental outcomes. A theoretical field of relevance for this study is polymer physics. Pioneers like Debye, Kuhn, Kramers, Flory and Huggins established the fundamental work during a period from the 1930s to the 1960s. Main principles of what today is considered modern polymer physics were developed in the following years (1960-1980) by de Gennes and others.[152] There is a growing awareness that an increased dialogue between polymer and biological science is needed to promote the progress of our understanding of many biological phenomena.[153]

In this section a few concepts from polymer theory that are relevant for the present work will be introduced. In particular, the physical description of flexible polymers (this concept will be explained in the following subsection more in detail) is relevant for the theoretical treatment of HA.[154-156] Polymer theory today can give a rather detailed description of surface confined polymers. I will provide a perspective of expectations about the presentation and conformation of surface bound HA films in terms of adsorbed masses and film heights as can be derived from polymer theory.

1.11.1 Polymer chains in solution

The ideal chain. Polymer chains adopt a certain conformations in solution, which depend on intrinsic properties of the polymer and the solvent. The simplest model is the so-called ideal chain, where it is assumed that no interaction neither between different monomers within the chain nor between the chain and the solvent take place. *The freely jointed chain model* assumes that the polymer chain is divided into N segments of length a, which are connected via flexible joints. Around these joints the chain can be rotated freely.[152] a also stands for Kuhn length. The end-to-end distance or contour length l_c of a polymer chain is then given by:

$$l_c = aN\,. \tag{1}$$

The conformation of the polymer chain is described by a *random walk*, i.e., each segment a can be oriented into a random direction. The polymer at each step can take each direction with

the same probability. A mean end-to-end distance, also called Flory radius,[157] can then be calculated:

$$R_F = aN^{1/2}. \tag{2}$$

The Flory radius (figure 1.14) is a reasonable parameter to describe the effective size of a polymer in solution. Another useful dimension is the so-called radius of gyration, which is the root mean square distance between each segment and the polymers' center of mass. For an ideal chain, the radius of gyration is:

$$R_g = \frac{1}{\sqrt{6}} \cdot aN^{1/2} = \frac{1}{\sqrt{6}} R_F \tag{3}$$

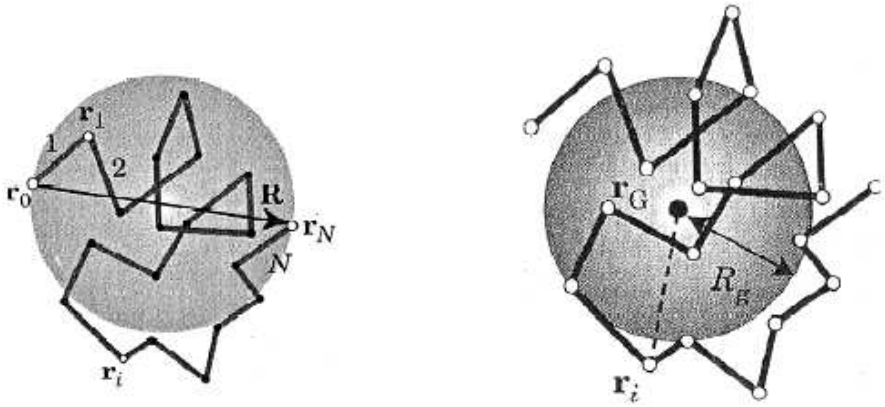

Figure 1.14: Left: Flory Radius R_F. Right: Radius of gyration R_g. Schemes from ref.[158].

The real chain. In the case of real polymer chains, long-range interactions between different parts of the polymer have to be considered (figure 1.15). The conformation of the real chain can be described as a *self avoiding random walk*. Here, two segments of the same chain cannot occupy the same volume (figure 15). This excluded volume effect increases the effective size of the polymer. The radius of gyration becomes[157]:

$$R_g \propto aN^{3/5}. \tag{4}$$

The main difference between ideal chains and real chains is the change in the scaling exponent *v*, also called Flory exponent, from $v = 1/2$ for ideal to $v = 3/5$ for real chains (see equations 2 and 4).[157]

Flexible polymer chains are characterized by their persistence length. A parameter that characterizes the flexibility of a polymer is the so-called persistence length l_p. The persistence length is the length, over which the directional memory of the chain is maintained.[159] Short-range interactions (e.g. hydrogen bonds) enhance the rigidity of the chain by imposing a preferential orientation at short distances. In contrast, entropy drives the polymer chain to random orientations over long distances. From the interplay of both factors the persistence length is determined. The l_p of a polymer can be assessed depending on the experimental determination of R_g. l_p scales as half of the Kuhn length[160]:

$$2l_p = a\,. \tag{5}$$

A polymer is called flexible, if the persistence length is much smaller than the polymer`s contour length ($l_p << l_c$).[161]

For flexible polymers the relationship between l_p and R_g can be approximated by[159]:

$$R_g \approx \sqrt{\frac{l_p l_c}{3}} \tag{6}$$

for ideal chains. For real chains R_g is given by:

$$R_g \approx \left(2l_p\right)^{2/5} l_c^{3/5} \tag{7}$$

Both formulas can directly be derived from combining equations (2) and (4) with (5), respectively.

Equations (6) and (7) illustrate that the extension of a polymer coil can be easily estimated, if the molecular weight (which is proportional to l_c) and the persistence length of the polymer are known.

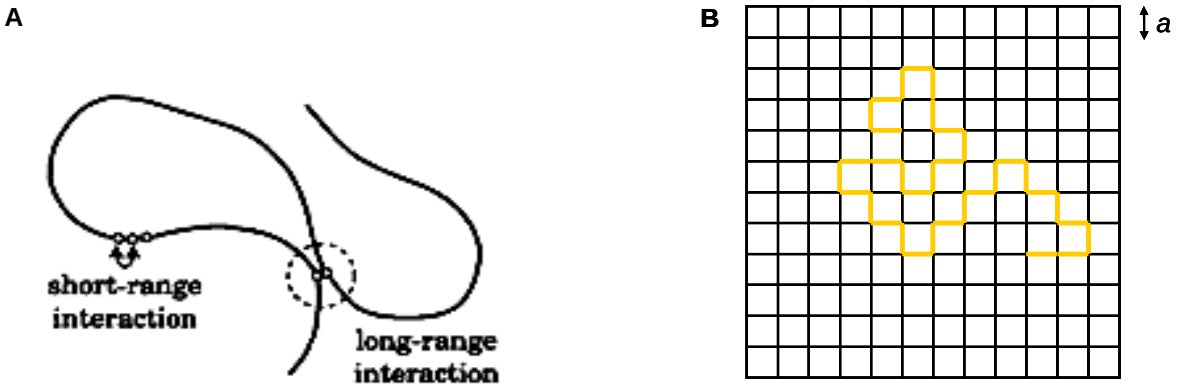

Figure 1.15: a) short range and long range interactions on a real polymer chain. Scheme from ref.[158]. b) self avoiding random walk (in 2D) of a real polymer depicted in a square lattice. The grid size corresponds to the segment size *a* of the polymer chain.

Concentration regimes of polymer solutions. According to their concentration, polymer solutions can be classified into a dilute and a semi-dilute regime[158] (figure 1.16). In the dilute solution no or little interaction takes place between individual polymer chains, whereas in semi-dilute regime the chains overlap strongly and interpenetrate each other. The transition between both occurs at the concentration, at which the polymer chains just start to overlap. This threshold concentration is termed overlap concentration c^*. Obviously, c^* depends on the molecular weight of the polymer:

$$c^* = \frac{M_w}{V_p N_A} \qquad (\mathrm{g} \times \mathrm{l}^{-1}) \qquad (8)$$

where V_p is the volume of the occupied by the polymer. V_p can be calculated assuming the polymer coil to occupy a spherical volume with radius R_g.

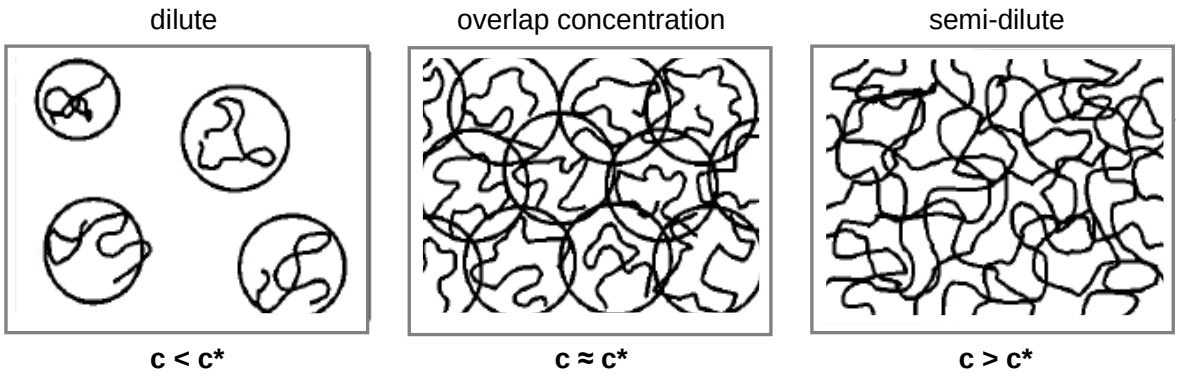

Figure 1.16: Dilution regimes for flexible polymers representing the diluted (c < c*), the overlap (c ≈ c*) and the semi-diluted (c > c*) state. Adapted from reference[152].

1.11.2 The blob model

External constrains, such as the confinement to a surface, will affect the polymer's conformation. These conformational changes will be most prominent when the polymer is considered at a large scale. At smaller scales, the random conformation of the polymer will be maintained. A simple but useful way to separate these two length scales was introduced with the "blob" model by de Gennes.[161] Herein, the polymer chain is divided into a number of successive spheres around parts of the chain - the blobs (figure 1.17). The size of a blob is given by ξ. Inside the blob the polymer chain is thought to be insensitive to external constrains, i.e. remains unperturbed. The polymer chain inside the blob has a free energy of kT. This concept, despite its simplicity, proved to be a reasonable description for long polymers in solution, as melts and at interfaces.[5, 162, 163]

1.11.3 Polymers on surfaces

Grafted polymer chains*:* When polymers are attached end-on to a surface, two conformationally different regimes can be distinguished: the "mushroom" and the "brush" regime (figure 1.17). The polymer takes a mushroom conformation, if no overlap occurs between two neighboring polymer chains, i.e., the distance between the neighboring grafting points D is larger than R_F. In this case, the polymer retains about the extension that it would have in solution. However, if the distance between the grafting points D becomes smaller than R_F, steric and repulsive forces between the chains oblige them to stretch out as so-called

brushes into the bulk. The simplest and one famous model of polymer brushes is known as Alexander-de Gennes brushes. This model is based on the assumptions of the real chain model to describe the conformation of polymers. The degree of stretching depends on the polymer size N and the grafting density σ, which relates to D as:

$$\sigma = \left(\frac{a}{D}\right)^2 . \tag{9}$$

The thickness of a brush can then be estimated by:

$$h \approx Na\sigma^{1/3} . \tag{10}$$

It is notable that the brush thickness scales linearly with the molecular weight of the polymer.

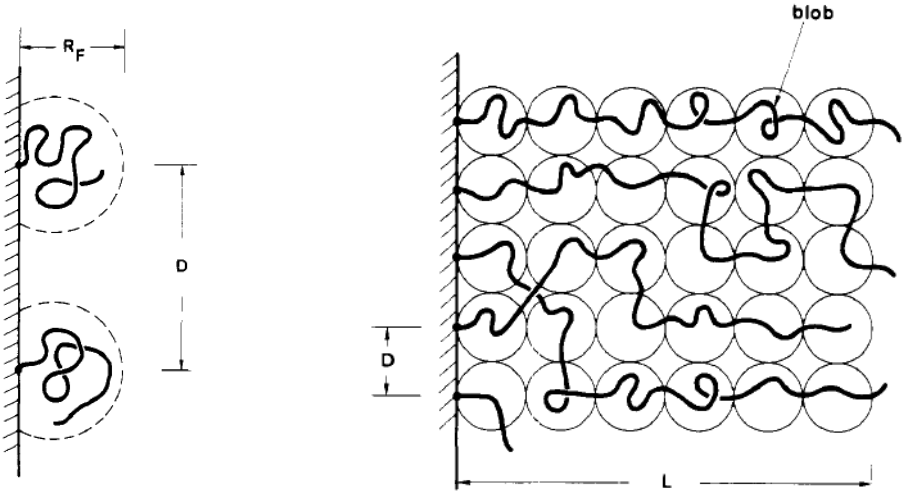

Figure 1.17: Different conformations of end-grafted polymers depicted according to the blob model[164]. Left: mushroom regime. Right: brush regime.

Adsorbed polymer chains. *Single adsorbed chains.* The adsorption of a single polymer chain to a surface can be described by using the blob model.[5, 152] In the adsorbed state, each blob (the so-called adhesion blob) is in contact with the surface (figure 1.18). The blob size ξ depends on the segment length a and the interaction potential δ (or adhesion strength) between the polymer and the surface. The polymer chain inside the blob is

unperturbed with a free energy of *kT*. Consequently, the binding energy of each blob to the surface is about *kT* and the total binding energy of the polymer chain is about *kT* times the number of blobs.

Many adsorbed chains. For the case of many adsorbed chains, de Gennes proposed the so-called self-similar grid of blobs. Essentially, ξ remains the characteristic parameter and determines the size of the adhesion blob - the surface-proximal layer of blobs. The concentration profile - as evolving into the bulk - is called self-similar, because every adjacent "blob-layer" doubles in size compared to the previous layer (figure 1.18). The blob size of the outmost blob reaches dimensions of the Flory radius R_F.[165] Consequently, it can be concluded that the strength of interaction of the polymer with the surface determines the size of the adhesion blob, but it does not affect the resulting height of a film of attached polymers. In contrast to the polymer brush model, the film height increases only weakly with surface coverage. The height increases with the size of the polymer according to $R_F \sim N^{3/5}$.

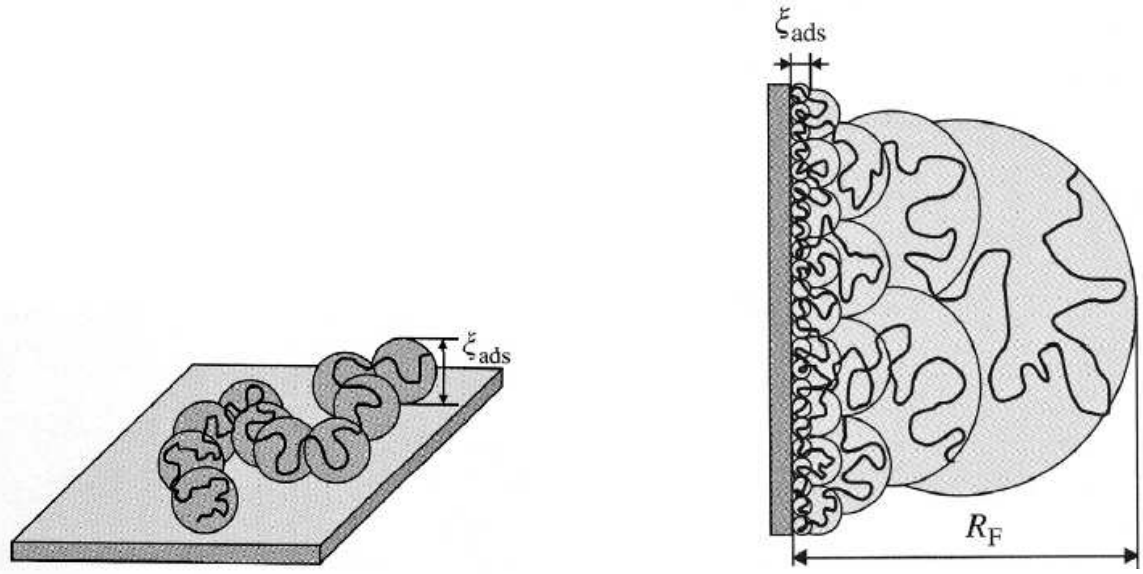

Figure 1.18: Left: Adsorption of a single chain to a surface. Right: The self-similar grid according to de Gennes describing the concentration profile of the adsorbed polymer as it evolves from the surface to the bulk. Schemes adapted from ref.[152].

In the following, the concepts of polymer theory to derive characteristic parameters for HA will be applied.

1.11.4 Estimates for the dimensions of HA in solution and on surfaces

Dimensions of HA in solution. From a polymer physics point of view, HA is well described as polyelectrolyte.[5, 166] With a pK_a of the glucuronic acid residues of 3-4, at pH ≈ 7 these groups are predominantly ionized and, hence, HA is a polyanion.[61] In solution it forms a stiffened extended random coil.[155, 156, 167, 168] Intramolecular hydrogen bonds stiffen the polymer.[168, 169] This together with repulsive forces of the carboxylate groups results in an extended conformation in solution with water trapped inside the structure (figure 1.19).

Although the hydrodynamic data on HA, as was obtained from early studies based on light scattering, sedimentation and osmometry,[170, 171] for example, gave a fair understanding of HA behavior, the molecular basis underlying HA behavior remained controversial. One model that was proposed suggested chain-chain self-associations due to hydrophobic interactions of the hydrophobic patches (figure 1.19) of the HA chain.[169, 172] This, however, would imply that HA does not behave like a flexible random coil in solution[155, 166, 170]. More recent experimental and theoretical studies,[173, 174] indicated that HA can be considered a flexible polymer chain in a good solvent.[166]

The persistence length of HA was determined to be in the range of l_p = 4-7.5 nm.[175, 176] It should be noted that l_p depends on the ionic strength of the solvent.[5, 156] Interestingly, the persistence length is about the size of one binding site for hyaladherins. This suggests that the conformational constrains (or entropic losses) upon binding of a hyaladherin are rather small.

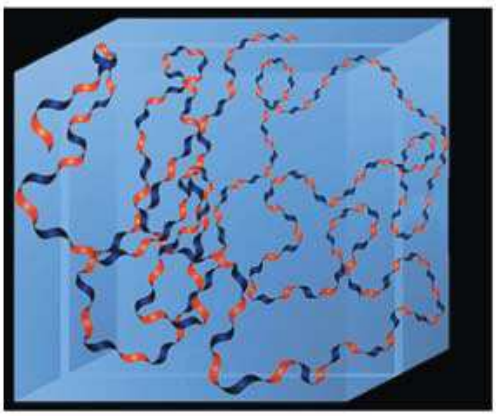

Figure 1.19: Model of the extension of a HA chain solution[61]. HA is depicted as a twisted ribbon structure with hydrophilic (blue) and hydrophobic (red) faces. The model is based on X-ray fiber diffraction and computer simulations[168, 169, 173].

The radius of gyration of HA can be calculated according to a formula that has been derived experimentally by Takahashi[175] for 0.2 M salt solutions:

$$R_g = 0.021\,nm \times M_w^{3/5} \qquad (11)$$

where M_w is the molecular weight of the polymer in Dalton (Da). For example, for HA of a molecular weight of 1 MDa the radius of gyration would be 88 nm. Table 1.1 summarizes the solution characteristics of different HA chains.

Table 1.1: Solution characteristics of HA. Molecular weight M_w, contour length l_c and radius of gyration R_g of HA are given for different HA types used within this thesis. Overlap concentration c^* and hydration of the individual HA chains, H, are estimated from polymer theory.

HA type	M_w [kDa]	l_c [nm][a]	R_g[b] [nm]	c* [mg ml^{-1}]	H [%]
HA50	30 ± 1.5	79	10.2	11.2	99.89
HA250	262 ± 13	693	37.4	1.97	99.99
HA500	450 ± 22.5	1190	51.8	1.29	99.99
HA1000	1156 ± 58	3056	91.2	0.6	99.99
HA2500	2400 ± 120	6344	141.1	0.34	99.99
b-HA50	58 ± 3	155	15.1	6.68	99.93
b-HA1000	1083 ± 54	2891	87.7	0.64	99.99

a: calculated assuming a size of one dimer to be about 1 nm[168] and 378,31 Da; b: R_g after Takahashi.[175]

For surface confined HA chains concepts from polymer theory allow an estimation of the HA film thickness created under the given conditions.

Adsorbed HA chains. In the context of this thesis work, adsorbed polymer chains were investigated predominantly. From table 1.1 it can be seen that the radius of gyration of the HA chains ranges between 10 and 150 nm. The thickness of a film of adsorbed HA chains would be expected to be in the same range.

In order to obtain an order-of-magnitude estimate of the mass of films of adsorbed HA, one may assume that a film of densely packed extended random coils of HA covers the surface.

The adsorbed mass can then be calculated from the product of the expected film thickness, R_g and the overlap concentration c^*.

Table 1.2 summarizes expected adsorbed masses, film heights and hydration of an HA film at overlap concentration ($c \approx c^*$), i.e. where the blobs are densely packed on a surface, but do not interpenetrate yet. These values are derived from calculations based on the formulas introduced before.

It can be seen that the predictions made above for adsorbed HA are covered by the resolution range of the ellipsometer.

Table 1.2: Estimated characteristics of adsorbed HA films of different HA polysaccharides according to predictions from polymer theory.

HA type	film mass expected at c* (ng cm^{-2})	expected HA film height [nm]	film hydration [%]
HA 50	3.8	20	99.89
HA250	2.5	75	99.99
HA500	2.2	104	99.99
HA1000	1.8	182	99.99
HA2500	1.6	283	99.99

Chapter 2

On the Functionalization of Homogeneous and Nanostructured Surfaces with Biotin-Receptors

The aim of this project was to find a suitable method for the functionalization of homogeneous and nanostructured gold surfaces with biotin-binding proteins, such as streptavidin (SAv), avidin (Av), or neutravidin (NAv). Despite the popularity of SAv, Av and NAv as molecular tools, rather little is currently known about the direct interaction between these proteins and surfaces of silica, glass or gold, i.e., materials that are commonly employed in biotechnological applications.

Regular arrays of gold nanoparticles with tunable particle size and inter-particle distance[177, 178] have been reported to serve as fascinating substrates for studies on receptor mediated (integrin) cell attachment.[179-181] Such substrates provide a material contrast between gold nanoparticles and the surrounding silica (SiO_2), which can be exploit for selective functionalization. The gold nanoparticles that display a highly ordered and tunable spatial organization can act as little anchors for the attachment of various targets (figure 2.1). Due to the size of the nanoparticles, only very few, ideally only one protein can interact with a given particle. The impact of distance rather than overall density effect on receptor-ligand binding events can be assessed.

Successful immobilization of (bio-)molecules, however, is closely connected to certain requirements for the employed surface. It should yield a surface on which (i) the optimum amount of protein is immobilized, (ii) the protein's activity (here biotin-binding activity) is maintained, and (iii) unspecific binding is limited. The design of this project is geared to these requirements. In order to achieve quantitative immobilization of biotin-binding proteins and, further, of the biotinylated targets, the adsorption behavior of the proteins is investigated systematically.

Although the functionalization with biotin-binding molecules has general applicability to a great number of biotinylated target molecules, this project emerged from the idea of exploiting nanostructured surfaces as a tool to control grafting of HA. The possibility to

control the distance between the anchor points seems particularly interesting in this context, since polymer theory predicts different film morphologies depending on the size and the grafting distance of the polymer (figure 2.1).[161] HA with a single biotin moiety at one of its ends is commercially available, and homogenous and nanostructured surfaces are, in contrast to an earlier approach by Richter et al.,[12] laterally immobile. A well-controlled model can possibly serve to shed light on how the HA film morphology is affected by spatial arrangement of HA.

QCM-D was used to follow each adsorption step and to probe the stability of the deposited protein layers. The study on the adsorption behavior of biotin-binding proteins to gold and silica was published in Langmuir[1] and will be reproduced here in modified form. Two other approaches to surface functionalization with SAv, based on the introduction of a linker layer, have been examined and will be critically discussed here. Further, initial results on the transfer of the developed methodology to nanostructured surfaces will be presented.

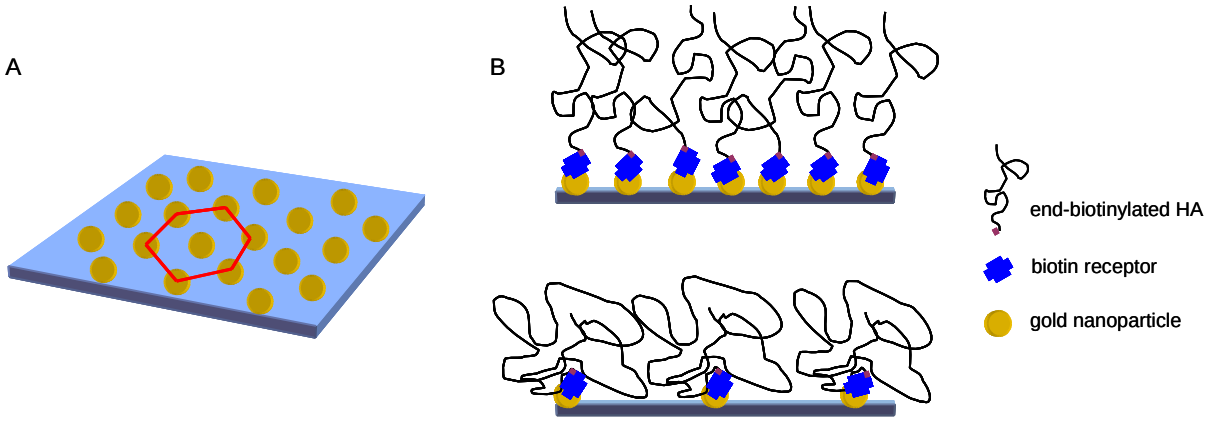

Figure 2.1: Sketch of a model system of HA chains end-grafted to a regular gold nanoarray. A: schematic drawing of a silica surface decorated with a quasi-hexagonal (red) pattern of gold nanoparticles. B: possible switching of end-grafted HA chains between brush (top) and mushroom (bottom) conformation by creating different inter-particle distances on the nanostructured surfaces.

2.1 Experimental design

2.1.1 Biotin binding proteins

The interaction between biotin and Av or its analogues SAv and NAv is known to be one of the strongest non-covalent biomolecular binding events, with an affinity of 10^{13} to 10^{15} M^{-1}.[182] These proteins consist of four monomeric subunits together forming a globular tetrameric protein with a total of four independent biotin binding sites (figure 2.2). The molecular origin of this strong interaction as well as the structure of both the protein and the protein-biotin complex, have been studied in detail.[183-187] Biotin-binding proteins are stable in aqueous solution over a wide range of temperature, pH and salt concentration.[188] Streptavidin differs from avidin in the source from which it is obtained. As a product of bacterial synthesis[189] (from *Streptomyces avidinii*) it is, unlike Av, not glycosylated. NAv stems from the original Av, which was chemically deglycosylated. The biotinylation of a variety of target molecules is well established and easily accomplishable in many cases. These features have rendered biotin-receptors very popular for biotechnological and biochemical applications.

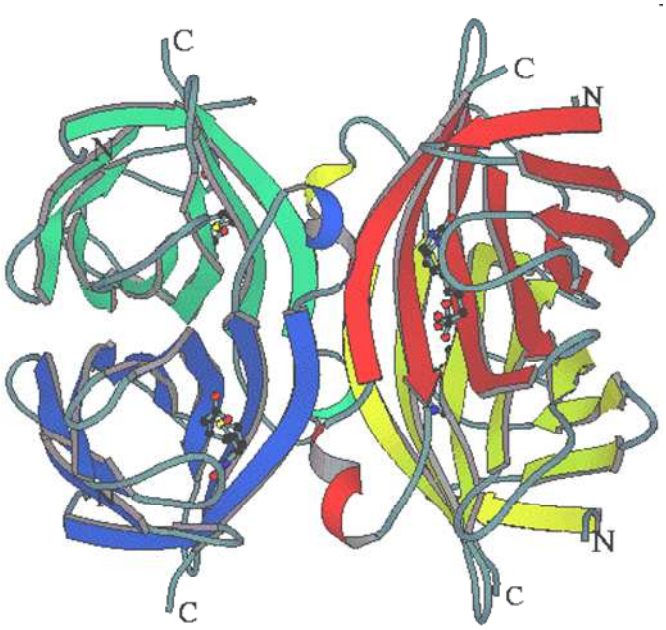

Figure 2.2: Model of the structure of streptavidin. Four biotins (displayed as ball-and-stick model) are shown in complex with the four binding sites available on the protein (shown colored in green, red, yellow and blue). Image adapted from ref.[190].

2.1.2 Existing immobilization strategies for biotin-binding proteins

With a total of 4 biotin binding sites, located on two opposing faces of the molecule, such biotin-binding proteins are particularly attractive for the functionalization of macroscopic surfaces or nanoparticles (see ref. [105] and references therein). Knoll et al.[191, 192] for example, have successfully employed SAv as a "bridge" between a biotinylated surface - a mixed self-assembled monolayer (SAM) made from biotinylated and non-biotinylated alkyl thiols on gold - and a biotinylated target. Other biotin-binding molecules have also been immobilized on layers of biotinylated thiols,[193] and photochemical approaches that use either photo-activated or photo-cleaved biotin groups have been reported.[194, 195] In all these approaches, the multivalency of the biotin-binding proteins is directly exploited to link a biotinylated target to a surface exposing biotin-groups.

Such sandwich strategies are not unique to gold surfaces.[196] Huang et al.[111] used assemblies of grafted copolymers of poly(L-lysine) and partially biotin-derivatized poly(ethylene glycol) to immobilize biotin-binding proteins on niobium oxide surfaces. Supported lipid bilayers that contain a fraction of biotin-functionalized lipids are attractive for the functionalization of mica and silica: the biotin-concentration can be easily tuned and biotin-binding proteins are immobilized in a highly oriented manner.[12, 132, 138, 139, 197]

In other strategies, biotin-binding proteins were covalently immobilized. Reznik et al.[198] for example mutated SAv with a C-terminal cystein-tag for immobilization to maleimid-coated surfaces. Primary amines or carboxyl groups on the proteins' surface have also been employed for covalent bonding to suitably pre-functionalized surfaces of silica[199, 200] and gold.[192] The nature of the coupling chemistry seldom allows for the orientation of the molecule on the surface to be controlled. Here, the multivalency increases the likelihood for biotin-binding sites to remain accessible for target molecules in solution.

All above-described functionalization approaches have in common that they require the presence of an additional linker layer between the solid support and the biotin-receptor. However, spontaneous adsorption of SAv and Av to gold and silver has been reported and suggested for potential immobilization applications.[201] The preparation of a suitable linker layer is not a trivial task: careful tuning of the layer assembly is often required to optimize performance in terms of biotin-binding activity and resistance to unspecific binding. For example, and contrary to what intuition may suggest, the display of too many biotin groups by the linker layer typically has adverse effects on the biotin-binding capacity of the final functionalized surface: an excess of biotin groups on densely packed molecular layers imposes steric constraints that limit binding of biotin-receptors, as nicely demonstrated for

SAMs;[191] a too high biotin density in a layer of flexible linkers can lead to the occupation of all four of the biotin-receptor's binding sites or burial of the biotin-receptors in the interior of the linker layer, thereby rendering the receptors inactive or inaccessible.[111] Also, the uncontrolled orientation of biotin-receptors upon covalent linkage has been reported to limit the functionality of immobilized target molecules.[192]

2.1.3 Biotinylated linker

In complementary studies a bridge-like architecture of the form biotin- Av- biotin was employed to mediate the immobilization of biotin-receptors to gold. Two linkers were tested. HPDP-biotin (N-(6-biotinamido)hexyl)-3-(2-pyridylthio)propionate) consists of a spacer-linked biotin and a pyridylthiol, which form a disufide. The second linker was a homodimer of two thiolated polyethylene-glycol spacers with biotin as end-functional head group (biotin-PEG-SS) (figure 2.3). Both display a double functionality, which enables the linkage to gold surfaces by the thiol group and to immobilize a ligand for SAv.

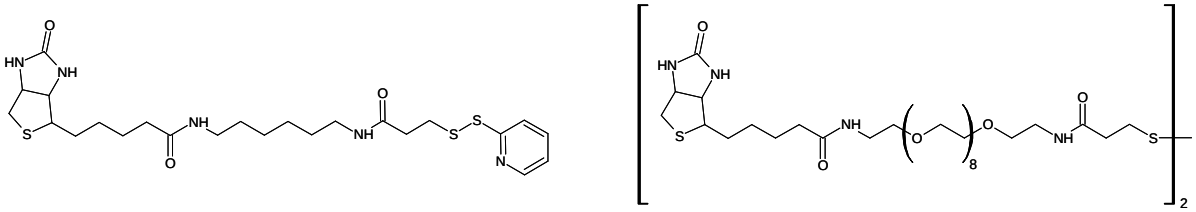

Figure 2.3: Chemical structures of both linkers, HPDP-biotin and biotin-PEG-SS.

2.2 Physisorption of biotin-receptors to gold and silica

This study focuses on a systematic examination of the immobilization of biotin-binding proteins by direct deposition on bare gold and bare silica surfaces. We start, however, by recalling and extending data for another immobilization platform: biotin-functionalized supported lipid bilayers. The adsorption of SAv to biotinylated supported lipid bilayers (biotin-SLBs) has already been characterized in detail by QCM-D and other methods,[132, 138, 139, 197] and was found to perform well in various applications.[12, 132, 133] It will serve as a reference system for the present study.

2.2.1 Results

Biotinylated SLBs - the reference system

Upon exposure to biotinylated SLBs, SAv adsorbed readily, as indicated by the monotonously decreasing frequency (figure 2.4A). The adsorption reached a plateau within less than 15 min, yielding overall changes in frequency of -28 Hz, which corresponds to a thickness of 5.2 nm, and dissipation of 0.5×10^{-6}. The adsorption kinetics and the final QCM-D response are consistent with earlier reports, and indicate the formation of a dense monolayer of SAv on the SLB.[132, 138, 139]

Biotin-BSA, successively added to the SAv-covered SLB, bound with a maximum frequency change of -14 Hz (d = 2.4 nm, figure 2.4C). Considering the shape of BSA, a flattened ellipsoid of 3 nm × 4 nm × 8 nm in size,[123] this frequency shift suggests that the protein adsorbs with its long axis parallel to the surface. Like for SAv, equilibrium was reached rather quickly, and the change in dissipation was low, consistent with the formation of a monolayer of globular proteins. Binding was irreversible as expected for the strong interaction between biotin and SAv. Native BSA did not bind to the SAv-covered SLB ($|\Delta f| < 0.5$ Hz, figure 2.4B), confirming that the binding of biotin-BSA was specific and SAv thus active.

Similar responses were observed for other biotin-binding proteins (figure 2.4A-C). Av and NAv adsorption to biotinylated SLBs equilibrated within about 15 min, with final frequency shifts of -26 Hz (4.7 nm) and -32 Hz (5.7 nm), respectively, indicating monolayer formation. Biotin-BSA bound stably to Av and NAv, while native BSA did not bind, indicating that these two proteins retain their activity upon immobilization. Some peculiarities were though notable for NAv: the dissipation shift for the NAv film (1×10^{-6}) was considerably larger than

for Av (0.6×10^{-6}) and SAv, and biotin-BSA binding was reduced, from -15 Hz to -9.5 Hz. We did also observe that the adsorption of NAv was not well reproducible. In some cases, absolute frequency shifts of 40 Hz and more were observed. The binding of biotin-BSA was not affected by this variability (data not shown).

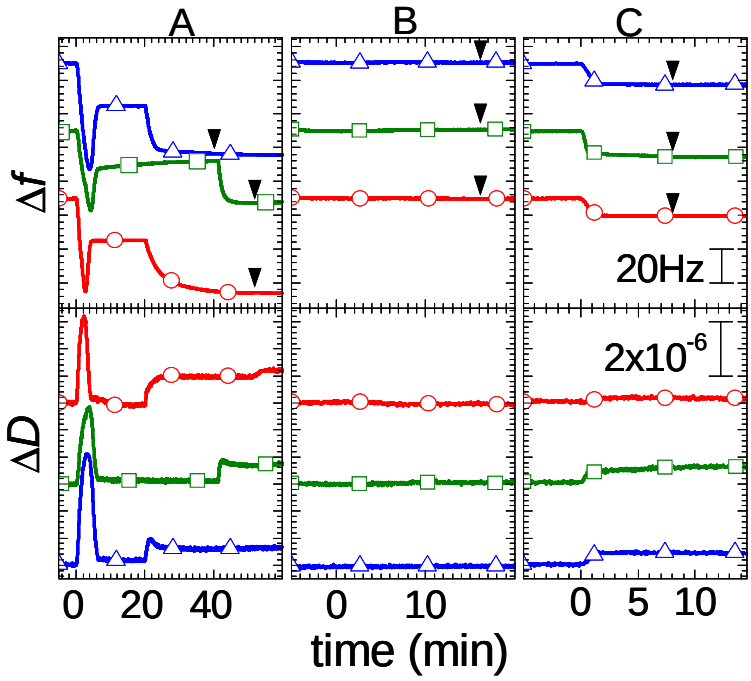

Figure 2.4: A: Representative QCM-D responses, Δf and ΔD, for the formation of biotinylated supported lipid bilayers and subsequent adsorption of biotin-binding proteins - SAv *(blue triangles)*, Av *(green rectangles)* and NAv *(red circles)*. Typical Δ*f* (-25Hz) and Δ*D*-shifts (<0.5x10^{-6}) were measured for the formation of the SLBs.[129, 130] B: Subsequent binding of native BSA on the same surfaces. C: Subsequent binding of biotin-BSA on the same surfaces. Each incubation step starts at 0 min, except for the incubation of SAv, Av and NAv which start at 20, 40 and 20 min, respectively; rinses in buffer are indicated *(arrowheads)*.

SAv adsorbs firmly to gold surfaces. Next, the adsorption of SAv to gold was investigated. Av and NAv were tested for comparison. All proteins adsorbed well to gold-coated sensor crystals (figure 2.5A). Adsorption kinetics and final frequency shifts for SAv (-30 Hz) and Av (-32 Hz) were similar to, albeit slightly higher than those observed on biotin-SLBs, indicating the formation of a dense monolayer. Binding of both molecules was stable upon rinsing in buffer. These experiments support earlier findings of spontaneous and direct binding of Av and SAv to gold and silver surfaces.[201]

The dissipation shifts for both proteins on gold were significantly smaller ($<0.2\times10^{-6}$) than on biotin-SLBs, indicating subtle differences in the mode of immobilization. Indeed, the unspecific binding to gold is direct, and likely to proceed via one of the extended faces of the cuboid-shaped proteins, while specific binding to biotin-SLBs is mediated by one or two short but flexible linkers. We suggest that it is this difference in linkage that gives rise to the different dissipation signals.[202]

The adsorption behavior of NAv differed markedly from the other two biotin-receptors. While the adsorption of Av and SAv reached a plateau after around 15 min of incubation, NAv continued to bind, albeit more slowly. Frequency shifts beyond -60 Hz were reached, which is two-fold the response for SAv or Av. The large difference is surprising, given that the dimensions of all proteins are similar. Δf = -60 Hz would correspond to a thickness of around 11 nm, or about two-fold NAv's molecular dimensions, suggesting that the adsorption of NAv on gold is not restricted to a monolayer. We speculated that aggregates in the stock solution may be the cause of increased adsorption. Indeed, centrifugation of freshly thawed aliquots at 10,000 *g* for 10 min resulted in decreased QCM-D responses (data not shown). The frequency shift remained though still at least 10 Hz higher than what was observed for SAv and Av. It is likely that gentle centrifugation is insufficient to remove all aggregates. It cannot be excluded, however, that surface-induced denaturation of NAv can also contribute to the unexpected adsorption behavior. Notably, the apparent instability of NAv may also explain the variability on the binding behavior, the increased dissipation and the reduced activity of NAv that we observed on biotin-SLBs.

Biotin-BSA was used to test if the immobilized molecules retain their biotin-binding activity. In order to reduce and exclude any unspecific binding, the surface was incubated with native BSA prior to exposing the biotinylated target. Interestingly, binding of native BSA was low ($|\Delta f|$ = 1.0 Hz for SAv, 3.0 Hz for Av and <1.0 Hz NAv, fiigure 2.5B). Since BSA adsorbs readily to bare gold[203] (figure 8), it could be concluded that the biotin-binding proteins themselves confer rather good resistance to unspecific protein binding. In contrast, biotinylated BSA bound stably to Av, SAv and NAv, with binding rates similar to those found on SLBs (figure 2.5C). The final frequency shifts did though vary from -12.5 Hz for SAv to -15.5 Hz and -18 Hz for Av and NAv, respectively. Differences in the arrangement of biotin-BSA most likely explain these variations: given BSA's elongated shape, adsorption in a slightly tilted orientation would easily result in a few Hz of additional frequency shift.

In addition to biotin-BSA binding of biotinylated hyaluronan (biotin-HA) of 58 kDa to SAv was tested. In control experiments, HA was found not to interact unspecifically with the

underlying SAv layer nor with the gold substrate (not shown). Physisorbed SAv bound biotin-HA with shifts for Δf = -30 Hz and $\Delta D = 12 \times 10^{-6}$ (figure 2.5D). The high dissipation is characteristic for the formation of HA brushes, indicating a strongly hydrated and viscoelastic film being deposited.[12] The obtained values are, however, lower than observed for the HA-brush model systems on biotin-SLBs ($\Delta f \approx$ -50 Hz and $\Delta D \approx 21 \times 10^{-6}$).[12] Both biotin targets thus confirm that, although unspecific adsorption is likely to lead to adsorption in various orientations, a large fraction of SAv retains its binding activity after immobilization. From comparison of the final values for grafted HA on both systems (biotin-SLB[12] and Au), the fraction of active physisorbed SAV can be estimated to about 60%.

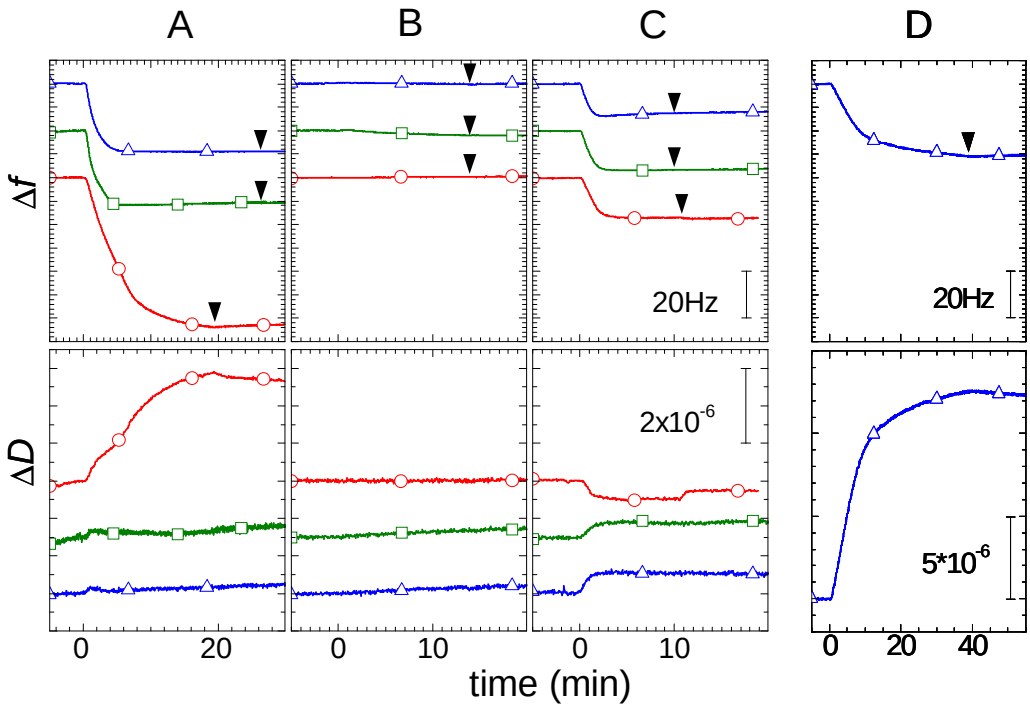

Figure 2.5: A: Representative QCM-D responses, Δ*f* and Δ*D*, for the adsorption of biotin-binding proteins to gold - SAv (*blue triangles*), Av (*green rectangles*) and NAv (*red circles*). B: Subsequent exposure of native BSA on the same surfaces. C: Subsequent binding of biotin-BSA on the same surfaces. D: binding of biotin-HA to a SAv covered surface. Each incubation step starts at 0 min; rinses in buffer are indicated (*arrowheads*).

SAv does not adsorb to silica surfaces. The binding behavior of SAv on silica differed strikingly from that observed on gold: no adsorption was observed (figure 2.6). Adsorption was pronounced for Av and NAv (figure 2.6A), with adsorption rates and maximum shifts in

frequency and dissipation similar to those observed for respective protein on gold. In contrast to gold, however, a fraction of the proteins desorbed upon rinsing with buffer, indicating that binding was not entirely stable.

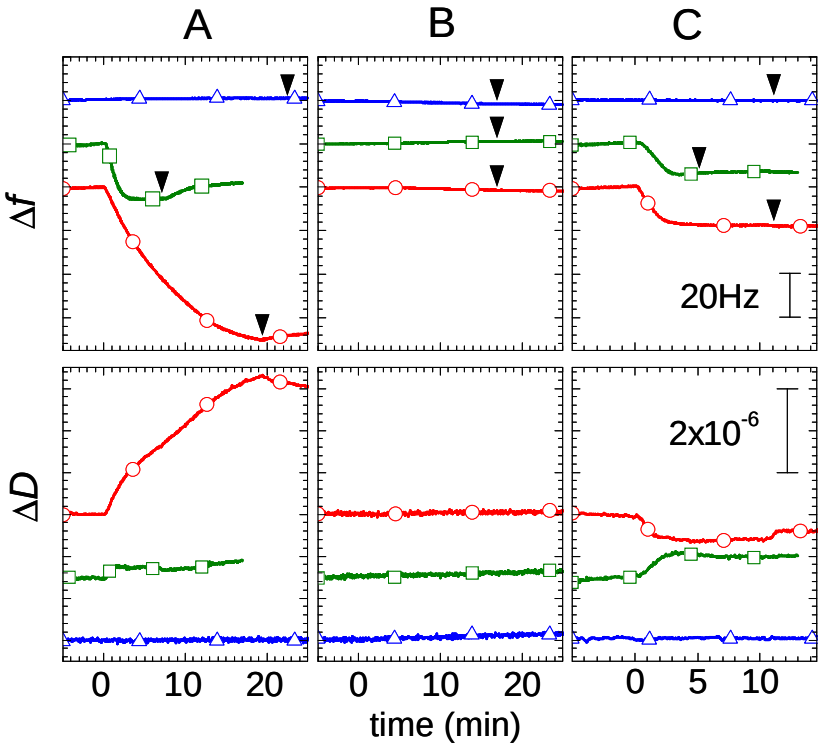

Figure 2.6: A: Representative QCM-D responses, Δf and ΔD, for the adsorption of biotin-binding proteins to silica - SAv *(blue triangles)*, Av *(green rectangles)* and NAv *(red circles)*. B: Subsequent exposure of native BSA on the same surfaces. C: Binding of biotin-BSA on other surfaces, prepared identically to those shown in (A). Each incubation step starts at 0 min; rinses in buffer are indicated *(arrowheads)*.

The lack of adsorption of SAv was unexpected and merited further examination. To this end, the effect of the buffer solution on binding was tested. A large range of pH was sampled (3.5, 4.5, 5.5, 6.5, 8.0, 9.0, and 10.0) at a salt concentration of 150 mM NaCl, and no significant adsorption could be found ($|\Delta f| \leq 0.5$ Hz) (figure 2.7A). The use of Hepes instead of PBS at similar ionic strength (150 mM NaCl) and pH did not result in any significant binding either. Variation of the NaCl concentration, in the range of 0 to 200 mM NaCl, at neutral pH also resulted in no or minor adsorption. The highest frequency shifts of -6 Hz were attained in Hepes buffer without NaCl. Even in this case, however, most of the adsorption was reversible, with only -2 Hz remaining after rinsing (figure 2.7B), corresponding to less than 7% of a SAv monolayer on gold.

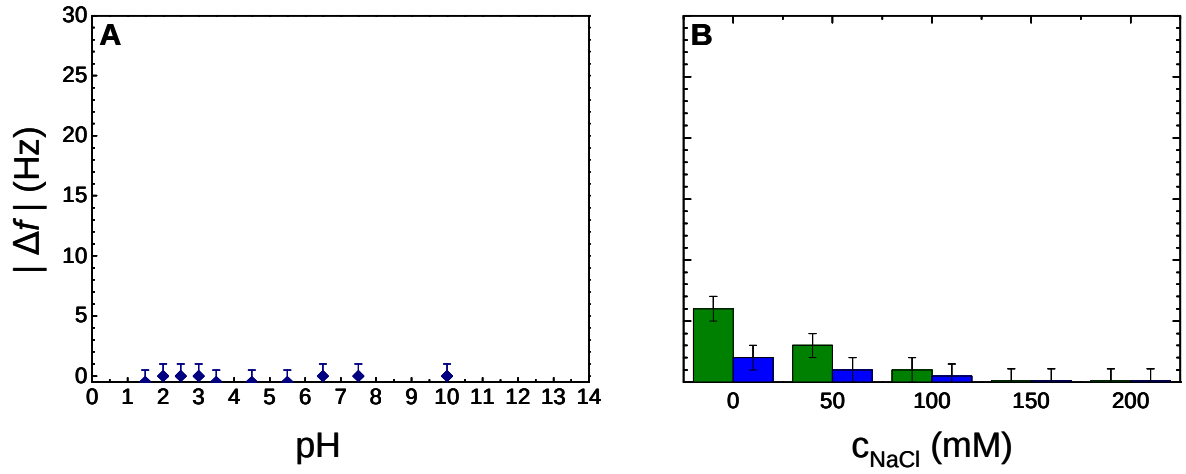

Figure 2.7: QCM-D frequency shifts upon exposure of silica surfaces to SAv as a function of pH (A) and ionic strength (B). Measurements in (A) were performed in 150 mM NaCl. Measurements in (B) were performed at pH 7.4. Values before *(green)* and after *(blue)* rinsing are shown. Error bars are derived from noise and drift instabilities during the measurements.

Exposure of Av and NAv-covered surfaces to biotin-BSA resulted in binding with final frequency shifts of -14 Hz and -16 Hz for Av and NAv, respectively (figure 2.6C, table 2.1). No binding occurred on surfaces, which had been in contact with SAv solution before. Native BSA did not bind (figure 2.6B), confirming that the immobilized Av and NAv retained their binding activity.

Physisorption of BSA to silica depends on protein concentration. It should be stressed that biotin-BSA did not bind to a bare silica surface. Even native BSA showed very low adsorption (figure 2.6B). This may at first appear surprising, given that BSA is widely used as a surface blocking agent. This observation, however, is consistent with previous findings.[11] Notably, the BSA concentrations that are typically applied for blocking are 1000-fold higher than the concentrations employed here.[204,205] Indeed, when incubating BSA at 10 mg/mL (1% BSA solution), frequency shifts of about -30 Hz were observed, confirming the formation of a stable protein layer of about 5 nm thickness (figure 2.8).

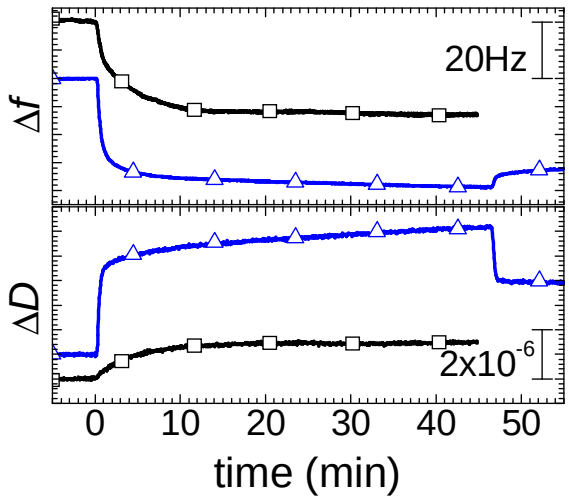

Figure 2.8: QCM-D responses, Δ*f* and Δ*D*, for the adsorption of native BSA to gold (*blue triangles*) and to silica (*black squares*). Incubation starts at 0 min with concentrations of 20 µg/mL on gold and 10 mg/mL on silica, respectively. Rinsing steps in buffer are indicated (*arrowheads*).

Table 2.1: QCM-D responses upon incubation of surfaces with biotin-binding proteins, BSA and b-BSA. Responses after rinsing in buffer are given.

		on b-SLB[a]		on gold		on silica	
		$\|\Delta f\|$ (Hz)	ΔD (10^{-6})	$\|\Delta f\|$ (Hz)	ΔD (10^{-6})	$\|\Delta f\|$ (Hz)	ΔD (10^{-6})
SAv	SAv	28±2	0.5±0.1	30±2	0.1±0.1	<0.5	<0.1
	BSA	<0.5	<0.1	1±1	<0.1	<0.5	<0.1
	b-BSA	13.5±1	0.3±0.1	12.5±1	0.5±0.1	<0.5	<0.1
Av	Av	26±1	0.6±0.1	32±2	0.1±0.1	20±4	0.3±0.2
	BSA	<0.5	<0.1	3±1	<0.2	<0.5	<0.1
	b-BSA	15±1	0.6±0.1	15.5±2	0.4±0.1	14±2	0.5±0.1
NAv	NAv	≥32	≥0.9	>40	>1.2	>60	>3
	BSA	<0.5	<0.1	0.5±0.5	0.1±0.1	<0.5	<0.1
	b-BSA	9.5±1	0.2±0.1	>10	±0.5	16±2	-0.3±0.2

Errors correspond to the spread of experimental data, obtained from 2 to 5 measurements per sample (see figs. 2.4, 2.5 and 2.6 for representative measurements). [a] adsorption values on biotinylated SLBs taken from Wolny et al.[1].

2.2.2 Discussion

The immobilization of streptavidin, and other biotin-receptors, to different surfaces has been investigated. Two main observations are particularly remarkable: First, SAv, as well as Av and NAv, bound well to gold and retained their biotin-binding activity after physisorption. Second, SAv was uniquely resistant to adsorption to silica.

Physisorption of SAv to gold as a biofunctionalization method. The results demonstrated that the physisorption of streptavidin (or other biotin-binding proteins, such as avidin) to gold presents a simple way to equip a surface with a high density of biotin-binding sites. The functionalized surfaces were stable, and exhibited little, if any, unspecific binding of BSA. Gold is an interesting and widely used material for biotechnological applications, in particular for biosensors.[206] In comparison to established strategies that require a linker layer between the solid support and the biotin-binding receptor, physisorption is attractive by its simplicity. Although unspecific adsorption is likely to lead to adsorption in various orientations, a large fraction of the immobilized molecules retained their biotin-binding activity. It should be noted, however, that sensor approaches that rely on fluorescent detection, may find a drawback in the direct immobilization of biotin receptors to gold:[207] The limited distance between the gold surface and fluorescent biotinylated targets can potentially quench the fluorescence.

The absence of SAv binding to silica surfaces. No significant response was observed by QCM-D upon exposure of SAv to silica over a wide range of pHs and ionic strengths. Given that the detection limit of our setup is better than 0.5 Hz, and considering that the solvent contributes by about 80% to the measured mass at low surface coverage of SAv,[139] we can derive an upper limit for the bound protein mass of 2 ng/cm^2, or about 1% of a complete monolayer.

What may explain the absence of binding for SAv, as compared to the strong binding of Av and NAv? In the simplest scenario, one may solely consider mean-field electrostatic and van-der-Waals interactions (DLVO-theory). Av has an isoelectric point of 10.5,[208] and thus carries a net positive charge at neutral pH. Electrostatic interactions would thus promote the adsorption of Av to the negatively charged silica surface, which was indeed observed. Several observations, however, argue against electrostatics to be the key interaction that prevents binding of SAv. Firstly, NAv readily bound to silica, although its isoelectric point of 6.3 [209] is similar to that of SAv (6.4 [210]). Secondly, SAv did not adsorb even at pH values between 3.5

and 7, a range in which silica and SAv would be expected to carry opposite net charges. A rigorous comparison of the magnitude of the surface charges of SAv and silica as a function of pH and ionic strength[211] and of the binding behavior of SAv on other metal oxide surfaces, such as titanium,may provide further insight into the role of electrostatics inSAv's resistance to binding but is outside the scope of this work. Apart from these mean-field considerations, discrete molecular interactions and steric effects may of course also be at play.[212]

To the best of our knowledge, the absence of unspecific interaction between SAv and silica or glass has not yet been reported in the literature. One earlier work, however, contradicts the finding of the present study: Bushan et al.[200] observed binding of FITC-labeled SAv to silica. Using QCM-D, no significant adsorption to cleaned silica could be detected (data not shown). The presence of the fluorescent dye alone thus cannot explain binding. Instead, variations in the surface preparation may explain the different adsorption behavior: the surfaces employed by Bushan et al. exhibited a contact angle of around 40º, while complete wetting was observed for the cleaned surface that have been used here. Indeed, the preparation and cleaning of surfaces have previously been found to strongly affect protein adsorption behavior.[213]

In conclusion, it could be demonstrated that the physisorption of biotin-binding proteins, such as streptavidin or avidin, to gold presents a simple way to equip a surface with a high density of biotin-binding sites. The functionalized surfaces were stable, and exhibited little, if any, unspecific binding of BSA. Given the plethora of available biotinylated biomolecules, such a surface represents an interesting immobilization platform. In comparison to established strategies that require a linker layer between the solid support and the biotin-binding receptor, our approach is attractive by its simplicity. It remains rather crude, however, in that the orientation of the biotin-binding sites on the surface is not well controlled.

In stark contrast to gold, streptavidin did not adsorb to silica over a wide range of pHs and ionic strengths. As part of the effort to develop the selective functionalization of nanostructured surfaces, the simple strategy of physisorption of SAv to gold and the resistance of silica to SAv seem to be more attractive than its crudeness may at first suggest.

2.3 Linker mediated immobilization of streptavidin to homogenous gold surfaces

Physisorption of SAv on gold is an interesting method as shown in the present study. However, this strategy does not provide control over the orientation of the protein, and SAv is likely to adsorb in random orientations, which can possibly limit the fraction of active protein on the surface. Another limitation of direct adsorption is that proteins can undergo denaturation upon close contact with the surface, and thus loose their biological activity.[106-108] To overcome these limitations various linker strategies have been proposed in the literature and reported to be successful.[12, 111, 191, 200, 214] Encouraged by these reports, two alternative binding strategies were also tested using biotin-PEG-SS and HPDP-biotin as linker. The results below illustrate that the immobilization of SAv through linkers is not a trivial task and rationalize, why this is so.

2.3.1 Results

HPDP-biotin. The frequency response upon exposure of a gold surface to HPDP-biotin was found to be -10.5 ± 1.5 Hz (figure 2.9A) corresponding to a layer thickness of around 2 nm. The thickness is comparable to, although lower than the molecule's contour length (2.9 nm for the spacer arm). The spacer is expected to be tilted with respect to the surface normal according to what is known about the conformation of SAMs, which could explain the difference.

Strong variations in the binding of SAv to HPDP-biotin layers were observed. In 50 % of the measurements a final frequency shift of -20 ± 2 Hz was found. In all other measurements the frequency shift was lower. Δf -values in the range of -30 Hz (as observed for physisorption on gold) were never reached.

Successively added biotin-BSA showed a decrease in frequency of -16 ± 1 Hz (figure 2.9). A control measurement with BSA, however, revealed unspecific interaction with the underlying surface in the range of several Hz (Figure 2.9B). Upon addition of biotin-HA (which did not interact unspecifically), only minor binding was observed (Δf = -1 ± 0.5 Hz) (Figure 2.9A), indicating that SAv did not retain its biotin-binding activity.

The strong variations in SAv binding may originate from the history of HPDP-layer formation. An altered protocol for HPDP-layer formation (overnight incubation in ethanol outside the QCM-D instead of *in-situ* addition in buffer just prior to SAv addition) improved

the binding of biotin-HA with values of $\Delta f \approx$ -24 Hz $\Delta D \approx 10\ 10^{-6}$, while the adsorption of SAv remained low ($\Delta f \approx$ -16 Hz) (data not shown). Values comparable to those expected for SAv monolayers (as on biotin-SLBs, or physisorbed on Au) were not reached.

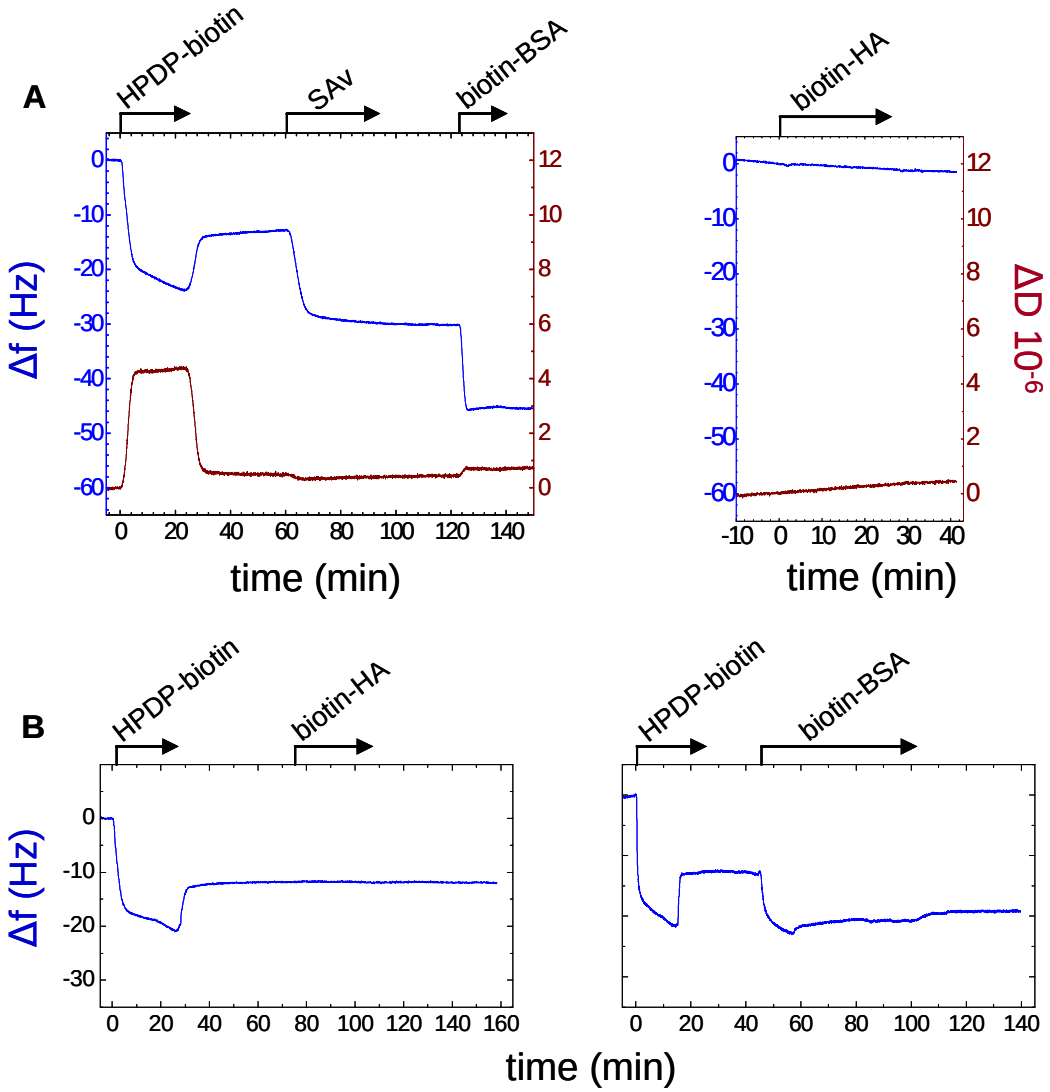

Figure 2.9: A: Representative experiments of SAv immobilization on HPDP-biotin with two different biotinylated targets: SAv + biotin-BSA *(left panel)* and SAv + biotin-HA of M_w = 58 kDa *(right panel)*. The addition of biotin-HA to the SAv layer is shown without the previous steps, and the SAv layer is offset to zero. The increase in Δf and ΔD upon rinsing after incubation with HPDP-biotin reflect a buffer change effect, which arises from the diluted solvent of the HPDP-biotin stock solution (DMF) being exchanged for pure Hepes buffer. B: Control measurements for the unspecific binding of biotin-HA *(left)* and biotin-BSA *(right)* to a HPDP-biotin layer in the absence of SAv. Start and duration of all incubation steps are indicated *(arrows)*

Biotin-PEG-SS. Biotin-PEG-SS adsorbed stably to the gold surface with a final frequency change of -9.5 ± 1.5 Hz (figure 2.10) corresponding to a thickness of 1.7 ± 0.3 nm. The thickness remains significantly smaller than the contour length (6.4 nm as calculated from bond lengths of the molecule). We hypothesize that the surface-bound PEG chains are stretched weakly and form a brush. The increase in dissipation, by 1.0×10^{-6}, is consistent with the formation of a flexible layer of rather short, grafted PEG chains.[215]

SAv bound readily to the linker film with kinetics and a final frequency shift (-30 Hz) similar to those observed on gold, indicating the formation of a dense monolayer (figure 2.10A). The dissipation shift was small ($< 0.1\times10^{-6}$) and significantly lower than observed on SLBs. This response may reflect a tight coupling of SAv onto or even partially into the film.

Despite the typical response for a monolayer of SAv, biotin-BSA did not bind to the biotin-PEG-coupled SAv ($|\Delta f| < 0.5$ Hz, Figure 2.10). Biotin-HA gave a shift of -1.5 Hz, which is also small compared to values obtained on physisorbed SAv (-30 Hz) or those reported by Richter and coworkers on biotin-SLBs[12] (-50 Hz). The response to both biotinylated targets thus suggests that SAv's binding activity is almost entirely lost, although the surface can be decorated with a dense layer of the protein.

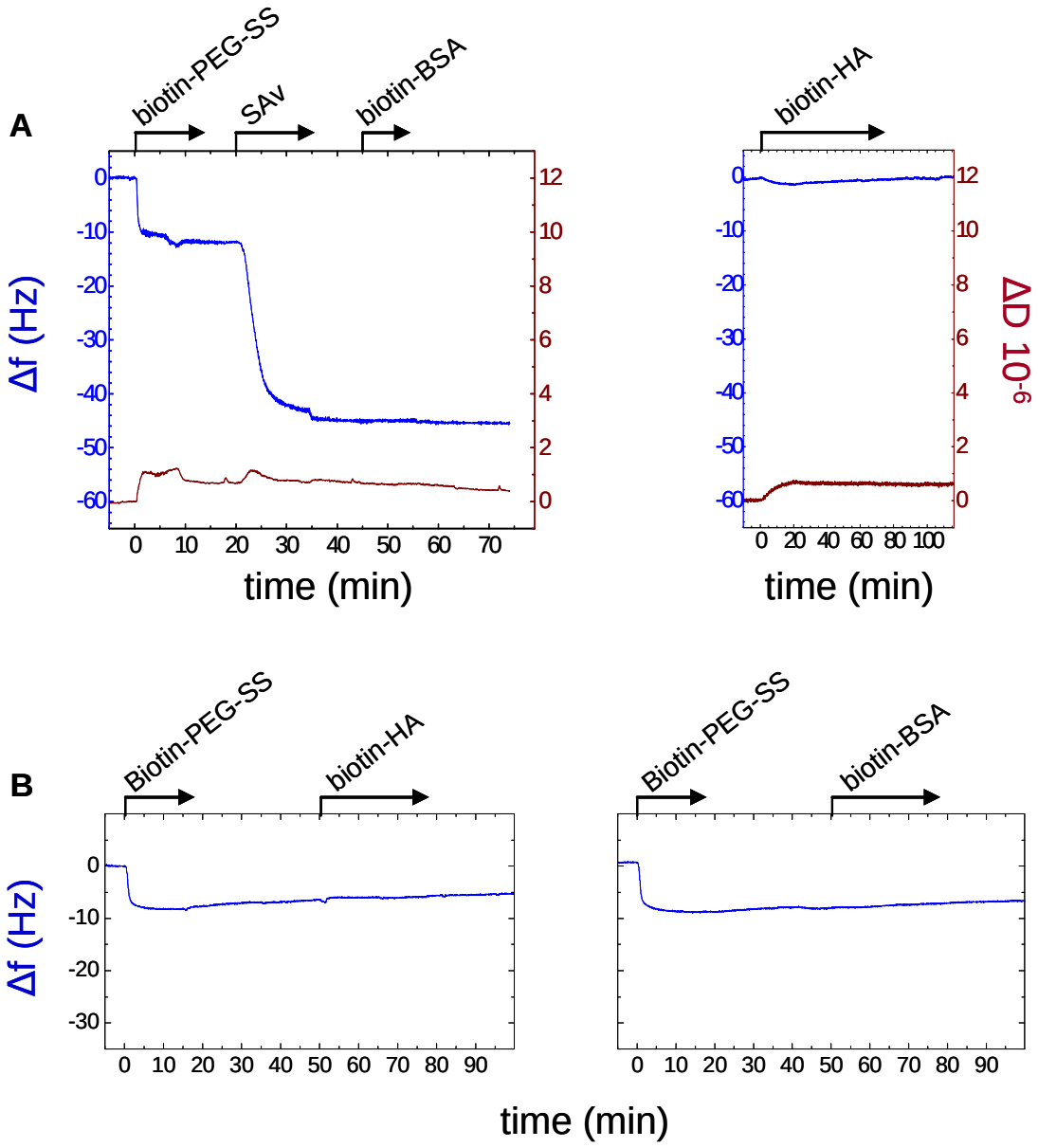

Figure 2.10: A: Representative experiments of SAv immobilization on biotin-PEG-SS with two different biotinylated targets: SAv + biotin-BSA *(left panel)* and SAv + biotin-HA of M_w = 58 kDa *(right panel)*. The addition of biotin-HA to the SAv layer is shown without the previous steps. The SAv layer is offset to 0. B: Control measurements for unspecific binding of biotin-HA (left) or biotin-BSA (right) to a biotin-PEG-SS layer in the absence of SAv. Start and duration of all incubation steps are indicated *(arrows)*

2.3.2 Discussion

The introduction of a linker molecule constitutes an additional experimental step to be performed and controlled. In the context of this work, I found that the employed linker

molecules, tested on homogenous gold surfaces, did not fulfill the demands for an appropriate bio-functionalization method.

On the effect of linker molecules for the biofunctionalization of gold surfaces. Among some studies, in which linkers were employed for immobilization of SAv[105, 191, 193, 200, 216] it has been pointed out that the use of a linker was not trivial. Huang et al.,[111]for example, employed PLL-g-PEG with varying ratios of biotinylated and not functionalized PEG. They found a clear decrease of SAv binding activity above a critical biotin surface coverage, although the amount of bound SAv further increased monotonously with increasing amount of biotin linkers. Interestingly, parallel experiments with Av instead of SAv did not reveal a similar transition. Similar steric crowding effects have been reported previously.[109, 110, 217] The low signal in dissipation that was obtained for the monolayer of SAv on biotin-PEG-SS implies tight coupling of the protein to the linker layer. It is therefore likely that in a similar scenario, as described above, a high density of biotins, attached to flexible linker, in the biotin-PEG-SS film is capable of blocking all four binding pockets of SAv. The use of HPDP-biotin as a linker and promoter of SAv immobilization has been reported earlier, though the low efficiency of this method was indicated, too.[218-220] It has been speculated that a high density of biotins may inhibit the optimum interaction with the protein.
The findings of the present thesis provide additional illustration and insight into the complexity that can be associated with the functionalization of surfaces.

2.4 Selective decoration of nanostructured surfaces with SAv - an initiating study

The resistance of silica to SAv binding over a wide range of experimental conditions suggests a very simple yet promising strategy for the selective functionalization of the gold nanoarrays.

2.4.1 Results

Generation of nanostructured arrays on QCM-D sensors. SEM micrographs (figure 2.11) revealed that gold nanoparticle arrays could be successfully generated on silica coated QCM-D sensor crystals by block copolymer micellar nanolithography (see chapter 6.1 for details). Three different polymers (451, 1056 and 2074) were used to obtain different mean nearest neighbor particle distances of about 50, 75 and 110 nm, respectively (figure 2.11).

In comparison with nanostructures from the same precursor solution on glass cover slips, a difference in the appearance of the background was visible. While the background on glass was totally homogenous, the QCM-D sensors exhibited a cloudy-like and heterogeneous appearance. This difference is likely to originate from the roughness of the sensor surface, which features typical corrugations of about 5nm height and a lateral extension of about 50 nm.[221] Indeed, sensor surfaces that were not decorated with nanostructures had a similarly heterogeneous appearance (figure 2.12B). The background heterogeneity of QCM-D sensors should not be confounded with a type of cloudy, network-like structure around gold nanoclusters that has been observed earlier when intact micelles were imaged.[222]

It can already be appreciated from figure 11 that the long-range order of gold nanoparticle arrays on QCM-D sensor surfaces was slightly worse than on glass. To quantify the degree of the order within a regular (hexagonal) structure, the order parameter ψ was employed (see chapter 6.3.1 for details). For $\psi > 0.5$, the structure is generally regarded to be of good quality.[222] Analysis of random samples revealed order parameters of $\psi \geq 0.55$ on QCM-D crystals and $\psi \geq 0.65$ on glass. It is reasonable to suggest that it is the nanoscale surface roughness of the QCM-D sensor crystals[221] that gives rise to the decrease in order.

The generated gold-nanostructures were stable throughout the experimental procedure as shown by SEM imaging after use of the surface (figure 2.12A).

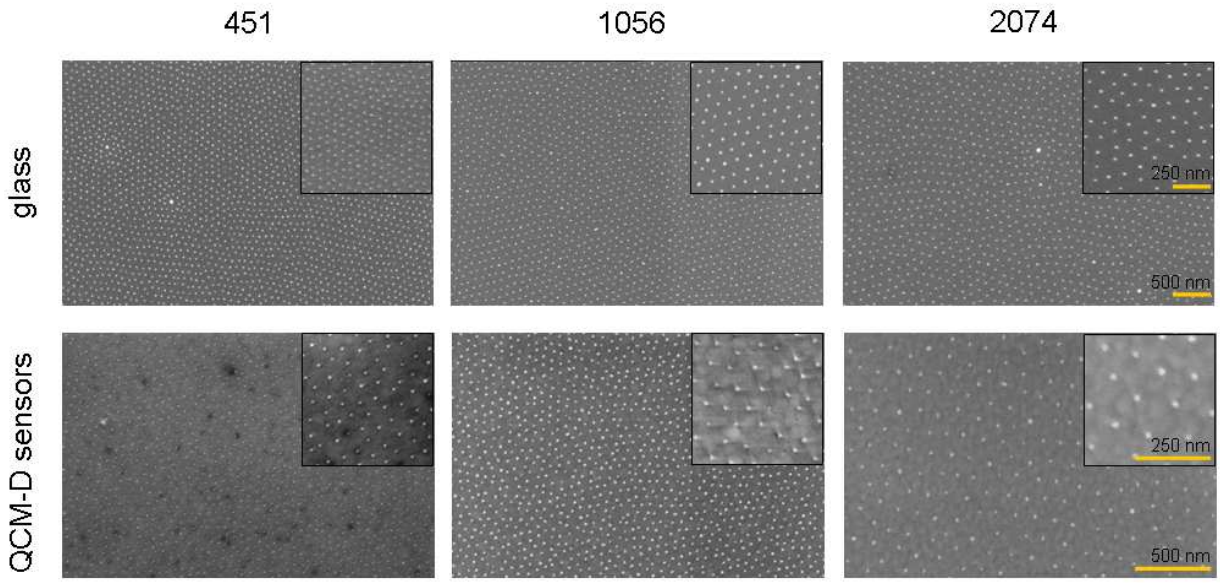

Figure 2.11: SEM micrographs of nanostructured surfaces. Nanostructures were generated with three different polymers (451, 1056 and 2074) on glass *(upper panel)* and on QCM-D sensor crystals *(bottom panel)*. The arrays of bright dots represent the quasi-hexagonal gold nanostructure. A cloudy-like background is visisble on QCM-D sensors (see insets), but not on glass surfaces. Insets show the structure at higher magnification. Scale bars are representative for all images in a given row.

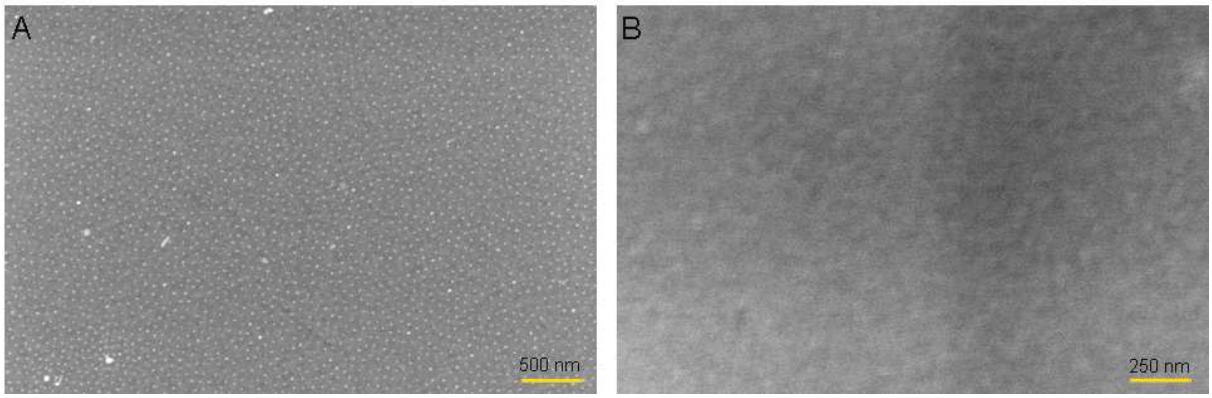

Figure 2.12: A: SEM micrograph of a QCM-D crystal with nanostructure generated from Polymer 451 after an experiment. Therein the nanostructured surface had been exposed to solutions of SAv and biotin-BSA subsequently and underwent successive rinsing steps in H_2O and SDS 3% in the Q-CM-D chamber. After the experiment the crystal had been rinsed in water and blow-dried with N_2 before being transferred to the SEM. The integrity of the nanostructure is preserved. B: SEM micrograph of a QCM-D sensor surface without nanostructure shows the same cloudy-like, heterogeneous features that were observed for nanostructured QCM-D sensors.

Functionalization of gold-nanoparticles by physisorbed SAv. From all tested biotin-binding proteins only SAv formed dense monolayers on gold by physisorption while resisting any interaction with silica (section 2.1). Therefore, SAv seemed best suited for the direct functionalization of gold nanoparticles, without the need for passivating the surrounding silica areas.

SAv adsorbed to nanostructured surfaces with an inter-particle distance of about 50 nm yielding QCM-D responses in the range of Δf = -2 to -7 Hz. This range of values was obtained on different surfaces with comparable inter-particle distances. Representative experiments are shown in figure 2.13. There was no obvious explanation for why the results spread over several Hz. The reproducibility of QCM-D responses typically lies within 1 to 2 Hz, and can hence, not explain the observed deviations. To exclude failures in the nanostructure, some surfaces were imaged after the measurement by SEM. The integrity of the nanostructure was preserved (figure 2.12A).

To probe whether the response for the adsorption of SAv to the gold nanoparticles was specific, control measurements were performed, in which surfaces without nanoparticles were used. These surfaces underwent the same pre-treatment steps, i.e. they were dipped into a diblock-copolymer solution that did not contain the gold precursor salt and were subsequently exposed to oxygen plasma (see chapter 6.1.1). In line with previous results on bare silica surfaces (see adsorption behavior of SAv on SiO_2), no response was detected, indicating that adsorption was not caused by residues of polymer solution and that binding was specifically due to the gold nanoparticles (inset figure 2.13B).

Notably, the the kinetics of SAv binding - regardless of the final value - was very slow (figure 2.13) Adsorption rates of about 0.2 Hz/min were found to be compared with values of about 10 Hz/min for the initial rates on SLBs or homogenous gold surfaces. The slower kinetics indicates that the binding of SAv to the gold nanoparticles must be kinetically hindered, in contrast to initial binding to SLBs or homogenous gold, which is mass transport limited.[223] It could be speculated, that the size of the gold nanoparticles (5-10 nm) was not sufficient to be recognized as an accessible substrate for SAv. The gold nanoparticles have a diameter of typiclly 5-10 nm which is similar to the size of SAv (4x5x6 nm[113]). The cuboid shape of SAv and the spherical shape of the gold particle may limit the effective interaction area and thus binding of SAv.

Addition of biotin-BSA in a subsequent step resulted in fast binding with distinct frequency shifts (figure 2.13B). The obtained responses correlated with the frequency shift of the previously deposited SAv and varied between Δf = -2 to -6 Hz in various measurements. In

contrast to SAv, binding kinetics were comparable to biotin-BSA binding on other SAv decorated surfaces (such as on SLBs (figure 2.4C) or homogenous gold surfaces (figure 2.5C).

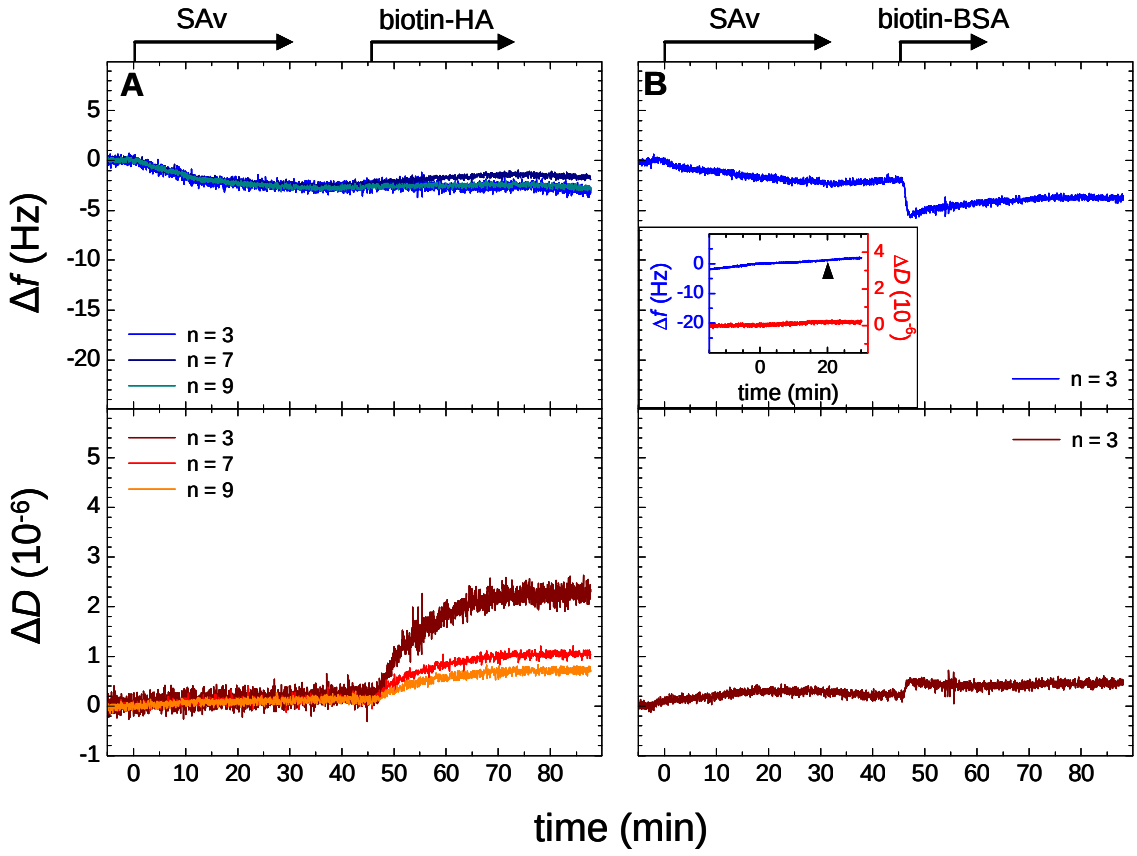

Figure 2.13: Δ*f* *(blue)* and Δ*D* *(red)* for the physisorption of SAv to gold nanostructured surfaces with inter-particle distances of ≈ 50 nm. Black arrows indicate the supply of SAv and the biotinylated target, respectively. A: Adsorption of SAv followed by addition of biotin-HA of M_w = 1083 kDa. The three curves correspond to three different overtones recorded by QCM-D in order to demonstrate the separation of overtones in Δ*D*, which is a typical response for end-grafted HA. B: Adsorption of SAv followed by addition of biotin-BSA. Inset: Control measurement on a non- nanostructured surface. A surface, which had been treated with a diblock-copolymer solution without gold precursor salt was exposed to SAv. Start of incubation is at t = 0. Start of rinsing is indicated *(arrowhead)*.

Grafting of hyaluronan to streptavidin decorated nanostructured surfaces. Initial tests have been performed with the grafting of end-biotinylated HA of about 1 MDa to SAv-decorated gold nanoparticles with interparticle distances of about 50 nm. Whereas only a small, if any, response could be detected in frequency, the change in dissipation was

pronounced (figure 2.13A). As typical for grafted HA[12], the various overtones, which were monitored simultaneously, spread as a response to the formation of a very soft and hydrated film. The obtained responses in dissipation were, however, about three fold smaller compared to HA chains that were grafted to SAv covered SLBs, with a grafting distance similar (≈ 60 nm)[12] to the gold nanoparticle separation (≈ 50 nm). These results indicate that a considerable fraction of the gold nanoparticles was not properly functionalized.
These initial measurements illustrate that HA can be immobilized to nanostructured surfaces. Improving the immobilization of SAv will be critical for future work in this direction.

Functionalization of gold-nanoparticles with biotin-PEG-SS. To probe, whether the accessibility to the gold nanoparticles could be improved if a molecule was smaller than SAv, nanostructured QCM-D crystals were exposed to biotin-PEG-SS.
Exposure of bare silica substrates to the linker revealed unspecific interaction with the surface (data not shown), which induced adsorption of SAv to silica. This interaction was influenced, but not abolished, by changing the solution from PBS buffer to various organic solvents (ethanol, toluene or DMF). To passivate the silica surface, a layer of mPEG(2000)-urea was attached covalently by silanization using an established protocol (see chapter 6.1.2). The sensor was then installed into the QCM-D chamber and the linker was introduced followed by rinsing and exposure to SAv. A change in frequency was observed when the linker was added (figure 2.14A). This change, however, was transient and the frequency returned to its initial value after rinsing. Such transient changes in frequency can be explained by the way the QCM-D senses the environment of the sensor. The properties of the solution, in particular its density and viscosity, and any changes of these properties are reflected in the responses of f and D due to coupling of the bulk liquid to the sensor surface. For the biotin-PEG-SS it is the comparably high concentration of the solution (1.5 mg/ml) that gives rise to transient changes in the QCM-D responses.
The successful functionalization of the gold nanoparticles with the linker could be shown by binding of SAv to the substrate. Responses of about -5 Hz could be detected (figure 14A). Controls showed that binding of SAv was specific: firstly, no response for SAv was observed on surfaces lacking the nanostructure (figure 2.14A). Secondly, the exposure of SAv to passivated, nanostructured surfaces (figure 2.14B) did not result in any significant response. The absence of any response upon SAv physisorption may originate from a "shielding effect" exerted by the PEG layer. XPS measurements have revealed a thickness of the dry PEG film of 2.2 nm and a grafting point density of 1.3 nm was deduced.[219] It can be expected that in

solution the PEG will form a brush resulting in a film thickness that may partly cover the gold particles. An alternative explanation for the absence of the QCM-D response relates to a scenario in which SAv would be embedded into the PEG film when binding to the gold particles. Then, the contribution by the exchange of adsorbed mass and water and, thus the QCM-D response would be small, if not canceled. This can be explained by the fact that QCM-D senses water that is embedded in a viscoelastic layer, such as a PEG film, as part of the layer. Given the similar densities of proteins, the PEG and water (ρ = 1.4 [132], 1.2 [219] and 1 g/cm^3, respectively) the absolute change in sensed mass due to exchange of one of these components by another will induce minor, if any, response.

When biotin-BSA was added, no binding could be observed on biotin-PEG-SS/SAv pre-functionalized gold nanoparticles, similar to what was observed on homogenous gold surfaces coated with the linker. When a nanostructured, passivated surface was directly exposed to SAv, and then to biotin-BSA (Figure 2.14B), a clear response of about -3 Hz was detected for biotin-BSA. Control measurements, in which biotin-BSA was added to the nanostructured, passivated surface prior to SAv exposure did not show any response (not shown). This indicates that SAv did physisorb to the gold nanoparticles and retained its biotin-binding activity.

It can be concluded that, immobilization of SAv through biotin-PEG-SS is accompanied by a at least partial loss of biotin-binding activity. This result is in line with the effects observed on homogenous gold surfaces in the presence of biotin-PEG-SS and likely to arise from the same origin, already discussed in this context.

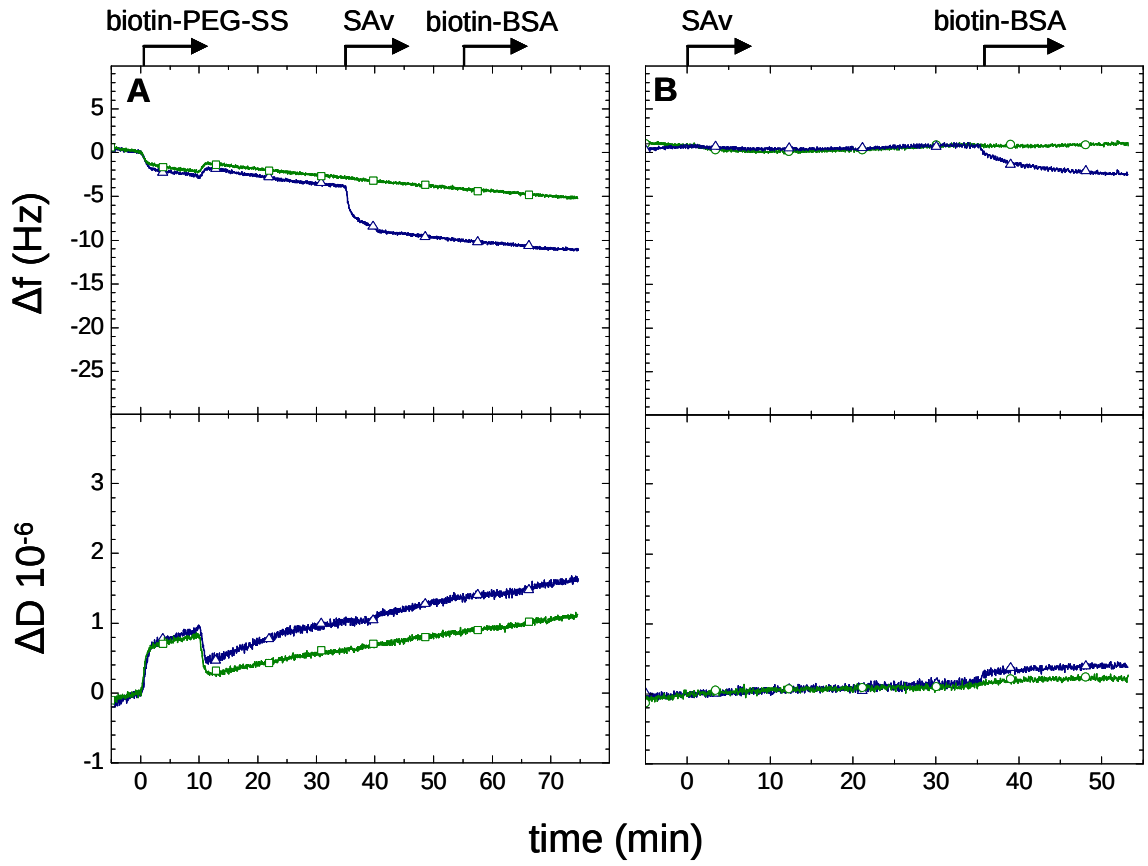

Figure 2.14: Immobilization of SAv via the biotin-PEG-SS linker. Top panels: frequency shifts as a function of time. Bottom panels: Dissipation shifts as a function of time. A: A nanostructured *(blue triangles)* and a SiO_2 *(green squares)* surface passivated with mPEG-urea were exposed to the linker and subsequently to SAv and biotin-BSA. The continuous decrease and increase Δf and ΔD, respectively stems from a drift during the measurement. B: A nanostructured *(blue triangles)* and a SiO_2 *(green squares)* surface passivated with mPEG-urea are exposed to SAv and subsequently to biotin-BSA in the absence of the linker. Start and duration of all incubation steps are indicated *(arrows)*.

2.4.2 Discussion

Regular arrays of gold nanoparticles have been created on silica-coated QCM-D sensor crystals by block copolymer micellar nanolithography, and initial steps to the functionalization of these particles with SAv were performed.

Physisorption of SAv to gold nanoparticles was detectable and specific, but strongly kinetically limited in contrast to homogenous gold surfaces. Final frequency values showed only poor reproducibility, for reasons which have not been identified as yet and which remain

to be investigated in further experiments. As on homogenous gold surfaces, SAv retained its biotin-binding activity.

The experimental data indicates that QCM-D has the sensitivity to detect the adsorption of proteins to the nanoparticles, and can provide information on binding kinetics. Based on the mean inter-particle spacing of about 50 nm, one can calculate that only 2% of the surface is covered with gold and the adsorbed amounts are hence expected to be small. However, rather high frequency changes of up to -7 Hz were measured for SAv, which correspond to almost 25% of the frequency shift of a SAv monolayer. A possible explanation may come from the way that QCM-D senses adsorbed mass. It has been shown recently that an isolated adsorbed particle contributes more strongly to the frequency response than a particle that adsorbs into an already rather dense monlayer. This effect was attributed to variations of hydrodynamically coupled water at different surface densities.[139]A similar effect may be responsible for the high frequency shifts observed here. However, the above mentioned study employed homogenous surfaces, and it remains to be elucidated to what extent such signal enhancement can occur on nanostructured surfaces.

Functionalization of the gold nanoparticles with biotin-PEG-SS, in line with previous findings on homogenous gold surfaces, resulted in a loss of biotin-binding activity of the subsequently immobilized SAv.

Initial results also indicated successful grafting of biotin-HA to the gold nanoparticles decorated with SAv. These, however, remain preliminary, as immobilization of SAv has to be improved.

2.5 Conclusion

From the obtained results it could be demonstrated that the spontaneous binding of SAv (and other biotin-binding proteins) to bare gold surfaces can be advantageously exploited for surface functionalization. Biotin-binding activity is maintained throughout surface functionalization. The direct physisorption of SAv to gold surfaces is therefore a promising approach to successful SAv immobilization avoiding any prior surface preparation or functionalization.

Exemplified on two different biotin containing thiolated linkers, which were supposed to promote SAv immobilization, unexpected complexities were discussed. For HPDP-biotin the reproducibility of SAv binding was poor, and the responses remained significantly below expectations. Binding of biotin-targets was strongly dependent on the history of surface functionalization and partly unspecific. Immobilization of SAv to a layer of biotin-PEG-SS resulted in a loss of biotin-binding activity, although a SAv monolayer formed. The lack of control over the system that arises from introducing the linker motivates SAv physisorption as the method of choice for further experiments.

As I could further show in the present study, the underlying material played a crucial role, whether and/ or to which extent a protein binds to the surface. Spontaneous adsorption of SAv to gold surfaces was found, while no binding of SAv occurred on silica surfaces. The same observation was made for biotin-BSA and for native BSA. However, other biotin binding proteins (Av, NAv) did adsorbed.

Functionalization of gold nanostructured substrates by physisorption of SAv could be demonstrated. Initial binding experiments of biotin-HA indicated HA-film formation on the nanostructured surface with qualitatively typical, albeit far lower responses than reported on other substrates that had been decorated with SAv. These results indicate the need of improving the immobilization of SAv to gold nanoparticles, which will be essential for further studies in this direction.

QCM-D was sensitive to the specific interaction of proteins with the gold nanostructures. This is remarkable, given that the gold particles cover only a small fraction (~2%) of the surface. Notably, the QCM-D response could also provide information on binding kinetics

Taken together, the direct physisorption of SAv to gold is attractive for its simplicity and should be a valuable alternative to established yet more complex strategies that require a linker layer between the solid support and the biotin receptor.

In contrast to gold, streptavidin did not adsorb to silica over a wide range of experimental conditions. This contrast suggests a particularly attractive application of physisorption as a simple route for the selective functionalization of nano- or microstructures of gold on silicon-based devices. Such devices include small-scale probes (microcantilevers and atomic force microscopy tips) and nanostructured surfaces.

Chapter 3

Novel CD44 Based Model Systems for the Investigation of Polyvalent Interactions with Hyaluronan

The aim of this project was the establishment of model systems that allow investigating the binding of HA to a receptor covered surface in a well-controlled environment. An assembly of biomolecular layers was designed which enabled the immobilization of CD44 receptors in biologically relevant arrangement. This design opened doors to the study of the specific interaction between the receptor CD44 and its ligand HA. Despite a multitude of existing literature in the field, a biophysical approach to untie the questions of the molecular and supra-molecular mechanisms underlying CD44-HA interactions is still missing.

These model systems were characterized by means of quartz crystal microbalance (QCM-D), ellipsometry and reflection interference contrast microscopy (RICM). QCM-D allowed tracking each adsorption step in real-time and provided information on hydrated mass, the conformational properties and the stability of the adsorbed layers. RICM measurements added further information about the morphology of the HA films. The absolute biomolecular mass of the deposited layers could be quantified using ellipsometry

3.1 Motivation

The propensity of CD44 to bind HA varies strongly across cell types and state of maturation, and such modulation of binding is thought to be functionally important. Whereas the structural origins of HA binding by CD44 are quite well understood,[72] little is currently known about the mechanisms on the supra-molecular level of CD44-HA interactions. Multiple low affinity interactions, which can result in a high total avidity system by polyvalent binding of CD44 to HA are proposed as one mechanism of the dynamic regulation of the PCC.[41]

Since the affinity between an individual ligand and CD44 was found to be rather weak ($K_D \approx 5$ to 150 µM [80, 224]), it is likely that much of the regulatory potential lies in the spatial arrangement of receptors on the cell surface. Apart from a range of studies that highlighted the role of dimerization in the regulation of HA binding,[79, 225] methods are scarce to investigate such effects in a controlled manner. Conventional *in vitro* binding assays are sensitive to interactions of individual ligand receptor pairs, but ignore the spatial confinement and arrangement of HA receptors in two dimensions that characterizes the cell membrane.[72] Cellular assays have provided valuable insights into overall patterns of regulation, but the complexity of the living cell makes it difficult to disentangle the relative contributions of the different types of interactions.[225] A simple yet pertinent question, for example, has to date not been addressed. How many receptors are required to bind HA stably to the cell surface?

The aim of the present project was the development of two new supported lipid bilayer based model systems for examining quantitatively polyvalent CD44-HA interactions. This approach differs from other HA immobilization methods[5, 12, 96, 100, 101] in that it employs HA`s natural cell surface receptor CD44 itself for binding of HA. CD44 is immobilized such, that it retains mobility in two dimensions in two dimensions similar to the cell surface confinement. Such an architecture can serve as a platform for the study of polyvalent CD44-HA binding events with less complexity than the cellular level, yet, beyond the single interaction of CD44 and HA.

3.2 Concepts of polyvalent binding events

It appears to introduce concise definitions of some important concepts related to polyvalent molecular interactions, which are commonly used in the context of this work.

Affinity. Affinity is the measure for the strength of a bond between a receptor and a ligand. It is an intrinsic characteristic of the complex made of the receptor-ligand pair. The higher the affinity, the longer is the lifetime of the bond. The affinity is commonly expressed

in form of the dissociation constant K_d (instead of the association constant*), the equilibrium constant for the dissociation of the receptor-ligand complex[76]:

$$K_d = \frac{[R]^x \times [L]^y}{[R_x L_y]} \tag{12}$$

with [*R*], [*L*] and [*RL*] being the concentrations of the receptor, the ligand and the receptor-ligand complex, respectively, and *x*, *y* the number of the respective component. K_d marks the ligand concentration, at which half of the receptor binding sites are occupied[76].

The association constant for the formation of a bond with free energy ΔG is given by:

$$\Delta G = -RT \ln(K). \tag{13}$$

The affinity of a receptor-ligand pair can be influenced by intermolecular interactions like electrostatic or van-der-Waals forces. It may also be sensitive to temperature, pH and ionic strength conditions.

Polyvalency. The valency, *N*, of a molecule is defined by the number of equivalent, independent sites that are able to form connections with other molecules by specific interactions.[226] In fact, many biological systems rely on polyvalency and polyvalent interactions (see, e.g., Mammen et al.[226]). For example, receptor-ligand interactions between the influenza virus[227, 228] or HIV[229] and host cells employ polyvalent interactions.[226]
Polyvalent interactions can occur if both the receptor and the ligand are polyvalent (figure 3.1).

* Both constants are related to each other by: $K = 1/K_d$. The units are M^{-1} and *M* for *K* and K_d, respectively.

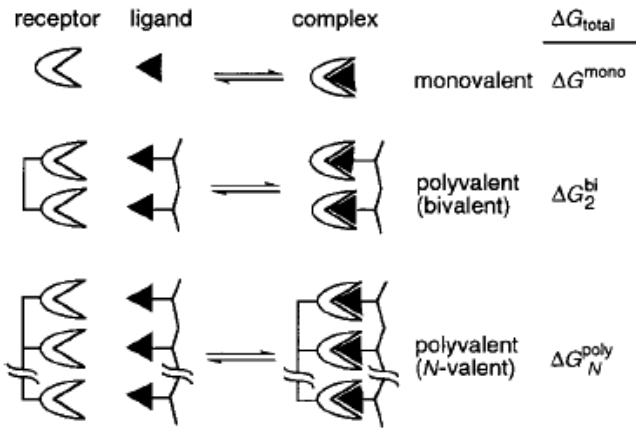

Figure 3.1: Polyvalent receptor-ligand interactions. Sketch of key-lock-like binding events between respective molecular entities and systematic nomenclature as proposed by Mammen et. al.[226].

The energy balance of polyvalent interactions is made up from enthalpic and entropic contributions, and can be written as[226]:

$$\Delta G_N^{poly} = \Delta H_N^{poly} - T\Delta S_N^{poly}, \tag{14}$$

where the index "*poly*" indicates that polyvalent interaction is considered and N is the valency (see figure 3.1). The average free energy per individual bond in a polyvalent system can be written as:

$$\Delta G_{avg}^{poly} = \frac{\Delta G_N^{poly}}{N}. \tag{15}$$

From eq. 13 and 14 the association constant for a polyvalent interaction can be deduced:

$$K_N^{poly} = (K_{avg}^{poly})^N. \tag{16}$$

Increase in binding strength by avidity. Avidity refers to the combined effect of multiple binding events of a receptor to a ligand. In contrast to affinity it is not an intrinsic parameter of the binding strength of a complex. Rather, it can be regarded as a synergistic, effective

binding strength that depends on the supra-molecular environment. By acting collectively, multiple weak interactions, otherwise unable to form stable binding, can result in a total binding strength, which is higher than the bare sum of the involved individual bonds[226] (eq. 16).

The enhancement of binding (β) can be described by the ratio of the dissociation constants of an individual component (K_d^{mono}, *affinity*) and the total dissociation constant (K_d^{poly}, *avidity*) of the polyvalent system:

$$\beta = \frac{K_d^{mono}}{K_d^{poly}} \tag{17}$$

The enhancement is strong for high values of β.

Cooperativity. A binding event is cooperative if the affinity for binding changes as a function of the ligands already bound[76] to a polyvalent receptor. By comparing the free energy of binding of the unperturbed monovalent interaction, ΔG^{mono}, with the average free energy per individual interaction in a polyvalent complex, ΔG_{avg}^{poly}, the degree of cooperativity can be defined:

$$\alpha = \frac{\Delta G_{avg}^{poly}}{\Delta G^{mono}}. \tag{18}$$

The interaction is:

positively cooperative for	$\alpha < 1$,
non-cooperative for	$\alpha = 1$,
negatively cooperative for	$\alpha > 1$.

The binding of oxygen to hemoglobin is one of the most popular examples for positive cooperativity*.[230, 231] Here, binding of the first oxygen molecule increases the affinity for binding of additional oxygen molecules.

* Cooperativity can be described quantitatively. The reader is referred to the method by Hill,[6, 7] where the cooperative binding of oxygen to hemoglobin was analyzed.

In general, cooperative effects arise from conformational changes of the receptor upon its interaction with the ligand, such that the new conformation adopts an altered affinity for the second ligand.[232] The phenomenon that an effector molecule changes the ligand binding properties of a receptor by binding to it (at a position different from the ligand binding site - the allosteric site), is also known as allostery.[76] In the special case of cooperativity the allosteric site corresponds to another ligand binding site on the receptor (figure 3.2).

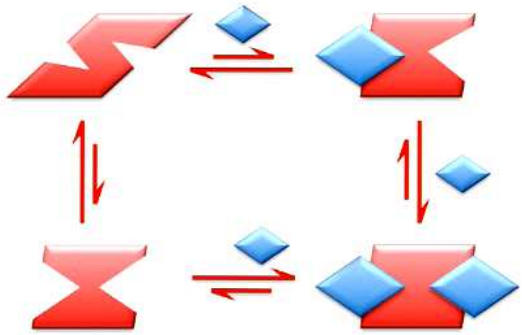

Figure 3.2: Allosteric cooperativity. The binding of the first ligand *(blue)* stabilizes a modified conformation of the receptor, thereby rendering it into a higher affinity form. The interacting ligands can be identical or different, and any number of ligands can be involved. Image adapted from ref.[232].

It should be stressed that cooperativity is not required in polyvalent interactions to enhance the binding between receptor and ligand. In fact, binding can be enhanced even for negative cooperativity ($\alpha < 1$). This can easily be seen from eq. 16, 17 and 18:

$$K_N^{poly} = \left(K_{avg}^{poly}\right)^N = \left(K^{mono}\right)^{\alpha N}. \qquad (19)$$

This equation shows that the avidity of the complex is larger than the affinity of individual bonds ($\beta > 1$) even for ($\alpha < 1$), as long as $\alpha > 1/N$.

I should be noted that the above given definition of cooperativity is not used consistently in the literature. Frequently, $\beta > 1$ is considered a sufficient criterion for (positive) cooperativity. For example, cooperativity is often attributed to a binding enhancement by configurational pre-organization of a polyvalent ligand.[232] The chelation of metal ions is one of the most prominent examples.[232, 233] After the first connection has been established, subsequent interactions with the same ligand become more favorable by reducing the entropic cost of

bringing an independent receptor into a bound state. The total affinity constant in this scenario is higher than the bare sum of the individual contributions ($\beta > 1$), while α can, in principle, be smaller or larger than 1.

In the context of this thesis I will repeatedly use the term avidity effect for the enhancement of binding between of receptors and ligands as a result of polyvalent interactions ($\beta > 1$).

´

3.3 Design of the model systems

Two different model systems for the immobilization of either monomeric or dimeric CD44 constructs were constructed. The choice of the specific building blocks and the step-by-step assembly will be described below.

3.3.1 Supported lipid bilayers as model membranes

Supported lipid bilayers (SLBs) have found wide application as models for biological membranes.[21, 22] Comprising the same molecular components as biological membranes, they are the most natural mimics with compositions, architectures and dynamics similar to their natural counterpart. Moreover, and importantly for surface functionalization processes, the bilayer withstands unspecific binding of most biomoecules[1, 234] thus leaving its surface accessible for direct immobilization without the need of an additional passivating step. Nowadays, SLB preparation and formation on a variety of solid supports, like e.g. silica or mica, is well characterized and controlled.[129-131, 235, 236] Bilayer properties are tunable by the possibility of using different lipids or mixtures of different lipids, which expose a number of functionalities. Such, doors are opened to various applications as for example, protein immobilization.

Within this work, SLBs play a major role as i. a reliable immobilization platform, ii. a functional mimic of the outer cell surface and iii. a passivating layer against undesired biomolecule interactions. Three types of phospholipids were employed: first, DOPC (1,2-dioleoyl-sn-glycero-3-phosphocholine), a zwitterionic unsaturated phospholipid with a zero net charge. DOPC is one of the standard phospholipids, which constitutes the main component in the lipid mixtures that were prepared for this study. Secondly, DOPS (1,2-dioleoyl-sn-glycero-3-phosphoserine), in which the serine headgroup gives rise to a negative charge. Finally, OEOA-bis-NTA (bis-NTA-Octadec-9-enyl-octadecyl-amine) which contains

two NTA moieties on its headgroup was used for nickel-ion mediated complex formation. The divalent presentation of NTA improves the binding stability of histidine-tagged proteins, with dissociation constants in the lower nM range.[237, 238] OEOA-bis-NTA was kindly provided by Prof. Jacob Piehler (Universität Osnabrück, Germany).

3.3.2 Annexin A5-Z

Annexin A5 (AnxA5) is a 35 kDa soluble protein with dimensions of 3x3x5 nm with slightly bent shape.[239, 240] It is known to bind to negatively charged phospholipid membranes. The convex face of the protein faces the membrane. Annexin A5 was subject to a number of studies, in which the binding behavior was investigated on model membranes.[7, 135, 241] Therein, it was shown that Annexin A5 forms 2D crystals on negatively charged lipid membranes spread on mica surfaces,[7] whereas closely packed assemblies of AnxA5 trimers exhibiting no long-range order are found on SLBs with silica as underlying substrate.[135, 221]

Protein A, a protein from the bacteria *Staphylococcus aureus*, consists of 5 N-terminal, equal subunits, each of which contains a 58 amino acid sequence, the so-called Z fragment.[242] Each subunit is capable to bind to the Fc-domain of immunoglobulins (IgGs). The crystal structure of the complex between a subunit of Protein A (B unit) and the Fc domain shows that the interaction takes place at the hinge region between heavy chains CH2 and CH3 with a high binding affinity ($K_D \approx 10^{-8}$ M).[243] The model in figure 3.3C illustrates this interaction.[244]

The coupling of the Z-fragment was realized at the C-terminal end of AnxA5, which is situated at the face of the protein that does not bind to lipid membranes. It has been previously shown that this modification does not perturb the membrane binding or the 2D crystallization of AnxA5.[245] The protein was kindly provided by Prof. Alain Brisson (Université Bordeaux 1, France). A model structure of the annexinA5-Z fusion protein is shown in figure 3.3B.

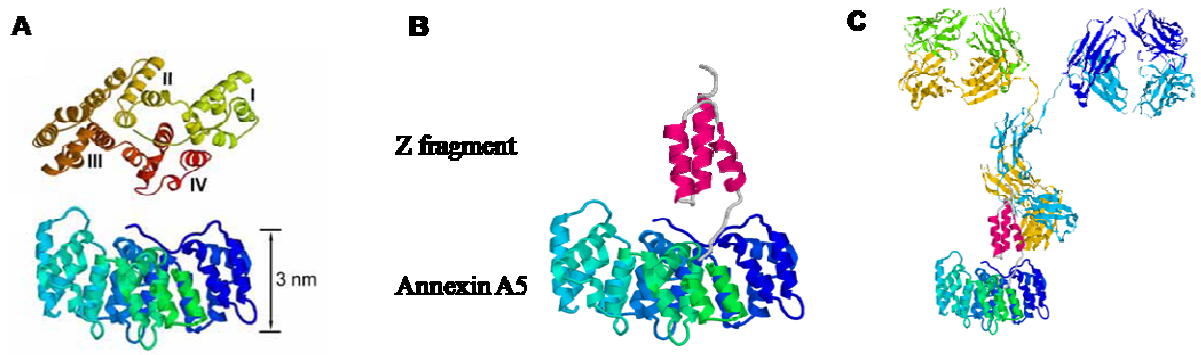

Figure 3.3: Annexin A5-Z. A: Top view *(top)* and side view *(bottom)* of a monomer of annexin A5. B: structure of the A5-Z fusion protein. C: Binding of the Fc-domain of an immunoglobulin (IgG) by A5-Z. Schemes adapted from ref.[245].

3.3.3. CD44 constructs

The CD44 receptors consisted of the hyaluronan binding domain (HABD) of the protein only. For oriented immobilization on a planar surface the CD44 constructs were equipped with two different functional tags, which were both present in the same fusion protein: The CD44 was expressed as a Fc-linked dimer ($(HABD)_2$-Fc)* and used in one of the model systems. For the second model system, the $(HABD)_2$-Fc construct was cleaved, releasing his10-tagged monomers of HABD (His-HABD). This strategy provided access to monomeric and dimeric HABD constructs from the same production cycle. All constructs have been kindly provided by Prof. David Jackson and Dr. Suneale Banerji (Weatherall Institute of Molecular Medicine, Oxford, UK). The CD44 constructs used for the present study are schematically depicted in figure 3.4.

* Fc domain was derived from IgG (see chapter 6.2.3).

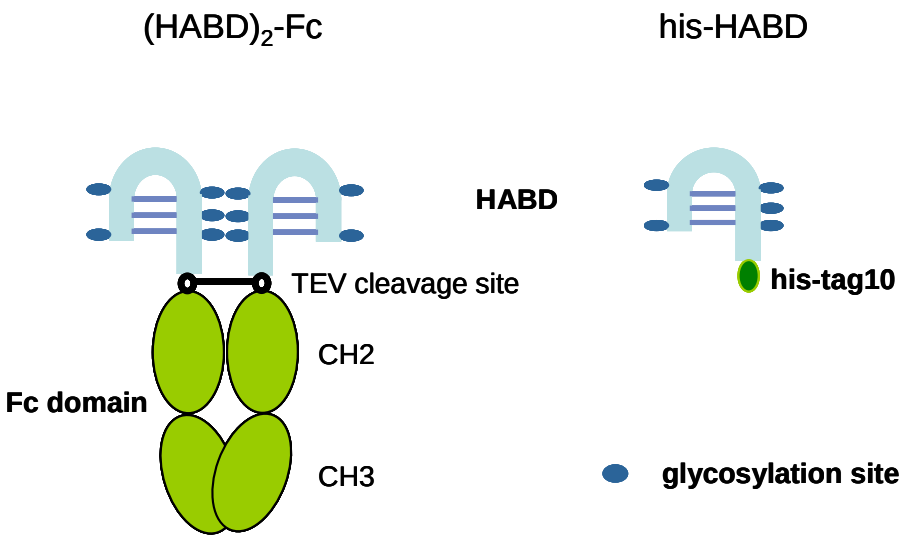

Figure 3.4: Schematic drawing of employed CD44 constructs. Left: Fc-domain fused with two hyaluronan binding domains (HABDs) $(HABD)_2$-Fc. Right: Monomeric HABD with a his_{10}-sequence at its C-terminal end (his-HABD). Cartoon kindly provided and adapted from S. Banerji (Weatherall Institute of Molecular Medicine, Oxford, UK).

3.3.4 Model system 1 - Annexin A5-Z for the immobilization of HABD dimers

In model system 1, HA was bound to a surface decorated with dimeric HABD constructs ($(HABD)_2$-Fc). A 4-level model system of the following structure was created: 1. negatively charged SLB (containing a fraction of DOPS lipids). 2. attachment of AnxA5-Z, 3. immobilization of CD44 Fc-tagged dimers and, finally, 4. binding of HA by immobilized receptors (figure 3.5A).

3.3.5 Model system 2 - Ni^{2+}-NTA for the Immobiliaztion of HABD monomers

HA binding was realized by the building a 3-level model systems of the form: 1. SLB containing bis-NTA headgroups, 2. immobilization of his-HABD, and 3. binding of HA by immobilized receptors. The model system is shown schematically in figure 3.5B.

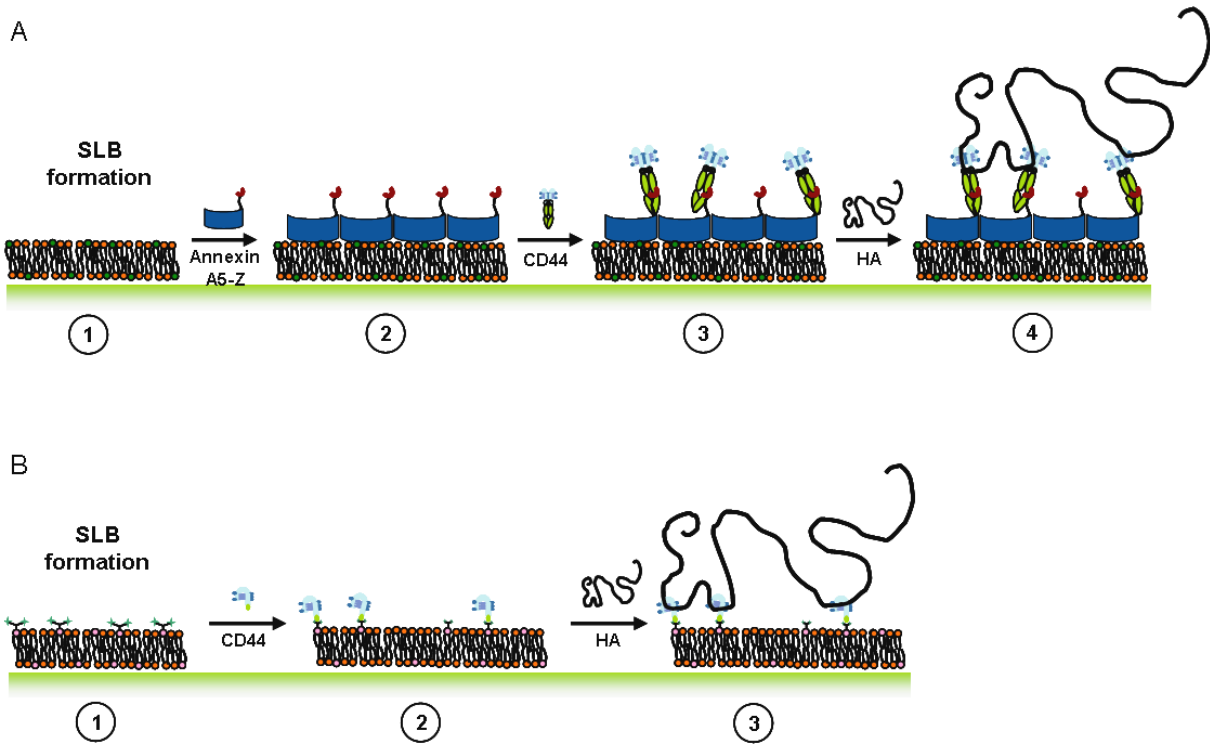

Figure 3.5: Design of the in-situ, multistep built-up of two model systems of the PCC. A: Annexin A5-Z based model for the immobilization of $(HABD)_2$-Fc (dimers). B: NTA-based model for the immobilization of his-HABD (monomers).

3.4 Results

3.4.1 Establishment of the model systems

All adsorption and rinsing steps were tracked in real time by QCM-D. The results on both immobilization systems will be presented separately in the following sections.

Construction of model system 1. Exposure of small unilamellar vesicles (SUVs) made of a mixture of DOPC and DOPS revealed the characteristic response for SLB formation (figure 3.6A). Subsequent incubation with AnxA5-Z yielded an additional frequency shift of about -27±1 Hz (figure 3.6A), or an acoustic thickness of 4.9 nm. It was previously shown that AnxA5-Z retains the capacity of native AnxA5 to bind to negatively charged SLBs in a stable and highly oriented manner, with the Z-fragment being exposed into the bulk solution.[245] The acoustic thickness of 4.9 nm is in reasonable agreement with the expected thickness of the AnxA5 layer (2.8 nm)[246] and the size of the Z-fragment (~3 nm). Changes in dissipation of about $1.0\pm0.2 \times 10^{-6}$ were observed for AnxA5-Z, while only minor changes are typically found for native A5.[135, 245] The increased dissipation can be attributed to the presence of a flexible linker that confers rotational freedom to the bulk exposed Z-fragment.[247]

$(HABD)_2$-Fc readily bound to AnxA5-Z covered SLBs (figure 3.6A). Adsorption was initially fast but slowed down progressively until stabilization of frequency and dissipation after about 30 minutes. Binding was specific (figure 3.6B) and stable to rinsing in buffer solution. The total acoustic thickness of the AnxA5-Z/$(HABD)_2$-Fc layer was about 12 nm. For comparison, the lengths of the HABD[72, 248] and the Fc-domain are 3.5 and 7 nm, respectively, while the thickness of AnxA5 and the average size of the Z-fragment are each about 3 nm. Since the Z-fragment binds to the hinge region of the Fc-domain (figure 3.3C), it is likely that about half of the Fc-domain intercalates into the layer of Z-fragments. The resulting protein layer would then have a total thickness of about 13 nm, in reasonable agreement with the acoustic thickness. From the design of the protein fusion constructs, and the QCM-D response, it is well-founded to conclude that the HA receptors are immobilized in a stable and suitably oriented manner on the surface.

HA with a selected molecular weight of 262kDa (HA250) bound fast to the receptor covered surface (figure 3.6A). Equilibrium was reached within less than 10 min, yielding

Δf = -7.5±1 Hz and ΔD = 1.7±0.2 × 10^{-6}. Binding of HA to the HABD construct was specific (figure 3.6C), as no response could be observed on AnxA5-Z covered surfaces in the absence of CD44. Although the interaction between HA and individual HABD domains is rather weak (K_D > 5 µM [224]), no or little desorption was observed upon rinsing (figure 3.6A). This provides a first indication that the interaction of individual HA chains with several surface-bound receptors must be stabilizing HA binding. A small decrease in dissipation upon rinsing hints at a minor reorganization of the HA film upon rinsing.

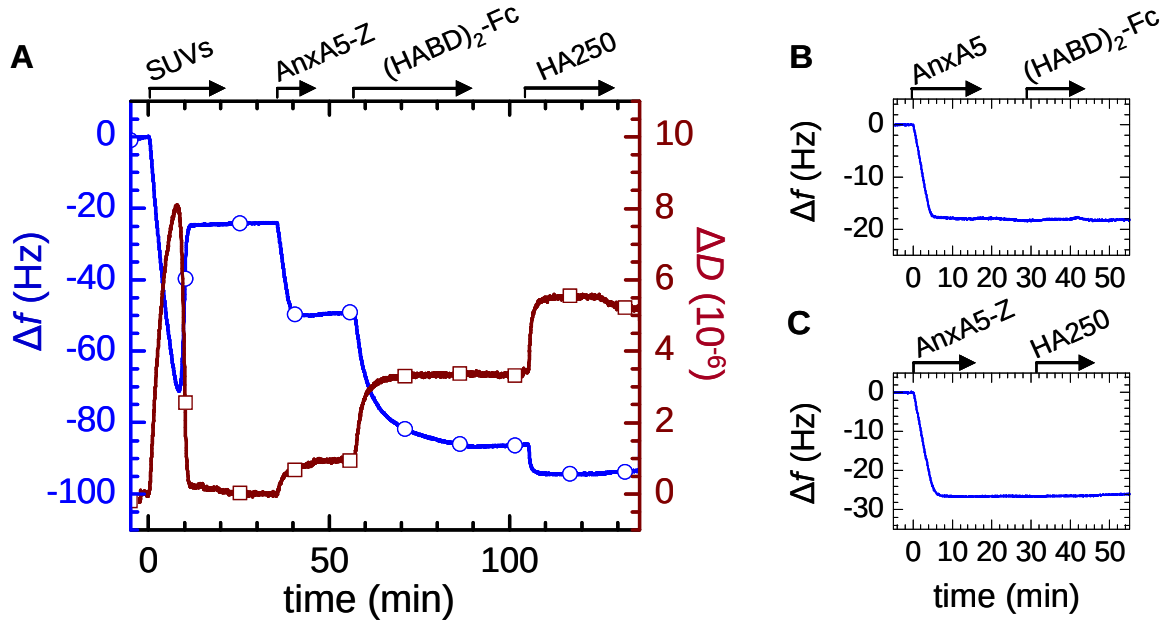

Figure 3.6: (*A*) Step-by-step assembly of model system 1, followed by QCM-D. Start and duration of all incubation steps is indicated (*arrows*). SLBs were formed by spreading of 50 µg/ml small unilamellar vesicles (SUVs), made of DOPC and DOPS (3:1), to a silica surface. The two-phase behaviour together with final changes in frequency (*blue circles*) of Δf = -25 Hz and in dissipation (*red squares*) of $\Delta D < 0.3\times10^{-6}$ characterise the formation of an SLB of good quality[128, 249]. Responses for the sequential incubation of 10 µg/ml AnxA5-Z and 10 µg/ml $(HABD)_2$-Fc indicate formation of stable monolayers. Binding of 10 µg/ml HA250 was readily detected. (*B*) $(HABD)_2$-Fc, incubated at 10 µg/ml, did not bind to native AnxA5, confirming that binding to AnxA5-Z was specific. (*C*) HA250 (10 µg/ml) did not bind to AnxA5-Z, indicating that binding to $(HABD)_2$-Fc was specific. For simplicity, SLB formation is not displayed for the assays in (*B*) and (*C*), and only frequency shifts are shown.

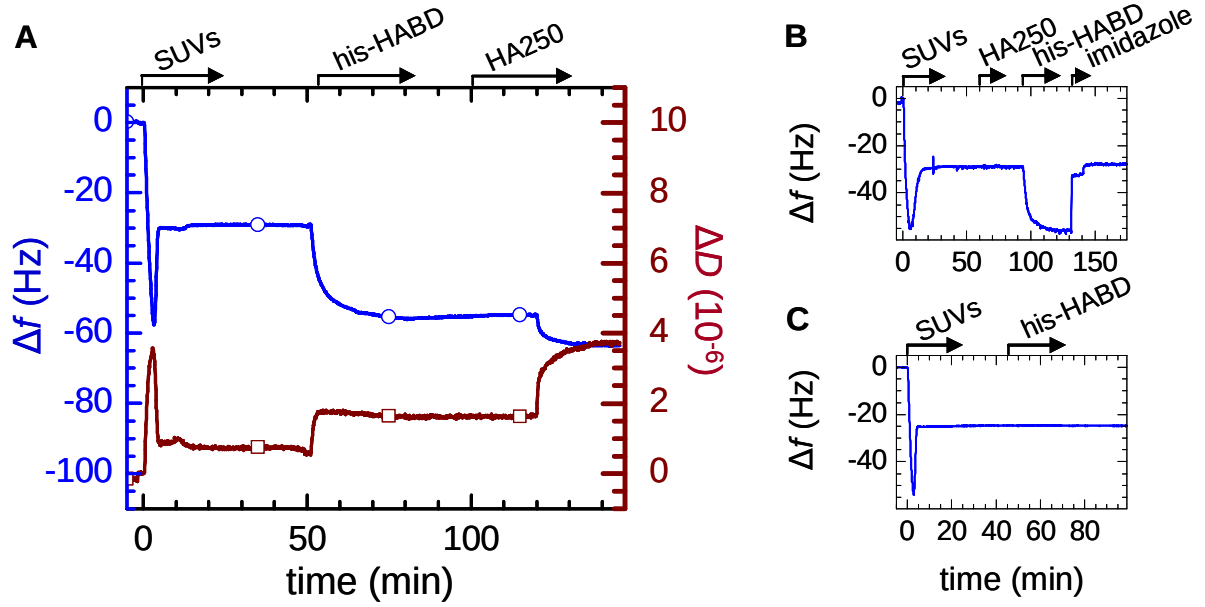

Figure 3.7: **(A) Construction of model system 2, followed by QCM-D. SLBs were formed by spreading of 50 µg/ml SUVs, made of DOPC and bis-NTA functionalized lipids (9:1), to a silica surface. The final absolute frequency shift, |Δf| = 29 Hz, was slightly higher than in fig. 4A, most likely due to the presence of the bulkier bis-NTA headgroups [250]. his-HABD, incubated at 10 µg/ml, formed a stable monolayer, and binding of 10 µg/ml HA250 is readily detected. (B) HA250 (10 µg/ml) did not adsorb to SLBs containing NTA-functionality, and the bound monolayer of his-HABD could be fully eluted by 200 mM imidazole. Changes in Δf and ΔD at about 130 min do not reflect any changes on the surface, but resulted from a change in the viscosity and/or density of the surrounding solution due to the presence of imidazole. (C) his-HABD (10 µg/ml) did not bind to SLBs that were made of pure DOPC and thus lacked NTA functionality.**

Construction of model system 2. SUVs that contained a fraction of bis-NTA functionalized lipids formed stable SLBs (figure 3.7A) with frequency and dissipation shifts of about Δf = -29±1 Hz and $\Delta D = 0.4 \pm 0.2 \times 10^{-6}$, respectively. In a second step, his-HABD was added. In contrast to the dimeric HABD, the monomer adsorbed fast with saturation being reached within 15 min. The acoustic thickness of the protein film, about 5 nm (Δf = 26 Hz*)*, corresponds well to the size of the HABD.[72, 248] The magnitude of the dissipation shift, $1.0 \pm 0.2 \times 10^{-6}$, and the slight maximum at intermediate coverage are in accordance with the molecules being linked *via* a flexible linker to the SLB.[247] The proteins remained stably bound upon rinsing in buffer. Control experiments (figure 3.7B-C) confirmed the stable and specific anchorage by the protein's C–terminal his-tag and the lipid's bis-NTA functionality.

Subsequent addition of HA250 resulted in shifts of Δf = -7±1 Hz and $\Delta D = 1.2 \pm 0.1 \times 10^{-6}$. Again, binding was specific (figure 3.7B) and irreversible upon rinsing in buffer (figure 3.7A). Notably, the $\Delta D/-\Delta f$ ratio of the HA films, both on monomeric and dimeric HABD, exceeded the values for the protein or lipid films by at least 2.5-fold, indicating that the carbohydrate film is considerably softer.

The results for all functionalization steps are summarized in table 3.1.

Table 3.1: *Δf* and *ΔD* values for each step of the formation of both model systems[a)].

biomolecular film	*model system 1*		*model system 2*	
	Δf (Hz)	**ΔD (10^{-6})**	**Δf (Hz)**	**ΔD (10^{-6})**
SLB	-25 ± 1	0.25 ± 0.1	-29 ± 1	0.4 ± 0.2
AnxA5-Z	-27 ± 1	1.0 ± 0.2	-	-
CD44-HABD	-37 ± 2	2.5 ± 0.1	-26 ± 2	1.0 ± 0.2
HA250	-7.5 ± 1	1.7 ± 0.2	-7 ± 1	1.2 ± 0.1

[a)] Values were determined after rinsing in buffer; error bars correspond to variations between 2 or more measurements, and experimental noise.

3.4.2 Quantifying the adsorbed amounts of CD44 and HA

After having characterized the thickness, morphology and stability of the functionalized surfaces in both model systems by QCM-D I aimed to determine the total amount of adsorbed material as absolute adsorbed mass per surface area. To this end the model systems were built on a silicon wafer with a native silica top layer for *in-situ* ellipsometry measurements, which allowed for the step-by-step tracking of the deposition of each layer (figure 3.8). From the measured parameters Δ and Ψ, the optical mass of each layer was obtained after fitting of an appropriate model to the experimental data (for details see chapter 6.3.3). The results are tabulated in table 3.2.

Adsorbed amounts of lipids, AnxA5-Z and CD44. The amounts of lipids in the SLBs were 380 and 360 ng/cm^2 for model systems 1 and 2, respectively. Within 10% error, these

values are in agreement with previously reported data.[251] The amount of surface bound AnxA5-Z was about 220 ng/cm^2, or 5.0 pmol/cm^2. This is similar to, although slightly less than the values expected for two-dimensional crystalline layers of AnxA5. For a monolayer of p6 symmetry, for example, a surface density of 5.5 pmol/cm^2 would be expected.[246] These values validate the quantitative ellipsometric approach within an error of about 10%.

A maximal surface density of 150 ng/cm^2 or 4.2 pmol/cm^2 was obtained for his-HABD (table 3.2). This corresponds to a surface area per molecule of 40 nm^2 or to a mean distance between neighboring anchor sites of 6.8 nm, which is about twofold the size of the peptidic core of HABD (3.5 nm). It is likely that the heavy glycosylation of HABD increases the receptor's effective size and thereby limits the packing density. In comparison the mean surface area per HABD monomer at saturation was about 50% higher for the $(HABD)_2$-Fc (75 nm^2) than for his-HABD. Since the surface density of AnxA5-Z is 4-fold higher than $(HABD)_2$-Fc, and hence unlikely to limit HABD binding, it is probably the elongated and rather bulky Fc domain that hinders further adsorption sterically. The pronounced slowdown of binding with increasing coverage that we observed for $(HABD)_2$-Fc (figure 3.6) would be consistent with such a scenario.

Notably, and in line with results from QCM-D, all protein layers were found to be stable upon rinsing in buffer, illustrating the stability of the assembled multilayer systems.

Quantification of HA binding. HA250 adsorbed in maximal amounts of about 11.5 ng/cm^2, or about 45 fmol/cm^2, on $(HABD)_2$-Fc and of about 15 ng/cm^2, or 60 fmol/cm^2, on his-HABD (figure 3.8, table 3.2). The bound masses of HA are hence an order of magnitude below those observed for any of the adsorbed proteins, yet still well above the detection limit (~0.5 ng/cm^2).

From the surface densities estimated by ellipsometry, it was possible to quantify the mean number of HABD monomers that are available per bound HA chain. For HA250, a ratio of CD44 per HA of about 50 for $(HABD)_2$-Fc and about 70 for his-HABD was found. Ellipsometry experiments revealed a higher surface density of monomeric receptors, and it is reasonable to assume that the higher ratio of receptors per HA arises from a difference in surface coverage.

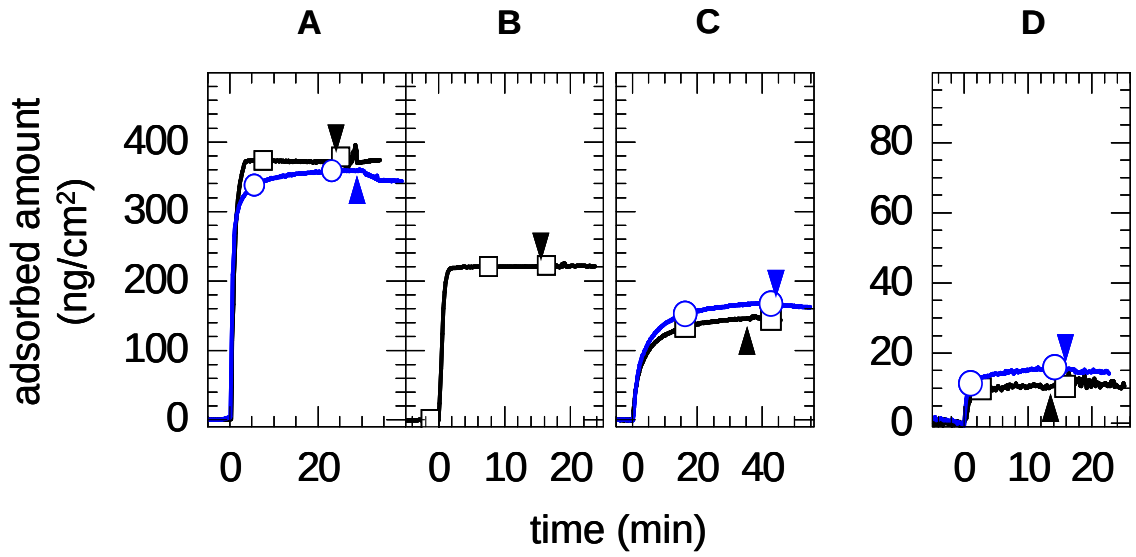

Figure 3.8: **Adsorbed amounts, as determined by ellipsometry, for model systems 1 *(black squares)* and 2 *(blue circles)*. SLB-formation (A), and the sequential adsorption of AnxA5-Z (B, model system 1 only), HABD constructs (C) and HA250 (D) were followed. Each incubation step started at 0 min; concentrations as in figs. 2 and 3 were employed; the start of rinsing in buffer is indicated *(arrowheads in respective color)*.**

Influence of HA size on HA binding. The results obtained above suggest that the system provides an abundance of CD44-HA interaction due to both, a high density of receptors and a large number of binding sites along the HA chain of HA250. As a logical consequence, it would be expected that HA binding on a surface saturated with CD44 becomes reversible, once a critical lower number of CD44-HA interaction is reached. To test this hypothesis, the effect of HA size on binding to receptor covered surfaces was investigated. Given the similarity in the stability of binding and in the adsorbed amount, that both model systems exhibited for HA250, this systematic analysis was restricted to $(HABD)_2$-Fc covered surfaces (figure 3.9, table 3.2).

For molecular weights above 250 kDa, variations in the adsorbed mass were below the detection limit. It should be pointed out that a constant adsorbed mass implies that the number of molecules that bind to a given surface area decreases with increasing molecular weight, and hence increases the number of receptors that are available per HA chain (table 3.2). Below 250 kDa, the adsorbed masses decreased considerably, with half maximal coverage being reached around 30 kDa. It is further notable that the reversibility of binding was strongly dependent on HA's molecular weight. At 250 kDa and more, HA was stably bound while binding was fully reversible for 10 kDa and less.

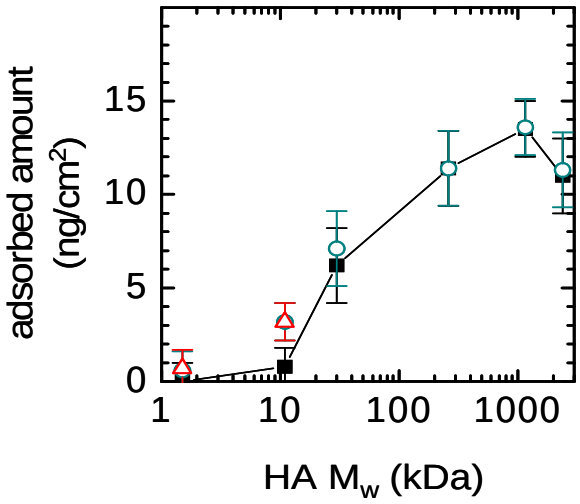

Figure 3.9: Dependence of HA binding on the molecular weight of HA, for model system 1. Adsorbed amounts at solution concentrations of 10 µg/ml (*blue circles*) and 50 µg/ml (*red triangles*) and after rinsing (*black filled squares*) are shown. Error bars correspond to variations between typically two measurements and experimental noise.

Table 3.2: Adsorbed amounts of HABDs and HA as determined by ellipsometry and stoichiometry of the interaction[a)].

	HABD			***HA***			***HABD monomers available per HA***
	***M*W**	**adsorbed amount**		***M*W**	**adsorbed amount**		
	(kDa)	**(ng/cm²)**	**(pmol/cm²)**	**(kDa)**	**(ng/cm²)**	**(fmol/cm²)**	
his-HABD	39	162	4.2	262	15	57	73
(HABD)₂-Fc	116	146 ± 15	1.26 ± 0.13	30	6.1 ± 2.0	200 ± 70	12 ± 5
		122 ± 15	1.05 ± 0.13	262	11.5 ± 2.0	44 ± 8	48 ± 15
		140 ± 15	1.21 ± 0.13	1156	13.5 ± 1.5	12 ± 1.3	207 ± 45
		133 ± 15	1.15 ± 0.13	2400	11.0 ± 2.0	4.6 ± 0.8	500 ± 150

[a)] Values were determined after rinsing in buffer; error bars correspond to variations between 2 measurements, and experimental noise.

3.4.3 Thickness and morphology of HA films

Colloidal probe reflection interference contrast microscopy (RICM) was employed to estimate the thickness of stably bound HA films. Again, $(HABD)_2$-Fc covered surfaces were chosen for a systematic investigation. Film thicknesses were determined after addition of each layer of the model system (figure 3.10) using PEG-passivated microspheres (see figure legend for details).

A change in the intensity in the center from dark to bright of the obtained interferographs (figure 3.10A) was observed for samples, in which long HA was present, indicating a considerable change in the film height. HA of different sizes in the range of 30 to 2500kDa was probed. For HA250, an apparent thickness of around 50 nm was found. The thickness increased with the molecular weight of HA, albeit weakly (figures 3.11 and 3.12). For the shortest employed HA (30 kDa) the determined thickness could not be distinguished from the height of the underlying receptor layer.

On a given substrate, the variations in measured heights were within a range of 15 to 25 nm, which is much smaller than the thickness of the HA films. This indicates that the HA film was laterally homogeneous on length scales that characterize the contact area between the bead and the substrate, which is on the order of 1 µm.

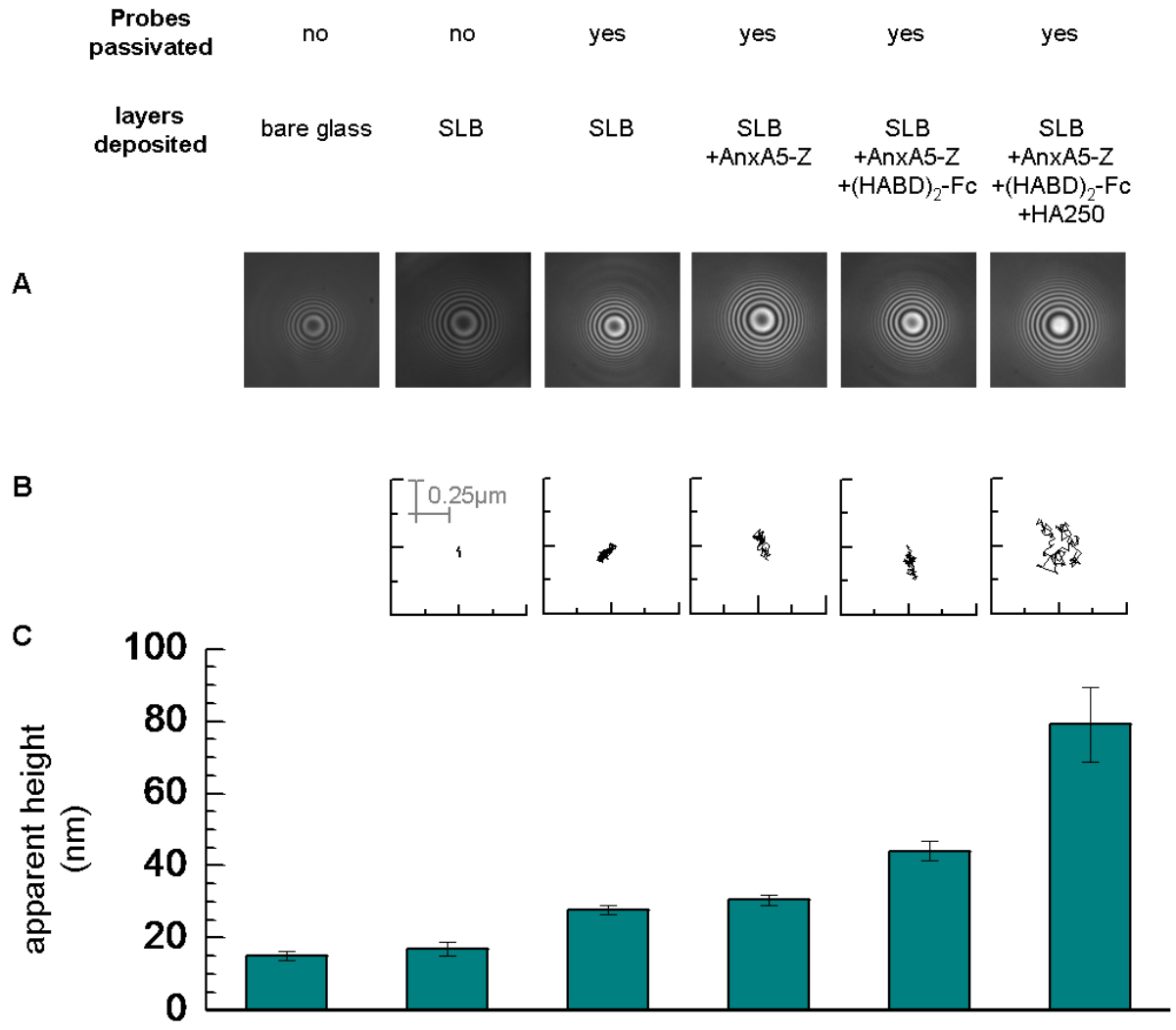

Figure 3.10: **RICM data acquired at different stages (noted on top) of the assembly of model system 1. (A) Representative interferographs (λ = 490 nm, image size 20 µm), displaying the characteristic pattern of concentric rings (Newtonian rings). (B) Typical traces of the in-plane movement of a bead's center over a period of 10 s. Non-passivated colloidal probes show no significant in-plane movement on SLBs, i.e., they are immobilized due to strong adsorption. Passivated probes show increasing diffusive motion on SLBs, and films of AnxA5-Z, $(HABD)_2$-Fc and HA250, indicating little or no attractive interaction with the surface adlayer. (C) Apparent heights. Error bars represent standard deviations from measurements at λ = 490 nm with 5 to 10 different beads at various positions on the same sample. An apparent height of 15 nm, instead of 0 nm, was found for non-passivated probes adsorbed to glass. Most likely, and as discussed in ref. [150], this discrepancy stems from limitations in the accuracy of the simple model. The nanoscale roughness of the probe may though also contribute. Addition of the SLB increased the thickness by only few nanometers, as expected. The increase in height of 11±4 nm for PEG passivated probes on SLBs is likely to reflect the hydrated PEG layer that now separates the bead from the surface. Indeed, a height of around 10 nm would agree with the thickness of rather dense brush of moderately stretched PEG chains. Upon addition of AnxA5-Z and $(HABD)_2$-Fc, the height increases by another 16±4 nm. This is similar to the dimensions of the adsorbed biomolecular layer (~15 nm).**

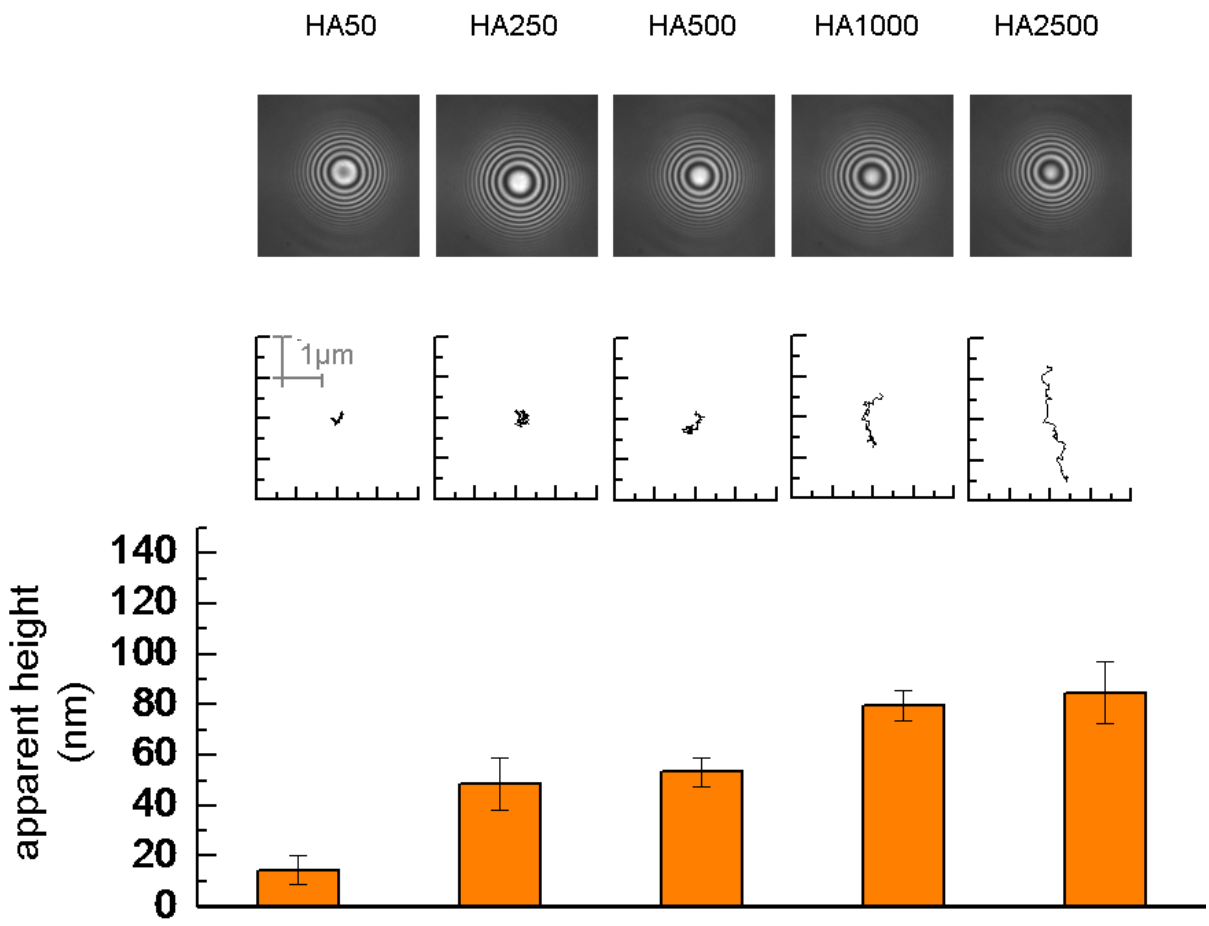

Figure 3.11: RICM data acquired for different sizes of HA (noted on top) on model system 1. (A) Representative interferographs (λ = 490 nm, image size 20 µm), displaying the characteristic Newtonian rings. (B) Typical traces of the in-plane movement of a bead's center over a period of 10 s. (C) Apparent heights. Displayed values represent the increase in the total measured film thickness upon addition of $(HABD)_2$-Fc and HA of different molecular weight. Error bars represent standard deviations from measurements at λ = 490 nm with 5 to 10 different beads at various positions on the same sample.

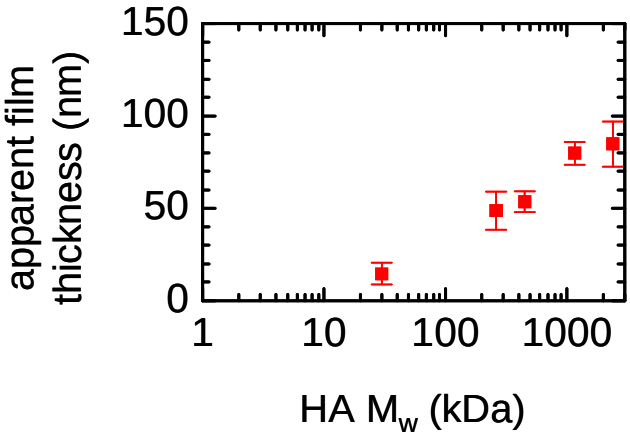

Figure 3.12: Apparent thickness of HA films, as determined by colloidal probe RICM on model system 1. Displayed values represent the increase in the total measured film thickness upon addition of $(HABD)_2$-Fc and HA of different molecular weight. Error bars represent standard deviations from measurements at λ = 490 nm with 5 to 10 different beads at various positions on the same sample

3.5 Discussion

In the framework of this project we have developed *in-vitro* model surfaces that reproduce the presentation of HA receptors on the plasma membrane in the sense that they expose the HA binding domain of CD44 in an oriented and stable manner and in a two dimensional configuration. The surface density of receptors can be controlled, and their rotational and lateral mobility is likely to be retained. Using a toolbox of surface sensitive characterization techniques, these model surfaces allowed for the binding of HA to be studied in a highly controlled, quantitative and systematic manner.

This new approach of studying receptor-HA interaction differs from conventional binding assays (plate assay etc.) in that the *polyvalent* interactions between multiple binding sites on each HA chain and multiple receptors on the surface can be investigated directly. The affinity of individual receptors for HA is rather low ($K_D > 5\ \mu M$ [224]), and the lifetime of individual bonds is thus short, as observed for HA_8 and molecular weights up to 10 kDa (figure 3.9). For large M_W of HA (≥ 250 kDa), binding was found to be irreversible. This drastic increase in stability is a direct consequence of the avidity increase incurred by polyvalent interactions.

3.5.1 Probing the magnitude of polyvalency in the binding of HA by CD44

From the ellipsometric measurements it was possible to derive a figure on the number of available receptors per HA chain. At transition between reversibly and irreversibly bound HA, i.e., for HA of 30 kDa, this number was found to be about 12. This molecular weight corresponds to about 15 receptor binding sites, assuming a footprint per receptor of HA_{10}. Interestingly, both values were of similar magnitude. It is instructive to relate these values to the number of ligand-receptor interactions that would be required for stable binding from the point of view of binding energies. The effective K_d of polyvalent interactions increases as the power law of the number of individual interactions (K_d^{N} [226]). Assuming an individual affinity of CD44 for HA of $K_d \approx 0.1$ mM (which represents the lower range), the collective action of three receptors would already result in a total avidity of $K_d \approx 0.1\ \mathrm{mM}^3 = 1$ pM, i.e., a very strong interaction. One may speculate that entropic losses upon stretching of the HA chain by the high occupancy of binding sites may have to be compensated by more binding events. The number of available binding sites on HA and the number of available receptors must thus be considerably higher than would be expected from the binding energies.

3.5.2 Comparison between monomeric and dimeric HABD

HA250 adsorbed stably and in similar amounts to surfaces covered with either monomeric or dimeric HABD constructs, suggesting that the strength of binding is not strongly affected by the dimeric presentation of HABD in the form of the Fc fusion. It should be noted, however, that the HABD surface density, in terms of monomers, was about 75% higher for monomeric HABD.

3.5.3 Theoretical considerations

HA in aqueous solution exhibits many features that are characteristic for a flexible polymer in a good solvent (see chapter 1.11.4). It is instructive to compare the theoretical predictions for the conformation of flexible polymers upon adsorption to surfaces with the adsorption behavior of HA.

For the adsorption at sufficiently high coverage (the so called pseudo-plateau regime),[252] a film thickness comparable to the polymer's radius of gyration and a rather strong decrease of the polymer concentration as a function of the distance from the surface would be expected (figure 3.13). For HA250, $R_g = 37$ nm, in reasonable agreement with the experimental data (figures 3.11 and 3.12). The film thicknesses, as measured by colloidal probe RICM, tended

to be smaller than R_g for higher molecular weights. This discrepancy is not unexpected since the colloidal probe is likely to compress very soft films to some extent, resulting in underestimated thickness values. In this respect, it should be noted that the surface-distal region of the HA film is likely to exhibit very low concentration of HA and thus a rather high degree of softness (figure 3.13).

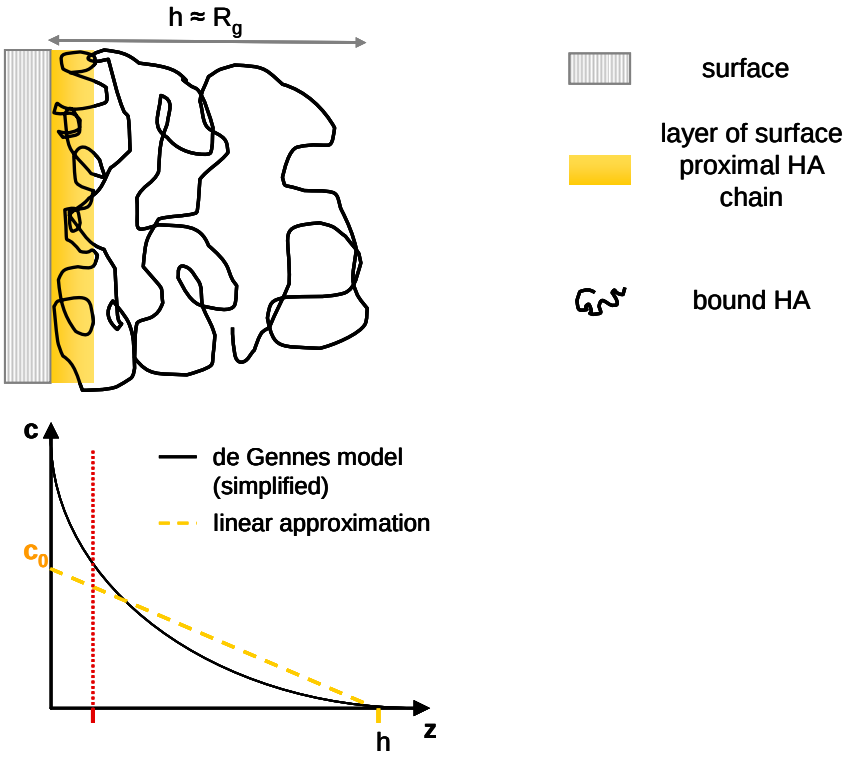

Figure 3.13: Theoretical prediction for the adsorption of flexible polymers in good solvent to an attractive surface. The total film thickness is about R_g and the polymer concentration (c) depends strongly on the distance from the surface (z). The black solid line in the lower plot indicates the concentration profile according to de Genne's self-similar grid model.[161] A linear approximation is also shown *(dashed yellow line)*. The area under both curves, corresponding to the adsorbed amount, was chosen to be identical. The linear approximation (c_0) is likely to underestimate the HA concentration in the vicinity of the surface. Only the surface proximal region *(yellow area)* of the HA film is accessible for the receptors.

Theory also predicts that the adsorbed amount becomes independent of molecular weight for high molecular weights,[252] and that adsorption to weakly adhesive surfaces decreases drastically below a threshold molecular weight. Experimentally, two different regimes could be distinguished. For high molecular weights of HA ($\geq$ 250 kDa), binding was irreversible and independent of molecular weight, with adsorbed amounts of about 12 ng/cm^2. For low

molecular weights (< 30 kDa), adsorbed amounts decreased strongly, and binding became progressively weaker, or reversible, with decreasing M_W. Stable half maximal binding occurred at $M_W^{50} \approx 30$ kDa and binding was fully reversible at $M_W \approx 10$ kDa.

It should be pointed out that theory assumes a homogenously attractive surface, whereas the experimental system displays discrete binding sites (the receptors). However, the surfaces employed here are saturated with receptors, and are expected to provide a statistical distribution of receptors across the surface. Such conditions can hence be considered to mimic a homogenously attractive surface.

Taken together, these observations indicate that binding of HA can be described well in terms of the adsorption of a typical flexible polymer.

HA may occupy a large fraction of surface bound receptors. At high M_W of HA ($\geq$ 250 kDa), 50 and more receptors were available per HA chain (table 3.2). Are all these receptors indeed engaged in binding at any given time? The total amount of surface bound HA would indeed be sufficient to saturate all surface bound receptors. This can easily be seen by expressing the maximal HA surface density in units of HA_{10}, the minimal footprint per receptor that is required for binding of several CD44 receptors to HA.[75, 225] The result, 6.0 pmol/cm^2 HA_{10}, exceeds both the $(HABD)_2$-Fc and the his-HABD density, by 150% and 40%, respectively. The HA film, however, has a total thickness of about 50 nm (and more), whereas the receptors can only sample its surface proximal part of 5 to 10 nm in thickness. A model of the conformation of adsorbed HA and the approximated concentration profile are depicted in figure 3.13. Amounts of 1.1 to 2.2 pmol/cm^2 HA_{10} would be estimated for the surface proximal region, when assuming that the concentration of HA in the film decreases linearly with the distance from the surface (figure 3.13). Polymer theory predicts a steeper gradient,[252] and the estimates are thus likely to represent lower limits for the amount of HA that is accessible to the receptors. These numbers are still in the same range as the total receptor concentration, suggesting that HA may indeed occupy a large fraction of the surface bound receptors.

3.5.4 Comparison to the cell surface

The model surfaces that we have investigated here presented a very high surface density of receptors, at least 60-fold higher than the overall densities that are typically found on CD44 expressing cells.[253, 254] Presumably, the total amount of adsorbed HA would decrease with decreasing receptor density while the molecular weight that is required for stable binding of

HA would increase. The extent of these changes and the impact of the lateral mobility of receptors on binding will be treated in chapter 4.

The receptor distribution on the cell surface is though likely to be heterogeneous, and local enrichment, e.g., in membrane domains, has indeed been proposed.[79, 225] The model surfaces may thus represent *local* receptor concentrations well, and hence provide quantitative insight into the mechanism of local accumulation of HA on the cell surface.

It is worth to emphasize that the receptor bound HA films in the model systems remain rather thin, when compared to the typical thickness of hyaluronan-rich cell coats that can be found on the endothelial cell surface [255] or around chondrocytes,[256, 257] for example. The thickness and HA surface density is also considerably lower than what has been reported previously for HA films in which the molecules were grafted by one of their ends to the surface,[258] in agreement with theoretical predictions for adsorbed and end-grafted polymers, respectively. These observations imply that binding of HA to a cell surface that is covered with CD44 or other HA receptors alone is not sufficient to create coats of several 100 nm or more in thickness. Other molecules, e.g., aggrecan[259] or TSG-6,[74] must affect the morphology of HA films by interaction with the film, in ways that remain to be elucidated.

3.6 Conclusions

Model systems have been developed that provide direct and quantitative information about the binding of HA to an assembly of HA receptors in a biologically relevant arrangement. It could be shown that the polyvalent interaction of a given HA chain with a receptor covered surface confers stable binding, provided that the HA chains are long enough, while binding decreased rapidly for HA smaller than 30 kDa. The results indicate that a rather large number of receptors per HA chain is required to stabilize HA binding.

From a physico-chemical point of view, there are many similarities between the binding behavior of HA and the typical behavior of a flexible polymer adsorbing to a homogenously attractive surface.

Our methodological approach can readily be extended to other HA receptors, and provides a rather simple tool for the quantitative investigation of HA with receptors in a biologically relevant and well-controlled environment.

Chapter 4

Tunable Model Surfaces - Untying the Supra-molecular Cues of CD44 and HA Interactions

In chapter 3, a model system has been developed which allows investigating the polyvalent interaction between HA and surface bound receptors. It was demonstrated that this interaction relies on polyvalent binding events in order to hold the HA film stably on the surface. Binding of HA of large M_w ($\geq$ 250 kDa) was found to be irreversible. Binding of HA became reversible for low M_w HA. It was the aim of the present project to investigate how other parameters affect the binding of HA, in particular:

- receptor surface density
- the interaction of isolated receptors in solution with surface bound HA
- Structural variations of the CD44 constructs, such as the glycosylation pattern and the presence of the membrane proximal region.
- HA concentration in solution.

4.1 Results

4.1.1 The effect of CD44 surface density on HA binding

In chapter 3 it was shown that HA binding is stable only above a critical molecular weight of HA. Here, the effect of receptor surface density on HA binding was studied by creating surfaces with varying amounts of immobilized hyaluronan binding domains (HABDs).

HA250 was chosen as a model molecule for this set of experiments for two reasons. Firstly, HA250 has been used for the study in chapter 3, and thus is already well characterized in its binding behavior to surfaces covered with a high density of receptors. Secondly, this size of HA was found to form stable films on HABD covered surfaces (chapter 3).

The immobilization of CD44 constructs and subsequent binding of HA were recorded by QCM-D. Lower surface coverages of the receptors were achieved by interrupting the incubation at different times. Both CD44 constructs, the HABD monomer (his-HABD) and dimer ($(HABD)_2$-Fc), were investigated (figure 4.1A and 4.2A)

(HABD)2-Fc. HA binding was probed for receptor surface coverages corresponding to frequency shifts, Δf_{HABD}, between -5 and -40 Hz giving rise to responses for HA, Δf_{HA}, between -2 and -7.5 Hz (figure 4.1B). HA binding increased monotonously with the density of receptors on the surface. The absolute final frequency shifts for HA, $|\Delta f_{HA}|$, increased linearly with $|\Delta f_{HABD}|$ for $|\Delta f_{HABD}| \leq 25$ Hz. Upon further increase in receptor density, Δf_{HA} remained constant at a level of about -7.5 Hz.

Notably, HA binding remained largely irreversible even at lowest receptor surface densities.

His-HABD. The monomeric CD44 construct was deposited at surface coverages between Δf_{HABD} = -7 and -27 Hz, yielding Δf_{HA} between -4 and -8 Hz (figure 4.2B). As observed for the $(HABD)_2$-Fc HA, binding depended on the HABD surface density and was irreversible at all receptor densities. Again, $|\Delta f_{HA}|$ increased linearly with $|\Delta f_{HABD}|$ for low receptor densities ($|\Delta f_{HABD}| \leq 20$ Hz), and reached a plateau (Δf_{HA} = -8 Hz) at high receptor densities.

I remind the reader that frequency shifts from QCM-D are not directly related to the absolute adsorbed mass, since Δf includes coupled solvent and viscoelastic properties of the adsorbent affect Δf.[119, 123, 136] The relative contribution of solvent to the total mass depends on surface coverage and the shape and size of the molecule.[139] It is therefore unclear, if the linear relationships observed between Δf_{HA} and Δf_{HABD} indeed reflect a linear relationship in adsorbed amounts.

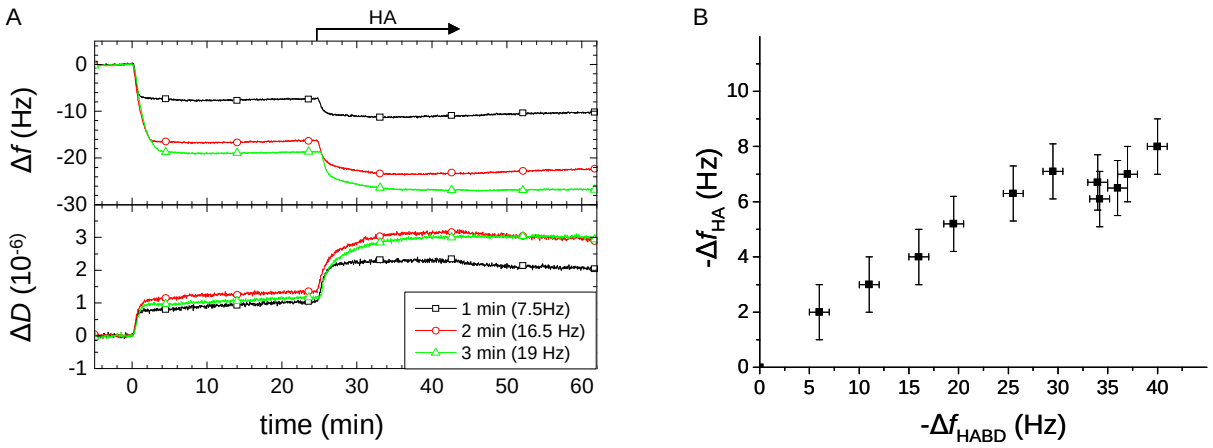

Figure 4.1: HA binding as a function of surface density of $(HABD)_2$-Fc (dimer). A: Selected QCM-D curves for low and intermediate coverage of $(HABD)_2$-Fc. $(HABD)_2$-Fc was incubated at 0 min, for 1, 2 and 3 min, respectively, as indicated. Incubation of HA is also indicated *(arrow)*. B: Δf_{HA} plotted as a function of Δf_{HABD}. Errors represent noise and minor drifts of the QCM-D set-up.

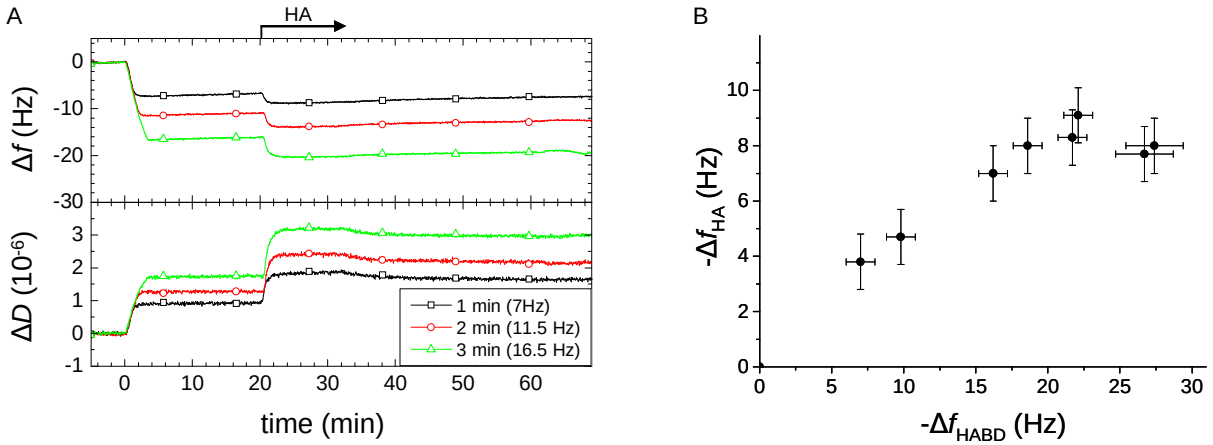

Figure 4.2: HA binding as a function of surface density of his-HABD (monomer). A: Selected QCM-D curves for low and intermediate coverage of his-HABD. his-HABD was incubated at 0 min, for 1, 2 and 3 min, respectively, as indicated. Incubation of HA is also indicated *(arrow)*. B: Δf_{HA} plotted as a function of Δf_{HABD}. Errors represent noise and minor drifts of the QCM-D set-up.

It is useful to compare the slopes, $\Delta D/-\Delta f$, in the limit of low HA coverage for various receptor surface densities (figure 4.3). These slopes relate to the viscoelastic properties of the HA film and, by extension, to its morphology. The slope decreases with increasing receptor

density, indicating that HA adopts a more rigid, and hence more flattened conformation when binding to a surface that exposes higher receptor density. In contrast, the slopes were similar when comparing HA binding on $(HABD)_2$-Fc and on his-HABD at similar molar receptor surface densities, suggesting that the mode of receptor presentation does not have a strong effect on the conformation of HA.

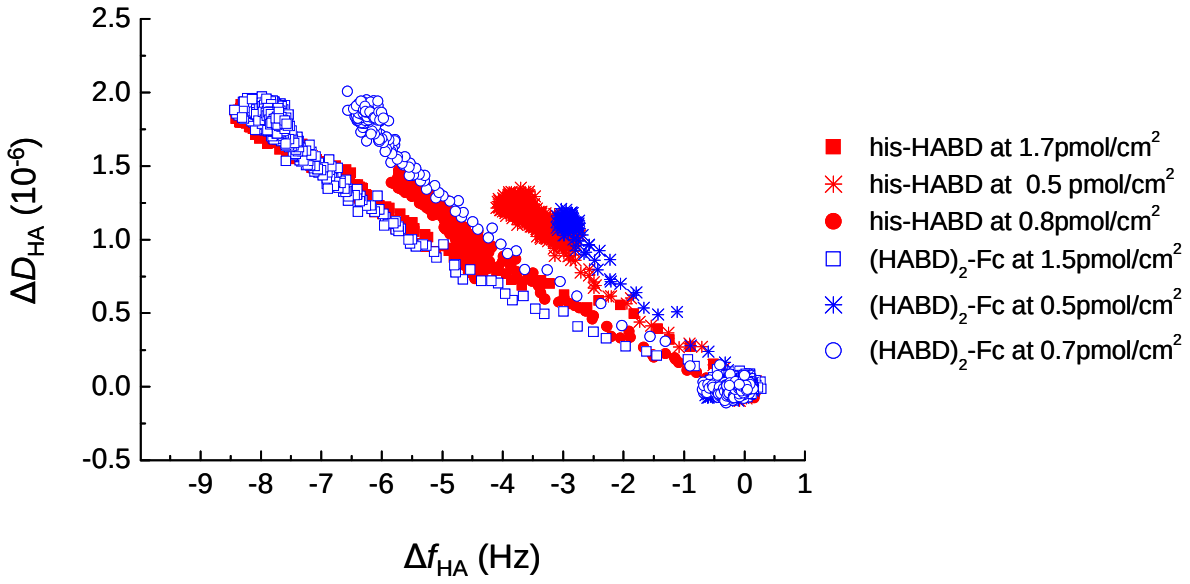

Figure 4.3: Parametric Δ*D*/Δ*f* plot for HA binding on different receptor surface densities of his-HABD and $(HABD)_2$-Fc. His-HABD and $(HABD)_2$-Fc are shown in red and blue, respectively, with the different symbols indicating different surface densities. The surface densities were chosen such that the molar adsorbed amount of HABD monomers was comparable. At similar molar receptor surface density, the *D*-*f*-plots for both HABD constructs overlap. The slope of the *D*-*f*-plots decreases with increasing receptor surface density.

4.1.2 Translating Δ*f* into adsorbed masses per surface area

To determine the absolute adsorbed masses of receptors and HA, measurements with a combined QCM-D/ellipsometry set-up were performed. The set-up provided simultanous access to data from both techniques on the same surface and under identical adsorption conditions (figure 4.4A and 4.5A). From the combined experiment it was possible to correlate Δ*f* to the corresponding biomolecular mass Δ*m* (as obtained from ellipsometry) at any time point of the measurement, i.e., for any surfaces coverage range (figures 4.4B-C and 4.5B-C).

Calibration of Δ*f* for immobilized CD44. Both constructs, $(HABD)_2$-Fc and his-HABD, revealed adsorbed masses at saturation that correspond within 8 % error to those previously found for identical model systems that were built on silica wafers and characterized with a conventional ellipsometry set-up (see chapter 3). Also the QCM-D response in the combined set-up was similar (within 6 %) to results from the stand alone QCM-D system (figures 4.1B and 4.2B), as expected. This agreement validates the quantitative data obtained in the combined set-up.

The correlation of both datasets allows for the translation of Δf_{HABD} into absolute surface densities of immobilized receptors. The calibration curves (figures 4.4B and 4.5B) illustrate that the relationship between Δf_{HABD} and Δm_{HABD} is not linear, as already reported for a number of other protein monolayers.[139] This non-linearity is particularly apparent for his-HABD (figure 4.5B).

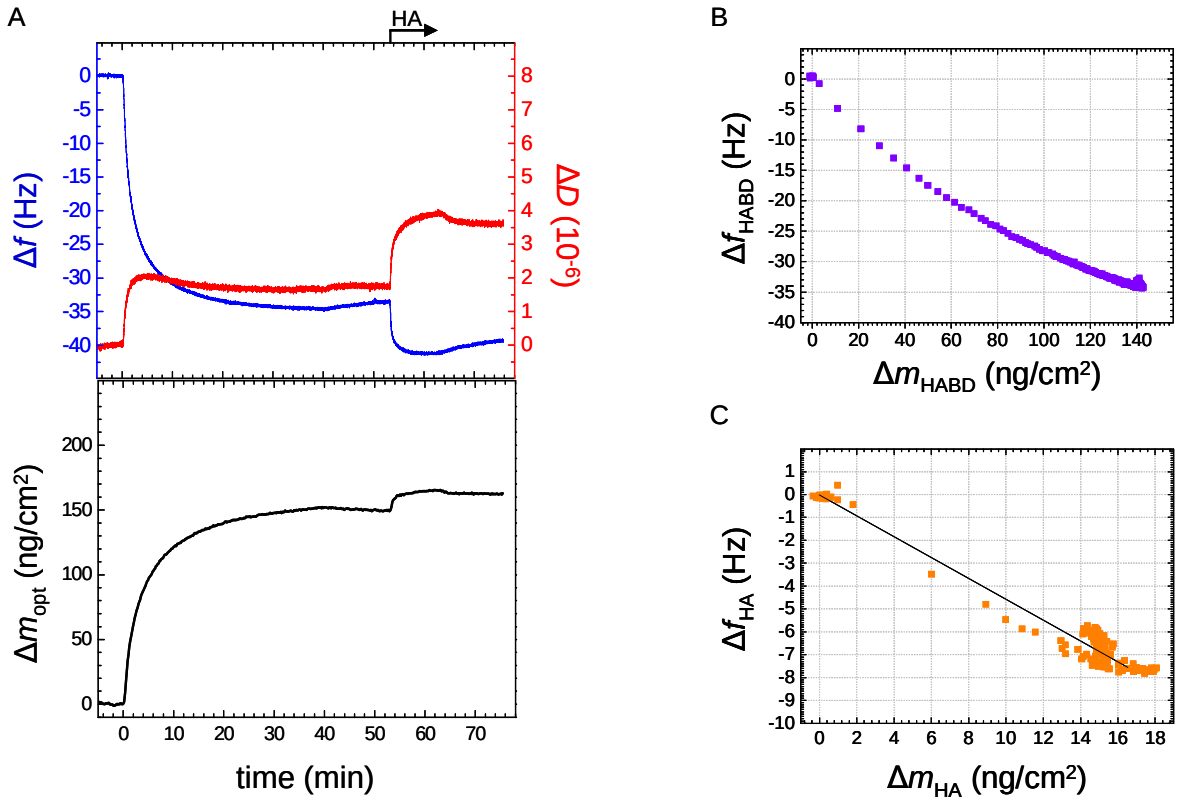

Figure 4.4: Correlation of the frequency shifts of $(HABD)_2$-Fc and HA to adsorbed amounts from a combined measurement of QCM-D and ellipsometry. A: QCM-D data Δ*f* and Δ*D (top)* and biomolecular mass as obtained from ellipsometry *(bottom)*. The receptor was added at time 0. Incubation with HA is indicated *(arrow)*. B: Parametric plot correlating Δf_{HABD} and Δm_{HABD}. C: Parametric plot correlating Δf_{HA} and Δm_{HA}. A linear approximation of the data is indicated *(solid black line)*.

Correlation of adsorbed amounts of HA to Δf_{HA}. Final adsorbed masses of HA were found at Δm_{HA} = 15 ng/cm^2 at a frequency shift of Δf_{HA} = -7.5 Hz and Δm_{HA} = 16 ng/cm^2 at a frequency shift of Δf_{HA} = -8 Hz, for $(HABD)_2$-Fc and his-HABD, respectively. The similar obtained masses on both HA receptor types indicate the maximum HA binding capacity of these surfaces.

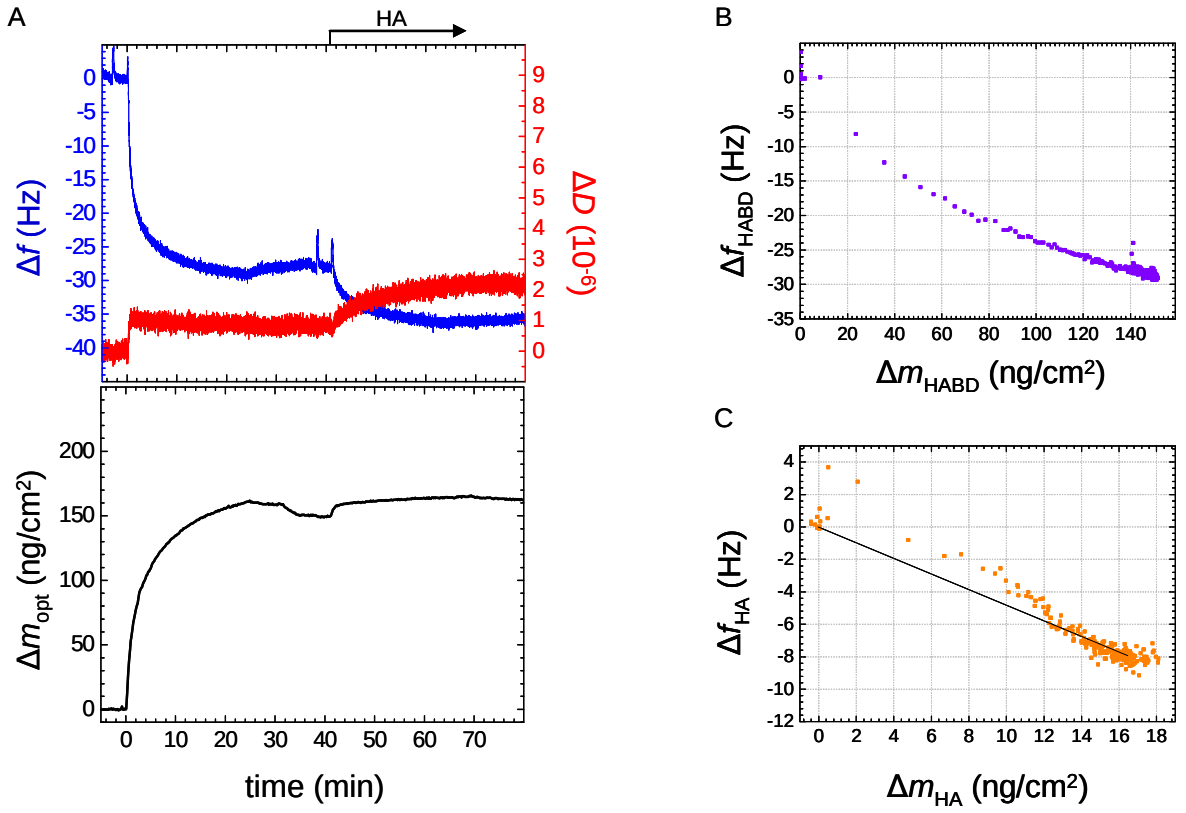

Figure 4.5: Correlation of the frequency shifts of his-HABD and HA to adsorbed amounts from a combined measurement of QCM-D and ellipsometry. A: QCM-D data, Δf and ΔD *(top)* and biomolecular mass as obtained from ellipsometry *(bottom)*. The receptor was added at time 0. Incubation with HA is indicated *(arrow)*. B: Parametric plot correlating Δf_{HABD} and Δm_{HABD}. C: Parametric plot correlating Δf_{HA} and Δm_{HA}. A linear approximation of the data is indicated *(solid black line)*.

4.1.3 Quantification of bound material per surface area

The correlation of Δf_{HABD} and Δf_{HA} with Δm_{HABD} and Δm_{HA}, respectively, from the combined QCM-D/ellipsometry measurements (figures 4.4B-C and 4.5B-C) enabled the direct translation of Δf into Δm from previous QCM-D experiments (figures 4.1B and 4.2B). Δf_{HABD} was translated into Δm_{HABD} using the calibration curves in figures 4.4B and 4.5B. Δf_{HA} at

maximal coverage was translated into Δm_{HA} using the data drom figures 4.4C and 4.5C. The finding that the morphology of the HA film at low coverage depends on receptor surface coverage (figure 4.3) implies that the correlation between frequency shift and adsorbed mass for HA at high receptor coverge (figures 4.4C and 4.5C) may not be readily employed to calculate the adsobed mass of HA at low receptor covergae from the QCM-D frequency shifts. As a first approximation, we assume instead that there is a linear relationship between adsorbed mass and frequency shift (black solid lines in figures 4.4C and 4.5C).

The results are shown in figure 4.6. As for Δf_{HA}, a fairly linear dependence of Δm_{HA} on Δm_{HABD} was found for low receptor densities up to $\Delta m_{HABD} \approx 65$ ng/cm^2 for his-HABD, and $\Delta m_{HABD} \approx 90$ ng/cm^2 for $(HABD)_2$-Fc. This linearity indicates that the ratio of available receptors per HA is nearly constant at low receptor densities.

As already argued, the masses of HA at low receptor density represent estimates with uncertainties that stem from the conversion of QCM-D shifts for HA binding into adsorbed masses. To get an idea of the quality of these estimates, binding was quantified by ellipsometry for two selected $(HABD)_2$-Fc densities (about 20 and 30ng/cm^2). The resulting values were only slightly below those estimated from QCM-D data (figure 4.6B). The correlation between Δm_{HA} and Δm_{HABD} at very low receptor coverage should thus be regarded tentatively.

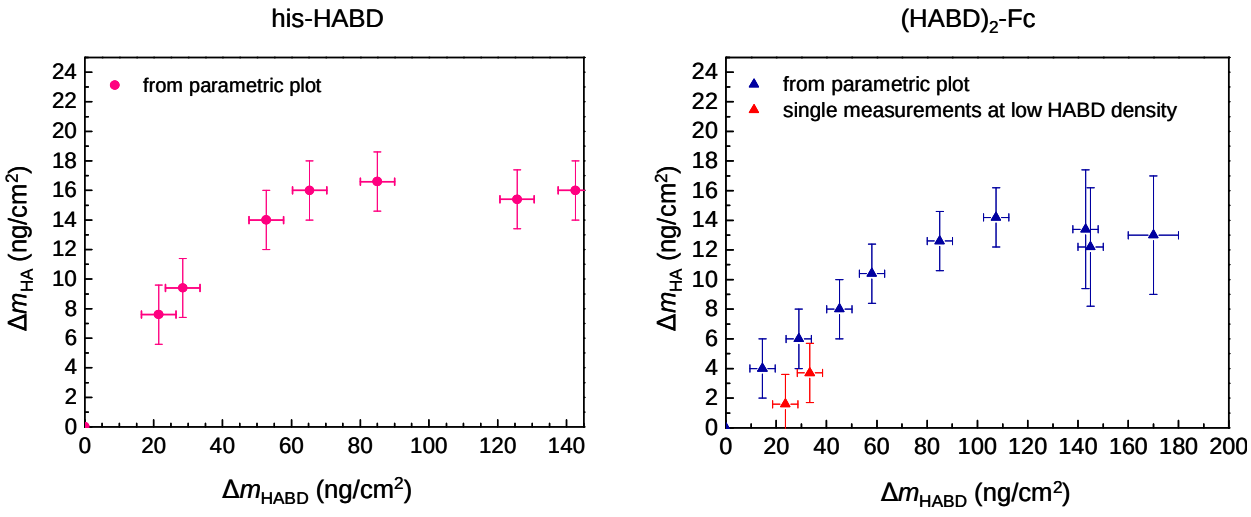

Figure 4.6: Absolute quantification of bound HA as a function of CD44 surface density. The monomer construct his-HABD is represented by pink circles *(left)* and the dimer $(HABD)_2$-Fc by blue triangles *(right)* for data derived from the parametric plots (figure 4.4B-C and 4.5B-C). Data from independent measurements by ellipsometry at low surface coverage of $(HABD)_2$-Fc are shown as red triangles.

In order to compare the HA binding behaviour on surfaces covered with the monomeric (his-HABD) and the dimeric ($(HABD)_2$-Fc) construct directly, the adsorbed masses were converted into molar surface densities (figure 4.7). Interestingly, the data points of both constructs coincide within the error bars. The data suggests that the presentation of HABD in the form of a Fc-dimer does neither enhance nor diminish HA binding.

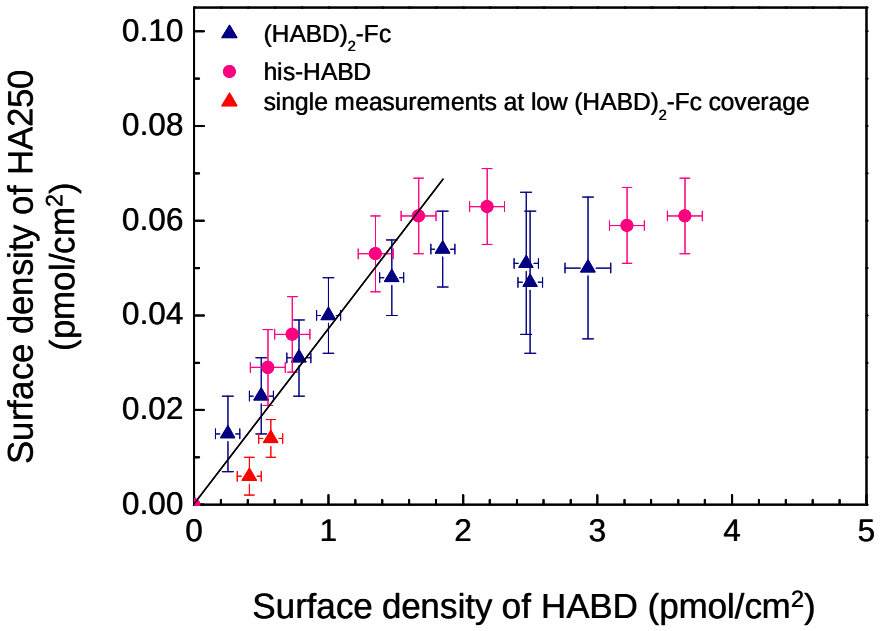

Figure 4.7: Estimated molar surface density of HA250 as a function of the molar surface density of his-HABD *(pink circles)* and $(HABD)_2$-Fc *(blue triangles)*. For $(HABD)_2$-Fc the results from independent ellipsometric measurements at low receptor density are shown additionally *(red triangles)*. A linear fit (through the origin) for low receptor surface densities is also shown *(solid black line)*.

The regime of close-to-linear increase of adsorbed HA extends to 1.5 pmol/cm^2 of HABD monomers. Assuming a hexagonally ordered arrangement of HABDs, this corresponds to a mean distance between neighboring receptors of about 11 nm. A linear fit (through the origin) in this regime provides a slope of 0.037 ± 0.005 pmol of HA250 per pmol of surface bound HABD for both HABD constructs, or 27 ± 4 HABD monomers per HA chain.

4.1.4 The interaction of soluble receptors with HA

Both CD44 constructs were able to bind HA irreversibly even at surface densities as low as 0.2 pmol/cm^2. Results in chapter 3 already indicated that stable binding requires polyvalent interactions. To provide further evidence, we investigated the role of surface confinement of the receptors on their ability to establish stable interaction between HA and isolated (soluble) receptors. To this aim a model system with surface bound HA was used, in which HA brushes were exposed to isolated his-HABD and (HABD)$_2$-Fc constructs.

Such a model system, in which HA with a single biotin moiety at one of its ends was immobilized on a SLB decorated with a monolayer of streptavidin (SAv), has been introduced recently[12] (figure 4.8). HA of 58 kDa (biotin-HA50) was employed, providing about 30 available binding sites per HA chain for the receptors.

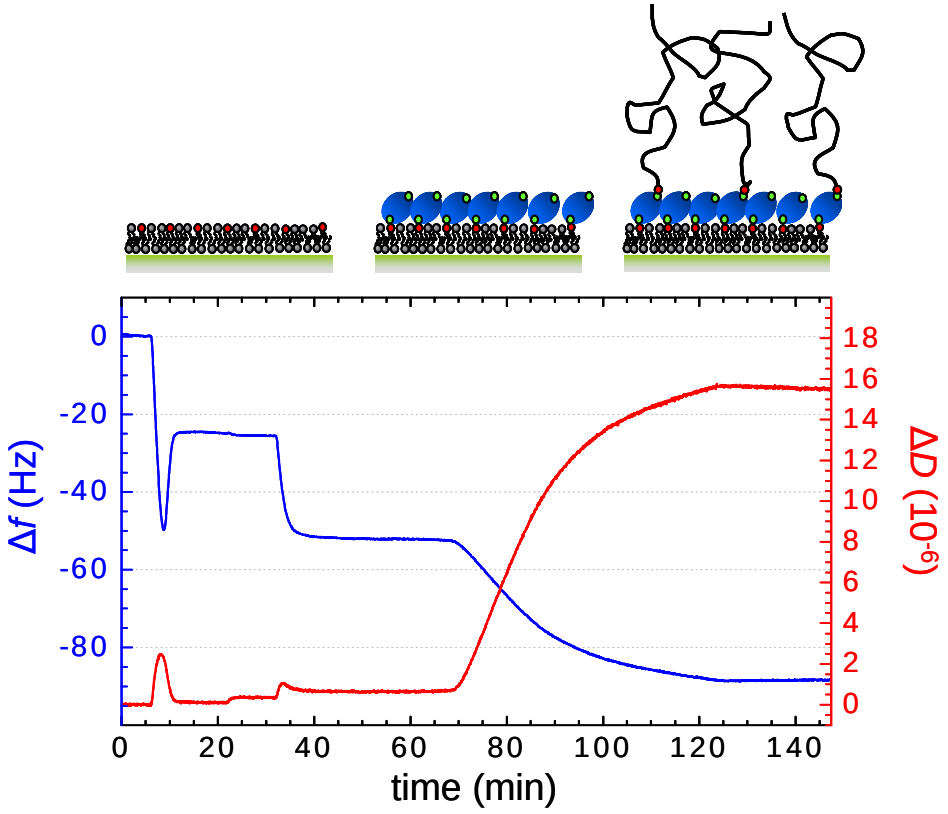

Figure 4.8: Representative QCM-D curve for the establishment of a HA-brush model system as reported by Richter et al.[12].

In strong contrast to receptors which were immobilized on the SLB, both constructs showed only transient interaction when exposed in solution to the surface bound HA film (figure 13). Upon addition of soluble his-HABD or (HABD)$_2$-Fc (at 10 µg/ml) a drop in frequency was

observed. The frequency shift was small compared to the values for the deposited HA brush (figure 4.9B) and for HA binding to receptor covered SLBs (figure 4.9A). The $(HADB)_2$-Fc construct yielded an about two fold higher shift ($|\Delta f|$= 5 Hz) than the his-HABD ($|\Delta f|$= 3 Hz), probably due to its higher molecular weight. Upon subsequent rinsing, the frequency shifts fully recovered for both CD44 forms, indicating only weak and reversible interaction with the bound HA. From these results it can be confirmed that isolated CD44 receptors can not confer stable binding of HA, but can do so under conditions where they can organize into polyvalent assemblies. Such conditions are provided by the plasma membrane, the natural residence of the receptor.

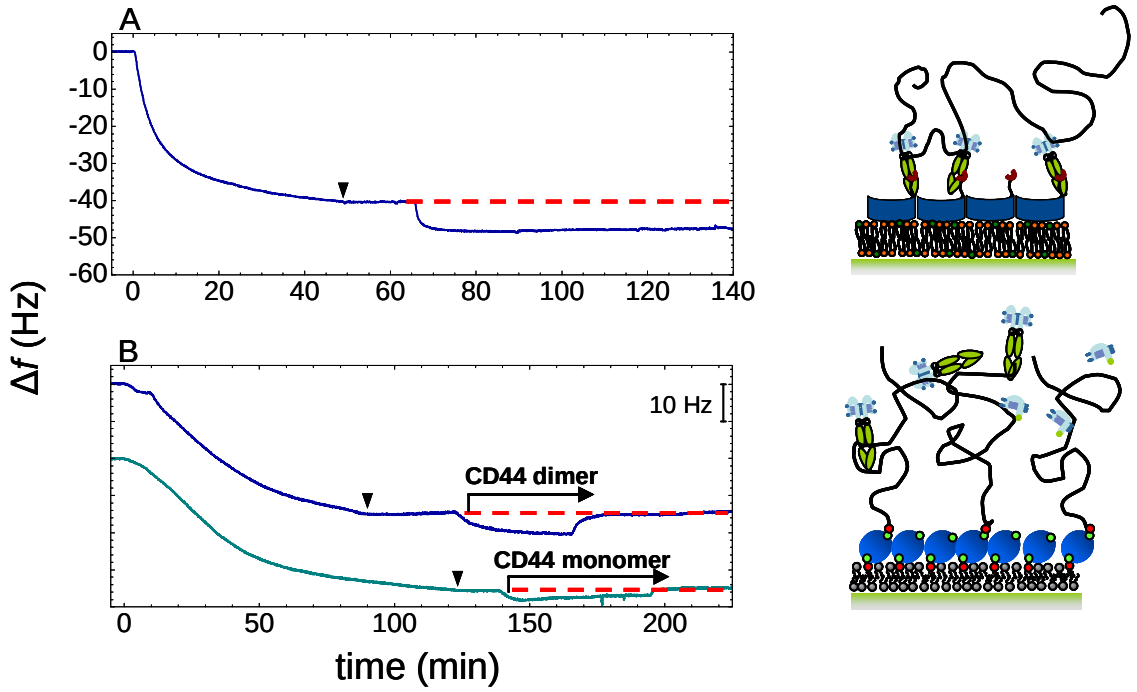

Figure 4.9: A: An assembly of multiple receptors, which are confined to the surface, confers stable binding of HA. The dashed lines indicate the frequency level before addition of HA to immobilzed receptor. $(HABD)_2$-Fc was added at time 0. Rinsing is indicated *(arrowheads)*. B: Soluble receptors bind reversibly to a HA film. The dashed red lines indicate the frequency level before addition of his-HABD *(cyan)* or $(HABD)_2$-Fc *(blue)* to grafted HA. HA was added at time 0. Rinsing is indicated *(arrowheads)*.

4.1.5 Effect of structural variations in the receptor construct on HA binding

We employed several additional CD44 constructs to investigate how different molecular features of the receptor affect the binding of HA. HA250 was again used as a model molecule,

and receptors were immobilized at close-to maximal coverage. The receptors can be classified into three groups:

- CD44 constructs comprising the whole extracellular domain (ECD), which consists of the HABD and the membrane proximal region, with variable exon extensions (V_x). These constructs were available as Fc-dimers only ($(ECD)_2$-Fc, see chapter 6.2.3 for details).
- A monomeric CD44 construct that lacked glycosylation (his-$HABD_{E.Coli}$).
- A CD44 construct with a critical mutation at the HA binding pocket at amino acid Arg41 (R41A). This extracellular domain mutant ($(ECD_{mutant})_2$-Fc) had previously been shown to exhibit an about 10fold lower affinity than the native form.[72]

Influence of the membrane proximal region on HA binding. A standard ECD construct, $(ECD)_2$-Fc and a variant with extended membrane proximal region, $(ECD\text{-}V_3)_2$-Fc, were compared with $(HABD)_2$-Fc for differences in HA binding by means of QCM-D (figure 4.10 A). All dimers could be successfully immobilized on the standard platform of model system type 1 (see chapter 3). Qualitatively, the binding curves for all CD44 constructs were similar, showing a monotonous decrease of frequency. Upon rinsing, all receptor types remained stably bound to the surface. The frequency shifts at saturation of receptor binding varied between the constructs (table 4.1) as expected from the differences in their size. Some differences between the CD44 forms were observed in the frequency shifts upon HA binding. However, these differences were small compared to the total shift (~ 30%). Highest frequency shifts were obtained for $(HABD)_2$-Fc with Δf = -7.5 Hz, whereas $(ECD)_2$-Fc and $(ECD\text{-}V_3)_2$-Fc showed shifts of Δf = -6 Hz and Δf = -5.6 Hz, respectively. Also, the changes in dissipation were comparable for all constructs (table 4.1).

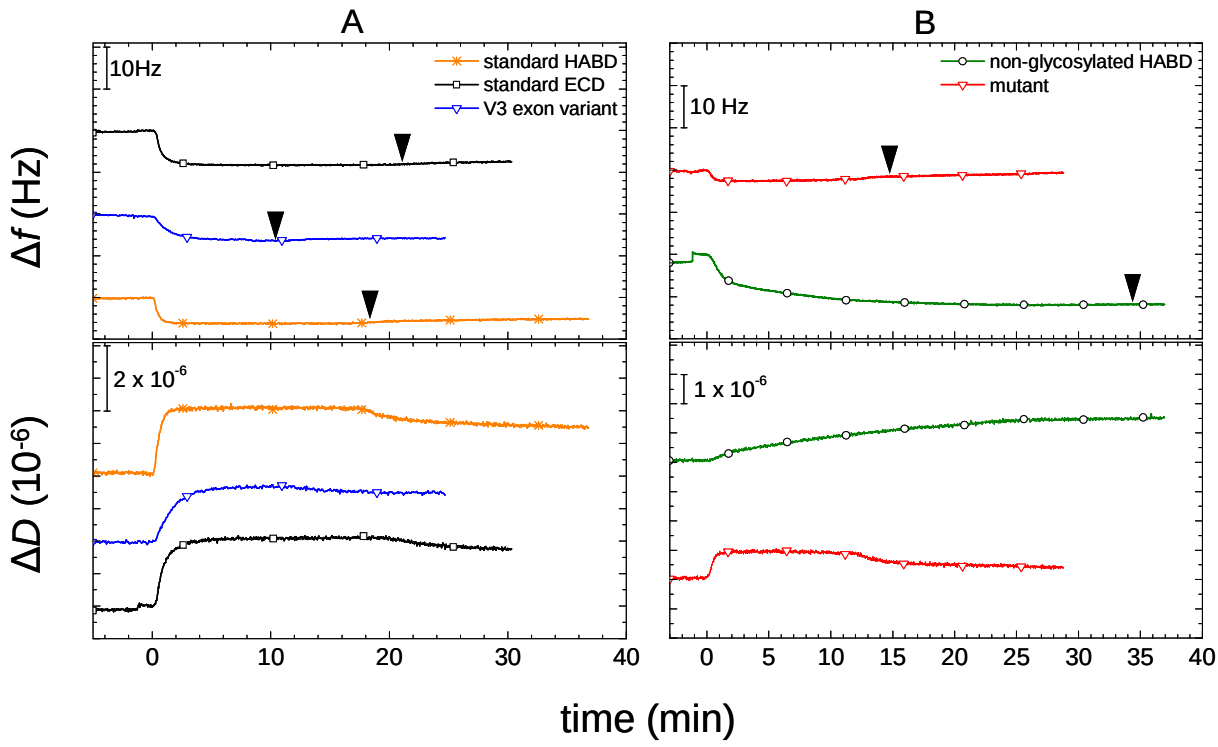

Figure 4.10: Differences in HA binding by different CD44 constructs. A: Three different dimeric CD44 constructs are shown, HA binding domain *(HABD, orange asterisks)*, full length extracellular domain *(ECD, black squares)* and full length V3 exon variant *(blue triangles)*. Injection of HA was started at 0 min. Arrowheads indicate start of rinsing. B: Two extreme cases for HA binding are represented by the R41A mutant, with ~10 fold lower affinity for HA *(red triangles)* and the non-glycosylated form of the HA binding domain, which shows maximun HA binding of all constructs *(green circles)*. In both graphs injection of HA was set to t = 0. Arrowheads indicate start of rinsing. Only injection of HA is shown.

Influence of glycosylation on HA binding. Monomeric non-glycosylated HABD (his-$HABD_{E.Coli}$) was stably immobilized on a type 2 model system (see chapter 3). The absolute frequency shift upon exposure to HA of $|\Delta f_{HA}|$ = 12.5 Hz was at least 50% higher than for all other tested constructs, indicating a significant enhancement in binding (figure 4.10B, table 4.1). The dissipation, in contrast, was close to the dissipation of standard his-HABD, ($\Delta D = 1.4 \times 10^{-6}$), implying differences in the morphology of the bound HA film. The receptor layer gave a frequency shift that was about $|\Delta f|$= 3 Hz higher than for the glycosylated HABD (table 4.1).

Interestingly, a clear slow-down in the apparent kinetics of HA binding for the his-$HABD_{E.Coli}$ was observed (figure 4.10B). The parametric plot of ΔD as a function of Δf provides information on the conformation of the HA chains on the surface, and it is instructive to

compare the *D*-*f*-plots for different constructs (figure 4.11). It can be seen that *D* for his-$HABD_{E.Coli}$ increases only slowly during the initial adsorption phase, suggesting that HA adopts a rather flattened conformation upon contact with the surface. The slope ($\Delta D/ -\Delta f$) gradually increases with increasing HA coverage, indicating the development of a progressively softer film. In comparison, the initial slope on $(HABD)_2$-Fc is significantly larger than on his-$HABD_{E.Coli}$, indicating that HA adopts a less flattened conformation.

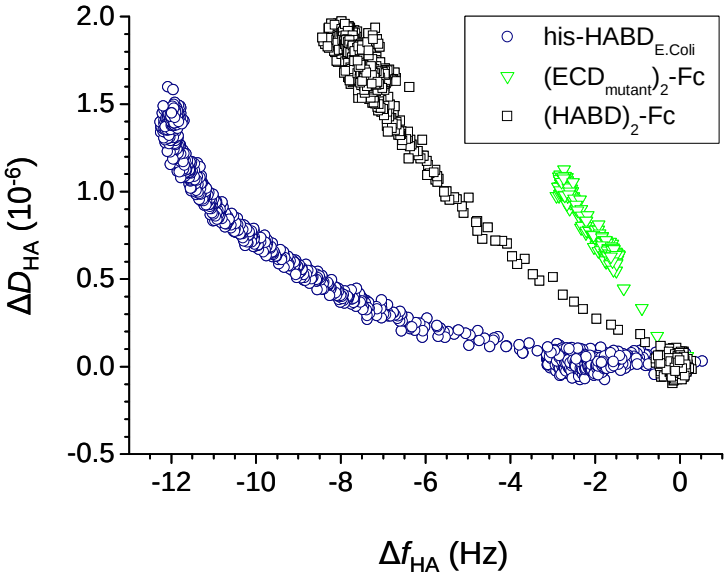

Figure 4.11: Δ*D*-Δ*f*-plots for HA binding at high surface density of different receptors: his-$HABD_{E.Coli}$ *(blue circles)*, $(HABD)_2$-Fc *(black squares)* and $(ECD_{mutant})_2$-Fc *(green triangles)* are shown.

A CD44 mutant with reduced binding affinity. The mutant CD44 construct, $(ECD_{mutant})_2$-Fc was immobilized on a type 1 model system, yielding a stable protein layer with similar frequency shifts as observed for native $(ECD)_2$-Fc constructs (table 4.1). Addition of HA resulted in little, but detectable binding (figure 4.10B). HA binding was partly reversible upon rinsing, and resulted in a final shift of Δf = -2 Hz. The capacity, to bind a fraction of HA, is likely to be the result of collective interactions with the polyvalent receptor surface. Although the affinity of an isolated $(ECD_{mutant})_2$-Fc is very low, the interaction with a small amount of HA can be stabilized due to avidity. The $(ECD_{mutant})_2$-Fc remains the construct with far lowest values for HA binding of all tested CD44 types (table 4.1). The $\Delta D/-\Delta f$-plot reveals further differences between the mutant and other CD44 constructs. The slope ($\Delta D/-\Delta f$) is significantly larger than for all other constructs (figure 4.11). From this behavior it can be concluded that the HA chains experience least flattening upon contact with the surface.

Table 4.1: QCM-D responses for different CD44 constructs.

construct	tag	receptor binding		HA binding	
		Δf (Hz)	ΔD (10^{-6})	Δf (Hz)	ΔD (10^{-6})
his-HABD$_{E.Coli}$	*his*	28 ± 0.5	0.4±0.05	12.5 ± 0.5	1.4± 0.05
his-HABD	*his*	26 ± 2	1 ± 0.2	7 ± 1	1.2 ± 0.1
(HABD)$_2$-Fc	*Fc*	37 ± 2	2.5 ± 0.1	7.5 ± 1.5	1.7 ± 0.2
(ECD)$_2$-Fc	*Fc*	38 ± 1	3 ± 0.5	6 ± 1	1.8 ± 0.2
(ECD-V3)$_2$-Fc	*Fc*	50	4.5	5.6	1.5
(ECD$_{mutant}$)$_2$-Fc	*Fc*	38 ± 1	3.3	2.5 ± 0.5	0.6 ± 0.2

Errors are derived from deviations between ≥ 2 measurements (1 in case of (ECD-V_3)$_2$-Fc).

4.1.6 Effect of HA concentration on HA binding

In order to figure out, how HA binding depends on HA concentration in the bulk, a series of QCM-D measurements with varying concentrations in the range of 1 to 50 µg/ml was performed. These assays were performed on both (HABD)$_2$-Fc and his-HABD [*]. Binding of HA to his-HABD revealed a dependence on the concentration (figure 4.12A). The adsorbed amount increased monotonously over the range of 1 to 10 µg/ml HA250. For higher HA concentrations, a plateau was observed. It should be noted that most other assays reported earlier in this work were performed at 10 µg/ml, i.e., at a concentration that corresponds to plateau coverage.

Binding of HA on (HABD)$_2$-Fc did not vary significantly across the employed range of concentrations (figure 4.12B). Apparently, the plateau was already attained at concentrations around 1 µg/ml. Notably, HA binding remained stable upon rinsing even at the lowest concentration tested on both CD44 constructs.

[*] Note that for this particular series of experiments a mouse-derived construct was used, in contrast to human-derived constructs for all other studies.

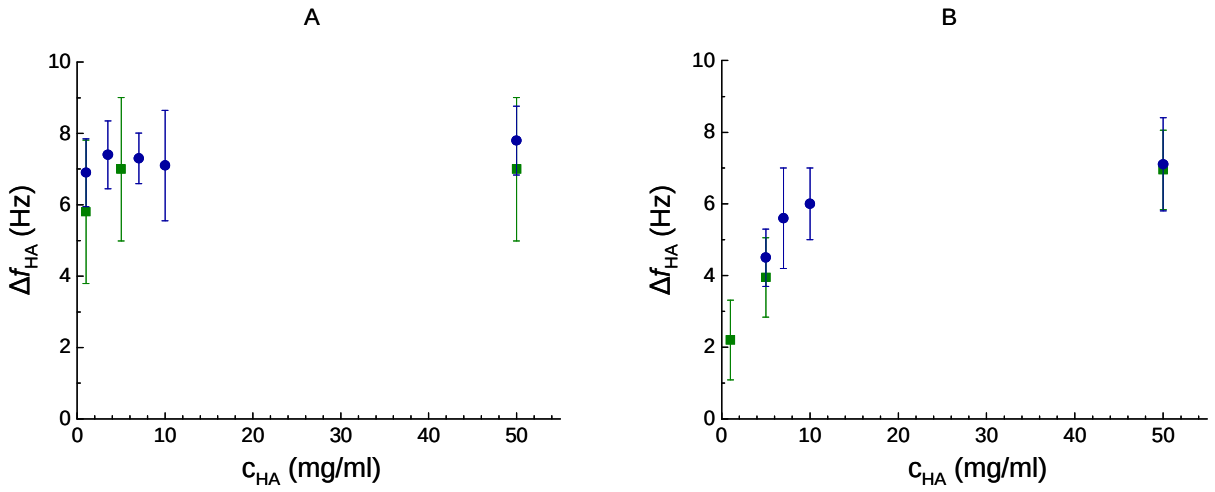

Figure 4.12: Effect of HA concentration on HA binding, measured by QCM-D for $(HABD)_2$-Fc (A) and mouse his-HABD (B). HA was added to receptor covered surfaces either by successive increase of the concentration in steps of 1, 5 and 50 µg/ml *(green squares)* or by directly applying a defined concentration *(blue circles)*. Mean values are shown; error bars correspond to variations from 2 or more independent measurements.

4.2 Discussion

Within the presented set of experiments I have asked the question, how the interaction between CD44 receptors and HA depends on receptor density, molecular features of the receptor and HA concentration. The in-situ combination of QCM-D and ellipsometry allowed correlating the surface density of receptors and binding of HA quantitatively. The data provided insight into the kinetics of formation and the stability of the HA films, as well as a quantification of the number of receptors available per bound HA chain.

4.2.1 HA binding at low surface density of receptors

We found that the amount of bound HA depends in a close-to-linear manner on the amount of immobilized HABD up to a surface coverage of about 1.5 pmol/cm^2 of HABD. This linearity implies that the ratio of available HABDs per HA chain is constant. For HA250 this ratio is about 30. This number is two fold smaller than the ratio found on CD44 covered surfaces at maximum coverage (chapter 3), although still rather large.

Polyvalent interactions at low receptor coverage. HA binding remained irreversible at even low receptor densities in our experiments. This result contrasts our previous finding that reducing the molecular weight of HA leads to reversible binding (see chapter 3).

From the experiments on HA brushes (figure 4.9), it becomes obvious that neither the dimeric nor the monomeric constructs can bind HA stably when acting as an isolated receptor. HA binding must hence be stabilized by an avidity effect. One may ask how polyvalent interactions are accomplished on a surface that is only poorly covered with CD44.

It is instructive to compare the surface area per receptor that can be attained in our assays (150 to 2000 nm^2) with the dimensions of HA in solution. In dilute solution, HA chains adopt the shape of an extended random coil with dimensions of the radius of gyration R_g.[167, 168] For HA250, R_g is about 40 nm. The projected surface area (figure 4.13) of such a coil (πR_g^2) would then be ~5000 nm^2. This value is only slightly larger than the surface area per receptor at the lowest coverage investigated here. On the other hand, a stoichiometry of about 30:1 between HABD and HA was found to be largely preserved even at lowest receptor coverage. Two scenarios appear plausible to explain this discrepancy. First, the HA chains may stretch and adopt a flattened, pancake-like conformation on the surface, thereby increasing their projected area and the number of accessible receptors. Secondly, the receptor density may increase locally in the vicinity of a bound HA chain. Notably, the design of the model systems

used here allows lateral displacement of the bound receptors with diffusion constants similar to those of the lipid bilayer (10^{-8}cm^2/s for DOPC/DOPS, 10^{-10} cm^2/s for the same SLB with a layer of Anx5[245]).

At present, neither of these two scenarios can be excluded. The ΔD-Δf-plots in figure 4.3 though provide insight into the conformation of surface-bound HA. These plots revealed some tendency of HA towards a flattened conformation on surfaces that exhibited high densities of receptors in the initial phase of adsorption. Flattening was found to be weaker at low receptor coverage. Given that the receptor induced flattening of HA chains is rather weak, we speculate that local enrichment of receptors contributes to the constant ratio of HABD per HA.

Clustering or oligomerization of CD44 was, indeed, proposed as one possible mechanism to enhance HA binding to cell surfaces [47, 71, 79, 260]. Further experiments with model surfaces carrying immobile receptors will be useful in order to investigate, inhowfar ligand-induced reorganization of receptors can enhance ligand binding.

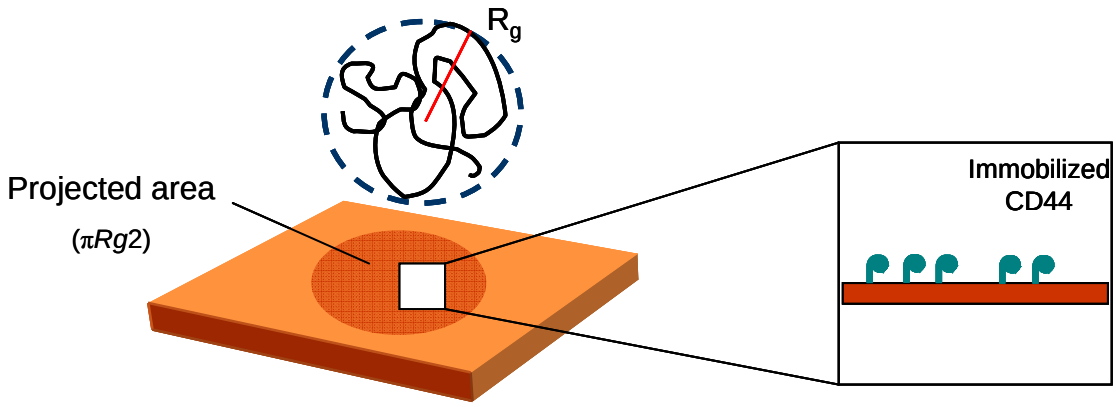

Figure 4.13: Projected area of a free HA chain.

4.2.2 Avidity vs. affinity

We found that the final frequency shift for HA on surfaces that are densely covered with receptors varied as a function of the employed CD44 construct (table 4.1). One may ask, if the changes in the responses for HA are the consequence of changes in the affinity of the individual receptor, or of variations in the avidity due to differences in the receptor surface density.

Out of the selection of CD44 constructs the $(ECD_{mutant})_2$-Fc showed lowest binding. Given its structural similarity with $(ECD)_2$-Fc and the qualitatively and quantitatively similar adsorption curves, the surface coverage of both receptors should be nearly equal. The difference in HA binding between mutant and wild type must hence originate from different affinities. This example is the only case within this study in which the response of HA binding unambiguously reflects a difference in affinity.

The presence of the membrane proximal region had only little effect on HA binding. When comparing CD44 constructs of varying membrane proximal region, a general, albeit weak, trend was that HA binding was reduced with increasing extension of the membrane proximal region. The membrane proximal region can be as large as ~25 nm. It is likely that this additional extension reduces the receptor surface density due to increased steric hindrance. In line with such a scenario, we previously found that the smaller, monomeric CD44 construct formed denser monolayers than the dimeric $(HABD)_2$-Fc (see chapter 3).

Along the same line, the surface density of his-$HABD_{E.Coli}$ at saturation is probably higher than that of his-HABD due to the lack of glycosylation. It is thus likely that HA binding correlates with receptor density. It is at present not clear inhowfar variations in the avidity of receptors do also contribute to the variations in HA binding.

How can avidity and affinity effects be disentangled experimentally? To address the effect of affinity on HA binding to a receptor covered surface, it is critical to exclude any contribution from avidity effects by creating surfaces with identical receptor coverage.

Parameters to quantify the binding strength of HA on receptor covered surfaces. Two parameters emerge from this study that provide direct information about the binding strength of HA.

(i) ΔD-Δf-plots in figure 4.11 revealed significant structural differences between the bound HA on the $(ECD_{mutant})_2$-Fc, the construct which is known to exhibit reduced affinity for HA, and the his-$HABD_{E.Coli}$, which exhibited highest responses for HA binding. While a soft film of HA formed on $(ECD_{mutant})_2$-Fc, the initially bound HA chains on his-$HABD_{E.Coli}$ adopt a strongly flattened conformation. From a polymer theoretical point of view, the conformation of an adsorbing polymer chain is determined by the adhesion energy per surface area. From these considerations it can be conjectured that the initial slope of the ΔD-Δf-plots can serve as a parameter to determine the polymer's conformation on a given receptor covered surface, and thus its binding strength.

(ii) A second parameter to obtain information on changes in binding strength is the final mass of bound HA. The difference in final shifts between the $(ECD_{mutant})_2$-Fc and the structurally

akin $(ECD)_2$-Fc (figure 4.10 and table 4.1) illustrates that different levels of affinity are reflected in final response for binding of HA.

It can be hypothesized that by determining these two parameters at equal receptor density, changes in the affinity of different receptor types can be quantified even on a surface of high avidity.

4.2.3 Comparison to cell surface

The receptor surface densities accessible with our approach range from about 0.1 to 4 pmol/cm^2 corresponding to a surface area per receptor of 2000 to 150 nm^2. It is interesting to compare these with receptor densities found on cell surfaces. Alves et al.[254], for example, reported a CD44 density of 233 receptors per µm, or an area per receptor of ≈ 4300 nm^2, on colon carcinoma cells. In another study the number of CD44 on monocytes was estimated to be in the range of 150000 to 300000 receptors per cell.[253] Assuming a cell diameter of about 15 µm,[261] these numbers yield a surface area per CD44 of about 2300 to 4700 nm^2. The receptor densities on the cell surface are thus comparable to the surface densities attainable in our model systems.

It should be pointed out that the local concentration of CD44 on cell surfaces may be significantly higher, e.g., due to enhanced expression or clustering. Hence, we can conclude that the experimental approach presented here can provide receptor surface densities that are likely to represent the *in-vivo* situation.

4.4 Conclusions

The developed model surfaces could be decorated with CD44 constructs in a highly controlled manner. The receptor densities could be tuned down to average inter-receptor distances of about 45 nm or surface distributions which represent well the upper limit of average receptor densities on cell membranes.

Tuning of receptor density allowed for the investigation of CD44-HA interactions at various conditions. By using a combined set-up of QCM-D and ellipsometry, the adsorbed amounts of HA as a function of receptor coverage could be estimated. For HABD densities up to 1.5 pmol/cm^2, the number of available receptors per HA250 chain remained nearly constant at around 30. HA binding was irreversible at lowest receptor densities. It is proposed that the binding of HA can induce local enrichment of the 2D mobile receptors, thereby enhancing the stability of HA binding. Studies with immobile receptors will be useful to test this hypothesis.

The amount of adsorbed HA to surfaces that were covered with various receptor types at saturation decreased weakly with increasing size of the membrane proximal region, and increased strongly upon deglycosylation of the HABD. Systematic measurements at comparable receptor densities will be needed to separate the contributions from changes in affinity and avidity effects in these polyvalent interactions.

The ratio of $\Delta D/-\Delta f$ and the final adsorbed mass of bound HA, were found to be suitable parameters to determine changes in the intrinsic receptor affinity, provided that the surface densities of different receptors are identical. From these and polymer physics considerations a model for the conformational dynamics of HA on surfaces with different affinities was derived, which, however, remains to be validated in systematic studies.

Chapter 5

Synopsis and Outlook

The major objective of this thesis was the development of *in-vitro* novel model systems of HA-rich films and their application as experimental platforms for the investigation of specific protein-HA interactions. Finding a suitable methodology for the bio-functionalization of gold surface with SAv was another goal. Both have been projected in order to find new designs for the model systems. The developed model systems (chapter 3 and 4) and the study on protein adsorption to gold and silica (chapter 2), however, are conceptually and methodologically very different approaches. In the framework of this thesis, they have also advanced differently. It is therefore worthwhile to draw a bow between these two major blocks with some concluding remarks.

5.1 Towards model systems of grafted HA

The physisorption of SAv represents a simple strategy of general applicability to equip gold surfaces with a high density of biotin-binding sites. The deposited protein layers were functional, stable and largely resistant to unspecific binding of non-biotinylated probes. Although the immobilization remains rather crude in that adsorption is likely to happen in random orientations, a large fraction of SAv retained its biotin-binding activity. This approach is attractive by its elementariness and should provide an alternative to established, yet more complex strategies, which employ linkers to mediate the binding between a surface and the biotin-receptor. In the context of this work we have also tested and critically discussed two alternative methods that rely on linkers. The results illustrated that the use of linkers is a complex additional step in the process of surface functionalization, which requires careful tuning. None of the linker methods was superior to the physisorption of SAv in our studies.

Among the biotin-binding proteins tested, SAv was unique in resisting adsorption to silica surfaces, a selectivity that was promising for the selective functionalization of gold nanostructures *via* physisorption of SAv. The transfer of this method included the depositions of gold nanostructures on silica coated quartz crystals for the analysis by means of QCM-D. Gold nanostructures could be successfully generated by block-copolymer micelle

nanolithography resulting in regular arrays of gold nanoparticles. The selective functionalization of the gold nanoparticles by physisorption of SAv could be demonstrated. In first attempts to bind biotin-HA to the functionalized gold nanoparticles typical, albeit low responses were obtained, indicating that only a fraction of nanoparticles was functionalized. Nevertheless, the potential and specificity of this method could be demonstrated.

Impressively, QCM-D was sensitive to the interaction of proteins with the nanostructured surfaces, even though the functional surface area is only about 2%, and could provided information on binding kinetics on different levels of the functionalization.

The results of the initial steps to immobilize HA on nanostructured surfaces in order to gain a high control over the distance between the individually grafted HA chains, indicated the need for improvement of the nanoparticle functionalization, which has to be addressed in future studies. These studies have to include the physico-chemical characterization of the resulting HA films under different nanoparticle spacings and comparison with existing HA-brush models on mobile substrates. Grafting of HA to nanoparticles that have been deposited on soft substrates[262] such as hydrogels appears particularly interesting, since such substrates would allow for the dynamic regulation of the inter-particle distance on the same sample.

Given the sensitivity of QCM-D to monitor adsorption processes on nanoparticles we conjecture that this tool can be exploited to gain control over specific reactions on such nanostructures. For example, the binding of various thiolated molecules could be investigated in further studies.

Taken together, the methods developed here provide a well-characterized and promising basis for the immobilization of biotinylated probes in general, an HA in particular, to homogeneous and nanostructured gold surfaces. The spontaneous physisorption of SAv to gold in a functional state together with its resistance towards silica holds the promise to become a simple, yet useful strategy for the functionalization of small-scale devices, such as microcantilevers, atomic force microscopy tips or nanosructured substrates, which find increasing application in biophysical or biotechnological studies.[263-265]

5.2 Model systems with CD44 bound HA

Two model systems have been developed that enable the immobilization of ectodomains of either monomeric or dimeric CD44 constructs in a well-controlled manner. Both methods provided stable and specific binding of both the receptor and HA, and receptor surface densities were tunable up to average receptor distances of about 45 nm. These model systems

were exploited for the quantitative investigation of specific polyvalent interactions between HA and an assembly of receptors in a biologically relevant arrangement under different experimental conditions. On surfaces with high receptor densities, binding of HA increased sigmoidally with molecular weight of HA, and became reversible for HA below 30 kDa, i.e., a HA chain that accommodates about 15 binding sites for CD44. Interestingly, this number was in good agreement with the number of available receptors for the same HA (~12), as was quantified for the adsorbed amounts. Our findings provide evidence that multivalency plays a crucial role in stabilizing the intrinsically weak interaction between CD44 and HA. For this type of HA films we found many parallels between the binding of HA to receptor covered surfaces and the behavior of flexible polymers adsorbing to a homogeneously attractive surface according to polymer theory.

On surfaces with low receptor densities binding of sufficiently long HA (HA250) increased in a close-to linear manner with the amount of receptors. Quantifying the adsorbed amounts revealed the number of available receptors per HA chain to be about 30. Notably, binding of HA was irreversible even at lowest receptor densities.

For various CD44 constructs the experimental data also indicated subtle differences in the final adsorbed amount of bound HA (Δf_{HA}) as well as in the conformation of the adsorbing HA chains to the various CD44 constructs (revealed by $\Delta D/-\Delta f$-plots). These two parameters were identified as measures of the binding strength between HA and CD44 covered surfaces. Both avidity effects (polyvalency) and the intrinsic affinity of the individual receptor determine binding of HA. We were able to outline a method that has the potential to disclose these two contributions. Predictions about the effect of affinity changes can be experimentally tested using surfaces with identical receptor surface densities of the different constructs in order to exclude any contribution from avidity effects. *In-vivo* both avidity and affinity, probably in combination, are likely to regulate CD44-HA interaction. The degree to which either mechanism is involved under certain physiological conditions remains to be elucidated, and may have important biological function.

The nearly constant number of available receptors per HA over a wide range of surface densities together with the particular property of the SLBs to provide 2D mobility of receptors support the idea that HA binding leads to local enrichment of receptors on the surface thereby enhancing binding of HA. To prove or reject this hypothesis in follow-up studies, it would be desirable to use analogue model systems, which differ only in that they do not provide the 2D mobility that is present in the current models. Possible routes could employ SLBs in the gel-phase as a substrate for the immobilization of CD44 receptors.

The results that were obtained on various aspects of the model HA films, such as film formation, morphology, stability and composition, impressively demonstrate the benefits of the use of complementary techniques in the examination of these highly hydrated films in combination with a well-controlled model system. Combining these techniques provided access to quantitative information about the impact of avidity as a regulatory mechanism for the specific interaction between CD44 and HA, and also about the physico-chemical properties of the supra-molecular assemblies. The new combined set-up of QCM-D and ellipsometry that was employed in this thesis can be further exploited for the quantification of the interaction between soluble hyaladherins and HA. The experiments with soluble CD44 on HA-brushes imply the possibility to determine affinity constants, and to investigate for potential cooperative behavior of the hyaladherin.

Taken together, these new approaches open doors towards the investigation of HA-rich films with average receptor amounts close to those on natural cell membranes. They can readily be expanded to other HA binding proteins of interest or by introducing further components, and serve as well-controlled experimental platforms for the study of cell-HA interactions. These model systems provide access to the supra-molecular regime of biochemical processes and have the potential to fill the gap between the molecular and cellular scale as an important piece of a puzzle for understanding the PCC and the mechanisms of its dynamic regulation.

Chapter 6

Methods

6.1 Nanostructure based model systems

6.1.1 Block-copolymer micelle nanolithography

General method. Block Copolymer Micelle Nanolithography (BCML) allows for the controlled generation of periodic arrays of metal clusters on a length scale below 100 nm.[177, 178] Besides giving access to surface patterning at a usually hardly attainable length scale, BCML has the advantage to be applied for a variety of substrates like for example glass, silicon or mica.[177] The principle of this technique is the use of amphiphilic polymers, which spontaneously form micelles above a critical micelle concentration (CMC).

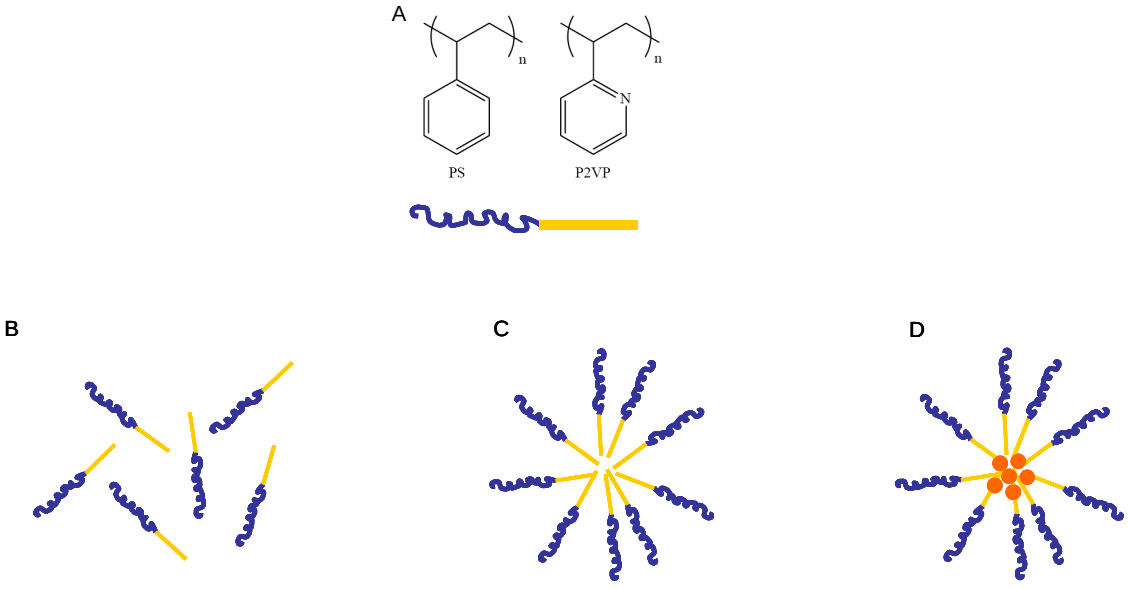

Figure 6.1: sketch of amphiphilic block copolymers and formation of micelles. A: block copolymers consisting of the hydrophobic block of polystyrene *(blue)* and the hydrophilic block of poly-2-vinyl-pyridine *(yellow)*. B and C: dissolved block copolymer and micelle formed above the critical micelle concentration. D: micelle loaded with gold precursor salt *(red)*.

The block-copolymer typically used consists of polystyrene (PS) as the hydrophobic and poly-2-vinyl-pyridine (P2VP) as the hydrophilic block. When dissolved in toluene, the preference of the PS for toluene as solvent drives the formation of spherical micelles with a hydrophilic core of P2VP and a hydrophobic shell of PS[266] (figure 6.1). The polar core of such micelles can be loaded with a metal salt, in my case a gold precursor ($HAuCl_4$).[267]
The gold-loaded micelles are transferred to the desired surface by dip coating of the substrate into the gold-copolymer solution. During retraction the micelles self-assemble into a hexagonally packed, micellar monolayer driven by capillary forces during fast evaporation of the solvent[177] at the dipping edge (figure 6.2). Subsequent plasma treatment of the micelle decorated surfaces has two effects: i. the precursor metal salt transforms into a pure metal cluster, and ii. the residual polymer matrix is removed[177]. The gold (or other metal) clusters reveal a quasi-hexagonal pattern with tunable particle size and inter-particle distances[268] (figure 6.2).

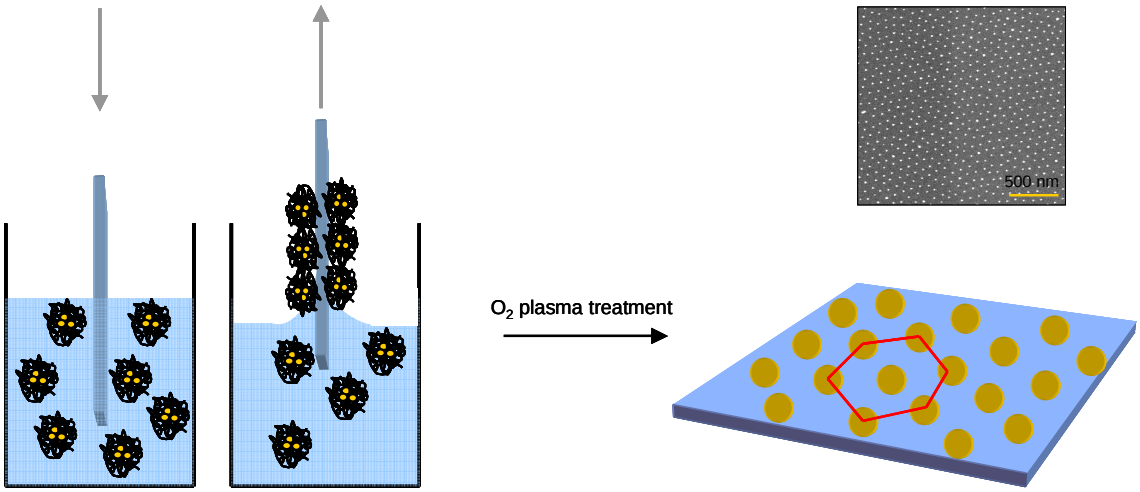

Figure 6.2: Generation of gold nanostructured surfaces. Left: dipping process. After dipping of a glass slide into a gold-polymer solution, a monolayer of micelles remains on the surface. Right: Plasma treatment removes organic material and discloses an array of gold clusters *(yellow dots)* with a quasi-hexagonal pattern *(red line)*. Top right: SEM micrograph of a representative nanostructured surface.

The size of the gold clusters can be adjusted by the size of the hydrophilic block (P2VP) of the used polymer and the loading *L* (the amount of gold salt per VP unit) resulting in a size range between 1 and 15 nm.[268]

Predominantly, it is the length of the hydrophobic block of the polymer (PS),[269] which determines the inter-particle distance. Other parameters, however, such as retraction speed[180, 270] or surface properties[177, 268] of the substrate also have an influence on the spacing. Distances between ~30 and ~200 nm can be generated.[222]

Within this work BCML was mostly employed for the nanostructuring of QCM-D sensor crystals. The procedure changes slightly as a consequence of the substrate (see next section).

Substrate cleaning. Glass slides (20×20 mm or 24×24 mm) were immersed into Piranha solution (H_2O_2 : H_2SO_4 = 1 : 3) for 1h. The glass slides were then extensively rinsed with ultrapure water, blow-dried in nitrogen and stored in sealed petri-dishes under nitrogen atmosphere until further use.

Silica coated QCM-D sensors were immersed into a 3 % SDS solution for 30 min followed by thorough rinsing with ultrapure water and 25 min UV/ozone treatment.

If cleaned substrates were not used immediately after cleaning, they were exposed to a 5 minute plasma treatment before dip-coating. Glass slides were exposed to hydrogen plasma (0.4 mbar, 150W), and QCM-D sensors to oxygen plasma (0.35 mbar, 200 W).

Table 6.1: Characteristics of used block copolymers and typical parameters of gold-polymer solutions.

PS(x)-*b*-P2VP(y)	M_wPS ($gmol^{-1}$)	M_w PVP ($gmol^{-1}$)	L	polymer concentration (mg/ml)	inter-particle distances (nm)
PS(451)-*b*-P2VP(228)	47000	24000	0.4	5	40-55nm
PS(1056)-*b*-P2VP(495)	110000	52000	0.5	5	60-90nm
PS(2074)-*b*-P2VP(571)	216000	60000	0.3	5	100-200nm

Gold-copolymer solutions. Diblock-colymers poly(styrene)(x)-*block*-poly(2)vinylpyridine(y), abbreviated generally as PS(x)-*b*-P(2)VP(y) were dissolved in toluene and stirred at room temperature for 24 hours to allow homogeneous micelle formation. A list of the used polymers, typically employed concentrations and volumes is given in table 6.1. After full dissolution, the precursor metal salt (tetrachloroaureate(III)-trihydrate $HAuCl_4 \times 3H_2O$) was added in stoichiometric amounts depending on the loading *L*, which is defined as:

$$L = \frac{n[HAuCl_4] \cdot M_w(VP)}{m(VP)} \tag{20}$$

with $M_w = m/n$, where n is the molarity and m the mass amount of the given compound. The amount of gold precursor to be added to the polymer solution can then be calculated according to:

$$m(HAuCl_4 \cdot 3H_2O) = \frac{m(polymer)}{M_w(polymer)} \cdot (VPunits \cdot L) \cdot M_w(HAuCl_4 \cdot 3H_2O) \tag{21}$$

where M_w is the molecular weight.

The solution was stirred for at least 24 hours until the precursor was completely dissolved and the mixture appeared as a clear yellowish solution. Typical loading parameters for different polymers are listed in table 6.1.

Sample preparation. For the deposition of a micellar monolayer on the substrate, cleaned glass slides or QCM-D sensors were dipped into the gold-copolymer solution and immediately retracted at constant speed of about 12 mm/min. To remove the polymer and to induce the formation of metal clusters, the glass slides were exposed to hydrogen plasma during 45 minutes (0.4 mbar H_2, 150 W) (plasma chamber TePla 100-E, PVA TePla AG, Feldkirchen, Germany). As the coating of the QCM-D sensors is sensitive to hydrogen plasma, QCM-D surfaces were exposed to oxygen during 1 hour, instead of 45 min, at conditions optimized for the treatment in O_2 (0.35 mbar O_2, 200 W).

The quality of the surface pattern of a batch was assessed by scanning electron microscopy. As scanning electron microscopy (SEM) requires conductive samples, a thin (a few nm) carbon layer was evaporated on top. Analysis of inter-particle distances was performed with ImageJ software as described elsewhere.[222]

6.1.2 Passivation of nanostructured surfaces with mPEG-urea

In order to inhibit unspecific adsorption to other places but the gold clusters, the silica area between the gold dots was coated with a covalently coupled mPEG2000-urea film

(figure 6.3).[271] mPEG200-urea was kindly provided by Jacques Blümmel (PCI Universität Heidelberg). Nanostructured surfaces were shortly activated by exposure to hydrogen or oxygen plasma, for glass slides or QCM-D sensors, respectively, (for respective conditions see above) and immediately immersed into dry toluene. 1mM of mPEG2000-urea was added under N_2 stream together with 0.05 % of triethylamine as a catalyst. The mixture was heated to 80°C and left for reaction for at least 16 hours. After cooling down, the samples were removed from the solution, rinsed thoroughly with ethyl acetate and methanol to remove residual PEG molecules and dried in N_2. Because of the propensity of PEG to oxidation, which changes the properties of the polymer chain, the samples were used directly after passivation to ensure maximal integrity of the PEG-layer.

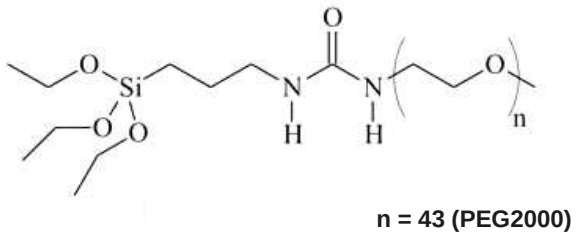

Figure 6.3: Chemical structure of mPEG-urea.

6.1.3 Functionalization of gold nanostructures with bi-functional linker molecules

Two different linkers were studied for the functionalization of gold surfaces, N-(6-biotinamido)hexyl)-3-(2-pyridylthio)propionate (HPDP-biotin) and biotin-PEG-SS (figure 6.4). HPDP-biotin was purchased from Pierce Biotechnology (Rockford, IL, USA). Biotin-PEG-SS was obtained from Polypure (Oslo, Norway). HPDP-biotin was dissolved in DMF to a concentration of 2 mg/ml, and further diluted to a final concentration of 100 µg/ml in working buffer. Biotin-PEG-SS was dissolved in HEPES buffer (pH 7.4) to a final concentration of 1 mM (1.54 mg/ml).

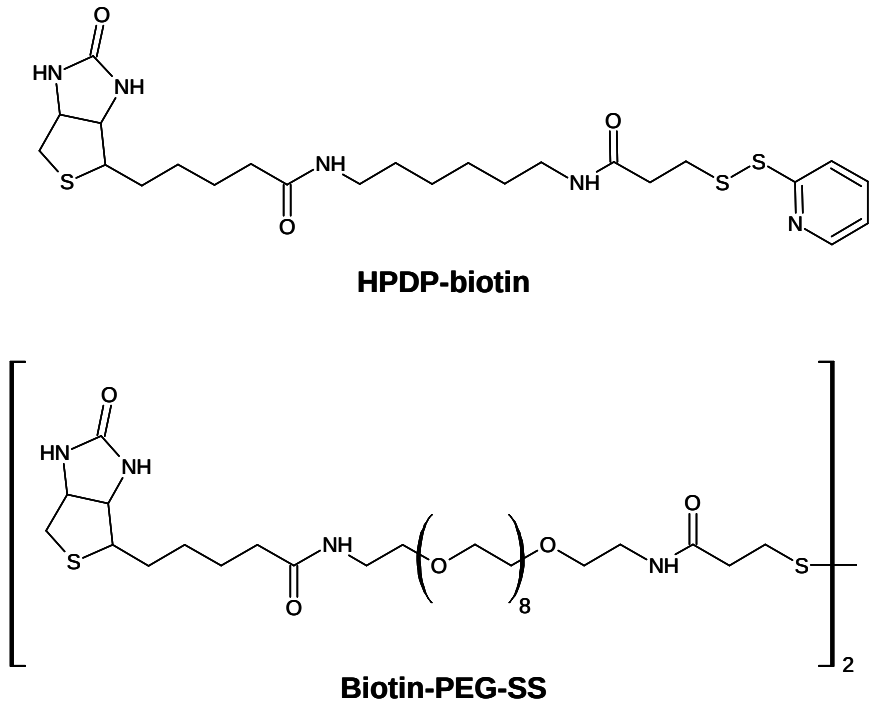

Figure 6.4: Chemical structures of both linkers: Top: HPDP-biotin. Bottom: biotin-PEG-SS.

6.1.4 General protocols for the immobilization of proteins

Avidin (Av), streptavidin (SAv), FITC-labeled streptavidin (FITC-SAv), bovine serum albumin (BSA) and biotinylated bovine serum albumin (biotin-BSA) were purchased from Sigma-Aldrich (Schnelldorf, Germany). Neutravidin (NAv) was purchased from Invitrogen (Karlsruhe, Germany). Proteins were dissolved in either PBS (10 mM phosphate, 137 mM NaCl, 2.7 mM KCl) or Hepes buffer (10 mM Hepes, 150 mM NaCl, with or without 2 mM $CaCl_2$) at a concentration of 1 mg/ml, aliquoted and stored at -20°C. Before use, the proteins were diluted in working buffer. The pH of the buffers was 7.4, unless otherwise stated, and adjusted with either HCl or NaOH.

6.2 Supported lipid bilayer based model systems

6.2.1 Preparation of small unilamellar vesicles (SUVs)

SUVs were prepared of either 1,2-Dioleoyl-sn-Glycero-3-Phosphocholine (DOPC) alone or from mixtures of DOPC with 1,2-Dioleoyl-sn-Glycero-3-Phospho-L-serine (DOPS 25% molar ratio), with Bis-nitrilotriacetic-acid (bis-NTA) functionalized Octadec-9-enyl-octadecyl-amine (OEOA-bis-NTA, 10% molar ratio) and 1,2-Dioleoyl-sn-Glycero-3-Phosphoenolamine-N-cap-biotinyl (DOPE-cap-biotin, 10% molar ratio). DOPC, DOPS and DOPE-cap-biotin were purchased from Avanti Polar Lipids (Alabaster, USA). OEOA-bis-NTA was obtained from Jacob Piehler (Department of Biophysics, Universität Osnabrück, Germany) (figure 6.5).

For the preparation of a lipid solution[272] the dry lipids were dissolved in chloroform in glass vials, which had been rinsed carefully with chloroform beforehand. For lipid mixtures, the desired amounts of lipid solution were mixed. Afterwards, the chloroform was removed by blowing N_2 into the glass vial. By rotating the vial continuously in the N_2 stream, a thin lipid film was deposited on the walls. Further drying in a vacuum oven during 2 hours was necessary to remove residual chloroform. Large multilamellar lipid vesicles formed, when the thin lipid film was hydrated upon addition of Hepes buffer (10 mM Hepes, 150 mM NaCl, pH = 7.4) to a final concentration of 1-2 mg/ml. For homogenization the suspension was subjected to 5 cycles of freeze-thawing (in liquid N_2 and room temperature water bath) and subsequent vortexing. To obtain small unilamellar vesicles (SUVs), the liposomes were either extruded (membrane with a pore size of about 30 nm) or sonicated with a tip sonicator. If sonicated, the vesicle mixture was placed in an ice bath under nitrogen atmosphere to prevent oxidation of the lipids upon heating. Sonication was carried in pulse mode at 30 % duty cycles until the solution appeared clear (about 30 min). After sonication the solution was centrifuged (10-15 minutes at 10,000 g) to remove titanium particles sedimented from the sonicator tip. SUVs were stored at 4°C (previously flushed with N_2 and sealed) for up to 12 months.

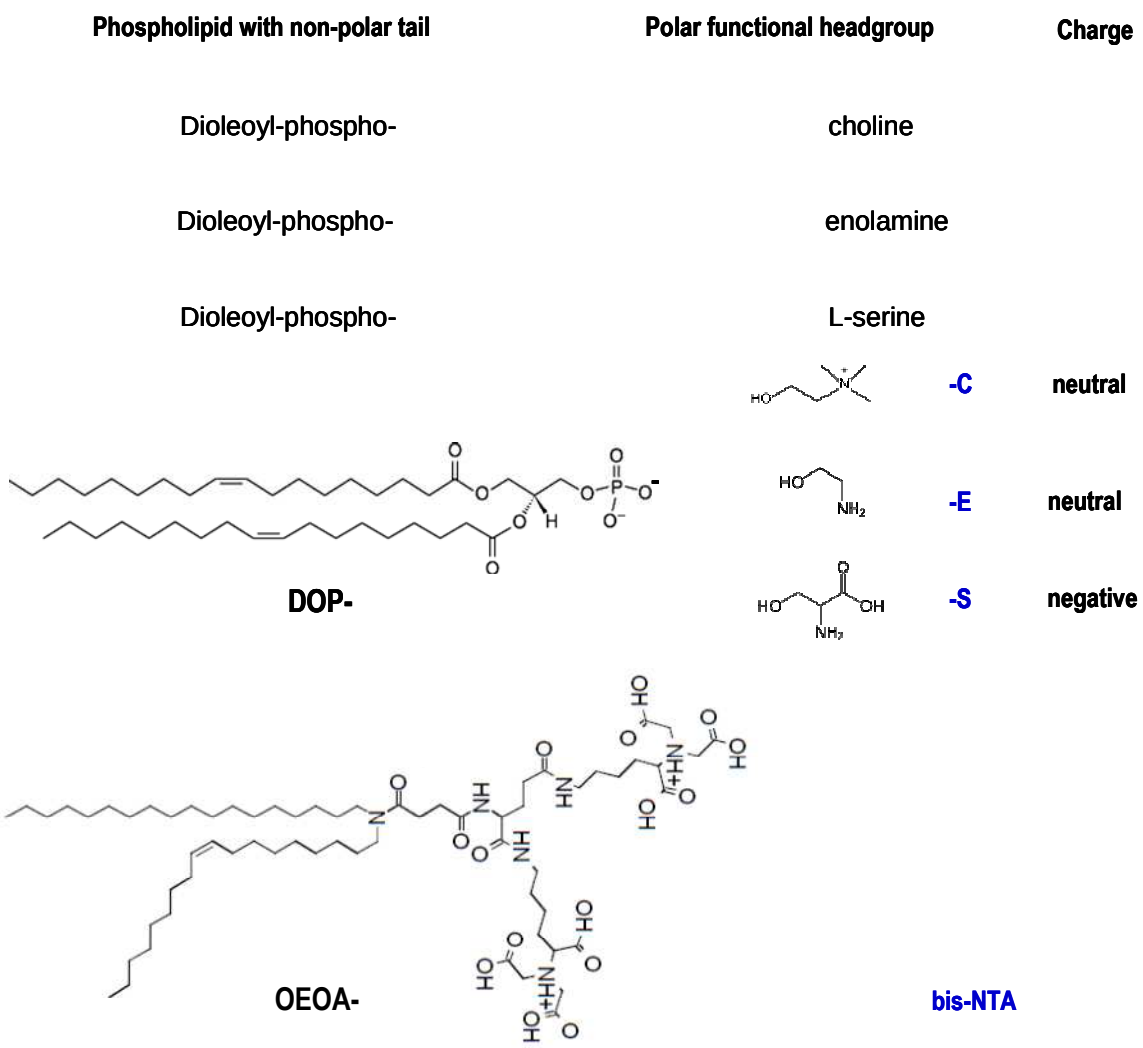

Figure 6.5: Structures of used lipids.

6.2.2 Bilayer formation on silica surfaces

Supported lipid bilayers (SLBs) were formed on either glass, silicon wafers or silica coated QCM-D sensor crystals. All substrates were cleaned in 2% SDS solution during 30 minutes followed by a 25 minute UV/ozone treatment. Due to oxidization of the surface, the substrates were highly hydrophilic (as shown by contact angle measurements). Surfaces cleaned in this way were exposed to a SUV solution in Hepes buffer at a concentration of typically 50 µg/ml under flow conditions and 100 µg/ml under static incubation conditions. The formation of a SLB passes two phases.[130] Initially, intact SUVs adsorb on the surface. At a critical surface

coverage, the vesicles start to rupture, promoting the rupture of further vesicles until complete bilayer formation. For mixtures of DOPC with DOPS or SOA-bis-NTA the presence of divalent cations facilitated for bilayer fromation.[273] A Hepes buffer containing 2mM $CaCl_2$ was used for DOPC/DOPS and DOPC/DOPE-cap-biotin mixtures; for DOPC/SOA-bis-NTA vesicles, 5 mM $NiCl_2$ were added. Doing so, the NTA headgroups were concurrently loaded with the divalent Ni^{2+}, later required for complex formation with the his-tagged protein. SLBs were formed within 15 minutes on silica coated crystals as tracked by QCM-D. The incubation time for incubation in standing solution was extended to 30 minutes followed by thorough rinsing with buffer.

6.2.3 Annexin A5-Z and CD44 fusion proteins

Annexin A5-Z. The fusion protein consisting of annexin A5 (AnxA5) and an immunoglobulin binding sequence (Z-fragment) derived from one of the homologue subunits of Protein A was generated by C. Gounou in the laboratory of Prof. Alain Brisson (Bordeaux, France).

The coupling of the Z-fragment to the annexin A5 was realized at the C-terminal end of the protein. The fusion protein had a molecular weight of M_w = 43.7 kDa. The protein was received as stock solution and stored at 4°C.

The hyaluronan receptor CD44. All CD44 constructs used in this thesis were obtained from Sunneale Banerji from the laboratory of Prof. David Jackson (Oxford, UK). The constructs were recombinant fusion proteins that were expressed in either HEK 293T cells or E.Coli (see appendix for details on protein expression and purification). The constructs were lacking the cytosolic and transmembrane part of the native protein and consequently consisted either of the full extracellular domain (ECD) of the protein, or the hyaluronan binding domain (HABD) only. Each protein was equipped with an N-terminal histidine-tag (his-tag, 6-10 repeats), which was adjacent to a double Fc domain sequence of an IgG, thus creating a CD44 dimer. The presence of a cleavage site (TEV) between both tags allowed for enzymatic cutting and dividing the dimer into two monomers. This strategy provided direct access to a monomeric and dimeric receptor from the same batch. This is of particular interest, as posttranslational modifications occur abundantly and are responsible for different degrees of glycosylation, which can account for differences in the affinity of the receptor for its ligand

HA.[80] Different subtypes of CD44 ECD and HABD were tested. The different constructs are depicted schematically in figure 6.6.

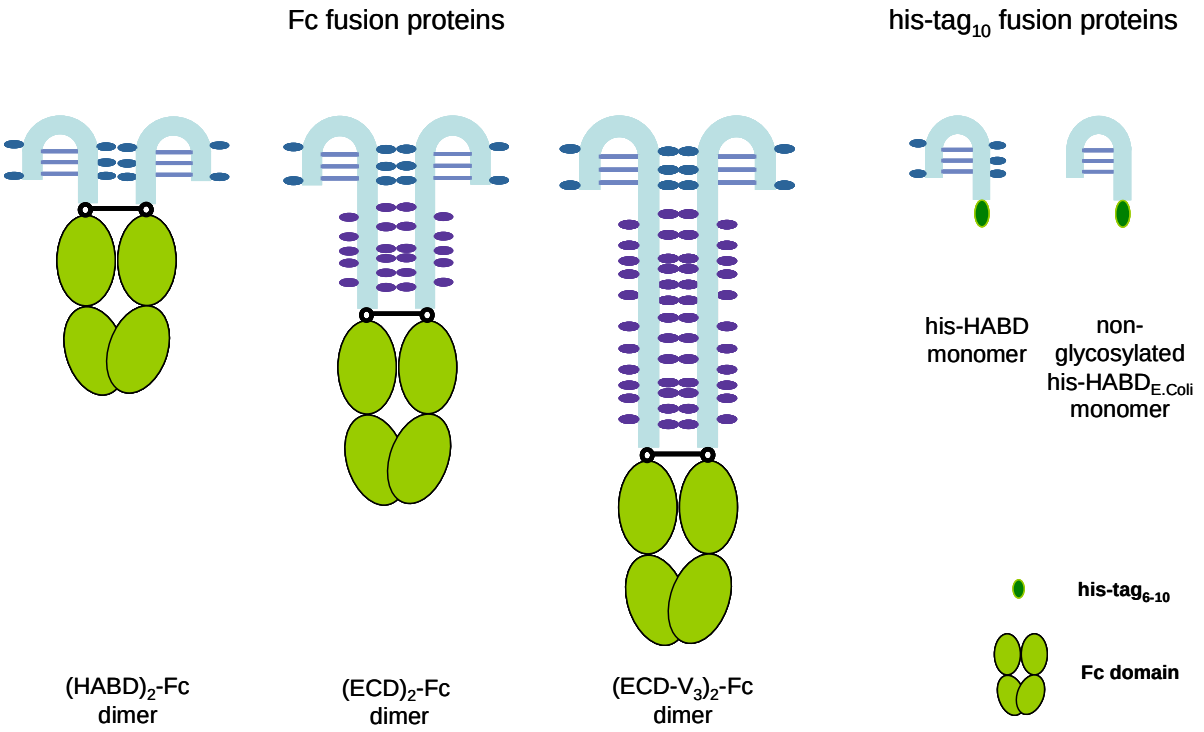

Figure 6.6: Cartoon of various CD44 constructs as used for the thesis. The prefix "h" denotes the particular amino acid sequence for the human form of CD44.

A mutant construct R41A (single mutation at R41), with an about 10 fold reduced affinity[72] was used next to the constructs shown above. The structural features of the mutant correspond to the full length ECD in form of a Fc dimer (figure 6.6).

The molecular weights of these CD44 constructs were estimated by gel electrophoresis under reducing conditions. The average size of employed proteins is listed in table 6.2.

Table 6.2: Molecular weights of CD44 constructs as determined by gel electrophoresis under reducing conditions.

CD44 type	size (kDa) monomer	average size (kDa) dimer
$(ECD)_2$-Fc (dimer)	64-97	160
$(ECD\text{-}V_3)_2$-Fc (dimer)	200	400
$(HABD)_2$-Fc (dimer)	51-64	116
his-HABD (monomer)	39	-
non-glycosylated his-HABD (monomer)	18	-

6.2.4 Hyaluronan

Hyaluronic acid of defined chain length (Select-HA/Prime-HA), and hyaluronic acid with a single biotin moiety at the reducing end (biotin-HA) were purchased from Hyalose (Oklahoma City, USA) at different chain sizes (table 6.3). Oligo HA (HA_8) was kindly provided by Prof. Anthony Day (University of Manchester, UK). HA was delivered as lyophilized powder and reconstituted in ultrapure water at a stock concentration of 1 mg/ml. For complete dissolution of HA the vials were kept under smooth shaking on a shaking plate (about 250 rpm) over night. The stock was then aliquoted, and stored at -20°C until use.

Table 6.3: Exact molecular weights for Select-HA as provided by the supplier. The molecular masses of all HA 50K/ 250K/ 1000K and b-HA 50K were obtained by Multi-Angle Laser Light Scattering-Size Exclusion Chromatography (MALLS-SEC). The molecular mass for HA 2500 was determined by agarose gel electrophoresis as an average of three gels ([a]). Data from the provider.

HA type	M_n(kDa)	M_w(kDa)	M_w / M_n
prime-HA	10-12	-	-
HA 50K	30.2	30.3	1.004
HA 250K	261	262	1.005
HA 1000K	1148	1156	1.007
HA 2500K	2400 ± 30^a	-	-
b-HA 50K	57	58	1.007
b-HA 1000K	1043	1083	1.039

6.3 Surface analysis techniques

6.3.1 Scanning electron microscopy (SEM)

Scanning electron microscopy (SEM) belongs to the most important and common surface imaging techniques with nanoscale resolution. The wavelength limit here is given by the wavelength of electrons and thus, a resolution much higher than for light microscopy techniques is attainable. Modern SEM systems can resolve objects below 1 nm.

The incident electron beam generates a number of signals when hitting the sample: back scattered electrons (BSE) and secondary electrons (SE) are most commonly detected in order to collect information about the sample. BSE with energies of typically more than 50eV are scattered at the atom nucleus, thus, directly providing information about the chemical composition of the material. Elements with high electron density appear bright, those with low electron density rather dark. The lower energy SE (≤ 50eV) are more sensitive to the topography of the sample.

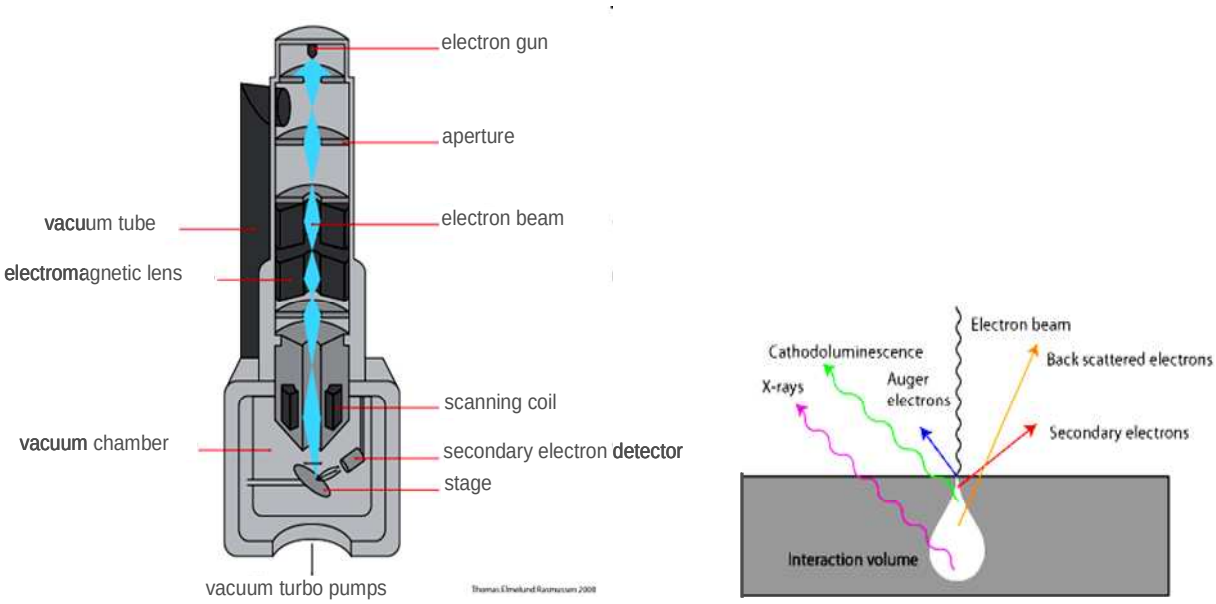

Figure 6.7: Left: schematic drawing of a SEM electron path. Right: Interaction of the electrons with the sample.

In this work a field emission SEM (LEO 1530) was used primarily for the imaging of gold-nanostructured surfaces. The high electron density of gold provides a high contrast between the clusters and the underlying substrate (silica). The system was typically operated at

accelerating voltages of 1 to 5 kV. An In-lense SE detector was used for image acquisition. Image acquisition can be perturbed due to charging effects caused by the electron beam if the sample is not capable to lead off irradiating electrons. As the investigated surfaces were not conductive, a thin (a few nm) layer of carbon had to be evaporated on top of the samples before imaging.

Image analysis. SEM micrographs of gold nanostructured surfaces were analyzed with ImageJ (Research Service Branch NIMH, image analysis software) using a special ImageJ Plugin for particle analysis. The Plugin was implemented by Dr. Phillipe Girard (EMBL, Heidelberg). The order parameter of a hexagonal pattern and the average spacing of the nanoparticle array were calculated. The underlying theoretical approach to this calculation is based on the radial distribution function (RDA).[274] The two-dimensional melting of a crystal theoretically resembles the transition of a nanoparticle pattern from perfect hexagonal order to disorder,[275, 276] wherefrom an orientational order parameter ψ can be derived. With respect to the six nearest neighbors of a center particle a six-fold bond-orientational order parameter ψ_6 is obtained, which can describe the global order parameter of a hexagonal latice.[277, 278]

$\psi = 1$	**perfect order**
$0 < \psi < 1$	**degree of disorder**
$\psi = 0$	**total disorder**

A detailed description of the theoretical approach can be found in [222] and references therein.

6.3.2 Quartz-crystal microbalance with dissipation monioring (QCM-D)

Surfaces. QCM-D sensors with a resonance frequency of 4.95 MHz, coated with either gold or silica, were purchased from Q-Sense AB (Västra Frölunda, Sweden). In some cases, an additional silica layer of 100 nm thickness was evaporated on the gold-coated sensors (G. Albert PVD Beschichtungen, Silz, Germany). Differences between this additional silica layer

and the silica coating provided by Q-Sense with respect to protein adsorption or SLB formation were not observed.

Gold-coated sensors were cleaned by immersion into a mixture of NH_3:H_2O_2:H_2O in a volume ratio of 1:1:4 at a temperature of 70°C for at least 5 min, rinsed thoroughly with ultrapure water (Barnstead, model D1193, Dubuque, USA) and blow-dried in N_2. Silica-coated sensors were immersed in an aqueous solution of 3% sodium dodecyl sulfate for 30 min, rinsed abundantly with ultrapure water, and blow-dried in N_2. Prior to use, the crystals were exposed to oxygen plasma (200 W, 0.35 mbar) (TePla 100-E, PVA TePla AG, Feldkirchen, Germany) or to UV/ozone for 25 min.

Method. QCM-D is an electro-mechanical method that allows adsorption processes on a solid surface to be followed in real-time.[121] The underlying principle is the piezoelectricity of quartz. A quartz crystal is sandwiched between two electrodes and excited into a shear movement by applying an oscillatory electric field. The cut off of the electric field results in a dampened oscillation curve (figure 6.8). Fitting the decay of the damping curve provides information on both, the resonance frequency, f, of the crystal and the degree of damping - the dissipative losses D. The changes in Δf and ΔD are the parameters that are acquired during the measurement. As shown by Sauerbrey[116] in the 1950s, the mass uptake, Δm, is directly proportional to the frequency change, Δf_n, of the oscillating sensor crystal, provided the adsorbed film is sufficiently thin, rigid and homogenous:

$$\Delta m = -C\frac{\Delta f_n}{n}, \tag{22}$$

where C is the mass sensitivity constant (for a 4.95 MHz crystal C = 18.06 ng/cm^{2}Hz), and n the overtone number. In solution, the QCM-D is also sensitive to water that is coupled to the adsorbed molecular film. The mass determined by equation (22) therefore typically exceeds the biomolecular mass of the film.[139]

The change in dissipation, ΔD, is related to frictional (viscous) losses in the adlayer[279] (figure 6.8). D is related to the Q factor, and describes the ratio of stored and dissipated energy in the system (per oscillation cycle).

$$D = \frac{1}{Q} = \frac{E_{dissipated}}{2\pi E_{stored}} \tag{23}$$

A soft adlayer will not fully couple with the induced shear movement of the crystal, leading to energy dissipation (*D* increases).

For operation in liquid, the bulk solution above the sensor surface causes a response reflecting the properties of the liquid. The relationship between the QCM-D response and the properties of the liquid can be written as:

$$\Delta f = \frac{1}{\sqrt{\pi \upsilon_q \rho_q}} \sqrt{n f_0^3 \eta_l \rho_l} \tag{24}$$

$$\Delta D = \frac{1}{\sqrt{\pi \upsilon_q \rho_q}} \sqrt{\frac{f_0}{n} \eta_l \rho_l} \tag{25}$$

With f_0 being the fundamental frequency, n the overtone number, and η_l and ρ_l the liquid`s viscosity and density, respectively and υ_q the speed of sound in quartz.

When proteins are adsorbed, the interaction of the crystal with the liquid changes and, again, gives rise to an increase in dissipation, which depends strongly on trapped liquid within the protein layer.[123, 136, 139, 280]

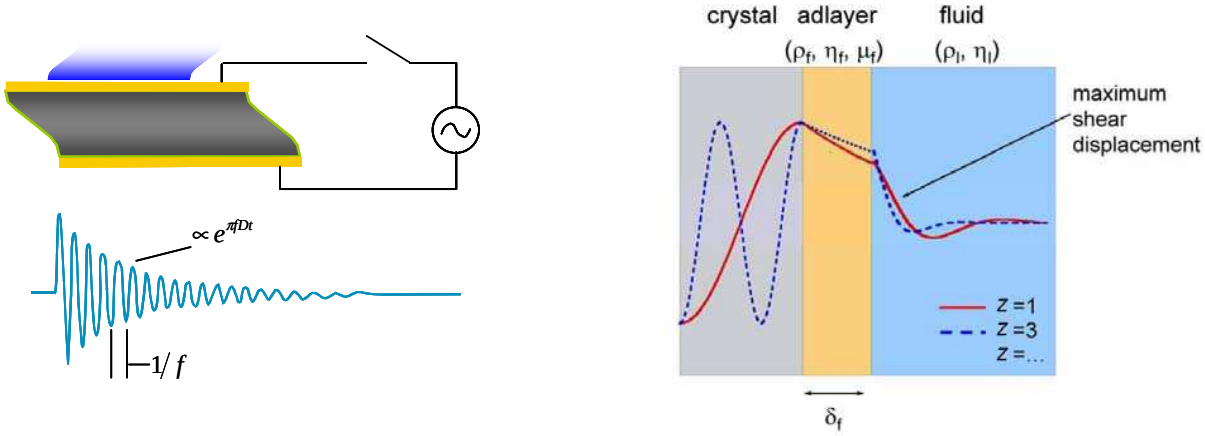

Figure 6.8: working principle of the QCM-D. Left: Oscillating, loaded sensor crystal with characteristic frequency and decay curve. Right: The viscoelastic model. The shear wave excited by the quartz crystal propagates and is dissipated depending on the properties of the adsorbed film (viscosity η_f, shear modulus μ_f and density ρ_f) immersed in a Newtonian fluid like water.

Quantitative data analysis. For a sufficiently rigid biomolecular film at high coverage, the frequency shift typically corresponds rather well to the biomolecular mass together with the mass of the solvent that is contained inside the film. Hence, it appears reasonable to represent the adsorbed film in terms of acoustic thickness.[138]

$$d = \frac{\Delta m}{\rho_{H_2O}} = -\frac{C}{\rho_{H_2O}} \frac{\Delta f_n}{n}. \quad (26)$$

The acoustic thickness neglects the density differences between the biomolecules ($\rho \approx 1.4$ g/cm^3 for proteins[132, 281]) and water ($\rho_{H_2O} = 1.0$ g/cm^3). With typically 50% or more water being present in the film,[139] d may thus overestimate the geometrical thickness by up to 20%. Within this work I chose to speak in terms of measured shifts in frequency and dissipation (ΔD, Δf), as well as acoustic thickness d.

The change in dissipation ΔD provides further qualitative insight. When ΔD is high and the ratio $\Delta D / \Delta f$ exceeds 0.2×10^{-6} Hz^{-1} the mass estimation according to Sauerbrey cannot be applied. This rule of thumb could be established once quantitative analysis was enabled by the development of models to derive the viscoelastic properties of the bulk and of adsorbed films.[137, 282] Viscoelastic models have been developed[141, 283] (figure 6.8), which relate properties like thickness, density, viscosity and shear modulus to the measured parameters Δf and ΔD.

Experimental set-up. QCM-D measurements were conducted with a Q-Sense E4 system. The system was operated in flow mode, with a continuous liquid flow of typically 20 µl/min being delivered by a peristaltic pump. In order to switch between sample liquids, the flow was interrupted for a few seconds without disturbing the QCM-D signal. The working temperature was 23.0° C. Resonance frequency and dissipation were measured at 6 harmonics simultaneously (n = 3, 5 ... 13), corresponding to frequencies of $f_n \approx 15, 25 \ldots 65$ MHz. For simplicity, only changes in dissipation and normalized frequency, $\Delta f = \Delta f_n / n$, of the 7th overtone ($n = 7$, i.e., ~35 MHz) are presented, if not otherwise mentioned. The experimental data was analyzed using the software QTools (Q.Sense).

<u>*Sample preparation*</u> The samples were diluted to a final concentration of typically 50 µg/ml for SUVs and, 10 µg/ml for proteins and HA. They were added after a stable baseline was

acquired in buffer. The incubation was performed at constant flow with a flow rate of about 20 µl/min using a peristaltic or a syringe pump. After equilibration of Δf and ΔD signals the chamber was rinsed during at least 10 minutes to remove residual and loosely bound material. The same conditions were maintained for gold, silica and nanostructured surfaces. In few cases higher protein concentrations were used for control measurements.

6.3.3 Ellipsometry

General method. Ellipsometry is an optical, non-destructive technique, which allows for the characterization of thin films deposited on a variety of surfaces. Upon reflection at a surface the polarized incident light beam undergoes a change in polarization state and becomes elliptically polarized. The ellipsometer measures the change in polarization in terms of two parameters Δ and Ψ. From the obtained values, several parameters can be derived, e.g., the film thickness, the refractive index, and adsorbed mass by fitting an adequate model to the measured values of Δ and Ψ.[144] The applied model relates both parameters to the optical properties of a multilayer system, which consists of the substrate, the adsorbed layer or layers and the ambient (figure 6.9).

Quantitative data analysis. The relationship between Δ and Ψ can be expressed in form of the ratio of the Fresnel coefficients:

$$\frac{r_p}{r_s} = \tan(\Psi)\, e^{(i\Delta)} = \rho \qquad (27)$$

where r_p and r_s are the complex Fresnel reflection coefficients for the s- (perpendicular to the plane of incidence) and p-(parallel to the plane of incidence) polarized waves, respectively. These coefficients describe the reflection of elliptically polarized light upon encounter with planar, multilayered materials[144] (figure 6.9). Their ratio depends on the wavelength (λ), the angle of incidence (Θ_0), the refractive indices of the surface, the adsorbed film and the ambient, and the film thickness of the involved layer(s).

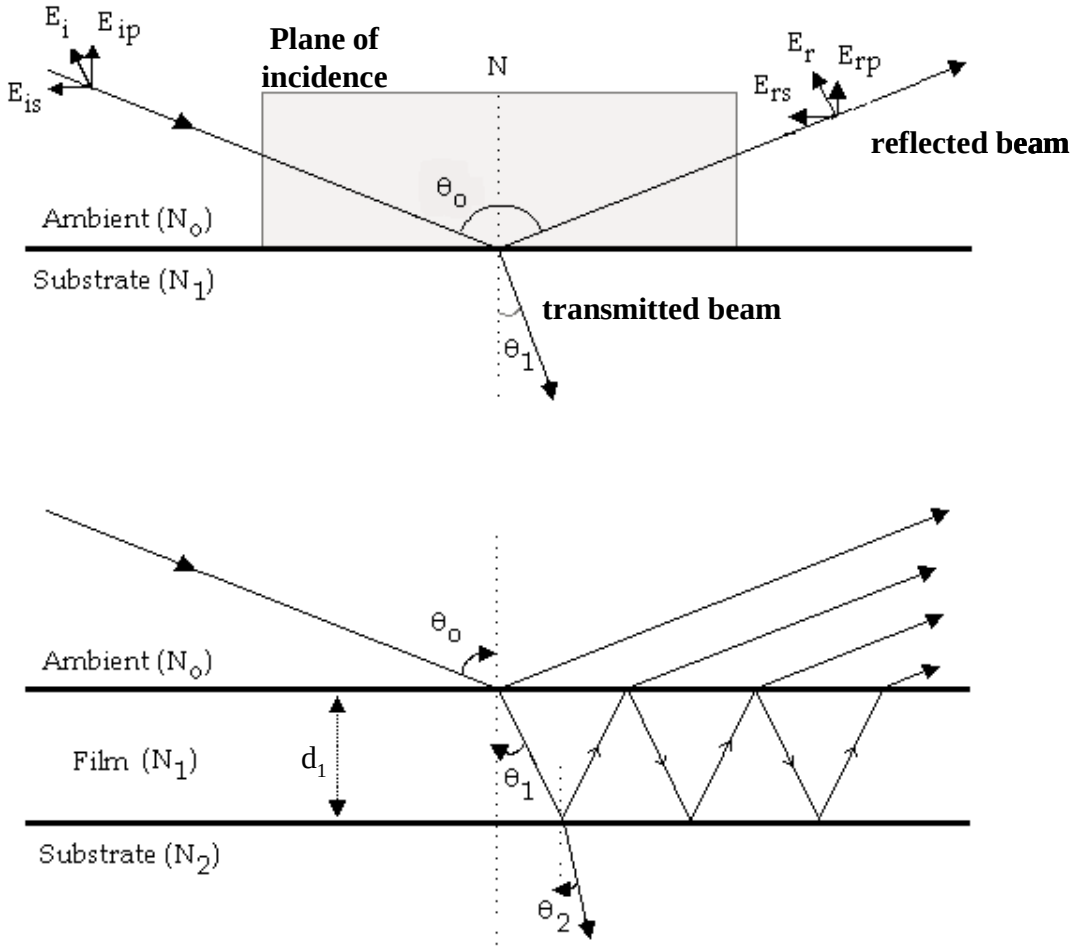

Figure 6.9: Interaction of polarized light with a bare surface (top) and a film covered surface (bottom). N_0, N_1 and N_2 are the complex refractive indices of the ambient, the adsorbed film and the substrate, respectively. Θ_0 denotes the angle of incidence, Θ_1 the angle of transmission and Θ_2 the angle of adsorption and d_1 the thickness of the film. Sketch adapted from ref.[284].

r_p / r_s can be expressed as a function ρ of the mentioned parameters and be written as:

$$\rho = f\left(N_0, N_1, N_2, \lambda, \Theta_0\right) \tag{28}$$

with N_0, N_1 and N_2 being the complex refractive indices of the ambient, the adsorbed film and the substrate, λ the wavelength of the incident light and Θ_0 the angle of incidence. The complex refractive index N consists of a real n and a complex component k, the optical constants of the material:

$$N(\lambda) = n(\lambda) + ik(\lambda) \tag{29}$$

where n is the refractive index and k the damping constant. The optical constants describe how light propagates through the given material. For transparent materials, k is close to zero and can be neglected.[284]

To extract information about the refractive index or the film thickness from the determined parametres Δ and Ψ, a model-dependent analysis has to be performed. From figure 6.9 and equations (27) and (28) it becomes clear that both ellipsometric parameters, can be related to the properties of the film (N_1, d_1), if the parameters N_0, N_2, λ and Θ_0 are known. Thus, the refractive index n and the film thickness d can be fitted to the experimentally obtained parameters.

Quantification of adsorbed biomolecular material The simplest way to calculate adsorbed masses from n and d was developed by deFeijter.[285]

$$\Delta m_{optic} = \frac{d \cdot (n_{bml} - n(\lambda)_{solvent})}{dn/dc} \tag{30}$$

with d being the film thickness, n_{bml} the refractive indices of the biomolecular layer and $n(\lambda)_{solvent}$ the refractive index of the solvent with λ = 632.5 nm. Here only the real component represents the refractive index, as for transparent materials (like biomolecular films) k takes values close to zero.[284] Values for the refractive index increment dn/dc have been experimentally determined for a number of adsorbents and can be found in the literature. Within this work dn/dc values of 0.169, 0.18 and 0.15 were employed for SLBs,[138, 286] protein layers[285, 287] and HA films,[175] respectively. For protein layers, and within an error of less than 5%, the refractive index increment is constant over the range of concentrations typically found in this study (up to 600 mg/ml,).[139]

Moreover, the exact determination of d and n simultaneously, becomes difficult in practice for very thin films (a few nm) due to limitations by the signal-to-noise-ratio. The adsorbed mass, however, can typically be derived accurately, as the product of n and d is well determined and proportional to the adsorbed mass.[112, 281]

In the context of this thesis, the adsorbed masses were determined by numerical fitting of the ellipsometric parameters Δ and Ψ over the full range of accessible wavelengths.

Experimental set up. Measurements were conducted with a spectroscopic rotating compensator ellipsometer (M22000V, Woollam, NE, USA). The system was operated at an incident angle of 70° and at wavelengths in the range of λ = 370 to 1000 nm with a time resolution of about 5 s. Two different liquid chamber set-ups were used, which will be described separately in the following.

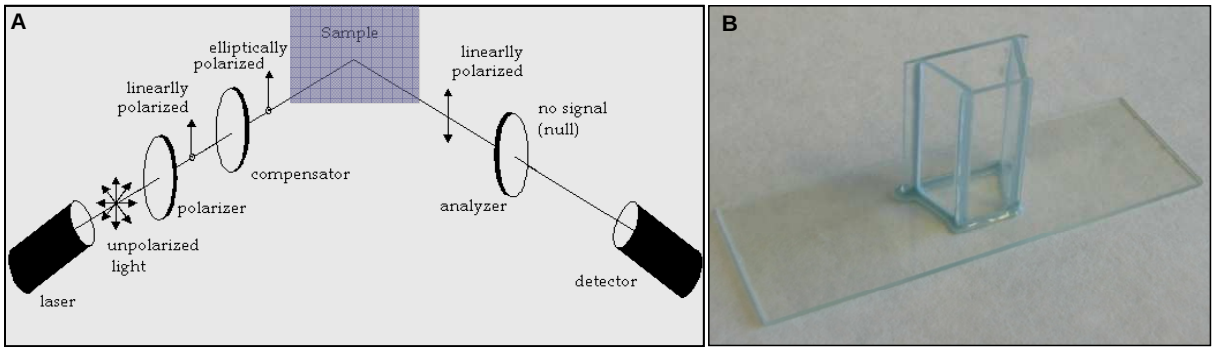

Figure 6.10: Sketch of a typical ellipsometry set-up. Adapted from ref.[284] B: custom-designed open glass chamber.

Open chamber

Measurements were performed in a homebuilt open glass cuvette (figure 6.10B) of about 2 ml volume under continuous stirring with a magnetic stirrer (≈ 200 rpm)[288] to ensure homogenisation of the cuvette content within a few seconds. A volume of about 1 ml of buffer was filled into the chamber. The material to be adsorbed was added directly to final concentrations as used for QCM-D experiments. After equilibrium was reached the cuvette content was diluted by repeated addition of at least a two fold excess of buffer and removal of excess liquid, until the concentration of soluble sample was below 10 ng/ml.

Surfaces Silicon wafers with a native oxide layer (≈ 2 nm) were cleaned in the same way as silica coated QCM-D sensors. Prior to use, they were submitted to a 25 minutes UV/ozone treatment. The glass chamber was cleaned with SDS followed by thorough rinsing with ultrapure water and dried with N_2. Before use, the chamber was passivated with a 10 mg/ml BSA solution for about 15 minutes, rinsed again with ultrapure water and dried with N_2. Wafers were fixed to the ellipsometer holder by a magnetic clip.

Calibration of the cuvette In order to verify that only negligible window effects (Δ-offset) were provoked by the cuvette, reference measurements were performed before each

experiment. To this end, first a reference wafer was measured in air, and secondly, inside the cuvette in air. The cells were used, if they induced a Δ-offset of less than 0.5°.

Fitting routines. The deposited films were analyzed in terms of adsorbed mass in order to quantify absolute amounts present on the surfaces. The experimental data was fitted using the software CompleteEASE (Wollam, NE, USA). Typically applied models will be described in the following.

Substrates The cleaned silicon wafers were characterized in air and in buffer prior to each measurement based on a three-layer model consisting of solvent, native silicon oxide and silicon. For bulk silicon tabulated optical constants (implemented in CompleteEASE software, Woollam) were used. The native oxide layer was treated as a transparent Cauchy layer. The Cauchy model is typically applied for fitting of optically transparent, dielectric films[145]:

$$n(\lambda) = A + \frac{B}{\lambda^2} + \frac{C}{\lambda^4} + \ldots \qquad k(\lambda) = 0 \tag{31}$$

A (dimensionless), B (μm^2), and C (μm^4) are the so-called Cauchy parameters. k is zero assuming a transparent material. Practically, the contribution from C is very small, and it was neglected for the evaluation of the data here.

To obtain the optical constants (A, B) and the thickness ($d(SiO_2)$) of the silica layer and the angle offset, a multiple sample analysis (msa) was performed. The datasets in air and buffer (before the *in-situ* measurement) were combined and analyzed simultanously to enable the accurate fitting of two pairs of determined sets of parameters (Δ and Ψ from both datasets for a range of λ) and derive four free parameters (A, B, $d(SiO_2)$, angle offset). The resulting values for the silica layer exhibited a thickness of typically 1.8 ± 0.1 nm and optical constants of A_{oxide} = 1.505 and B_{oxide} = 0.0186 μm^2. Mean squared errors (MSE) around 1 were obtained, indicating a good fit. The aqueous bulk solution was also treated as a Cauchy medium. The refractive index ($n_{solvent}$ = 1.325 + 0.00322 $\mu m^2/\lambda^2$) was calculated from tables in the literature.[289, 290]

Biomolecular films All adsorbed layers were treated as a single Cauchy medium. A four-layer model (solvent, biomolecular film, native silicon oxide, silicon) was used to model the biomolecular film.[145] It seems well suited for protein films, as such films are hydrated by 50 % and more,[139] as well as for hyaluronan films with a water content of about 99 %.

The previously derived optical constants of the substrate were implemented. To obtain the thickness *d* and the refractive index *n* of the biomolecular layer, B_{bml} was fixed to the buffer value (0.00322), while d_{bml} and Abml were fitted. The MSE was usually found to be smaller than 1.5.

The adsorbed mass of each layer was calculated according to eq. (30). Typically, multiple biomolecular layers were deposited in the course of the experiment. *d* and *n* were determined for each step, but all layers were treated as 1 Cauchy layer. To obtain the properties of the individual layers, the final value of the respective former layer was subtracted (taking into consideration eventual differences in the employed refractive index increment).[288]

Experimental set-up for combined ellipsometry/QCM-D

Sensor crystals The nominal thickness of the titania and silica layer was 100 nm for both materials. The QCM-D sensors for combined ellipsometry/QCM-D measurements differed from usual sensors in that the titania layer was thicker. For fitting, the thick titanium layer could be considered as substrate bulk material, and was modeled as a single layer. Cleaning and pre-treatment of the crystals was the same as for QCM-D measurements.

Flow chamber. A combined flow chamber for simultaneous measurements by ellipsometry and QCM-D was provided by Q-Sense AB. The chamber was connected with the E1 module of the QCM-D and operated with standard QCM-D software (QSoft). For combined measurements the module was mounted on the holder stage of the ellipsometer (figure 6.11). As a consequence of the chamber architecture, the ellipsometer had to be set to an angle of 65° (instead of 70°). The chamber was supplied with liquid by one inlet tubing. Three outlet tubings attachend to a peristaltic pump were connected to the chamber to ensure an effective rinsing.

Sample preparation For adsorption steps the material was injected (≈ 400 µl of the sample) quickly followed by incubation until equilibration of the adsorption curves. Incubation in still solution was chosen to ensure homogenous adsorption rates across the surface. The final concentration of all samples was doubled with respect to standard QCM-D measurements. During rinsing of the chamber (at least 10 minutes), the pump was operated under constant flow (≈ 300 ml/min).

Fitting routines

Substrates For the specialized silica-coated QCM-D sensor crystals three layers determine the optical properties: titanium as bottom layer, a titanium oxide (titania) interlayer and silica

as a topmost layer. The substrate was thus characterized with a four-layer model (solvent, silicon oxide, titanium oxide, titanium). The solvent was treated as a Cauchy medium as described above. The titanium layer was treated as bulk. A B-spline derived model with titanium as starting material (tabulated values for polycrystalline titanium from CompleteEASE) was used to fit the optical constants *n* and *k*. The silica and titania layers were treated as Cauchy-layers, with optical constants as tabulated below (table 6.4).

Table 6.4: Refractive indeces of silica and titania for QCM-D sensor crystalls for ellipsometric application.

Material	optical properties		
	A	B	C
silica	1.461	0.00451	0.00007
titania	2.159	0.02770	0.00467

The optical constants $n(\lambda)$ and $k(\lambda)$ of titanium and the thickness of both oxide layers were determined by multiple sample analysis (msa) of the datasets obtained in air and in buffer (obtained before the in-situ measurement). Typically, values for the both, the titania and the silica layer of about 1 nm and 76 nm, respectively, were obtained with an MSE of about 3, indicating a fit of good quality.

Biomolecular films For modeling of the adsorbed biomolecular films, the previously determined optical constants and oxide layer thicknesses were loaded as substrate into a model with a sequence of Cauchy layers[145] and treated further as described for the open chamber set-up. Good fits with a MSE of around 1 - 2 were obtained.

Both datasets (from QCM-D and ellipsometry) were first analyzed separately with the corresponding equipment software (QTools for QCM-D and CompleteEase for the ellipsometer). For further evaluation and correlation of both datasets, the analyzed data was transferred to Origin software (Origin 8).

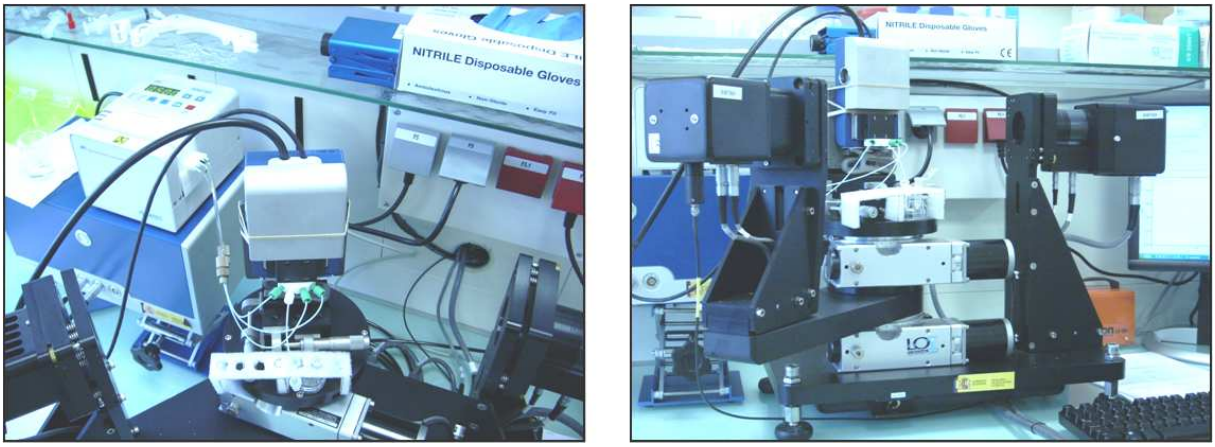

Figure 6.11: Images of the combined QCM-D/ellipsometry set-up.

6.3.4 Reflection Interference Contrast Microscopy (RICM)

Method. The interference of two beams, one reflected at the top surface of the substrate with intensity I_1 and the second reflected from bottom surface of a colloidal probe (I_2) (figure 6.12) gives rise to a characteristic interference pattern (figure 6.13B). For spherical objects, the interference pattern consists of concentrical rings of intensity maxima and minima (Newtonian Rings), from which the distance of the probe from the surface can be determined. The intensity of the resulting interference beam is given by:

$$I\left(h(x,y),\lambda\right) = I_1 - I_2 + 2\sqrt{I_1 I_2}\cos\left(\frac{4\pi n h(x,y)}{\lambda} + \delta\right) \qquad (32)$$

with n being the refractive index of the medium, δ (neglected in the simple model) the phase shift upon reflection from the object, λ the wavelength and h the distance separating the probe from the surface at the lateral position (x,y).

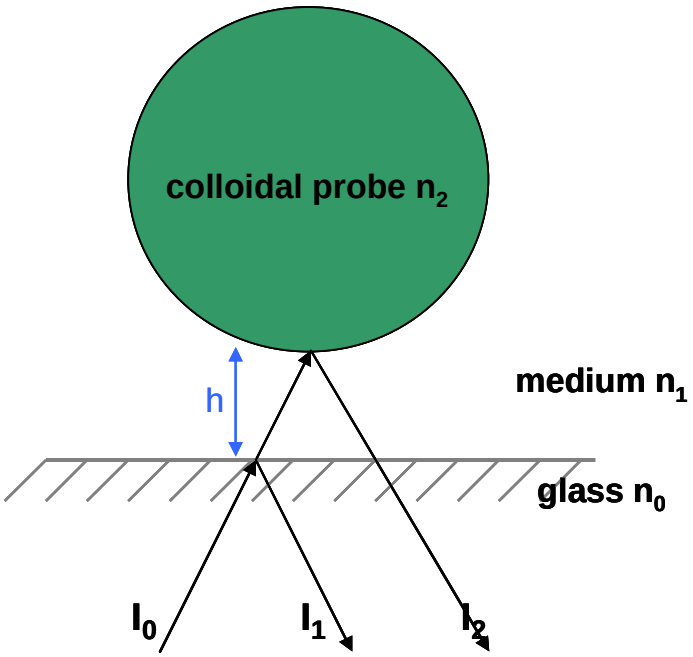

Figure 6.12: Principle of reflection interference. A beam with intensity I_0 is reflected first on the top surface of the substrate and a second time at the bottom surface of the object. Both reflected beams (with intensities I_1 and I_2) interfere and give rise to a characteristic interference pattern.

Reflection contrast was implemented by a so-called antiflex illumination, which reduces the undesired contributions from stray light.[291] The antiflex method implements a polarizer, a quarter-wave-plate (λ/4 plate) and an analyzer into the standard set-up. The polarizer generates linearly polarized light, which becomes circularly polarized after passing the quarter-wave- plate. Upon reflections within the specimen the polarization direction of the light is inverted. After passing the quarter-wave-plate a second time, the reflected beam changes its polarization back to linear, but with a direction perpendicular to the incident beam. The analyzer ensures, that only light with the correct direction (perpendicular to the incident beam) can pass and be detected, while all scattered beams are blocked (figure 6.13A).

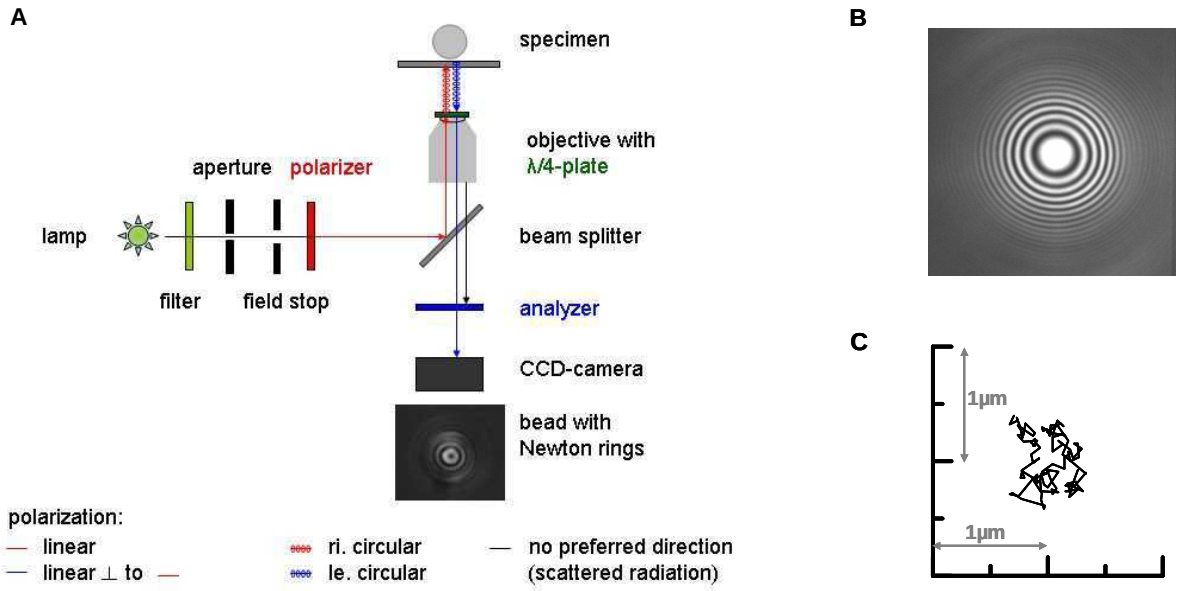

Figure 6.13: A: a typical RICM set-up. Sketch from ref. [292]. B: Newtonian rings generated by RICM imaging of a colloidal probe. C: Lateral Brownian motion of a colloidal probe hovering above a HA film.

Dual/ Triple-wavelength RICM. A drawback of conventional RICM is that for each wavelength a number of heights are in agreement with the experimentally obtained intensity. This is, because the intensity profile is a periodic function, meaning that with each period another height corresponds to the given intensity. To overcome this problem, Schilling et al. introduced dual wavelength RICM (DW-RICM). The authors compared the periodicity of two interferographs, which had been taken simultaneously at different wavelengths.[293] A unique solution for the distance of the object from the surface can be found, for a given pair of intensities, i.e. where the periodicities of both observed wavelengths overlap at a given intensity (figure 6.14). The choice of a pair of wavelengths not only allows for the unambiguous determination of height, but also extends the range within which the height can be determined.[293, 294] The range is determined by the common periodicity of the chosen wavelengths.[293] The use of a third wavelength has been reported by Richter et al.[12] where the upper limit of the unambiguity was pushed beyond 800 nm as proposed by.[293] In principle, any combination of wavelengths can be used.[294]

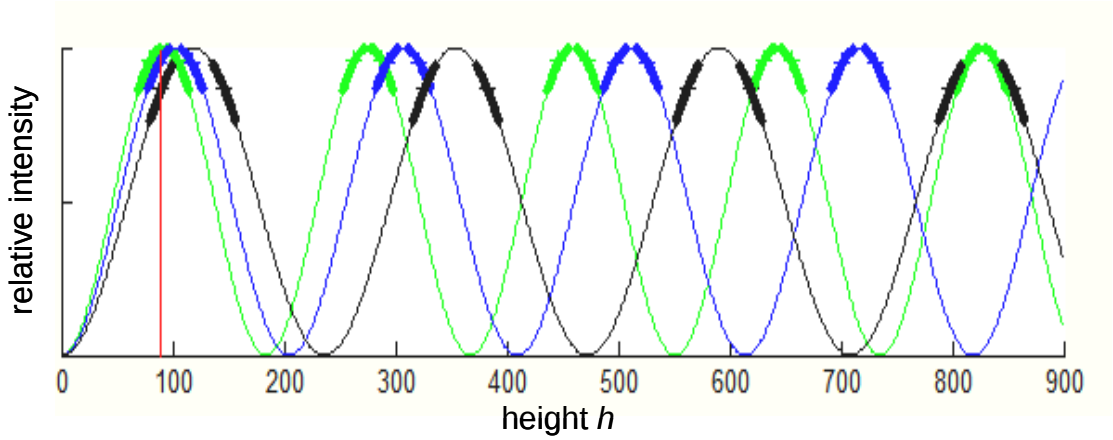

Figure 6.14: The relative Intensities of three wavelengths as obtained from 3W-RICM. At overlap (red line) a unique solution for the height of the probe above the surface can be determined.

Reconstruction of film heights. From equation 32 it turns out that the intensity depends on the distance of the probe from the surface (height *h*) and the wavelength. There are several methods, by which the height can be reconstructed from the information behind the intensity profile, which have recently been reviewed by Limozin and Sengupta.[294]

For colloidal probes the interference pattern consists of concentric circular fringes. The radius r_l from the center (of the radially averaged interferometric intensity profile) to the first extremum (maximum or minimum) consequently changes with the intensity in center (figure 6.15). The height can then be determined according to[293]:

$$h(r_l) = \frac{\lambda l}{2n} - R + \sqrt{R^2 - r_l^2} \tag{33}$$

for maxima, and:

$$h(r) = R + \sqrt{R^2 - r_l^2}\,, \tag{34}$$

for minima, by considering the radius of the bead *R* and the radius r_l of the *l*-th extremum. In real experiment the position of two or three fringes can be determined in order to gain higher accuracy for the value of *h*.

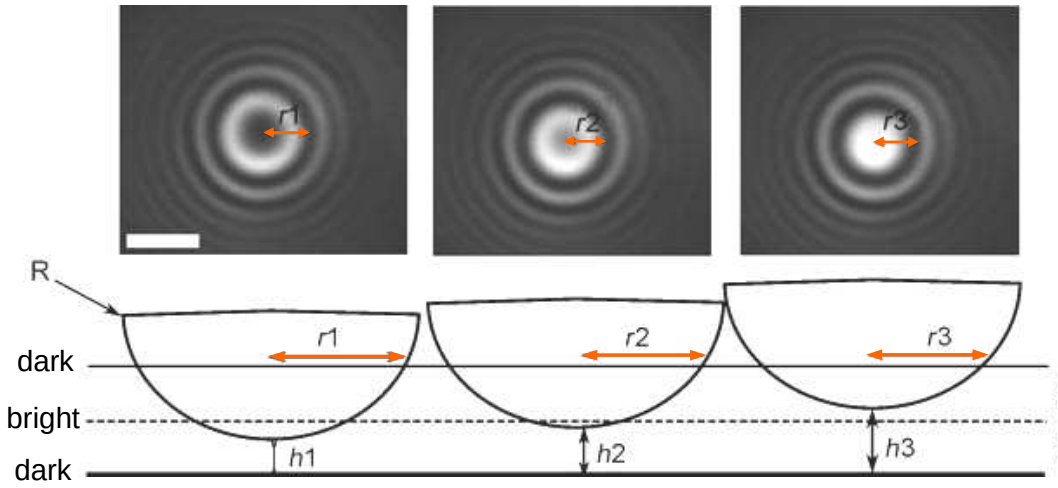

Figure 6.15: Top: RICM images showing fringe pattern of a colloidal bead at different heights from the surface (*h1, h2, h3*). The intensity in the center changes as a function of the height, and the radius of the first fringe r_1 changes accordingly (scale bar: 2µm). Bottom: schematic of the intensity profile corresponding to different bead heights. The solid lines represent intensity minima, the dashed line the maxima. Figure adapted from ref.[294].

Experimental set-up. A 3-wavelength RICM setup as described by[12] was implemented. The setup was based on an inverted microscope (Zeiss Observer Z1) with antiflex technique consisting of a filter cube with crossed polarizers and an antiflex objective (EC Plan Neofluar Antiflex, 63×/1.25, Zeiss). A Xenon lamp (XBO 75, Zeiss) was used as light source. Reflected light was split by a custom built beam splitter unit with integrated band pass filters (with 10 nm width). Two cameras (Orca-ER Hamamatsu Photonics, Massy, France) took images at three different wavelengths simultaneously (λ = 490, 546, 630 nm) using the software SimplePCI (Hamamatsu). Interferographs at 490 nm and 546 nm were recorded in one camera and at 630 nm in the second.

Sample preparation. A glass slide was glued with two component dental glue (Picodent Twinsil, Wipperfürth, Germany) to a custom-made Teflon holder with an opening (diameter 0.5 cm) placed in the center. The assembly provided a cylinder shaped reaction chamber with a volume of about 50 µl (figure 6.16). The model systems were prepared on the glass cover slip with incubation steps as established in QCM-D. The samples were directly injected into a volume of about 50µl at the desired concentration. Incubation took place in still solution with two fold increased concentrations and incubation times with respect to QCM-D measurements. Excess material was removed by repeatedly adding a threefold amount of

buffer, pipette assisted homogenization and withdrawal of excess liquid. The surface was maintained wet at any time.

Polystyrene beads (Polyscience, Eppelheim Germany) with an average diameter of 25 µm were used as colloidal probes. The beads were washed 5 times with ultrapure water before further use. Additionally, some beads were functionalized with a polyethylene-glycol layer (PEG-layer) to prevent interaction with the HA film. For PEGylation of the beads a triblock-copolymers with a number averaged molecular weight, M_n = 8.4 kDa and a fraction of 80 weight-% PEG* was used (poly(ethylene glycol)-block-(polypropylene glycol)-block-(polyethylene glycol), Pluronic F68, Sigma). The method by Kim[296], based on solvent-assisted entrapment of the triblock-copolymer on the particle surface, was applied with adjusted parameters with respect to the Pluronic used and the bead size. The detailed protocol used here can be found in the appendix.

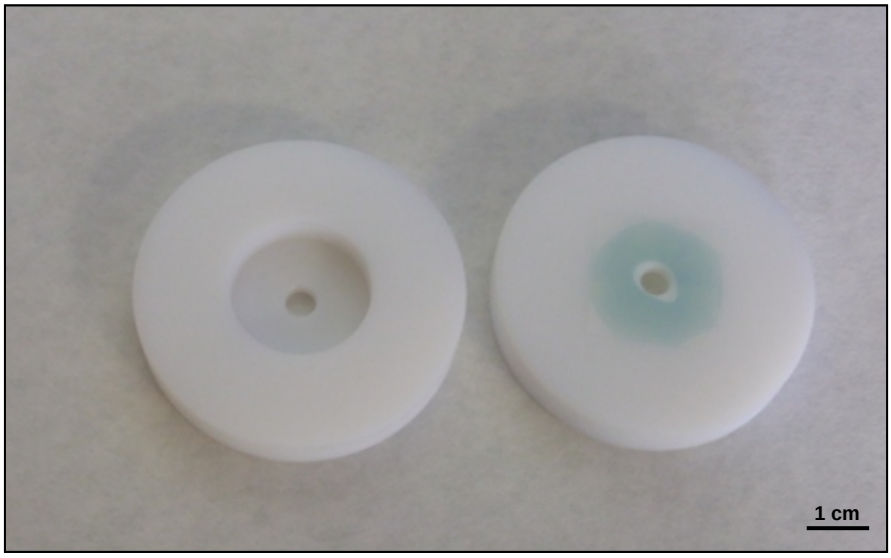

Figure 6.16: Teflon holder for RICM experiments. Left: top view. Right: bottom view. The glass coverslip is fixed up-side down with two-component dental glue to the bottom of the holder.

Data analysis. The interferographs were analyzed with a custom developed algorithm implemented in MATLAB software. The layer thickness of the adsorbed HA films was determined following a simple method[150] (parallel plate approximation with incident light parallel to the surface normal), from the radial position of the extremum in the interferometric

* From the M_n of the triblock-copolymer the average size of each PEG block results in 3.4 kDa, or N = 76 monomer units. This corresponds to a radius of gyration of 2.2 nm,[295] and a contour length of ~30 nm.

intensity profile (see section: height reconstruction) The diameter of the observed beads was calculated from bright field images taken prior to the RICM images for each bead. Based on the estimated accuracy in the determination of the bead diameter (±0.5 µm) and the focus position (±0.2 µm), and the noise in the intensity profile, we estimate the setup-specific variations in the apparent height to be smaller than ± 6 nm. The heights determined from all three wavelengths (λ = 490, 546 and 630 nm) were usually found to agree within an interval of less than 10 nm. Bead random movement was tracked in-plane over about 100 frames to check for interaction of the beads with the underlying surface layer.

6.3.5 Contact angle measurements

The contact angle of a droplet of liquid on a surface provides information on the interaction energy between the liquid and the surface. When a droplet of liquid is placed on a surface, two situations can occur: 1. complete spreading of the liquid (complete wetting), or, 2. a drop with a finite angle to the surface forms (partial wetting).[297] The degree of wetting is determined by a force balance between the surface energies of the liquid and the solid phase. Young`s equation relates the surface energies of the three phases solid, liquid and gaseous assuming equilibrium:

$$\gamma_{sv} = \gamma_{sl} - \gamma_{lv} \cos\Theta \qquad (35)$$

representing the surface energy of the solid-vapor (gaseous), solid-liquid and liquid-vapor interface, respectively. As illustrated in figure 6.17, complete wetting occurs when $\theta = 0$.

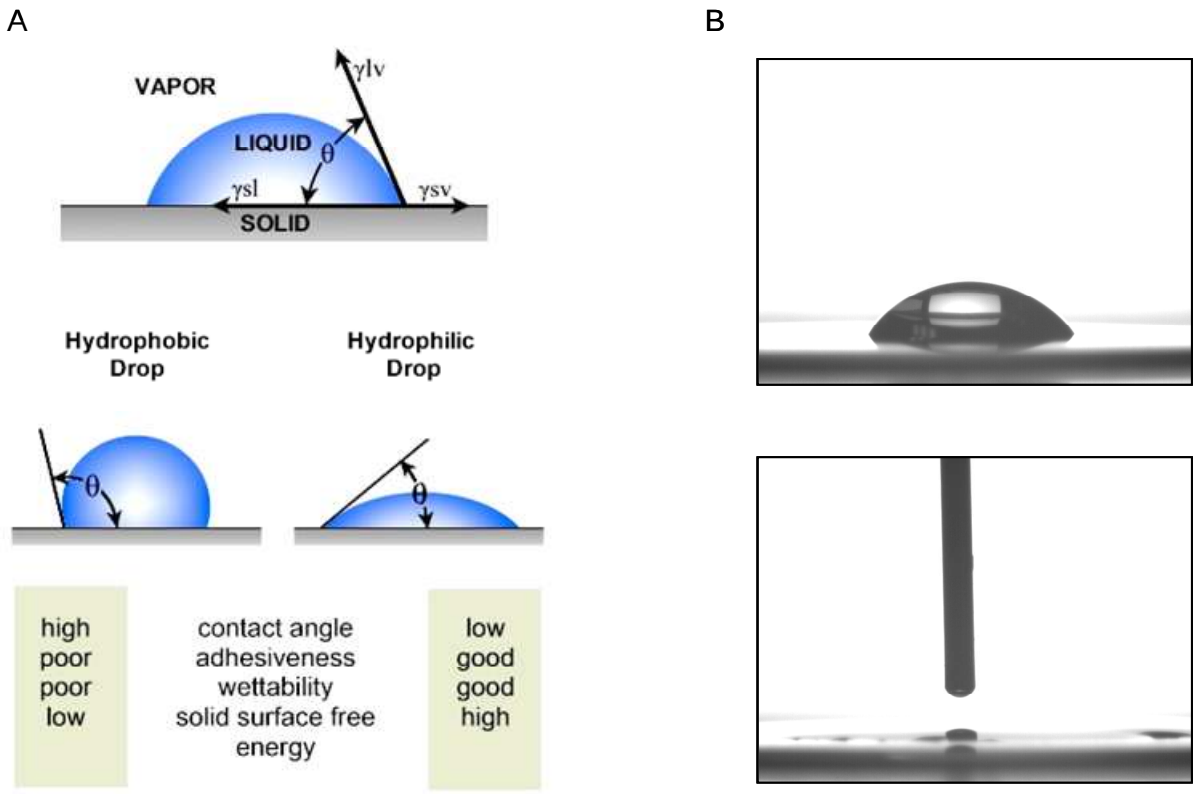

Figure 6.17: A: Principle of contact angle measurments and dependence on the wettability of the surface. B: Images of two surface exhibiting different degrees of wetting.

Contact angle measurements within this study were performed using a DSA100 goniometer (Krüss GmbH, Hamburg, Germany) instrument. The static contact angle of a water droplet (ultrapure water) was measured at three spots of the same surface. Contact angle values were determined on the right and the left contact point of the droplet and averaged. Cleaned glass slides, silicon wafers and QCM-D sensors were sampled. Pretreatment of the surfaces, if not otherwise noted, corresponded to the treatment during the usual experimental procedure.

Bibliography

1. Wolny, P. M.; Spatz, J. P.; Richter, R. P., On the Adsorption Behavior of Biotin-Binding Proteins on Gold and Silica. *Langmuir* **2009, *in press***.

2. Alberts, B.; Johnson, A.; Lewis, J.; Raff, M.; Roberts, K.; Walter, P., *Molecular Biology of the Cell*. fifth edition ed.; Garland Science: **2008**.

3. Yeagle, P., *The Membranes of Cells*. Academic Press, Inc.: Orlando, **1987**.

4. Sackmann, E., Supported Membranes: Scientific and Practical Applications. *Science* **1996,** 271, (5245), 43-48.

5. Albersdörfer, A.; Sackmann, E., Swelling behavior and viscoelasticity of ultrathin grafted hyaluronic acid films. *European Physical Journal B* **1999,** 10, (663-672).

6. Lipowski, R.; Sackmann, E., *Structure and Dynamics of Membranes*. Elsevier: Vol. 1A, 1B, 1995.

7. Reviakine, I.; Bergsma-Schutter, W.; Morozov, A. N.; Brisson, A., Two-Dimensional Crystallization of Annexin A5 on Phospholipid Bilayers and Monolayers: A Solid-Solid Phase Transition between Crystal Forms. *Langmuir* **2001,** 17, 1680-1686.

8. Andree, H. A.; Stuart, M. C.; Hermens, W. T.; Reutelingsperger, C. P.; Hemker, H. C.; Frederik, P. M.; Willems, G. M., Clustering of lipid-bound annexin V may explain its anticoagulant effect. *Journal of Biological Chemistry* **1992,** 267, (25), 17907-17912.

9. Azzaroni, O.; Mir, M.; Knoll, W., Supramolecular Architectures of Streptavidin on Biotinylated Self-Assembled Monolayers.Tracking Biomolecular Reorganization after Bioconjugation. *Journal of Physical Chemistry B* **2007,** 111, 13499-13503.

10. Shi, J.; Yang, T.; Kataoka, S.; Zhang, Y.; Diaz, A. J.; Cremer, P. S., GM1 clustering inhibits cholera toxin binding in supported phospholipid membranes. *Journal of the American Chemical Society* **2007,** 129, (18), 5954-5961.

11. Svedhem, S.; Pfeiffer, I.; Larsson, C.; Wingren, C.; Borrebaek, C.; Höök, F., Patterns of DNA-Labeled and scFv-Antibody-Carrying Lipid Vesicles Directed by Material-Specific Immobilization of DNA and Supported Lipid Bilayer Formation on an Au/SiO2 Template. *ChemBioChem* **2003,** 4, 339-343.

12. Richter, R. P.; Hock, K. K.; Burkhartsmeyer, J.; Boehm, H.; Bingen, P.; Wang, G.; Steinmetz, N. F.; Evans, D. J.; Spatz, J. P., Membrane-Grafted Hyaluronan Films: A Well-Defined Model System of Glycoconjugate Cell Coats. *Journal of the American Chemical Society* **2007,** 129, 5306-5307.

13. Steinmetz, N. F.; Bock, E.; Richter, R. P.; Spatz, J. P.; Lomonossoff, G. P.; Evans, D. J., Assembly of multilayer arrays of viral nanoparticles via biospecific recognition: a quartz

crystal microbalance with dissipation monitoring study. *Biomacromolecules* **2008,** 9, (2), 456-462.

14. In Winship Cancer Institute, Emory University Atlanta, http://cancerquest.emory.edu/index.cfm?page=37.

15. Evanko, S. P.; Tammi, M. I.; Tammi, R. H.; Wight, T. N., Hyaluronan-dependent pericellular matrix. *Advanced Drug Delivery Reviews* **2007,** 59, (13), 1351-1365.

16. Toole, B. P., Hyaluronan: From extracellular glue to pericellular cue. *Nature Reviews Cancer* **2004,** 4, 529-539.

17. Kultti, A.; Rilla, K.; Tiihonen, R.; Spicer, A. P.; Tammi, R. H.; Tammi, M. I., Hyaluronan synthesis induces microvillus-like cell surface protrusions. *Journal of Biological Chemistry* **2006,** 281, (23), 15821-15828.

18. Knudson, W.; Knudson, C. B., Assembly of a chondrocyte-like pericellular matrix on non-chondrogenic cells: Role of the cell surface hyaluronan receptors in the assembly of a pericellular matrix. *Journal of Cell Science* **1991,** 99, 227-235.

19. Clarris, B. J.; Fraser, J. R. E., On the pericellular zone of some mammalian cells in vitro. *Experimental Cell Research* **1968,** 49, (1), 181-193.

20. Udabage, L.; Brownlee, G. R.; Nilsson, S. K.; Brown, T. J., The over-expression of HAS2, Hyal-2 and CD44 is implicated in the invasiveness of breast cancer. *Experimental Cell Research* **2005,** 310, (1), 205-217.

21. Grundmann, S.; Schirmer, S. H.; Hekking, L. H. P.; Post, J. A. P.; Ionita, M., G. ; Groot, D. d.; Royen, N. v.; Berg, B. v. d.; Vink, H.; Moser, M.; Bode, C.; Kleijn, D. d.; Pasterkamp, G.; Piek, J. J.; Hoefer, I. E., Endothelial glycocalyx dimensions are reduced in growing collateral arteries and modulate leukocyte adhesion in arteriogenesis. *Journal of Cellular and Molecular Medicine* **2009,** NA.

22. Rilla, K.; Tiihonen, R.; Kultti, A.; Tammi, M.; Tammi, R., Pericellular Hyaluronan Coat Visualized in Live Cells With a Fluorescent Probe Is Scaffolded by Plasma Membrane Protrusions. *Journal of Histochemistry and Cytochemistry* **2008,** 56, (10), 901-910.

23. Cohen, M.; Klein, E.; Geiger, B.; Addadi, L., Organization and adhesive properties of the hyaluronan pericellular coat of chondrocytes and epithelial cells. *Biophysical Journal* **2003,** 85, (3), 1996-2005.

24. Qiao, R. L.; Wang, H. S.; Yan, W.; Odekon, L. E.; Del Vecchio, P. J.; Smith, T. J.; Malik, A. B., Extracellular matrix hyaluronan is a determinant of the endothelial barrier. *American Journal of Physiology and Cell Physiology* **1995,** 269, (1), C103-109.

25. Bastow, E. R.; Lamb, K. J.; Lewthwaite, J. C.; Osborne, A. C.; Kavanagh, E.; Wheeler-Jones, C. P. D.; Pitsillides, A. A., Selective Activation of the MEK-ERK Pathway Is Regulated by Mechanical Stimuli in Forming Joints and Promotes Pericellular Matrix Formation. *Journal of Biological Chemistry* **2005,** 280, (12), 11749-11758.

26. Kasemo, B., Biological surface science. *Surface Science* **2002,** 500, (1-3), 656-677.

27. Templin, M. F.; Stoll, D.; Schrenk, M.; Traub, P. C.; Vohringer, C. F.; Joos, T. O., Protein microarray technology. *Trends in Biotechnology* **2002,** 20, (4), 160-166.

28. DiVentra, M.; Evoy, S., *Introduction to Nanoscale Science and Technology*. Springer: **2004**.

29. Cavalcanti-Adam, E. A.; Volberg, T.; Micoulet, A.; Kessler, H.; Geiger, B.; Spatz, J. P., Cell spreading and focal adhesion dynamics are regulated by spacing of integrin ligands. *Biophysical Journal* **2007,** 92, (8), 2964-2974.

30. Cohen, M.; Joester, D.; Geiger, B.; Addadi, L., Spatial and temporal sequence of events in cell adhesion: from molecular recognition to focal adhesion assembly. *Chembiochem* **2004,** 5, (10), 1393-1399.

31. Knudson, C. B., Hyaluronan receptor-directed assembly of chondrocyte pericellular matrix. *Journal of Cell Biology* **1993,** 120, (3), 825-834.

32. Fraser, J. R.; Laurent, T. C., Turnover and metabolism of hyaluronan. *Ciba Foundation Symposuim* **1989,** 143, 41-53; discussion 53-59, 281-285.

33. de la Motte, C. A.; Hascall, V. C.; Drazba, J.; Bandyopadhyay, S. K.; Strong, S. A., Mononuclear leukocytes bind to specific hyaluronan structures on colon mucosal smooth muscle cells treated with polyinosinic acid:polycytidylic acid: inter-alpha-trypsin inhibitor is crucial to structure and function. *American Journal of Pathology* **2003,** 163, (1), 121-133.

34. Salustri, A.; Yanagishita, M.; Underhill, C. B.; Laurent, T. C.; Hascall, V. C., Localization and synthesis of hyaluronic acid in the cumulus cells and mural granulosa cells of the preovulatory follicle. *Dev Biol* **1992,** 151, (2), 541-51.

35. Meyer, K., The Biological Significance of Hyaluronic Acid and Hyaluronidase. *Physiological Reviews* **1947,** 27, (3), 335-359.

36. Comper, W. D.; Laurent, T. C., Physiological function of connective tissue polysaccharides. *Physiological Reviews* **1978,** 58, (1), 255-315.

37. Van Teeffelen, J. W.; Brands, J.; Stroes, E. S.; Vink, H., Endothelial glycocalyx: sweet shield of blood vessels. *Trends in Cardiovascular Medicine* **2007,** 17, (3), 101-105.

38. Weinbaum, S.; Zhang, X.; Han, Y.; Vink, H.; Cowin, S. C., Mechanotransduction and flow across the endothelial glycocalyx. *Proceedings of the National Acadamy of Science USA* **2003,** 100, (13), 7988-7995.

39. Henry, C. B. S.; Duling, B. R., Permeation of the luminal capillary glycocalyx is determined by hyaluronan. *American Journal of Physiology, Heart and Circulatory Physiology* **1999,** 277, (2), H508-514.

40. Reitsma, S.; Slaaf, D. W.; Vink, H.; van Zandvoort, M. A.; oude Egbrink, M. G., The endothelial glycocalyx: composition, functions, and visualization. *Pflugers Archiv* **2007,** 454, (3), 345-359.

41. Day, A. J.; Sheehan, J. K., Hyaluronan: polysaccharide chaos to protein organisation. *Current Opinion in structural Biology* **2001,** 11, 617-622.

42. Toole, B. P., Hyaluronan and its binding proteins, the hyaladherins. *Current Opinion in Cell Biology* **1990,** 2, (5), 839-844.

43. Hascall, V. C.; Majors, A. K.; De La Motte, C. A.; Evanko, S. P.; Wang, A.; Drazba, J. A.; Strong, S. A.; Wight, T. N., Intracellular hyaluronan: a new frontier for inflammation? *Biochimica Biophysica Acta* **2004,** 1673, (1-2), 3-12.

44. Mochizuki, S.; Vink, H.; Hiramatsu, O.; Kajita, T.; Shigeto, F.; Spaan, J. A.; Kajiya, F., Role of hyaluronic acid glycosaminoglycans in shear-induced endothelium-derived nitric oxide release. *American Journal of Physiology, Heart and Circulatory Physiology* **2003,** 285, (2), H722-726.

45. Day, A. J.; de la Motte, C. A., Hyaluronan cross-linking: a protective mechanism in inflammation? *Trends in Immunology* **2005,** 26, (12), 637-643.

46. Seyfried, N. T.; Day, A. J.; Almond, A., Experimental evidence for all-or-none cooperative interactions between the G1-domain of versican and multivalent hyaluronan oligosaccharides. *Matrix Biology* **2006,** 25, 14-19.

47. Lesley, J.; Hascal, V. C.; Tammi, M.; Hyman, R., Hyaluronan Binding by Cell Surface CD44. *Journal of Biological Chemistry* **2000,** 275, (35), 26967–26975.

48. Salustri, A.; Garlanda, C.; Hirsch, E.; De Acetis, M.; Maccagno, A.; Bottazzi, B.; Doni, A.; Bastone, A.; Mantovani, G.; Beck Peccoz, P.; Salvatori, G.; Mahoney, D. J.; Day, A. J.; Siracusa, G.; Romani, L.; Mantovani, A., PTX3 plays a key role in the organization of the cumulus oophorus extracellular matrix and in in vivo fertilization. *Development* **2004,** 131, (7), 1577-86.

49. Meyer, K.; Palmer, J. W., The Polysacchaide of The Vitreous Humor. *Journal of Biological Chemistry* **1934,** 107, (3), 629-634.

50. Jackson, D. G., Immunological functions of hyaluronan and its receptors in the lymphatics. *Immunological Reviews* **2009,** 230, (1), 216-231.

51. DeAngelis, P. L., Hyaluronan synthases: fascinating glycosyltransferases from vertebrates, bacterial pathogens, and algal viruses. *Cellular and Molecular Life Sciences* **1999,** 56, (7-8), 670-682.

52. Weigel, P. H.; DeAngelis, P. L., Hyaluronan synthases: a decade-plus of novel glycosyltransferases. *Journal of Biological Chemistry* **2007,** 282, (51), 36777-81.

53. Itano, N.; Sawai, T.; Yoshida, M.; Lenas, P.; Yamada, Y.; Imagawa, M.; Shinomura, T.; Hamaguchi, M.; Yoshida, Y.; Ohnuki, Y.; Miyauchi, S.; Spicer, A. P.; McDonald, J. A.; Kimata, K., Three Isoforms of Mammalian Hyaluronan Synthases Have Distinct Enzymatic Properties. *Journal of Biological Chemistry* **1999,** 274, (35), 25085-25092.

54. Frost, G. I.; Csoka, T.; Stern, R., The Hyaluronidases: A Chemical, Biological and Clinical Overview. *Trends in Glycoscience and Glycotechnology* **1996,** 8, 419-434.

55. Asari, A., Novel Functions of Hyuluronan Oligosaccharides. *Glycoforum. Hyaluronan Today* **2005**.

56. Camenisch, T. D.; McDonald, J. A., Hyaluronan. Is Bigger Better? *American Journal of Respiratory Cell And Molecular Biology* **2000,** 23, 431-433.

57. Stern, R.; Asari, A. A.; Sugahara, K. N., Hyaluronan fragments: An information-rich system. *European Journal of Cell Biology* **2006,** 85, 699-715.

58. Nakamura, K.; Yokohama, S.; Yoneda, M.; Okamoto, S.; Tamaki, Y.; Ito, T.; Okada, M.; Aso, K.; Makino, I., High, but not low, molecular weight hyaluronan prevents T-cell-mediated liver injury by reducing proinflammatory cytokines in mice. *Journal of Gastroenterology* **2004,** 39, (4), 346-354.

59. McKee, C. M.; Lowenstein, C. J.; Horton, M. R.; Wu, J.; Bao, C.; Chin, B. Y.; Choi, A. M. K.; Noble, P. W., Hyaluronan Fragments Induce Nitric-oxide Synthase in Murine Macrophages through a Nuclear Factor kB-dependent Mechanism. *Journal of Biological Chemistry* **1997,** 272, (12), 8013-8018.

60. McKee, C. M.; Penno, M. B.; Cowman, M.; Burdick, M. D.; Strieter, R. M.; Bao, C.; Noble, P. W., Hyaluronan (HA) fragments induce chemokine gene expression in alveolar macrophages. The role of HA size and CD44. *Journal of Clinical Investigation* **1996,** 98, (10), 2403-2413.

61. Hascall, V. C.; Laurent, T. C., Hyaluronan: Structure and Physical Properties. *Glycoforum. Hyaluronan Today* **1997**.

62. Balazs, E. A.; Gibbs, D. A., *The rheological properties and the biological function of hyaluronic acid*. Academic press, New York: **1970**.

63. Coleman, P. J.; Scott, D.; Mason, R. M.; Levick, J. R., Characterization of the effect of high molecular weight hyaluronan on trans-synovial flow in rabbit knees. *Journal of Physiology* **1999,** 514 (Pt 1), 265-282.

64. Toole, B. P., *Proteoglycans and hyaluronan in morphogenesis and differentiation.* 2nd ed.; Plenum Press: New York, **1991**.

65. Hughes, E. N.; Mengod, G.; August, J. T., Murine cell surface glycoproteins. Characterization of a major component of 80,000 daltons as a polymorphic differentiation antigen of mesenchymal cells. *Journal of Biological Chemistry* **1981,** 256, (13), 7023-7027.

66. Gallatin, W. M.; Wayner, E. A.; Hoffman, P. A.; St John, T.; Butcher, E. C.; Carter, W. G., Structural homology between lymphocyte receptors for high endothelium and class III extracellular matrix receptor. *Proceedings of the National Acadamy of Science USA* **1989,** 86, (12), 4654-4658.

67. Haynes, B. F.; Telen, M. J.; Hale, L. P.; Denning, S. M., CD44 - a molecule involved in leukocyte adherence and T-cell activation. *Immunology Today* **1989,** 10, (12), 423-428.

68. Haynes, B. F.; Liao, H.-X.; Patton, K. L., The transmembrane Hyaluronan receptor (CD44): Multiple Functions, Multiple Forms. *Cancer Cells* **1991,** 3, (9), 347-350.

69. Banerji, S.; Day, A. J.; Kahmann, J. D.; Jackson, D. G., Characterization of a Functional Hyaluronan-Binding Domain from the Human CD44 Molecule Expressed in Escherichia coli. *Protein Expression and Purification* **1998,** 14, 371-381.

70. Pure, E.; Cuff, C. A., A crucial role for CD44 in inflammation. *Trends in Molecular Medicine* **2001,** 7, (5), 213-221.

71. Sleeman, J.; Rudy, W.; Hofmann, M.; Moll, J.; Herrlich, P.; Ponta, H., Regulated clustering of variant CD44 proteins increases their hyaluronate binding capacity. *Journal of Cell Biology* **1996,** 135, (4), 1139-1150.

72. Banerji, S.; Wright, A. J.; Noble, M.; Mahoney, D. J.; Campbell, I. D.; Day, A. J.; Jackson, D. G., Structures of the Cd44–hyaluronan complex provide insight into a fundamental carbohydrateprotein interaction. *Nature Structural and Molecular Biology* **2007,** 14, (3), 234-239.

73. Aruffo, A.; Stamenkovic, I.; Melnick, M.; Underhill, C. B.; Seed, B., CD44 is the principal cell surface receptor for hyaluronate. **1990,** 61, (7), 1303-1313.

74. Lesley, J.; Gál, I.; Mahoney, D. J.; Cordell, M. R.; Rugg, M. S.; Hyman, R.; Day, A. J.; Mikecz, K., TSG-6 Modulates the Interaction between Hyaluronan and Cell Surface CD44. *Journal of Biological Chemistry* **2004,** 279, 25745–25754.

75. Tammi, R.; MacCallum, D.; Hascall, V. C.; Pienimaki, J. P.; Hyttinen, M.; Tammi, M., Hyaluronan bound to CD44 on keratinocytes is displaced by hyaluronan decasaccharides and not hexasaccharides. *Journal of Biological Chemistry* **1998,** 273, (44), 28878-28888.

76. Nelson, D. L.; Cox, M. M., *Lehninger. Principles of Biochemistry*. 4th ed.; W.H. Freeman and Company: New York, **2005**.

77. Dustin, M. L.; Springer, T. A., Role of Lymphocyte Adhesion Receptors in Transient Interactions and Cell Locomotion. *Annual Review of Immunology* **1991,** 9, (1), 27-66.

78. English, N. M.; Lesley, J. F.; Hyman, R., Site-specific de-N-glycosylation of CD44 can activate hyaluronan binding, and CD44 activation states show distinct threshold densities for hyaluronan binding. *Cancer Research* **1998,** 58, (16), 3736-3742.

79. Perschl, A.; Lesley, J.; English, N.; Trowbridge, I.; Hyman, R., Role of CD44 cytoplasmic domain in hyaluronan binding. *European Journal of Immunology* **1995,** 25, (2), 495-501.

80. Skelton, T. P.; Zeng, C.; Nocks, A.; Stamenkovic, I., Glycosylation Provides Both Stimulatory and Inhibitory Effects on Cell Surface and Soluble CD44 Binding to Hyaluronan. *Journal of Cell Biology* **1998,** 140, (2), 431-446.

81. Hardingham, T., Proteoglycans: their structure, interactions and molecular organization in cartilage. *Biochemical Society Transactions* **1981,** 9, (6), 489-497.

82. Kahmann, J. D.; O`Brien, R.; Werner, J. M.; Heinegård, D.; Ladbury, J. E.; Campbell, I. D.; Day, A. J., Localization and characterization of the hyaluronan-binding site on the Link module from human TSG-6. *Structure* **2000,** 8, 763-774.

83. Parkar, A. A.; Kahmann, J. D.; Howat, S. L.; Bayliss, M. T.; Day, A. J., TSG-6 interacts with hyaluronan and aggrecan in a pH-dependent manner via a common functional element: implications for its regulation in inflamed cartilage. *FEBS Lett* **1998,** 428, (3), 171-176.

84. Lesley, J.; English, N.; Perschl, A.; Gregoroff, J.; Hyman, R., Variant cell lines selected for alterations in the function of the hyaluronan receptor CD44 show differences in glycosylation. *Journal of Experimental Medicine* **1995,** 182, (2), 431-437.

85. Lesley, J.; Hyman, R.; English, N.; Catterall, J. B.; Turner, G. A., CD44 in inflammation and metastasis. *Glycoconjugate Journal* **1997,** 14, 611-622.

86. Ruffel, B.; Johnson, P., The regulation and function of hyaluronan binding by CD44 in the immune system. *Hyaluronan Today* **2009**.

87. Katoh, S.; Zheng, Z.; Oritani, K.; Shimozato, T.; Kincade, P. W., Glycosylation of CD44 negatively regulates its recognition of hyaluronan. *Journal of Experimental Medicine* **1995,** 182, (2), 419-429.

88. Lokeshwar, V. B.; Bourguignon, L. Y., Post-translational protein modification and expression of ankyrin-binding site(s) in GP85 (Pgp-1/CD44) and its biosynthetic precursors during T-lymphoma membrane biosynthesis. *Journal of Biological Chemistry* **1991,** 266, (27), 17983-17989.

89. Lesley, J.; Hyman, R., CD44 can be activated to function as an hyaluronic acid receptor in normal murine T cells. *European Journal of Immunology* **1992,** 22, (10), 2719-23.

90. Blumberg, P. M., Protein Kinase C as the Receptor for the Phorbol Ester Tumor Promoters: Sixth Rhoads Memorial Award Lecture. *Cancer Research* **1988,** 48, (1), 1-8.

91. Zheng, Z.; Katoh, S.; He, Q.; Oritani, K.; Miyake, K.; Lesley, J.; Hyman, R.; Hamik, A.; Parkhouse, R. M.; Farr, A. G.; et al., Monoclonal antibodies to CD44 and their influence on hyaluronan recognition. *Journal of Cell Biology* **1995,** 130, (2), 485-495.

92. Mohamadzadeh, M.; DeGrendele, H.; Arizpe, H.; Estess, P.; Siegelman, M., Proinflammatory stimuli regulate endothelial hyaluronan expression and CD44/HA-dependent primary adhesion. *Journal of Clinical Investigation* **1998,** 101, (1), 97-108.

93. Huang, L.; Yoneda, M.; Kimata, K., A serum-derived hyaluronan-associated protein (SHAP) is the heavy chain of the inter alpha-trypsin inhibitor. *Journal of Biological Chemistry* **1993,** 268, (35), 26725-26730.

94. Zhao, M.; Yoneda, M.; Ohashi, Y.; Kurono, S.; Iwata, H.; Ohnuki, Y.; Kimata, K., Evidence for the covalent binding of SHAP, heavy chains of inter-alpha-trypsin inhibitor, to hyaluronan. *J Biol Chem* **1995,** 270, (44), 26657-26663.

95. Zhuo, L.; Kanamori, A.; Kannagi, R.; Itano, N.; Wu, J.; Hamaguchi, M.; Ishiguro, N.; Kimata, K., SHAP potentiates the CD44-mediated leukocyte adhesion to the hyaluronan substratum. *Journal of Biological Chemistry* **2006,** 281, (29), 20303-20314.

96. Morra, M., Engineering of biomaterials surfaces by hyaluronan. *Biomacromolecules* **2005,** 6, (3), 1205-1223.

97. Delpech, B.; Bertrand, P.; Maingonnat, C., Immunoenzymoassay of the hyaluronic acid-hyaluronectin interaction: application to the detection of hyaluronic acid in serum of normal subjects and cancer patients. *Analytical Biochemistry* **1985,** 149, (2), 555-565.

98. Picart, C.; Mutterer, J.; Richert, L.; Luo, Y.; Prestwich, G. D.; Schaaf, P.; Voegel, J. C.; Lavalle, P., Molecular basis for the explanation of the exponential growth of polyelectrolyte multilayers. *Proceedings of the National Acadamy of Science USA* **2002,** 99, (20), 12531-12535.

99. Burke, S. E.; Barrett, C. J., pH-responsive properties of multilayered poly(L-lysine)/hyaluronic acid surfaces. *Biomacromolecules* **2003,** 4, (6), 1773-1783.

100. Joester, D.; Klein, E.; Geiger, B.; Addadi, L., Temperature-sensitive micrometer-thick layers of hyaluronan grafted on microspheres. *Journal of the American Chemical Society* **2006,** 128, (4), 1119-1124.

101. Benz, M.; Chen, N.; Israelachvili, J., Lubrication and wear properties of grafted polyelectrolytes, hyaluronan and hylan, measured in the surface forces apparatus. *Journal of Biomedical Materials Research A* **2004,** 71, (1), 6-15.

102. Sengupta, K.; Schilling, J.; Marx, S.; Fischer, M.; Bacher, A.; Sackmann, E., Mimicking Tissue Surfaces by Supported Membrane Coupled Ultrathin Layer of Hyaluronic Acid. *Langmuir* **2003,** 19, (1775-1781).

103. Deb, T. B.; Datta, K., Molecular cloning of human fibroblast hyaluronic acid-binding protein confirms its identity with P-32, a protein co-purified with splicing factor SF2. Hyaluronic acid-binding protein as P-32 protein, co-purified with splicing factor SF2. *Journal of Biological Chemistry* **1996,** 271, (4), 2206-2212.

104. Predki, P. F., Functional protein microarrays: ripe for discovery. *Current Opinion in Chemical Biology* **2004,** 8, (1), 8-13.

105. Rusmini, F.; Zhiyuan, Z.; Jan, F., Protein Immobilization Strategies for Protein Biochips. *Biomacromolecules* **2007,** 8, 1775-1789.

106. Andrade, J. D.; Feng, L. In *Proteins at Interfaces II*, Proteins at Interfaces II, 1995; Horbett, T. A. B., J. L., Ed. 1995; 66.

107. Norde, W., In *Macromolecular Symposium*, 1996; Vol. 103, pp 5-81.

108. Welzel, P. B., Investigation of adsorption-induced structural changes of proteins at solid/liquid interfaces by differential scanning calorimetry. *Thermochimica Acta* **2002,** 382, (1-2), 175-188.

109. Alonso, J. H.; Reichel, A.; Piehler, J.; del Campo, A., Photopatterned Surfaces for Site-Specific and Functional Immobilization of Proteins. *Langmuir* **2008,** 24, (2), 448-457.

110. Deckert, A. A.; Farrell, C.; Roos, J.; Waddell, R.; Stubna, A., Steric Considerations in the Covalent Binding of Myoglobin to Thin Films. *Langmuir* **1999,** 15, 5578-5583.

111. Huang, N.-P.; Vörös, J.; De Paul, S. M.; Textor, M.; Spencer, N. D., Biotin-Derivatized Poly(L-lysine)-g-poly(ethylene glycol): A Novel Polymeric Interface for Bioaffinity Sensing. *Langmuir* **2002,** 18, 220-230.

112. Hemker, H. C.; Andree, H. A.; Giesen, P. L. A., Anwendung der Ellipsometrie zur Untersuchung von Biomaterialien. *Haemostaseologie* **1990,** 10, 71-76.

113. Brisson, A.; Bergsma-Schutter, W.; Oling, F.; Lambert, O.; Reviakine, I., Two-dimensional crystallization of proteins on lipid monolayers at the air-water interface and transfer to an electron microscopy grid. *Journal of Crystal Growth* **1999,** 196, (2-4), 456-470.

114. Yu, X.; Danke, X.; Quan, C., Label-free detection methods for protein microarrays. *Proteomics* **2006,** 6, (20), 5493-5503.

115. Sun, Y. S.; Landry, J. P.; Fei, Y. Y.; Zhu, X. D.; Luo, J. T.; Wang, X. B.; Lam, K. S., Effect of Fluorescently Labeling Protein Probes on Kinetics of Protein-Ligand Reactions. *Langmuir* **2008,** 24, (23), 13399-13405.

116. Sauerbrey, G., Verwendung von Schwingquarzen zur Waegung duenner Schichten und zur Mikrowaegung. *Zeitschrift für Physik A* **1959,** 155, 206-222.

117. Muratsugu, M.; Ohta, F.; Miya, Y.; Hosokawa, T.; Kurosawa, S.; Kamo, N.; Ikeda, H., Quartz crystal microbalance for the detection of microgram quantities of human serum albumin: relationship between the frequency change and the mass of protein adsorbed. *Analytical Chemistry* **1993,** 65, (20), 2933-2937.

118. Janshoff, A.; Wegener, J.; Sieber, M.; Galla, H. J., Double-mode impedance analysis of epithelial cell monolayers cultured on shear wave resonators. *European Biophysics Journal* **1996,** 25, (2), 93-103.

119. Caruso, F.; Furlong, D. N.; Kingshott, P., Characterization of Ferritin Adsorption onto Gold. *Journal of Colloid and Interface Science* **1997,** 186, (1), 129-140.

120. Nomura, T.; Hattori, O., *Analytica Chimica Acta* **1980,** 115, 323-326.

121. Rodahl, M.; Höök, F.; Krozer, A.; Brzezinski, P.; Kasemo, B., Quartz crystal microbalance setup for frequency and Q-factor measurements in gaseous and liquid environments. *Review of Scientific Instruments* **1995,** 66, (7), 3924-3930.

122. Höök, F. Development of a novel QCM technique for protein adsorption studies. Chalmers University of Technology, Göteborg, **1997**.

123. Höök, F.; Rodahl, M.; Brzezinski, P.; Kasemo, B., Energy Dissipation Kinetics for Protein and Antibody-Antigen Adsorption under Shear Oscillation on a Quartz Crystal Microbalance. *Langmuir* **1998,** 14, (4), 729-734.

124. Höök, F.; Rodahl, M.; Kasemo, B.; Brzezinski, P., Structural changes in hemoglobin during adsorption to solid surfaces: Effects of pH, ionic strength, and ligand binding. *Proceedings of the National Academy of Sciences USA* **1998,** 95, (21), 12271-12276.

125. Marie, R.; Beech, J. P.; Voros, J.; Tegenfeldt, J. O.; Hook, F., Use of PLL-g-PEG in micro-fluidic devices for localizing selective and specific protein binding. *Langmuir* **2006,** 22, (24), 10103-10108.

126. Asberg, P.; Bjork, P.; Hook, F.; Inganas, O., Hydrogels from a water-soluble zwitterionic polythiophene: dynamics under pH change and biomolecular interactions observed using quartz crystal microbalance with dissipation monitoring. *Langmuir* **2005,** 21, (16), 7292-7298.

127. Notley, S. M.; Eriksson, M.; Wagberg, L., Visco-elastic and adhesive properties of adsorbed polyelectrolyte multilayers determined in situ with QCM-D and AFM measurements. *Journal of Colloid and Interface Science* **2005,** 292, (1), 29-37.

128. Keller, C. A.; Kasemo, B., Surface Specific Kinetics of Lipid Vesicle Adsorption Measured with a Quartz Crystal Microbalance. *Biophysical Journal* **1998,** 75, (3), 1397-1402.

129. Keller, C. A.; Glasmästar, K.; Zhdanov, V. P.; Kasemo, B., Formation of Supported Membranes from Vesicles. *Physical Review Letters* **2000,** 84, (23), 5443-5446.

130. Richter, R.; Mukhopadhyay, A.; Brisson, A., Pathways of Lipid Vesicle Deposition on Solid Surfaces: A Combined. *Biophysical Journal* **2003,** 85, 3035-3047.

131. Richter, R. P.; Berat, R.; Brisson, A. R., Formation of solid-supported lipid bilayers: an integrated view. *Langmuir* **2006,** 22, (8), 3497-3505.

132. Larsson, C.; Rodahl, M.; Höök, F., Characterization of DNA Immobilization and Subsequent Hybridization on a 2D Arrangement of Streptavidin on a Biotin-Modified Lipid Bilayer Supported on SiO2. *Analytical Chemistry* **2003,** 75, 5080-5087.

133. Berquand, A.; Mazeran, P.-E.; Pantigny, J.; Proux-Delrouyre, V.; Laval, J.-M.; Bourdillon, C., Two-Step Formation of Streptavidin-Supported Lipid Bilayers by PEG-Triggered Vesicle Fusion. Fluorescence and Atomic Force Microscopy Characterization. *Langmuir* **2003,** 19, 1700-1707.

134. Kunze, A.; Svedhem, S.; Kasemo, B., Lipid transfer between charged supported lipid bilayers and oppositely charged vesicles. *Langmuir* **2009,** 25, (9), 5146-5158.

135. Richter, R. P.; Him, J. L.; Tessier, B.; Tessier, C.; Brisson, A. R., On the kinetics of adsorption and two-dimensional self-assembly of annexin A5 on supported lipid bilayers. *Biophysical Journal* **2005,** 89, (5), 3372-3385.

136. Rodahl, M.; Hook, F.; Fredriksson, C.; Keller, C. A.; Krozer, A.; Brzezinski, P.; Voinova, M.; Kasemo, B., Simultaneous frequency and dissipation factor QCM measurements of biomolecular adsorption and cell adhesion. *Faraday Discussions* **1997**, (107), 229-246.

137. Rodahl, M.; Kasemo, B., A simple setup to simultaneously measure the resonant frequency and the absolute dissipation factor of a quartz crystal microbalance. *Review of Scientific Instruments* **1996,** 67, (9), 3238-3241.

138. Reimhult, E.; Larsson, C.; Kasemo, B.; Höök, F., Simultaneous Surface Plasmon Resonance and Quartz Crystal Microbalance with Dissipation Monitoring Measurements of

Biomolecular Adsorption Events Involving Structural Transformations and Variations in Coupled Water. *Analytical Chemistry* **2004,** 76, 7211-7220.

139. Bingen, P.; Wang, G.; Steinmetz, N. F.; Rodahl, M.; Richter, R. P., Solvation Effects in the Quartz Crystal Microbalance with Dissipation Monitoring Response to Biomolecular Adsorption. A Phenomenological Approach. *Analytical Chemistry* **2008,** 80, 8880-8890.

140. Edvardsson, M.; Svedhem, S.; Wang, G.; Richter, R.; Rodahl, M.; Kasemo, B., QCM-D and Reflectometry Instrument: Applications to Supported Lipid Structures and Their Biomolecular Interactions. *Analytical Chemistry* **2009,** 81, 349-361.

141. Voinova, M. V.; Rodahl, M.; Jonson, M.; Kasemo, B., Viscoelastic Acoustic Response of Layered Polymer Films at Fluid-Solid Interfaces: Continuum Mechanics Approach. *Physica Scripta* **1999**, (5), 391-396.

142. Heuberger, M.; Drobek, T.; Voros, J., About the role of water in surface-grafted poly(ethylene glycol) layers. *Langmuir* **2004,** 20, (22), 9445-9448.

143. Voros, J., The density and refractive index of adsorbing protein layers. *Biophysical Journal* **2004,** 87, (1), 553-561.

144. Woollam, J. A.; Johs, B.; Herzinger, C. M.; Hilfiker, J.; Synowicki, R.; Bungay, C. L., Overview of Variable Angle Spectroscopic Ellipsometry (VASE) Part I: Basic Theory and Typical Applications. *Critical Reviews of Optical Science and Technology* **1999,** CR72 (Conference Proceedings, Denver, Colorado).

145. Fujiwara, H., *Spectroscopic Ellipsometry: Principles and Applications*. Wiley Interscience: **2007**.

146. In J. A. Woollam Co., Inc.: 2000; pp from conference talk: Characterization and Metrology for ULSI Technology 200, International Conference.

147. Wang, G.; Rodahl, M.; Edvardsson, M.; Svedhem, S.; Ohlsson, G.; Hook, F.; Kasemo, B., A combined reflectometry and quartz crystal microbalance with dissipation setup for surface interaction studies. *Rev Sci Instrum* **2008,** 79, (7), 075107.

148. Curtis, A. S., The Mechanism of Adhesion of Cells to Glass. A Study by Interference Reflection Microscopy. *J Cell Biol* **1964,** 20, 199-215.

149. Rädler, J.; Sackmann, E., Imaging optical thicknesses and separation distances of phospholipid vesicles at solid surfaces. *J. Phys. II France* **1993,** 3, (5), 727-748.

150. Kühner, M.; Sackmann, E., Ultrathin Hydrated Dextran Films Grafted on Glass: Preparation and Characterization of Structural, Viscous, and Elastic Properties by Quantitative Microinterferometry. *Langmuir* **1996,** 12, (20), 4866-4876.

151. Raedler, J.; Sackmann, E., On the measurement of weak repulsive and frictional colloidal forces by reflection interference contrast microscopy. *Langmuir* **1992,** 8, (3), 848-853.

152. Rubinstein, M.; Colby, R. H., *Polymer Physics*. Oxford University Press: **2003**.

153. In *the Importance of Polymer Science for Biological Systems*, University of York, UK, 2008; Earis, P., Ed. RSC Publishing: University of York, UK, 2008.

154. Cowman, M. K.; Matsuoka, S., Experimental approaches to hyaluronan structure. *Carbohydrate Research* **2005,** 340, 791-809.

155. Gribbon, P.; Heng, B. C.; Hardingham, T. E., The analysis of intermolecular interactions in concentrated hyaluronan solutions suggest no evidence for chain-chain association. *Biochemical Journal* **2000,** 350, (1), 329-335.

156. Almond, A.; Hardingham, T., Hyaluronan: Current Macromolecular and Micromolecular Views. **2008**.

157. Flory, P., *Principles of Polymer Chemistry*. Cornell University Press: Ithaca, NY, **1971**.

158. Teraoka, I., *Polymer Solutions*. Wiley - Interscience: **2002**.

159. Evans, D. F.; Wennersröm, H., *The Colloidal Domain*. 2nd ed.; Wiley-VCH: **1999**.

160. Kratky, O.; Porod, G., Röntgenuntersuchung gelöster Fadenmoleküle. *Rec. Trav. Chim. Pays Bas* **1949,** 68, 1106-1123.

161. deGennes, P.-G., *Scaling Concepts in Polymer Physics*. Cornell University Press: Ithaca, NY, **1979**.

162. Sevick, E. M.; Williams, D. R. M., Anomalous height increases upon bending for an Alexander--de Gennes polymer brush. *The Journal of Chemical Physics* **1996,** 105, (20), 9334-9338.

163. Aubouy, M.; Meglio, J. M. d.; Raphael, E., Irreversible Adsorption of a Polymer Melt on a Colloidal Particle. *Europhysics Letters* **1993**, (2), 87-92.

164. de Gennes, P. G., Conformations of Polymers Attached to an Interface. *Macromolecules* **1980,** 13, (5), 1069-1075.

165. DeGennes, P.-G., Polymers at Interface; A Simplified View. *Advances in Colloide and Interface Science* **1987,** 27, 189-209.

166. Cleland, R. L., Viscometry and sedimentation equilibrium of partially hydrolyzed hyaluronate: Comparison with theoretical models of wormlike chains. *Biopolymers* **1984,** 23, (4), 647-666.

167. Morris, E. R.; Rees, D. A.; Welsh, E. J., Conformation and dynamic interactions in hyaluronate solutions. *Journal of Molecular Biology* **1980,** 138, (2), 383-400.

168. Sheehan, J. K.; Atkins, E. D. T., X-ray fibre diffraction study of conformational changes in hyaluronate induced in the presence of sodium, potassium and calcium cations. *International Journal of Biological Macromolecules* **1983,** 5, (4), 215-221.

169. Scott, J. E.; Cummings, C.; Brass, A.; Chen, Y., Secondary and tertiary structures of hyaluronan in aqueous solution, investigated by rotary shadowing-electron microscopy and computer simulation. Hyaluronan is a very efficient network-forming polymer. *Biochemical Journal* **1991,** 274 (Pt 3), 699-705.

170. Cleland, R. L.; Wang, J. L., Ionic polysaccharides. 3. Dilute solution properties of hyaluronic acid fractions. *Biopolymers* **1970,** 9, (7), 799-810.

171. Ogston, A. G.; Preston, B. N., The exclusion of protein by hyaluronic acid. Measurement by light scattering. *Journal of Biological Chemistry* **1966,** 241, (1), 17-9.

172. Scott, J. E.; Heatley, F., Hyaluronan forms specific stable tertiary structures in aqueous solution: a 13C NMR study. *Proceedings of the National Acadamy of Science USA* **1999,** 96, (9), 4850-4855.

173. Almond, A.; Brass, A.; Sheehan, J. K., Deducing polymeric structure from aqueous molecular dynamics simulations of oligosaccharides: predictions from simulations of hyaluronan tetrasaccharides compared with hydrodynamic and X-ray fibre diffraction data. *Journal of Molecular Biology* **1998,** 284, (5), 1425-1437.

174. Blundell, C. D.; Deangelis, P. L.; Almond, A., Hyaluronan: the absence of amide-carboxylate hydrogen bonds and the chain conformation in aqueous solution are incompatible with stable secondary and tertiary structure models. *Biochemical Journal* **2006,** 396, (3), 487-498.

175. Takahashi, R.; Kubota, K.; Kawada, M.; Okamoto, A., Effect of Molecular Weight Distribution on the Solution Properties of Sodium Hyaluronate in 0.2M NaCl Solution. *Biopolymers* **1999,** 50, 87-98.

176. Mendichi, R.; Soltes, L.; Scieroni, A. G., Evaluation of Radius of Gyration and Intrinsic Viscosity Molar Mass Dependence and Stiffness of Hyaluronan. *Biomacromolecules* **2003,** 4, 1805-1810.

177. Spatz, J. P.; Mössmer, S.; Hartmann, C.; Möller, M., Ordered deposition of inorganic clusters from micellar block copolymer films. *Langmuir* **2000,** 16, 407-415.

178. Glass, R.; Möller, M.; Spatz, J. P., *Nanotechnology* **2003,** 14, 1153-1160.

179. Cavalcanti-Adam, E. A.; Micoulet, A.; Blummel, J.; Auernheimer, J.; Kessler, H.; Spatz, J. P., Lateral spacing of integrin ligands influences cell spreading and focal adhesion assembly. *European Journal of Cell Biology* **2006,** 85, (3-4), 219-224.

180. Arnold, M.; Hirschfeld-Warneken, V. C.; Lohmüller, T.; Heil, P.; Blümmel, J.; Cavalcanti-Adam, E. A.; Lopez-Garcia, M.; Walther, P.; Kessler, H.; Geiger, B.; Spatz, J. P., Induction of Cell Polarization and Migration by a Gradient of Nanoscale Variations in Adhesive Ligand Spacing. *Nano Letters* **2008,** 8, (7), 2063-2069.

181. Selhuber-Unkel, C.; Lopez-Garcia, M.; Kessler, H.; Spatz, J. P., Cooperativity in adhesion cluster formation during initial cell adhesion. *Biophysical Journal* **2008,** 95 (11), 5424-5431.

182. Wilchek, M.; Bayer, E. A., Foreword and introduction to the book (strept)avidin–biotin system. *Biomolecular Engineering* **1999,** 16, 1-4.

183. Chilkoti, A.; Stayton, P. S., Molecular Origins of the Slow Streptavidin-Biotin Dissociation Kinetics. *Journal of the American Chemical Society* **2002,** 117, (43), 10622-10628.

184. Hendrickson, W. A.; Pähler, A.; Smith, J. L.; Satow, Y.; Merritt, E. A.; Phizackerley, R. P., Crystal structure of core streptavidin determined from multiwavelength anomalous diffraction of synchrotron radiation. *Proceedings of the National Academy of Sciences of the United States of America* **1989,** 86, (7), 2190-2194.

185. Freitag, S.; Le Trong, I.; Klumb, L.; Stayton, P. S.; Stenkamp, R. E., Structural studies of the streptavidin binding loop. *Protein Science* **1997,** 6, (6), 1157-1166.

186. Weber, P. C.; Cox, M. J.; Salemme, F. R.; Ohlendorf, D. H., Crystallographic data for Streptomyces avidinii streptavidin. *Journal of Biological Chemistry* **1987,** 262, (26), 12728-12729.

187. Weber, P. C.; Ohlendorf, D. H.; Wendoloski, J. J.; Salemme, F. R., Structural origins of high-affinity biotin binding to streptavidin. *Science* **1989,** 243, (4887), 85-88.

188. Green Michael, N., Avidin-Biotin Technology. *Methods in Enzymology* **1990,** 184, 51-67.

189. Tausig, F.; Wolf, F. J., Streptavidin - a substance with avidin-like properties produced by microorganisms. *Biochemical and Biophysical Research Communications* **1964,** 14, 205-209.

190. Freitag, S., Department of Biological Structure, University of Washington, http://faculty.washington.edu/stenkamp/stefanieweb/abstract.html

191. Knoll, W.; Zizlsperger, M.; Liebermann, T.; Arnold, S.; Badia, A.; Liley, M.; Piscevic, D.; Schmitt, F.-J.; Spinke, J., Streptavidin arrays as supramolecular architectures in surface-plasmon optical sensor formats. *Colloids and Surfaces A* **2000,** 161, 115-137.

192. Su, X.; Wu, Y.-J.; Robelek, R.; Knoll, W., Surface Plasmon Resonance Spectroscopy and Quartz Crystal Microbalance Study of Streptavidin Film Structure Effects on Biotinylated DNA Assembly and Target DNA Hybridization. *Langmuir* **2005,** 21, 348-353.

193. Yue, M.; Stachowiak, J. C.; Henry, L.; Ram, D.; Richard, C.; Arun, M., Label-Free Protein Recognition Two-Dimensional Array Using Nanomechanical Sensors. *Nano Letters* **2008,** 8, (2), 520-528.

194. Pritchard, D. J.; Morgan, H.; Cooper, J. M., Micron-Scale Patterning of Biological Molecules. *Angewandte Chemie International Edition* **1995,** 34, 91-93.

195. Kim, K., Protein Patterning Based on Electrochemical Activation of Bioinactive Surfaces with Hydroquinone-Caged Biotin. *Journal of the American Chemical Society* **2004,** 126, 15368-15369.

196. Weisser, M.; Tovar, G.; Mittler-Neher, S.; Knoll, W.; Brosinger, F.; Freimuth, H.; Lacher, M.; Ehrfeld, W., Specific bio-recognition reactions observed with an integrated Mach–Zehnder interferometer. *Biosensors and Bioelectronics* **1999,** 14, (4), 405-411.

197. Reviakine, I.; Brisson, A., Streptavidin 2D Crystals on Supported Phospholipid Bilayers: Toward Constructing Anchored Phospholipid Bilayers. *Langmuir* **2001,** 17, 8293-8299.

198. Reznik, G. O.; Vajda, S.; Cantor, C. R.; Sano, T., A Streptavidin Mutant Useful for Directed Immobilization on Solid Surfaces. *Bioconjugate Chemistry* **2001,** 12, 1000-1004.

199. Baselt, D. R.; Lee, G. U.; Hansen, K. M.; Chrisey, L. A.; Colton, R. L., A high-sensitivity micromachined biosensor. *Proceedings of the IEEE* **1997,** 85, (4), 672-680.

200. Bhushan, B.; Tokachichu, D. R.; Keener, M. T.; Lee, S. C., Morphology and adhesion of biomolecules on silicon based surfaces. *Acta Biomaterialia* **2005,** 1, 327-341.

201. Ebersole, R. C.; Miller, J. A.; Moran, J. R.; Ward, M. D., Spontaneously Formed Functionally Active Avidin Monolayers on Metal Surfaces: A Strategy for Immobilizing Biological Reagents and Design of Piezoelectric Biosensors. *Journal of the American Chemical Society* **1990,** 112, 3239-3241.

202. Johannsmann, D.; Reviakine, I.; Richter, R. P., Dissipation in films of adsorbed nanospheres studied by quartz crystal microbalance (QCM). *Analytical Chemistry* **2009,** 81, (19), 8167-8176.

203. Reimhult, K.; Petersson, K.; Krozer, A., QCM-D Analysis of the Performance of Blocking Agents on Gold and Polystyrene Surfaces. *Langmuir* **2008,** 24, (16), 8695-8700.

204. Pierce Biotechnology, Product instructions for Blocker BSA (Art.-No. 37525). In.

205. Hedge, P.; Qi, R.; Abernathy, K.; Gay, C.; Dharap, S.; Hughes, J. E.; Snesrud, E.; Lee, N.; Quackenbush, J., A Concise Guide to cDNA Microarray Analysis. *Biotechniques* **2000,** 29, 548-550.

206. Knoll, W., Interfaces and thin films as seen by bound electromagnetic waves. *Annual Review of Physical Chemistry* **1998,** 49, 569-638.

207. Liebermann, T.; Knoll, W., Surface-plasmon field-enhanced fluorescence spectroscopy. *Colloids and Surfaces A* **2001,** 171, 115-130.

208. Savage, M. D., *Avidin-Biotin Chemistry: A Handbook*. Pierce Chemical Co.: **1992**.

209. Pierce Biotechnology, Product instructions for NeutrAvidin Biotin-Binding Protein (Art.-No. 31000) In.

210. *Techniques in Immunocytochemistry*. Academic Press: London/New York, **1983;** Vol. 2, p 236.

211. Parsegian, V. A.; Gingell, D., On the electrostatic interaction across a salt solution between two bodies bearing unequal charges. *Biophys J* **1972,** 12, (9), 1192-1204.

212. Israelachvili, J. N., *Intermolecular and Surface Forces*. Second Edition ed.; Academic Press: **1991**.

213. Ying, P.; Yu, Y.; Jin, G.; Tao, Z., Competitive protein adsorption studied with atomic force microscopy and imaging ellipsometry. *Colloids and Surfaces B - Biointerfaces* **2003,** 32, (1-10).

214. Larrson, C.; Rodahl, M.; F., H., Characterization of DNA Immobilization and Subsequent Hybridization on a 2D Arrangement of Streptavidin on a Biotin-Modified Lipid Bilayer Supported on SiO2. *Anal. Chem.* **2003,** 75, 5080-5087.

215. Pasche, S.; De Paul, S. M.; Vörös, J.; Spencer, N. D.; Textor, M., Poly(L-lysine)-graft-poly(ethylene glycol) Assembled Monolayers on Niobium Oxide Surfaces: A Quantitative Study of the Influence of Polymer Interfacial Architecture on Resistance to Protein Adsorption by ToF-SIMS and in Situ OWLS. *Langmuir* **2003,** 19, 9216-9225.

216. Herrwerth, S.; Rosendahl, T.; Feng, C.; Fick, J.; Eck, W.; Himmelhaus, M.; Dahint, R.; Grunze, M., Covalent Coupling of Antibodies to Self-Assembled Monolayers of Carboxy-Functionalized Poly(ethylene glycol): Protein Resistance and Specific Binding of Biomolecules†. *Langmuir* **2003,** 19, 1880-1887.

217. Bonanno, L. M.; DeLouise, L. A., Steric Crowding Effects on Target Detection in an Affinity Biosensor. *Langmuir* **2007,** 23, 5817-5823.

218. Shu, W.; Laue, E. D.; Seshia, A. A., Investigation of biotin-streptavidin binding interactions using microcantilever sensors. *Biosensors and Bioelectronics* **2007,** 22, (9-10), 2003-2009.

219. Blümmel, J. Entwicklung biofunktionalisierter Nanostrukturen an Grenzflächen zur Untersuchung der Kinetik des molekularen Motorproteins Eg5. Ruprecht-Karls Universität, Heidelberg, **2005**.

220. Michel, B.; Rohrer, H.; Ringsdorf, H.; Häußling, L., Rastertunnelmikroskopische Beobachtung von spezifisch adsorbiertem Streptavidin auf Biotin-funktionalisierten, selbstorganisierten Monoschichten. *Angewandte Chemie* **1991,** 103, (5), 568-572.

221. Richter, R. P.; Brisson, A., Characterization of Lipid Bilayers and Protein Assemblies Supported on Rough Surfaces by Atomic Force Microscopy. *Langmuir* **2003,** 19, (5), 1632-1640.

222. Lohmüller, T. Nanostructured functional Materials. Ruprecht-Karls-Universität, Heidelberg, **2008**.

223. Richter, R. P. The Formation of Solid-Supported Lipid Membranes and Two-Dimensional Assembly of Proteins. A Study Combining Atomic Force Microscopy and Quartz Crystal Microbalance with Dissipation Monitoring. Université Bordeaux I, **2004**.

224. Banerji, S.; Hide, B. R. S.; James, J. R.; Noble, M. E. M.; Jackson, D. G., Distinctive properties of the hyaluronan binding domain in the lymphatic endothelial receptor Lyve-1 and their implications for receptor function. *Journal of Biological Chemistry* **2009,** in press.

225. Lesley, J.; Hascall, V. C.; Tammi, M.; Hyman, R., Hyaluronan Binding by Cell Surface CD44. *The Journal of Biological Chemistry* **2000,** 275, (35), 26967-26975.

226. Mammen, M.; Seok-Ki, C.; Whitesides, G., M., Polyvalent Interactions in Biological Systems: Implications for Design and Use of Multivalent Ligands and Inhibitors. *Angewandte Chemie International Edition* **1998,** 37, (20), 2754-2794.

227. Mammen, M.; Dahmann, G.; Whitesides, G. M., Effective inhibitors of hemagglutination by influenza virus synthesized from polymers having active ester groups. Insight into mechanism of inhibition. *Journal of Medicinal Chemistry* **1995,** 38, (21), 4179-4190.

228. Lees, W. J.; Spaltenstein, A.; Kingery-Wood, J. E.; Whitesides, G. M., Polyacrylamides bearing pendant alpha-sialoside groups strongly inhibit agglutination of erythrocytes by influenza A virus: multivalency and steric stabilization of particulate biological systems. *Journal of Medicinal Chemistry* **1994,** 37, (20), 3419-3433.

229. Marcon, L.; Choe, H.; Martin, K. A.; Farzan, M.; Ponath, P. D.; Wu, L.; Newman, W.; Gerard, N.; Gerard, C.; Sodroski, J., Utilization of C-C chemokine receptor 5 by the envelope glycoproteins of a pathogenic simian immunodeficiency virus, SIVmac239. *Journal of Virology* **1997,** 71, (3), 2522-2527.

230. Barcroft, J.; Hill, A. V., The nature of oxyhemoglobin, with a note on its molecular weight. *The Journal of Physiology* **1910,** 39, (6), 411-428.

231. In *Hill, A. V.*, The Journal of Physiology, Proceedings of the physiological society: January 22, 1910i-vii.

232. Whitty, A., Cooperativity and biological complexity. *Nature Chemical Biology* **2008,** 4, (8), 435-439.

233. Loll, P. J.; Axelsen, P. H., The Structural Biology of Molecular Recognition by Vancomycin. *Annual Review of Biophysics and Biomolecular Structure* **2000,** 29, (1), 265-289.

234. Kraft, M. L.; Foster Fishel, S.; Galli Marxer, C.; Weber, P. K.; Hutcheon, I. D.; Boxer, S., Quantitative analysis of supported membrane composition using the NanoSIMS. *Applied Surface Science* **2006,** 252, 6950-6956.

235. Reimhult, E.; Kasemo, B.; Hook, F., Rupture pathway of phosphatidylcholine liposomes on silicon dioxide. *International Journal of Molecular Sciences* **2009,** 10, (4), 1683-1696.

236. Scomparin, C.; Lecuyer, S.; Ferreira, M.; Charitat, T.; Tinland, B., Diffusion in supported lipid bilayers: Influence of substrate and preparation technique on the internal dynamics. *European Physical Journal E* **2009,** 28, 211-220.

237. Lata, S.; Reichel, A.; Brock, R.; Tampé, R.; Piehler, J., High-Affinity Adaptors for Switchable Recognition of Histidine-Tagged Proteins. *Journal of the American Chemical Society* **2005,** 127, (29), 10205-10215.

238. Lata, S.; Piehler, J., Stable and functional immobilization of histidine-tagged proteins via multivalent chelator headgroups on a molecular poly(ethylene glycol) brush. *Analytical Chemistry* **2005,** 77, (4), 1096-105.

239. Huber, R.; Romisch, J.; Paques, E. P., The crystal and molecular structure of human annexin V, an anticoagulant protein that binds to calcium and membranes. *EMBO J* **1990,** 9, (12), 3867-74.

240. Huber, R.; Schneider, M.; Mayr, I.; Romisch, J.; Paques, E. P., The calcium binding sites in human annexin V by crystal structure analysis at 2.0 A resolution. Implications for membrane binding and calcium channel activity. *FEBS Letters* **1990,** 275, (1-2), 15-21.

241. Brisson, A.; Olofsson, A.; Ringler, P.; Schmutz, M.; Stoylova, S., Two-dimensional crystallization of proteins on planar lipid films and structure determination by electron crystallography. *Biology of the Cell* **1994,** 80, (2-3), 221-228.

242. Nilsson, B.; Moks, T.; Jansson, B.; Abrahmsen, L.; Elmblad, A.; Holmgren, E.; Henrichson, C.; Jones, T. A.; Uhlen, M., A synthetic IgG-binding domain based on staphylococcal protein A. *Protein Engineering* **1987,** 1, (2), 107-113.

243. Langone, J. J., Protein A of Staphylococcus aureus and related immunoglobulin receptors produced by streptococci and pneumonococci. *Advances in Immunology* **1982,** 32, 157-252.

244. Deisenhofer, J., Crystallographic refinement and atomic models of a human Fc fragment and its complex with fragment B of protein A from Staphylococcus aureus at 2.9- and 2.8-A resolution. *Biochemistry* **1981,** 20, (9), 2361-2370.

245. Berat, R. Assemblages 2D de l`Annexine A5; Applications biotechnologiques & Aspects fonctionnels. Universite Bordeaux 1 Bordeaux **2007**.

246. Richter, R. P.; Brisson, A., QCM-D on mica for parallel QCM-D - AFM studies. *Langmuir* **2004,** 20, (11), 4609-4613.

247. Johannsmann, D.; Reviakine, I.; Richter, R. P., Dissipation in Films of Adsorbed Nanospheres Studied by QCM. *Analytical Chemistry* **2009,** 81, (19), 8167-8176.

248. Teriete, P.; Banerji, S.; Noble, M.; Blundell, C. D.; Wright, A. J.; Pickford, A. R.; Lowe, E.; Mahoney, D. J.; Tammi, M. I.; Kahmann, J. D.; Campbell, I. D.; Day, A. J.; Jackson, D. G., Structure of the regulatory hyaluronan binding domain in the inflammatory leukocyte homing receptor CD44. *Mol Cell* **2004,** 13, (4), 483-96.

249. Richter, R. P.; Bérat, R.; Brisson, A. R., The formation of solid-supported lipid bilayers - an integrated view. *Langmuir* **2006,** 22, (8), 3497-3505.

250. Bingen, P.; Wang, G.; Steinmetz, N. F.; Rodahl, M.; Richter, R. P., Solvation effects in the QCM-D response to biomolecular adsorption - a phenomenological approach. *Analytical Chemistry* **2008,** 80, (23), 8880-8890.

251. Benes, M.; Billy, D.; Benda, A.; Speijer, H.; Hof, M.; Hermens, W. T., Surface-dependent transitions during self-assembly of phospholipid membranes on mica, silica, and glass. *Langmuir* **2004,** 20, (23), 10129-10137.

252. Fleer, G. J.; Cohen Stuart, M. A.; Scheutjens, J. M. H. M.; Cosgrove, T.; Vincent, B., *Polymers at Interfaces*. Chapman & Hall: London, **1993**.

253. Visintin, A.; Mazzoni, A.; Spitzer, J. H.; Wyllie, D. H.; Dower, S. K.; Segal, D. M., Regulation of Toll-like receptors in human monocytes and dendritic cells. *J Immunol* **2001,** 166, (1), 249-55.

254. Alves, C. S.; Burdick, M. M.; Thomas, S. N.; Pawar, P.; Konstantopoulos, K., The dual role of CD44 as a functional P-selectin ligand and fibrin receptor in colon carcinoma cell adhesion. *American Journal of Physiology - Cell Physiology* **2008,** 294, C907-916.

255. Nijenhuis, N.; Mizuno, D.; Spaan, J. A.; Schmidt, C. F., Viscoelastic response of a model endothelial glycocalyx. *Phys Biol* **2009,** 6, (2), 25014.

256. Boehm, H.; Mundinger, T. A.; Boehm, C. H. J.; Hagel, V.; Rauch, U.; Spatz, J. P.; Curtis, J. E., Mapping the mechanics and macromolecular organization of hyaluronan-rich cell coats. *Soft Matter* **2009,** 5, 4331-4337.

257. Lee, G. M.; Johnstone, B.; Jacobson, K.; Caterson, B., The Dynamic Structure of the Pericellular Matrix on Living Cells. *Journal of Cell Biology* **1993,** 123, (6), 1899-1907.

258. Richter, R. P.; Hock, K. K.; Burkhartsmeyer, J.; Boehm, H.; Bingen, P.; Wang, G.; Steinmetz, N. F.; Evans, D. J.; Spatz, J. P., Membrane-Grafted Hyaluronan Films: a Well-Defined Model System of Glycoconjugate Cell Coats. *Journal of the American Chemical Society* **2007,** 127, (17), 5306-5307.

259. Hardingham, T. E., The role of link-protein in the structure of cartilage proteoglycan aggregates. *Biochemical Journal* **1979,** 177, (1), 237-247.

260. Lesley, J.; Hyman, R.; Kincade, P. W.; Frank, J. D., CD44 and Its Interaction with Extracellular Matrix. In *Advances in Immunology*, Academic Press: **1993;** Vol. Volume 54, pp 271-335.

261. Nichols, B. A.; Bainton, D. F.; Farquhar, M. G., Differentiation of monocytes. Origin, nature, and fate of their azurophil granules. *J Cell Biol* **1971,** 50, (2), 498-515.

262. Graeter, S. V.; Huang, J.; Perschmann, N.; Lopez-Garcia, M.; Kessler, H.; Ding, J.; Spatz, J. P., Mimicking Cellular Environments by Nanostructured Soft Interfaces. *Nano Letters* **2007,** 7, (5), 1413-1418.

263. Dahlin, A.; Zäch, M.; Rindzevicius, T.; Käll, M.; Sutherland, D. S.; Höök, F., Localized Surface Plasmon Resonance Sensing of
Lipid-Membrane-Mediated Biorecognition Events. *JACS* **2005,** 127, 5043-5048.

264. Glass, R.; Arnold, M.; Blümmel, J.; Küller, A.; Möller, M.; Spatz, J. P., Micro-Nanostructured Interfaces Fabricated by the Use of Inorganic Block Copolymer Micellar Monolayers as Negative Resist for Electron-Beam Lithography. *Advanced Functional Materials* **2003,** 13, (7), 569-575.

265. Hanarp, P.; Sutherland, D. S.; Gold, J.; Kasemo, B., Control of nanoparticle film structure for colloidal lithography. *Colloids and Surfaces A: Physicochemical and Engineering Aspects* **2003,** 214, (1-3), 23-36.

266. Izzo, D.; Marques, C. M., Formation of micelles of diblock and triblock copolymers in a selective solvent. *Macromolecules* **2002,** 26, (26), 7189-7194.

267. Spatz, J. P.; Thomas, H.; Stefan, M. m.; Paul, Z.; Martin, M., Micellar Inorganic-Polymer Hybrid Systems - A Tool for Nanolithography. *Advanced Materials* **1999,** 11, (2), 149-153.

268. Kästle, G.; Boyen, H. G.; Weigl, F.; Lengl, G.; Herzog, T.; Ziemann, P.; Riethmüller, S.; Mayer, O.; Hartmann, C.; Spatz, J. P.; Möller, M.; Ozawa, M.; Banhart, F.; Garnier, M. G.; Oelhafen, P., Micellar Nanoreactors - Preparation and Characterization of Hexagonally Ordered Arrays of Metallic Nanodots. *Advanced Functional Materials* **2003,** 13, (11), 853-861.

269. Meiners, J. C.; Elbs, H.; Ritzi, A.; Mlynek, J.; Krausch, G., Chemically functionalized surfaces from ultrathin block-copolymer films. *Journal of Applied Physics* **1996,** 80, (4), 2224-2227.

270. Hirschfeld-Warneken, V. C.; Arnold, M.; Cavalcanti-Adam, A.; Lopez-Garcia, M.; Kessler, H.; Spatz, J. P., Cell adhesion and polarisation on molecularly defined spacing gradient surfaces of cyclic RGDfK peptide patches. *European Journal of Cell Biology* **2008,** 87, (8-9), 743-750.

271. Blümmel, J.; Perschmann, N.; Aydin, D.; Drinjakovic, J.; Surrey, T.; Lopez-Garcia, M.; Kessler, H.; Spatz, J. P., Protein repellent properties of covalently attached PEG coatings on nanostructured SiO(2)-based interfaces. *Biomaterials* **2007,** 28, (32), 4739-4747.

272. Gregoriadis, G., *Interactions of Liposomes with the Biological Milieu*. 2 ed.; CRC-Press: **1992;** Vol. III.

273. Benes, M.; Billy, D.; Benda, A.; Speijer, H.; Hof, M.; Hermens, W. T., Surface-Dependent Transitions during Self-Assembly of Phospholipid Membranes on Mica, Silica, and Glass. *Langmuir* **2004,** 20, (23), 10129-10137.

274. Becherer, G.; Herms, G.; Ahrenholz, P., Die Ermittlung von radialen Verteilungsfunktionen aus dem Beugungsbild 2-Dimensionaler Strukturen. *Annalen der Physik* **1966,** 17, (3), 166-176.

275. Angelescu, D. E.; Harrison, C. K.; Trawick, M. L.; Register, R. A.; Chaikin, P. M., Two-Dimensional Melting Transition Observed in a Block Copolymer *Physical Review Letters* **2005,** 95, 025702.

276. Murray, C. A.; Van Winkle, D. A., Experimental observation of two-dimensional melting in a classical, two-dimensional screened coulomb system. *Physical Review Letters* **1987,** 58, (12), 1200-1204.

277. Halperin, B. I.; Nelson, D. R., Theory of two-dimensional melting. *Physical Review Letters* **1978,** 41, (2), 121-124.

278. Nelson, D. R.; Halperin, B. I., Dislocation-mediated melting in two dimensions. *Physical Review B* **1979,** 19, (5), 2457-2484

279. Rodahl, M.; Kasemo, B., On the measurement of thin liquid overlayers with the quartz-crystal microbalance. *Sensors and Actuators A: Physical* **1996,** 54, (1-3), 448-456.

280. Rodahl, M.; Hook, F.; Kasemo, B., QCM Operation in Liquids: An Explanation of Measured Variations in Frequency and Q Factor with Liquid Conductivity. *Analytical Chemistry* **1996,** 68, (13), 2219-2227.

281. Cuypers, P. A.; Corsel, J. W.; Janssen, M. P.; Kop, J. M. M.; Hermens, W. T.; Hemker, H. C., The Adsorption of Prothrombin to Phosphatidylserine Multilayers Quantitated by Ellipsometry. *Journal of Biological Chemistry* **1983,** 258, (4), 2426-2431.

282. Gordon, R.; Sinton, D.; Kavanagh, K. L.; Brolo, A. G., A new generation of sensors based on extraordinary optical transmission. *Accounts of Chemical Research* **2008,** 41, (8), 1049-1057.

283. Domack, A.; Prucker, O.; Rühe, J.; Johannsmann, D., Swelling of a polymer brush probed with a quartz crystal resonator. *Physical Review E* **1997,** 56, (1), 680-689.

284. Goncalves, D.; Irene, E. A., Fundamentals and applications of spectroscopic ellipsometry. *Quimica Nova* **2002,** 25, (9), 794-800.

285. Feijter, J. A. d.; Benjamins, J.; Veer, F. A., Ellipsometry as a Tool to Study the Adsorption Behavior of Synthetic and Biopolymers at the Air- Water Interface. *Biopolymers* **1978,** 17, 1759-1772.

286. Salamon, Z.; Tollin, G., Optical anisotropy in lipid bilayer membranes: coupled plasmon-waveguide resonance measurements of molecular orientation, polarizability, and shape. *Biophysical Journal* **2001,** 80, (3), 1557-1567.

287. Sober, H. A., *Handbook of Biochemistry*. The Chemical Rubber Co.: Cleveland, Ohio, **1960**.

288. Eisele, N. B.; Frey, S.; Piehler, J.; Görlich, D.; Richter, R. P., Ultrathin nucleoporin FG repeat films and their interaction with nuclear transport receptors. **submitted**.

289. Daimon, M.; Masumura, A., Measurement of the refractive index of distilled water from the near-infrared region to the ultraviolet region. *Applied Optics* **2007,** 46, (18), 3811-3820.

290. Lide, D. R., *Handbook of Chemistry and Physics*. 85 ed.; CRC Press: Boca Raton, FL, USA, **2004**.

291. Ploem, J. S., *Reflection-Contast Microscopy as a Tool for Investigation of the Attachment of Living Cells to a Glass Surface*. Blackwell Scientific: Oxford, **1975**.

292. Forschungszentrum, J.; http://www.fz-juelich.de/ibn/IBN4_RICM_en; 2008, O. http://www.fz-juelich.de/ibn/IBN4_RICM_en

293. Schilling, J.; Sengupta, K.; Goennenwein, S.; Bausch, A. R.; Sackmann, E., Absolute interfacial distance measurements by dual-wavelength reflection interference contrast microscopy. *Physical Review E* **2004,** 69, (2 Pt 1), 021901.

294. Limozin, L.; Kheya, S., Quantitative Reflection Interference Contrast Microscopy (RICM) in Soft Matter and Cell Adhesion. *ChemPhysChem* **2009**, NA.

295. Kawagushi, S.; Imai, G.; Suzuki, J.; Miyahara, A.; Kitano, T.; Ito, K., Aqueous solution properties of oligoand poly(ethylene oxide) by static light scattering and intrinsic viscosity. *Polymer* **1997,** 38, 2885-2891.

296. Kim, A. J.; Manoharan, V. N.; Crocker, J. C., Swelling-based method for preparing stable, functionalized polymer colloids. *Journal of the American Chemical Society* **2005,** 127, (6), 1592-1593.

297. deGennes, P.-G., Wetting: statics and dynamics. *Reviews of modern Physics* **1985,** 57, (3), 827-863.

Appendix

Abbreviations

AnxA5	Annexin A5
Au	Gold
Av	Avidin
Ca^{2+}	Divalent Calcium ion
CD44	Cluster of differentiation 44; main HA surface receptor
DOPC	1,2-dioleoyl-*sn*-glycero-3-phosphocholine
DOPE-cap-biotin	1,2-dioleoyl-*sn*-glycero-3-phosphoethanolamine-N-(cap-biotinyl)
DOPS	1,2-dioleoyl-*sn*-glycero-3-phospho-L-serine
ECD	Extracellular domain
Fc-domain	Stalk-like domain of an IgG
HA	Hyaluronan (altern. hyaluronic acid, hyaluronate)
HABD	Hyaluronan binding domain
Hepes	2-(4-(2-Hydroxyethyl)- 1-piperazinyl)-ethansulfonsäure
N_2	Nitrogen
NaCl	Sodium chloride
NAv	Neutravidin
Ni^{2+}	Divalent nickel ion
NTA	Nitrilotriacetic acid
O_2	Oxygen
PBS	Phosphate buffered saline
PCC	Pericellular Coat
PEG	Polyethylenglycol
PPG	Polypropylenglycol
QCM-D	Quartz Crystal Microbalance with Dissipation Monitoring
RICM	Reflection Interference Contarst Microscopy
SAM	Self assembled monolayer
SAv	Streptavidin
SDS	Sodiumdodecylsulfate; surfactant
SEM	Scanning Electron Microscopy

SiO_2	Silicon dioxide, silica
SLB	Supported Lipid Bilayer
OEOA	Octadec-9-enyl-octadecyl-amine
-Z	Z-fragment, sugar binding domain from a subunit of protein A

Mathematical abbreviations

a	Kuhn length
c	Concentration
C	Material constant of a QCM-D sensor crystal
D	Distance
d	Thickness
G	Free energy
H	Enthalpy
h	Height
Hz	Hertz
k	Imaginary component of the refractive index
k_B	Botzmann constant, $k = 1.38 * 10^{-23}$ J/K
K_D	Dissosiation constant
l_c	Contour length
l_p	Persistence length
m	Mass
MSE	Mean square error
M_w	Molecular mass
n	Real component of the refractive index
N	Refractive index
N_A	Avogadro constant; $N_A = 6.022 * 10^{23}$ mol^{-1}
N_m	Number of monomers
R_F	Flory radius
R_g	Radius of gyration
S	Entropy

T	Temperature
Δ	Delta
ΔD	Shift in dissipation (as measured by QCM-D)
Δf	Shift in resonance frequency (as measured by QCM-D)
η	Viscosity
Θ	Surface coverage
λ	Wavelength
ν	Excluded volume exponent (Flory exponent)
ξ	Characteristic dimension of a blob
ρ	Density
σ	Grafting density
Ψ	Psi
ψ	Orientational order parameter

List of machines

Centrifuge, Eppendorf, MiniSpin	Eppendorf AG, Hamburg, Germany
Combined QCM-D/ellipsometer flowchamber E1	Q-Sense AB, Västra Frölunda, Sweden
Contact Angle Meter	DSA100, Krüss GmbH, Hamburg, Germany
Diener Pico, plasma chamber	Diener electronics GmbH + Co KG, Nagold, Germany
Ellipsometer EC-400	J. A. Woollam Co., Inc., Lincoln, USA
Hamamatsu Camera Cntroller ORCA-ER	Hamamtsu Photonics K.K., Japan
Liposome Extruder, LipoFast™	Avestin, Inc., Mannheim, Germany
NANOpure Diamond™ water system	Barnstead, Dubuque, USA
QCM-D, E4	Q-Sense AB, Västra Frölunda, Sweden
SEM, LEO1530	Zeiss SMT, Oberkochen, Germany
Shaker, Vibramax 100	Heidoplph Elektro GmbH & Co. KG, Kelheim, Germany

Sonicator Elmasonic S	Elma Hans Schmidtbauer GmbH & Co. KG, Singen, Germany
Syringe pump KDS230	KD Scientific Inc., Holliston MA
Tepla Dry Plasma Etcher, 100E	PVA TePla AG, Asslar, Germany
Thin Film Coating Chamber	BAL-TEC MED 020 Modular High Vaccum Coating System, Witten, Germany
Tip Sonicator Branson Sonofier® S-450A	Branson Ultrasonics Corp., Danbury, USA
UV tip cleaner, model UV.TC.220	Bioforce Nanoscience, Ames, USA
Zeiss Observer Z1, RICM	Carl Zeiss MicroImaging GmbH, Jena, Germany

List of Materials

Ammonia	Scharlab S.L., Barcelona, Spain
Annexin A5-Z	Prof. Alain Brisson, Université de Bordeaux 1, France
Biotin-PEG-disulfide	Polypure AS, Oslo, Norway
CD44 fusion proteins	Dr. Suneale Banerji, Prof. David Jachson, Oxford, UK
Cysteamin	Sigma-Aldrich Chemie GmbH, Munich, Germany
Chloroform $CHCl_3$	Scharlab S.L., Barcelona, Spain
Dental 2 component glue picodent twinsil	picodent Dental-Produktions- und Vertriebs-GmbH, Wipperfürth, Germany)
EGTA	Sigma-Aldrich Chemie GmbH, Munich, Germany
Ethanol p.A.	Scharlab S.L., Barcelona, Spain
Glas coverslips	Menzel Gläser, Braunschweig, Germany

Hepes	Sigma-Aldrich Chemie GmbH, Munich, Germany
HPDP-biotin	Pierce Biotechnology, Thermo Scientific, Rockford, USA
Hyaluronan oligomers (HA8)	Prof. Anthony Day, University of Manchester, UK
Hyaluronic acid, Select-HA®	Hyalose L.L.C., Oklahoma City, USA
Hydrogen peroxide 30%	Scharlab S.L., Barcelona, Spain
Imidazole	Sigma-Aldrich Chemie GmbH, Munich, Germany
methanol p.A.	Scharlab S.L., Barcelona, Spain
mPEG-urea	Jaques Blümmel, Universität Heidelberg
Neutravidin	Pierce Biotechnology, Thermo Scientific, Rockford, USA
$NiCl_2$	Sigma-Aldrich Chemie GmbH, Munich, Germany
PBS	Sigma-Aldrich Chemie GmbH, Munich, Germany
Phospholipids, bis-NTA EOEA	Prof. Jacob Piehler, Universität Osnabrück, Germany
Phospholipids, DOPC, DOPS, DOPE	Avanti Polar Lipids Inc., Alabaster, USA
Pluronic®, F-68	Sigma-Aldrich Chemie GmbH, Munich, Germany
Polystyrene Microbeads, 25µm	Polyscience, Eppelheim , Germany
QCM-D sensors	Q-Sense AB, Västra Frölunda, Sweden
SDS	Sigma-Aldrich Chemie GmbH, Munich, Germany
Streptavidin, Avidin, BSA, biotin-BSA,	Sigma-Aldrich Chemie GmbH, Munich, Germany
Sulfuric acid 98%	Scharlab S.L., Barcelona, Spain
Toluene	Merck
Triethylamine	Sigma-Aldrich Chemie GmbH, Munich, Germany
Ultrapure water	in house

Protocol for the PEGylation of polystyrene microspheres

Material:

- microbeads (2R = 25µm)
- Ultrapure water
- PEG-PPG-PEG triblock-copolymer (Pluronic®)
- Toluene

Step 1:

- Prepare a 1wt% solution of Pluronic in distilled water in a 5ml Schlenk:
  - 2.25 ml H_2O
  - 22.5 mg Pluronic
- Add washed particle solution (2R = 25µl; concentration stock: solid % = 2.68g/100ml)
  - 22.4 ul
- Stir on a magnetic strirrer (stirring at 300rpm) for 5 h at RT (cap Schlenk).

Step 2:

- Add 45µl of toluene and keep on stirring for 2 h (at 300rpm).

Step 3:

- For toluene stripping heat an oil bath to 98ºC
- Place the reaction vial in the bath and keep stirring (at 300rpm)
- Apply a slight nitrogen blow over the open Schlenk to remove toluene vapors
- Keep stirring until no toluene can be smelled any more

Step 4:

- To remove excess Pluronic add 1ml ultrapure water
- Centrifuge at 4100 rpm for 12 minutes
- Repeat procedure 5 times (if the solution remains turbid repeat up to 10x)

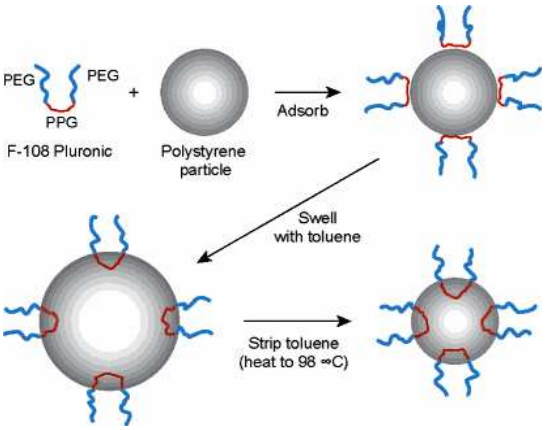

Original citation: A. J. Kim, V. N. Manoharan and J. C. Crocker "Swelling-Based Method for Preparing Stable, Functionalized Polymer Colloids" JACS 2005, 127, 1592-1593.
Protocol adapted from H. Böhm, MPI Stuttgart, Germany

Expression and purification of proteins

CD44 fusion proteins. The $HABD_2$-Fc construct was prepared in a modified version of the expression vector pCDM7Ig which encodes the hinge, CH2 and CH3 regions of human IgG1. The modification consisted of a linker inserted into the BamHI site such that a ten histidine tract followed by a TEV protease cleavage site (ENLYFQG) was placed in frame with the Fc coding sequence. The HABD region consisting of the first 170 residues of human CD44 (including the N-terminal signal peptide) was amplified using *Pyrococcus furiosus* (Pfu) DNA polymerase from full length human CD44 cDNA using the following primers:

huCD44 -12 HindIII For 5'CGCGaagcttCGCTCCGGACACCATGGACAAG3'

huCD44 465 BglII Rev 5'CGagatctGGGTAGATGTCTTCAGGATTCG3'

Appropriately digested PCR products were ligated into the modified pCDM7Ig vector that had been digested at the Hind III site and at a new BamHI site created at the 5' end of the linker. Candidate recombinant plasmids were sequenced to confirm integrity of the clones.

HEK 293T cells were transiently transfected and cultured in CHO-S-SFM II serum free medium (Invitrogen) for 3 days before supernatant was collected and passed over protein A sepharose (Sigma) before elution of the Fc fusion with 0.1 M glycine pH 3 followed by addition of 1/20 volume 2 M Tris HCl pH 8 to eluted fractions.

To produce monomeric his-HABD, DTT and EDTA were added (to final concentrations of 0.1 and 0.05 mM respectively) to samples of $HABD_2$-Fc prior to addition of AcTEV protease (Invitrogen) at a rate of 1 unit per 5 μg protein and digested for 2 h at 20^{o}C before removal of uncleaved fusion protein and digested Fc by passing the digest over protein A sepharose and removal of AcTEV protease by passing the sample over Ni-NTA agarose (Invitrogen). Finally, the digested monomeric HABD was subjected to gel filtration using a HiLoad 26/60 Superdex 75 pg chromatography column (GE Healthcare).

Danksagung

Mein erster, besonderer Dank geht an Herrn Prof. Joachim Spatz, der mir die Möglichkeit gegeben hat, in seiner Gruppe zu promovieren sowie an Herrn Dr. Ralf Richter, der meine Arbeit betreut hat. Herrn Spatz danke ich für die stets engagierte Unterstüzung, sowohl während meiner Zeit in Heidelberg als auch in San Sebastian. Herrn Richter danke ich für die Betreuung und Förderung, durch die ich in der Lage war, ein interessantes und spannendes Projekt zu bearbeiten. Vielen Dank, Ralf, für lange, manchmal anstrengende aber immer produktive Diskussionen und eine lehrreiche Zeit.

I would like to especially acknowledge Prof. Dr. Alain Brisson, who readily agreed to be referee for this thesis and for his interest in the topic.

Essential parts of this work would not have become reality without the support of Prof. David Jackson, Dr. Suneale Banerji, Prof. Alain Brisson, Prof. Anthony Day and Prof. Jacob Piehler, who readily provided the fusion proteins, hyaluronan and bis-NTA lipids. Extra thanks to Suneale Banerji for fruitful discussions about CD44 and his patience in explaining the biology of CD44 to a chemist and a physicist.

Mein Wechsel von Heidelberg nach San Sebastian, Spanien, brachte mit sich, dass ich in zwei Instituten mit zwei Arbeitsgruppen zusammen arbeiten durfte. Ich möchte meinen Dank daher unbedingt an beide richten. Vielen Dank an alle Heidelberger Kollegen, die mir bei einer Menge von kleineren und grösseren Problemen helfen konnten. Meinen Büromitstreitern, Aaron Lindner, Patrick Heil, Nadine Walter und später Vera Hirschfeld-Warneken, Mercedes Dragovits und Mark-Oliver Diesner danke ich für eine immer gute und entspannte Atmosphäre. Mark-Oliver und Nadine Perschmann muss besonders gedankt werden für die arbeitsgruppeninternen Tanzstunden, die viel zum Zusammenhalt und Spass in der unserer kleinen Runde beigetragen haben. Nicht zu vergessen sei die unverzichtbare administrative Arbeit unserer Sekräterinnen Frau Bozcek und Frau Schönig-Erdinger. Auf Stutgarter Seite stand Frau Pfeilmeier, der ich besonders danken möchte. Sie hat zusammen mit Frau Dierstein meine adminstrativen Belange auch während meines Aufenthalts in Spanien weiter bearbeitet und viel administrativen Stress von mir abgehalten.

Special thanks go to my "basque-ukrainian-indian-german" team in CICbiomaGUNE, Ixaskun Carton, Natalia Baranova, Seetharamaiah Attili (Ram) and Nico Eisele. It was a pleasure to start-up with you as a group in a new institute and to experience ourselves to become a real team. Eskerrrik asko, Ixaskun, por haberme recibido en tu país de una forma

mas amable, por ser una genial compañera, y, tambien, por ayudar corregir partes de mi tesis. Further I want to say thanks to Ram and Nico not only for sharing a lot of coffee and breakfast with me, but also for helpful discussions o RICM and ellipsometry. I also would like to thank Kathryn Melzcak, Marta Gallego Gonzalez and Santiago Fernández López, who carefully read chapters of this thesis and contributed with many suggestions and corrections. Many sincere thanks and "muchas gracias" to all other people from CICbiomaGUNE, whom I do not mention by name here. Thank you for helping at work, fruitful discussions or just for enjoyable company throughout the whole time in and outside of the institute. There have been many more people around me during the time in San Sebastian, who essentially contributed to make my live in San Sebastian be an unforgettable time. I would like to mention here, Manuela and Oscar, Paola and Davide, Yaiza, Itziar and "nanogune people".

Ich möchte nun den Menschen danken, die definitiv an erster Stelle meines Dankes stehen. Das sind meine Eltern und mein Freund Johannes. Ohne Euch, Mama und Papa, wäre weder mein Studium noch diese Doktorarbeit möglich gewesen. Ihr habt mich stets unterstützt, nie gebremst, in jeder Hinsicht immer gefördert und wart immer für mich da. Speziell in der letzten Phase dieser Arbeit habt ihr viel Geduld beim zuhören aufbringen müssen, wenn ich, oft müde, genervt oder ausgelaugt, viel mehr über mich und meine Arbeit gesprochen habe und viel zu wenig über Eure Belange. Ich hoffe, dass ich all das zurückgeben kann und diese Zeilen reichen bei weitem nicht aus, um meinen grossen, aufrichtigen Dank auszudrücken für all das, was eben nicht selbstverständlich ist.

Johannes, mein Freund und auch Kollege, hat mich über meine gesamte Doktorandendzeit hin begleitet, erst in Heidelberg, dann in San Sebastian. Unermüdlich stand er mir zur Seite, hat mich immer wieder neu motiviert. Besonders widerstandsfähig musste er in der letzten Phase meiner Arbeit sein. Er hat meine Arbeit Korrektur gelesen, die Fehler und Macken meines Computers behoben und mich mit Stimmungsschwankungen zwischen arbeitswütig und verzweifelt ertragen. Ich danke Dir, mein Liebling.

Ich erkläre hiermit, dass ich diese Dissertation selbst verfasst und mich keiner anderen ausser der von mir ausdrücklich bezeichneten Quellen und Hilfen bedient habe.

Heidelberg, den 07.01.2010 .....

Patricia Wolny